WELDING JOURNAL

JANUARY 2025

AI in Automotive Welding

Oxyfuel Tips

IN THIS ISSUE: 2025 AWS NATIONAL AND DISTRICT OFFICERS ■ DIVERSITY AND WELDING ■ LASER TECHNOLOGY

BUY THE BEST

BUY AMERICAN

PROUDLY MADE IN AMERICA

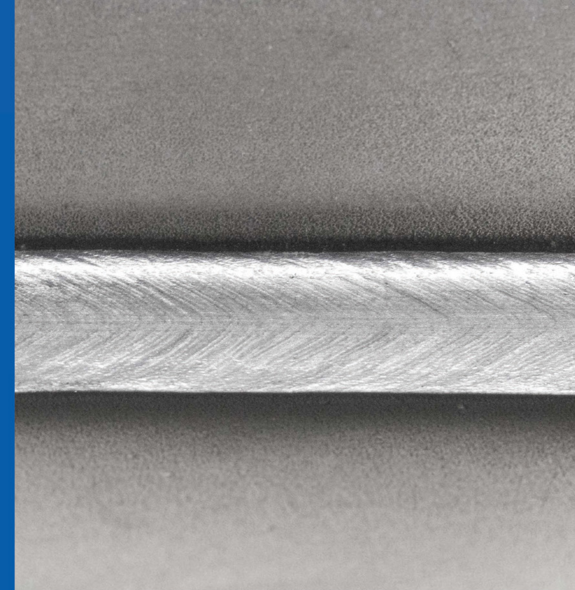

SelectAlloy 308L – Horizontal

SelectAlloy 308L-AP – Vertical Up

SELECT ARC INC.®

Ask your local distributor for SelectAlloy flux cored stainless products.

800-341-5215 | www.select-arc.com


NOZZLE STATION
NS-01
Maintenance the Nozzle
Within 6 sec
CONTAINS THE FUNCTION:
· Wire Cutter
· Nozzle Cleaner
· Anti spatter Spray
AUTO CONTACT TIP
CHANGER
CTC-001
Change the Contact Tip Within 40 sec Without Stopping the Production Line
Remove the Old Contact Tip
and Attach a New One Automatically!
tipman
AUTO CONTACT TIP
REFORMER
CTR-001
Automatically Reform
the Contact Tip and Recycle
Capable to feed
150 Contact tip
all at once
Automate the Maintenance
for Robotic Welding
tipman
info@tipman.jp
+1-859-413-7880
2526 Regency Rd, suite 140, Lexington, KY 40503

ACCOMPLISH THE MISSION!

DON'T MISS THESE EXPERT SPEAKERS!

Wayne Rivers
President
Performance Construction Advisors

REGISTRATION IS NOW OPEN!

Anirban Basu
Chairman & CEO
Sage Policy Group, Inc.

Randy Dye
President
Race to Stop Suicide

Heidi DeBenedetti
Chief Operating Officer
Gilbane Building Company

2025 IRON WORKERS/IMPACT CONFERENCE

FEBRUARY 23-26, 2025

DISNEY'S CORONADO SPRINGS RESORT

PROMINENT KEYNOTE SPEAKERS | VALUE-ADDED BREAKOUTS EXPLORING CONSTRUCTION INDUSTRY HOT TOPICS | TWO DAYS OF NETWORKING OPPORTUNITIES TO CONNECT WITH END USERS, CONTRACTORS & IRONWORKERS

Visit our website for more information www.impact-net.org

Email: info@impact-net.org | Phone: (202) 393-1147 or (800) 545-4921

January 2025 | Volume 104 | Number 1

CONTENTS

On the cover: 3D rendering of a modern car production line with robotic arms and welding components. (Credit: iStock/studio-fi.)

POINT OF VIEW

FEATURES

DEPARTMENTS

CONTENTS

January 2025 | Volume 104 | Number 1

WELDING RESEARCH SUPPLEMENT

OFFICERS

President Richard L. Holdren
Welding Consultants LLC/ARC Specialties

Vice President D. Joshua Burgess
Tennessee Valley Authority

Vice President Kerry E. Shatell
Pacific Gas & Electric Co.

Vice President J Jones
The Harris Products Group

Treasurer Mary Bihrle
Consultant

Interim Executive Director & CEO Robert "Bob" W. Roth
American Welding Society

DIRECTORS

R. Ashelford (Dist. 13), Rock Valley College
A. Blakeney (Dist. 9), Southeastern Louisiana University
B. Brandmeir (Dist. 3), Lehigh Career & Technical Institute
C. Brown (Dist. 18), Madskills Certified Welding Services
D. E. Clark (Dist. 20), DEClark Welding Engineering PLLC
A. Classens (Dist. 4), A. E. Classens & Associates
W. Doneth (Dist. 11), Fronius
R. Emery (Dist. 22), College of the Sequoias
R. E. Hilty (Dist. 7), Hilty Sign & Fabrication Co.
J. Jones (Dist. 16), Evergy Inc.
T. Jumper (Dist. 14), Lewis and Clark Community College
T. Kinnaman (Dist. 1), T. C. Kinnaman Welding Solutions
T. Kostreba (Dist. 10), Erie High School
V. Kuruvilla (Dist. 17), Lexicon Inc.
N. Martinez (Dist. 21), Salt River Project
J. Mixon (Dist. 2), Empirical Testing and Inspection LLC
B. Newcomb (Dist. 12), Madison College
W. F. Newell (At Large), Euroweld Ltd.
D. Peterson (Dist. 5), Central Maintenance and Welding
N. Peterson (At Large), Miller Electric Mfg. LLC
W. R. Polanin (Past President), WRP Associates
S. Raghunathan (At Large), Saudi Aramco
L. E. Showalter (At Large), Newport News Shipbuilding
M. M. Skiles (At Large), Consultant
R. H. Stahura (Dist. 6), ESAB Welding & Cutting Products
D. Szabla (Dist. 15), nVent—Hoffman Enclosures
J. Thompson (Dist. 8), Consultant
B. Towell (Dist. 19), Industrial Inspection & Services LLC
H. J. Wolf (At Large), Madison Area Technical College

WELDING JOURNAL

Publisher/Editor Annette Alonso

Editorial

Managing Editor Kristin Campbell
Sr. Editor Cindy Weihl
Associate Editor Roline Pascal
Associate Editor Alexandra Quiñones
Peer Review Coord. Brenda Flores
Peer Review Assistant Editor Tiffany Herrera
Peer Review Editor Thomas J. Lienert
Publisher Emeritus Jeff Weber

Design and Production

Managing Editor, Digital and Design Carlos Guzman
Production Manager Zaida Chavez
Assistant Production Manager Brenda Flores

Advertising

Senior Sales Executive Scott Beller
Manager, Sales Operations Lea Owen

Subscriptions

Subscriptions Representative Giovanni Valdes
gvaldes@aws.org

aws.org
8669 NW 36 St., # 130, Miami, FL 33166-6672
(305) 443-9353 or (800) 443-9353

AWS Mission Statement

The mission of the American Welding Society is to advance the science, technology, and application of welding and allied joining processes worldwide, including brazing, soldering, and thermal spraying.

AWS Promotes Diversity

AWS values diversity, advocates equitable and inclusive practices, and engages its members and stakeholders in establishing a culture in the welding community that welcomes, learns from, and celebrates differences among people. AWS recognizes that a commitment to diversity, equity, and inclusion is essential to achieving excellence for the Association, its members, and employees.

Welding Journal (ISSN 0043-2296 Print) (ISSN 2689-0445 Online) is published monthly by the American Welding Society for $150.00 per year in the United States and possessions, $195.00 per year in foreign countries: $15.00 per single issue. Not available for resale in either print or electronic form. American Welding Society is located at 8669 NW 36 St., # 130, Miami, FL 33166-6672; telephone (305) 443-9353. Periodicals postage paid in Miami, Fla., and additional mailing offices. POSTMASTER: Send address changes to *Welding Journal*, 8669 NW 36 St., # 130, Miami, FL 33166-6672. Canada Post: Publications Mail Agreement #40612608 Canada returns to be sent to Bleuchip International, P.O. Box 25542, London, ON N6C 6B2, Canada.

AWS Claims Policy: All hardcopy editions are shipped FOB Origin. Publisher reserves the right to investigate and make a determination on all claims submitted for missing editions not received by a subscribing member or institution. Any claim request determined to be valid will be fulfilled with a digital copy of the edition. Publisher will NOT send any hardcopy replacement issues for any reason.

Readers of the *Welding Journal* may make copies of articles for personal, archival, educational, or research purposes, and which are not for sale or resale. Permission is granted to quote from articles, provided customary acknowledgment of authors and sources is made. Starred (*) items excluded from copyright.

Copyright © 2025 by American Welding Society in both printed and electronic formats. The Society is not responsible for any statement made or opinion expressed herein. Data and information developed by the authors of specific articles are for informational purposes only and are not intended for use without independent, substantiating investigation on the part of potential users.

Welding: Strength through Diversity

Richard L. Holdren
AWS president

At first glance, the connection between diversity and welding might not seem obvious. However, after reflecting on this idea at a recent AWS Board meeting, I realized that diversity is a tremendous strength. In that room, I saw a various people with different professional backgrounds, technical expertise, and visions for the future of our industry. This diversity is a powerful force that drives innovation and success in welding.

In this article, I will highlight how diversity benefits various aspects of welding — its people, technologies, technical standards, career paths, and more.

People. People in welding come from various backgrounds and job categories, including welders, welding inspectors, technicians, engineers, and supervisors. In recent years, we've also seen an increase in women entering the field, which is a welcome change. These diverse perspectives contribute to the strength and innovation of the welding industry, and they continue to push the boundaries of what we can achieve.

But diversity means being diverse — having numerous qualities and elements — so welding's diversity expands beyond the people themselves.

Science and Technology. Various scientific phenomena occur at the point of welding. For an arc weld, there must be consideration given to physics, chemistry, thermodynamics, metallurgy, and mechanical properties. This interdisciplinary approach makes welding a rich and complex field, with technology benefiting from a range of scientific perspectives.

Welding Engineering. This field requires the selection and control of many factors, such as design, base and filler materials, process, control, quality, inspection, safety and health, and productivity and economics. By considering these diverse factors, a welding engineer is prepared to make decisions that ensure the integrity, safety, and efficiency of welded joints.

Processes and Materials. There are more than 100 joining and allied processes, such as welding, brazing, soldering, adhesive bonding, cutting and machining, thermal spraying, and more. These processes can be used to join just about any material. In addition to metals, there is also the joining of plastics, ceramics, and organics. AWS provides guidance for all these choices in terms of both selection and control.

Standards. AWS has produced over 350 technical standards for welding various materials, product forms, and sizes and thicknesses for many applications.

Education and Certification. With so many different job categories in welding, education and training play a critical role in career development. AWS provides a range of educational resources and training programs to help individuals gain the necessary skills to excel in the field. Whether through seminars, apprenticeships, or certifications, welding professionals constantly learn and adapt to new technologies and methodologies. The Certified Welding Inspector is one of the most recognized certifications, but AWS offers numerous other certifications that recognize expertise in various areas of welding. These certifications validate an individual's knowledge and experience, providing opportunities for job advancement both domestically and internationally.

Welding is a fascinating and rewarding career with endless opportunities for advancement. The diversity within our industry — whether in technologies, people, or processes — gives us the strength to adapt and innovate. For more than 50 years, I have witnessed the incredible growth and evolution of welding, and I continue to learn and mentor the next generation of welding professionals.

AWS plays a crucial role in fostering diversity, connecting people from different backgrounds and disciplines to advance the art, science, and technology of welding. By embracing diversity, we turn it into a source of strength. Let's continue celebrating diversity in our field, as it makes our industry stronger and more resilient than ever. WJ

"AWS plays a crucial role in fostering diversity, connecting people from different backgrounds and disciplines to advance the art, science, and technology of welding. By embracing diversity, we turn it into a source of strength."

QUANTUM
MACHINERY GROUP

YOUR TRUSTED PARTNER FOR METALWORKING MACHINERY & WELDING TABLES

SCAN HERE TO ORDER

siegmund®

ITEM NO. USWS168210.1
SYSTEM 16 IMPERIAL SERIES 32″x48″ WORKBENCH WELDING TABLE

IN-STOCK

21 PIECE PROMOTIONAL BUNDLE

x4 x8 x4 x4

BUNDLE VALUE OF ~~$2,595~~

- MAX WEIGHT : 550 lbs.
- WEIGHT: 221 lbs.
- MATERIAL THICKNESS: 0.5″
- WORKING HEIGHT: 32″- 38″
- TOOL STEEL + PLASMA NITRATION

$999
+$300 FLAT RATE SHIPPING

METALWORKING MACHINERY SPECIALS

WE STOCK THOUSANDS OF WELDING TABLES, MACHINES & TOOLS IN THE USA

IN-STOCK

$6,999 + SHIPPING

⌀ BEND UP TO 2″ O.D. ROUND TUBE

MC150B: ROLL BENDER

⌀ 4-1/4″ ROUND TUBE CAPACITY

$5,918 + SHIPPING

IN-STOCK

NEW 350 EDV: 14″ COLD SAW

- MAX. SCROLLING & BENDING OF FLAT BAR: 1-1/4″ x 3/8″

IN-STOCK

$9,999 + SHIPPING

MT150A: BAR TWISTING AND SCROLLING MACHINE

BE SURE TO VISIT US ONLINE OR CONTACT US FOR A QUOTE: *(704) 703-9400*

QUANTUM MACHINERY GROUP

NARGESA®

QUANTUM MACHINERY GROUP IS THE EXCLUSIVE USA IMPORTER OF NARGESA METALWORKING & ORNAMENTAL MACHINERY

SPECIAL PRICING IS VALID UNTIL 1/31/2025

NEW

PH50: POWER HAMMER

110 lbs. DROPPING STROKE

- STROKES PER MINUTE: 240 STROKES
- WEIGHT: 2,186 lbs.
- RAM RANGE: 7″
- MAX ROUND CAPACITY: 2.75″
- MAX SQUARE CAPACITY: 2.36″

$14,999
+ SHIPPING

NEW

PV21: HYDRAULIC HOT FORGING PRESS

23 TONS OF OPERATING POWER

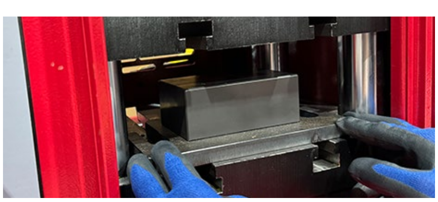

- STROKE LENGTH: 11.65″
- REPETITIVENESS: 0.001″
- OPERATING SPEED: 0.5″/s
- OPERATING HEIGHT: 40″
- BLOWS PER MINUTE: 22

$11,999
+ SHIPPING

ALL IN-STOCK ORDERS SHIP WITHIN 1-3 BUSINESS DAYS

QUANTUMMACHINERY.COM

(704) 703-9400

BYU and Toyota Collaborate to Improve Welding of Minivan Doors

Engineers at Brigham Young University (BYU), Provo, Utah, have teamed up with Toyota to develop a new welding technique that could significantly improve the strength, safety, and environmental footprint of the Toyota Sienna's automatic sliding doors.

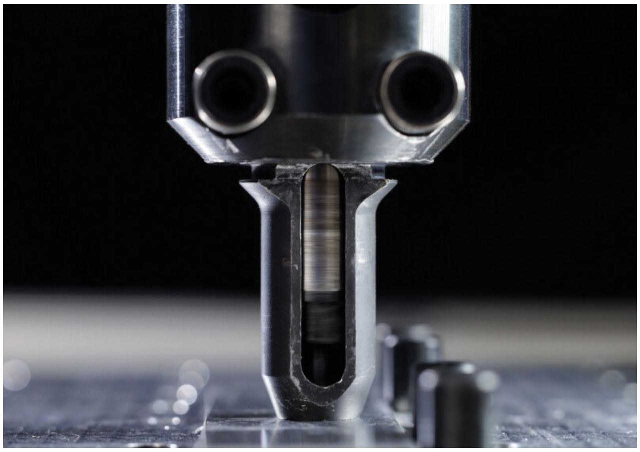

Refill friction stir spot welding joins the metal without ever melting it; the metal remains in a solid state. (Photo by Jaren Wilkey/BYU photo.)

The new process, known as refill friction stir spot welding, uses 40 times less energy, produces fewer emissions, and creates welds that are 10 times stronger than those made by traditional methods. The technique, designed to work with lightweight aluminum, could be crucial as automakers, including Toyota, increasingly rely on aluminum for vehicle body panels to reduce weight and improve fuel efficiency.

"Ultimately we are looking for ways to do things more efficiently, greener, and cleaner," said Yuri Hovanski, the BYU manufacturing engineering professor overseeing this project. "It is super exciting to demonstrate that what we're working on is helping the environment. Ultimately, as engineers, we believe in trying to be good stewards of the planet."

Aluminum has become a popular material in vehicle manufacturing due to its light weight, but welding it has posed challenges. Traditional resistance spot welding, designed for steel, doesn't perform as effectively on aluminum. Refill friction stir spot welding, by contrast, is tailored specifically for aluminum, adjusting the welding process to account for the metal's unique properties.

The new welding process joins the metal without ever melting it; the metal remains in a solid state. Pressure is applied and a pin is inserted into the metal, softened by friction. The two sheets of aluminum are stirred together with a tool, and when pressure is released, the hole fills in, leaving a strong quality joint. The new joints are also strong enough that fewer spot welds would be required in a vehicle. Since no filler material is required and less equipment is used, the new process cuts down on consumables, leading to greener manufacturing.

"Working with a partner like Toyota has been great because they are very sensitive to wanting to use cleaner technologies," Hovanski said. "It creates a meaningful situation that aligns well with our mission here at BYU."

Comau Delivers Assembly Solution for JMC Ford's Pickup Truck Manufacturing

Comau, Turin, Italy, a provider of industrial automation solutions, systems, products, services, advanced robotics, and digital manufacturing, has designed and deployed a flexible and comprehensive body-in-white (BIW) manufacturing solution for JMC Ford to produce high-end pickup trucks at the Xiaolan plant in China's Jiangxi province. The project established a production line capable of accommodating various models and configurations, including JMC Ford's new pickup truck brand Dadao and Ford's first pickup truck model introduced in the Chinese market, the Ranger. The fully scalable solution delivers a 100% automation rate while ensuring vehicle quality and performance.

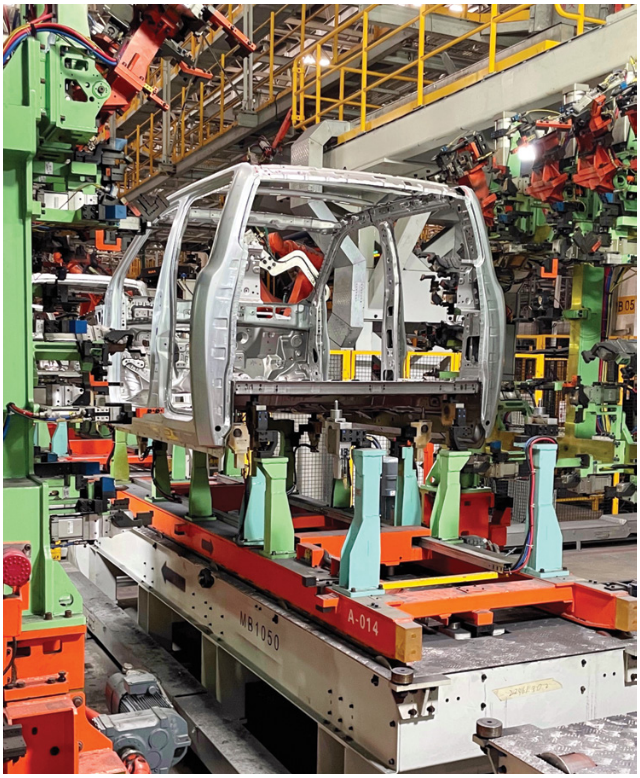

Comau's flexible welding automation solution has enabled a 3+1 multivehicle coproduction line with a 100% automation rate.

Comau's BIW welding solution improves welding accuracy and stability, thus ensuring the final product's structural integrity and safety. The solution also optimizes production processes and includes the adoption of advanced automation technologies to enhance production efficiency, reduce cycle times, and increase output. Incorporating both the welding and tightening guns within an integrated system minimizes the need for frequent tool changes. The solution also leverages advanced vision inspection technology for better quality control and allows the automaker to reduce its equipment investment and maintenance costs. The manufacturing setup also features Comau's OpenGate system, which ensures geometrical accuracy while granting inherent flexibility with an aggressive average switching cycle time of 50 seconds.

"Our goal was to create a more efficient, reliable, and flexible production line for the rapidly expanding pickup truck market, and we have achieved impressive outcomes," said Ma Jian, JMC Ford head of manufacturing engineering. "Partnering with Comau marks an important milestone in our journey toward manufacturing excellence. Comau's innovative approach and commitment to quality provide us with a solid foundation, paving the way for future advancement and continued success."

ISS National Lab-Sponsored Research to Test Cold Welding for Spacecraft Repairs

A new experiment aboard the International Space Station (ISS) aims to revolutionize spacecraft repairs by using cold welding, a technique that could offer a safer and more efficient method for patching hull breaches in space. The ASTROBEAT experiment, which arrived at the ISS on SpaceX's 31st Commercial Resupply Services mission, is exploring the potential of this technology to address damage caused by space debris or micrometeoroids.

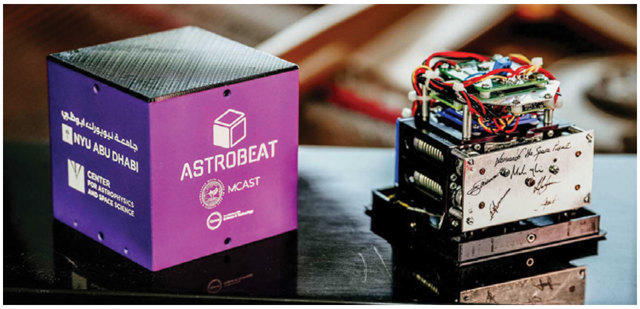

The Nanolab ASTROBEAT module hull and core side by side. (Photo credit: Dr. Leonardo Barilaro, the Malta College of Arts, Science & Technology.)

This project is spearheaded by Leonardo Barilaro, a senior lecturer in aerospace engineering at the Malta College of Arts, Sciences, and Technology (MCAST).

"Cold welding has long been considered an adverse phenomenon in space, but with ASTROBEAT, we're transforming a problem into a viable repair mechanism," Barilaro explained. "It aims to create a paradigm shift in conducting structural repairs in space — swiftly, efficiently, and with minimal external intervention."

Cold welding employs a calibrated force to join metallic materials without heat, minimizing risks like structural damage to spacecraft from high temperatures. This technique benefits from the space station's microgravity environment, where metals don't reoxidize quickly, allowing for cleaner and stronger bonds. The ASTROBEAT technology demonstration project will evaluate cold welding in space by testing metal patches on simulated spacecraft hulls, offering a safer and potentially more reliable method for in-orbit repairs than traditional techniques.

The remotely controlled experiment consists of four chambers with calibrated metallic samples. If successful, the project could establish cold welding as a crucial tool for in-space repair, significantly boosting the durability of spacecraft and the safety of crewed missions.

"The introduction of ASTROBEAT to the ISS represents a crucial step from theoretical concepts to practical, potentially life-saving technology," Barilaro added. "We aim to provide astronauts with the capability to seal breaches from within the spacecraft, leveraging the unique conditions of cold welding adhesion in space."

Upon completion of the space station testing, the project will return to Earth so the team can thoroughly analyze the cold-welded joints, assessing their effectiveness and resilience.

GM and Hyundai Explore Partnership on EVs, Clean Energy Tech, and More

General Motors (GM), Detroit, Mich., and Hyundai Motor Co., Seoul, South Korea, have signed an agreement to explore future collaboration across key strategic areas. The automakers will look for ways to leverage their complementary scale and strengths to reduce costs and bring a wider range of vehicles and technologies to users faster.

Potential collaboration projects center on codevelopment and production of passenger and commercial vehicles; internal combustion engines; and clean-energy, electric, and hydrogen technologies.

The two original equipment manufacturers will also review opportunities for combined sourcing in battery raw materials, steel, and other areas.

The framework agreement was signed by Hyundai Motor Group Executive Chair Euisun Chung and GM Chair and CEO Mary Barra.

"GM and Hyundai have complementary strengths and talented teams," Barra said. "Our goal is to unlock the scale and creativity of both companies to deliver even more competitive vehicles to customers faster and more efficiently."

"This partnership will enable Hyundai Motor and GM to evaluate opportunities to enhance competitiveness in key markets and vehicle segments, as well as drive cost efficiencies and provide stronger customer value through our combined expertise and innovative technologies," Chung said.

KEEL Funds $34.5 Million Expansion in Michigan Facilities and Capabilities

KEEL Holdings LLC, a high-end defense manufacturer, has invested $34.5 million in its Alma and Merrill, Mich., locations to expand a facility, purchase advanced machinery, and reinvest in workforce training programs.

At the Alma location, the company implemented a variety of manufacturing equipment to enhance production efficiency. Notable additions include the installation of a 4400-ton press brake for precise metal bending, a shotblasting machine for surface treatment, and a laser detection and ranging system for detailed measurement and inspection. Upgrades to existing software and the integration of a new rotary table into the ARC-05i cladding system have also been undertaken to optimize operational capabilities.

"Our Alma facility has long been at the forefront of welding innovation," said Brian Englehardt, Alma plant manager. "These new additions allow us to increase our throughput and continue delivering the high-quality products our customers expect. This investment reinforces our commitment to maintaining our leadership in welding and fabrication."

KEEL's Merrill location also underwent significant enhancements, including a 36,000-sq-ft expansion and the addition of four advanced high-speed 5-axis machining centers. This major investment enables the facility to efficiently handle

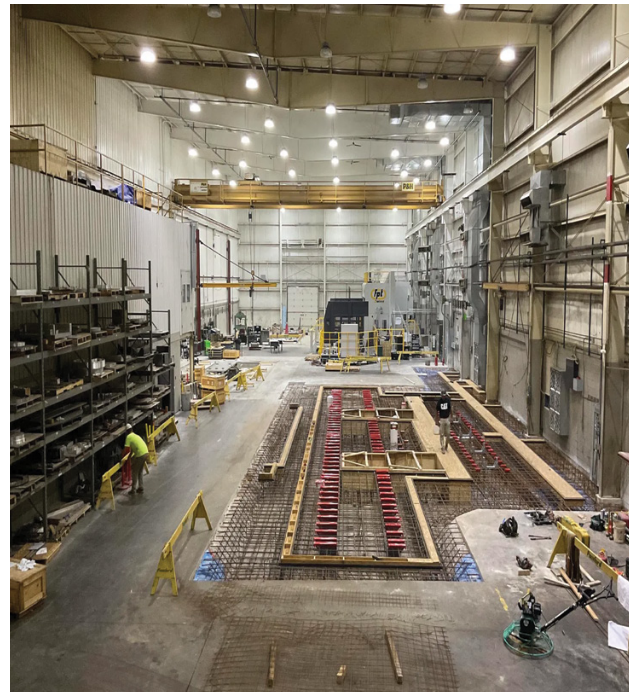

The 36,000-sq-ft expansion at Keel's Merrill location will accommodate four new advanced high-speed 5-axis machining centers.

AWS

American Welding Society®
FOUNDATION

$2.5 MILLION IN SCHOLARSHIPS

Let AWS Foundation scholarships help pay for school

This academic year, let AWS help foot the bill. Through the AWS Foundation, more than $2.5 million in scholarships are available for bachelor's, associate, and certificate-seeking students.

Scholarships range from $1,000 to $5,000 or more. No matter where you are in your academic journey, an AWS Foundation scholarship can be the extra support that helps you fulfill your goals.

The Deadline to Apply for National, District, and Section Scholarships is March 1st, 2025.

For more information on all scholarship programs, visit **aws.org/scholarships**

Stay Connected

aws.org

larger and more-complex projects. "We are excited about the expansion of our Merrill facility," said Troy Genow, Merrill plant manager. "This additional space and new machinery not only boost our capacity but also diversify the types of projects we can take on."

The company has also prioritized investment in the Merrill Institute, located within the Alma facility. The school has been providing students with comprehensive, hands-on welding training since its inception in 2011. Here, students have the opportunity to experience a manufacturing environment in action, learning from AWS-certified instructors.

India's Welspun Corp. to Invest $100 Million for Expanding U.S. Pipe Manufacturing

Welspun Corp, Mumbai, India, a welded line pipe manufacturer, plans to invest $100 million in upgrading its high-frequency induction welding pipe manufacturing and coating capabilities through its U.S. subsidiary, Welspun Pipes Inc.

The upgrade will allow the company to produce pipes with larger sizes, up to 24 in. O.D. and up to 0.750 in. wall thickness.

The expansion will strengthen Welspun Pipes' position in the U.S. oil and gas field, especially in the oil, liquids, gas, and distribution markets.

Industry Notes

■ **Lincoln Electric**, Cleveland, Ohio, is expanding its Buy America-compliant product offering. The company has enhanced its Buy America portfolio through its UltraCore® (gas shielded flux cored arc welding) product line. The Buy America policy emphasizes infrastructure procurement, and the Lincoln Electric Buy America portfolio assists customers in complying with four regulatory standards commonly encountered in government-funded projects: Buy America; Buy American; Build America, Buy America; and American Iron and Steel.

■ **Airgas**, Radnor, Pa., an Air Liquide company, has been awarded Gold Level Recognition on the 2025 Military Friendly® Employers list by VIQTORY for the third consecutive year, following three years at the Silver Level designation. Military Friendly identifies the organizations whose commitment to serving the military and veteran community is comprehensive in scope and meaningful in actual outcomes and impact.

■ **Konecranes**, Springfield, Ohio, will supply a fully customized 125-ton hoist crane, including a 15-ton auxiliary hoist and a top-running overhead crane with dual trolleys, to TerraPower's Natrium® Reactor Demonstration Plant (a TerraPower and GE-Hitachi technology project) in Wyoming. The order, from TerraPower's engineering, procurement, and construction partner Bechtel, was placed in June 2024, and delivery and installation of the crane system are planned for autumn 2025. WJ

BY RICHARD D. CAMPBELL

Q: During a recent shop visit where 304 stainless steel was being welded, a welder asked why some stainless steels are magnetic while others are not. Why is this the case?

A: The answer has to do with the chemical composition and metallurgical structure of the base metal and weld metal.

Historically, welding personnel learned a trick of the trade: To determine if a metal is stainless steel, use a magnet. If the metal is nonmagnetic, it is stainless steel. But that isn't true for all stainless steels.

The *Professional's Advisor on Welding of Stainless Steels* (Ref. 1) identifies five categories of stainless and provides the following definitions:

- Austenitic stainless steel: a stainless steel that contains chromium, nickel, and sometimes manganese, which produce austenite.
- Martensitic stainless steel: a stainless steel that contains chromium and carbon, which produce martensite.
- Ferritic stainless steel: a stainless steel that contains chromium (and often molybdenum), which produces ferrite.
- Duplex stainless steel: a stainless steel that contains chromium plus other alloying elements designed to produce a duplex structure at room temperature consisting of a mixture of austenite and ferrite.
- Precipitation-hardening stainless steel: a stainless steel that contains chromium plus other alloying elements designed to produce a hardened structure by precipitation of constituents. The main structure can be austenite, ferrite, or martensite.

Austenitic stainless steels are the most widely used of all stainless steels (Ref. 2). Austenitics, such as types 304 (18.0–20.0% Cr, 8.0–10.5% Ni, and 0.08% C maximum) and 316 (16.0–18.0% Cr, 10.0–14.0% Ni, and 0.08% C maximum), produce a face-centered cubic austenitic structure and are essentially nonmagnetic in the annealed condition. These steels can be cold worked, which produces some martensite and gives them some magnetic properties.

Depending on the chemical composition and cooling rate, some magnetic delta ferrite forms at high temperatures in the weld metal; this can be retained at room temperature. This delta ferrite helps reduce hot cracking. Various diagrams have been developed to predict the amount of delta ferrite in the austenitic stainless steel weld metal. Since this delta ferrite is magnetic, the amount of magnetism in the ferrite is used to evaluate its presence and amount through the use of a percent ferrite or Ferrite Number (FN). Magnetic instruments are available to measure the amount of magnetic ferrite (Ref. 3). Typically, 2–8% ferrite or FN is specified to reduce hot cracking.

Most diagrams that predict the amount of delta ferrite in austenitic stainless steels are based on the chromium and nickel equivalents, which reflect the effects of various elements on the formation of ferrite or austenite. An early diagram (Fig. 1) was the Schaeffler Diagram, a modified version of which shows weld metal structures based on various filler metals (Ref. 1) for different stainless steels. The top portion of this diagram is austenite, the bottom left is martensite, and the bottom right is ferrite. This diagram can also indicate the magnetic properties in the weld metal, keeping in mind that martensite and ferrite are magnetic; thus, the lower on the diagram, the more magnetic the weld. Therefore, 316 can be wholly austenitic or up to approximately 5% ferrite, and the weld metal may have some magnetic pull. Type 304 base metal would be represented on the diagram by 308 (the filler metal used on 304) and can have from 0 to about 20% delta ferrite. Types 410 and 430 contain martensite and ferrite (magnetic), while 446 contains nearly totally ferrite (and magnetic).

Martensitic stainless steels, such as types 403 and 410 (approximately 11.5–13.5% Cr, 0.15% C maximum), typically have a tempered martensite structure (body-centered tetragonal structure) with fine carbides (Ref 2). This martensite is magnetic and produces a strong response to a magnet.

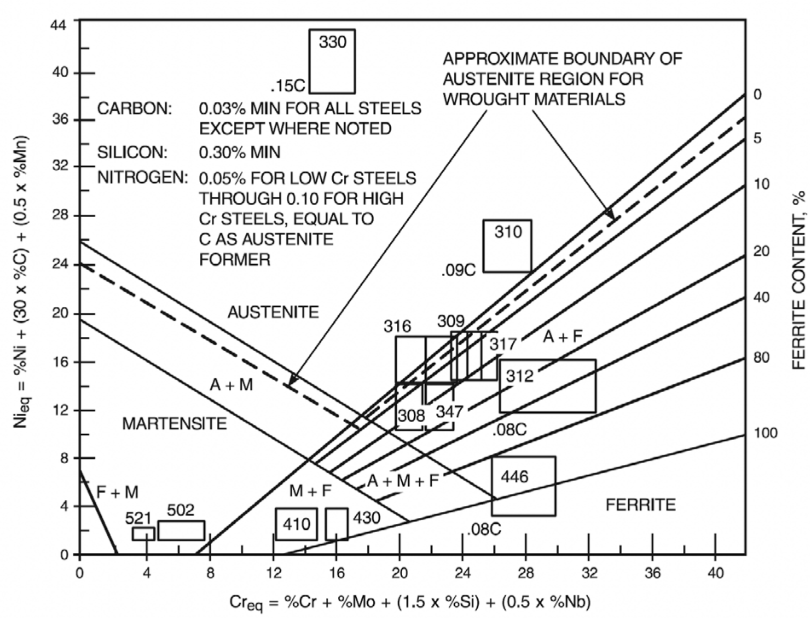

Fig. 1 — Schaeffler Diagram with superimposed weld metal (Ref. 1, page 79).

Ferritic stainless steels contain chromium and often other alloying elements with lower carbon content. Types 430 (16.0–18.0% Cr with 0.12% C maximum) and 446 (23.0–27.0% Cr with 0.20% C maximum) typically have a ferrite structure (body-centered cubic) with some martensite. Both ferrite and martensite are magnetic. Types 405 (11.5–14.5% Cr with 0.08% C maximum) and 409 (10.5–11.7% Cr with 0.030% C maximum) are predominantly ferrite but may contain small amounts of martensite. The superferritics, such as type 444 (17.5–19.5% Cr, 1% Mo, with 0.025% C maximum), are ferritic and, thus, magnetic.

Duplex stainless steels, such as 2205 (21.0–23.0% Cr and 4.5–6.5% Ni), are iron-chromium-nickel alloys that produce roughly 30–70% austenite and ferrite. Since ferrite is magnetic, these steels will be slightly magnetic.

Precipitation-hardening (PH) stainless steels form precipitates to harden them. There are three main categories: martensitic PH (mainly martensite or martensite with some ferrite), semiaustenitic PH (mainly austenite with some delta ferrite), and austenitic PH (austenite). The amount of magnetism depends on the amount of martensite or ferrite.

Summary

Austenitic stainless steel base metals will not form ferrite; however, when cold worked, some austenite can transform to magnetic martensite, which gives the base metal some magnetic properties. When austenitic stainless steels are welded, they typically produce some delta ferrite in the weld metal, which is magnetic, giving the weld metal some magnetic properties.

Martensitic and ferritic stainless steels have martensite and/or ferrite structures, both of which are magnetic. Duplex alloys contain 30–70% ferrite and austenite, so they are at least slightly magnetic. Some PH stainless steels are magnetic (martensitic or semiaustenitic). WJ

References

1. Campbell, R. D. 1999. *The Professional's Advisor on Welding of Stainless Steels*, 1–4, 79. Miami, Fla.: American Welding Society.

2. American Welding Society. 2011. *Welding Handbook*, Ninth Edition, 4: 255–391. Miami, Fla.: American Welding Society.

3. AWS A4.2M:2020 (ISO 8249:2018 MOD), *Standard Procedures for Calibrating Magnetic Instruments to Measure the Delta Ferrite Content of Austenitic and Duplex Ferritic-Austenitic Stainless Steel Weld Metal.* Miami, Fla.: American Welding Society.

RICHARD D. CAMPBELL, PhD, P.E., SCWI, is an AWS Fellow and contractor for AWS. He is a past chair of the D1K Subcommittee on Stainless Steel and a member of multiple AWS committees. Questions may be sent to Richard D. Campbell c/o *Welding Journal*, 8669 NW 36 St., #130, Miami, FL 33166-6672 or via email at *WeldingSol@aol.com.*

ESAB Sponsors Western Welding Academy's Blue Collar Tour

ESAB is backing Western Welding Academy's 2025 Blue Collar Tour, a 31-city American journey with a mission to get high school students interested in the skilled trades.

ESAB, North Bethesda, Md., a fabrication technology manufacturer, will sponsor Western Welding Academy's 2025 Blue Collar Tour, a 31-city U.S. journey aimed at encouraging high school students to explore skilled trades. At each stop, students can try gas tungsten arc welding with the Renegade VOLT™ ES 200i or Rebel™ EMP 205ic welding machines. The company will also donate Victor Medalist oxyacetylene welding kits, Goldrox 7018 electrodes, and Tweco® electrode holders to participating schools.

The Blue Collar Tour travels around the country with ten to 13 representatives from Western Welding Academy, a trade school located in Gillette, Wyo., that offers a 960-hour pipe welding course. ESAB representatives will join the tour this year, where they will answer questions about careers in welding, provide hands-on welding guidance, and more.

"The Blue Collar Tour's mission perfectly aligns with ESAB's Future Fabricators goal of supporting the next generation of fabricators, instructors, and institutions through hands-on experience and access to professional equipment," said Eleanor Lukens, ESAB's president of the Americas. "There is a misconception that the skilled trades are a fallback option for those who don't go to college, and nothing could be further from the truth. With skilled pipe welders commanding a six-figure income, it ought to be a first choice-career for those who love to work with their hands."

The tour kicks off on January 21 in Lakewood, Colo., and continues through March. For dates and locations, go to *westernweldingacademy.com*.

Renishaw Receives Industry Partner Award at Davis Technical College Foundation's Luncheon

Renishaw Inc., West Dundee, Ill., a measuring and manufacturing systems supplier, received the Industry Partner Award at Davis Technical College Foundation's Annual Life Changer Luncheon. The company supports the Davis Tech CNC Machining program, which prepares students for careers in the industrial workforce using industry-standard tools and equipment.

Students utilize industry-standard tools, equipment, and procedures as entry-level machinists. They study blueprint reading, inspection, part design, CNC operation, and CNC programming using the company's Equator™ gauging systems, machine tool probes, and styli as well as a 5-axis REVO® CMM measuring system and QC20-W wireless ballbar system. Students are provided with a learning environment similar to what they would encounter in small shops and large production firms throughout the country.

Denis Zayia, president of Renishaw Inc., accepts the Industry Partner Award at Davis Technical College Foundation's Annual Life Changer Luncheon.

"We see the importance of addressing the manufacturing skills gap and this is a natural way for us to get involved," said Denis Zayia, president of Renishaw.

Career and Tech Center in Mississippi Receives Almost $1 Million to Expand Welding Instruction

The Career and Technical Center in Houston, Miss., is being awarded $921,860 to expand its welding program. The funds, announced by Governor Tate Reeves as a series of economic development projects, will be used to construct a 2850-sq-ft facility, providing much-needed space for welding instruction. This expansion will significantly benefit students who are currently limited to a small corner of the center. WJ

AWS®

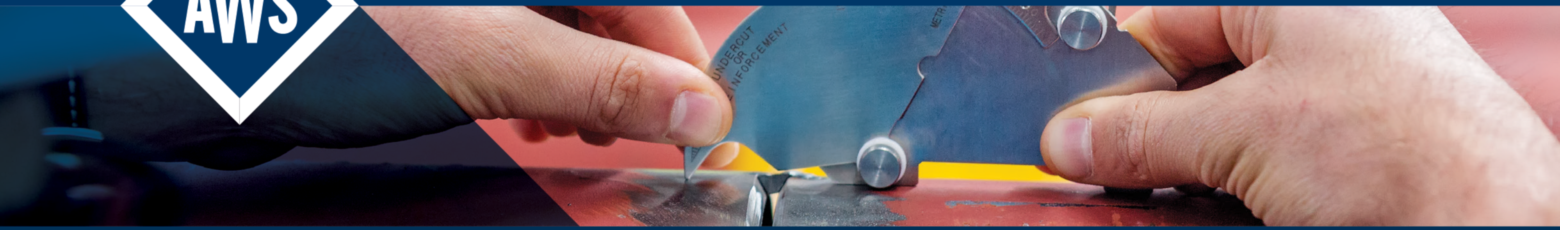

CERTIFIED WELDING INSPECTOR LIFETIME ACHIEVEMENT AWARD

Friends and Colleagues:

In 2018, The American Welding Society established the honor of the **Certified Welding Inspector Lifetime Achievement Award (CWI-LAA)**. The award is intended to recognize individual members for a career of distinguished service, outstanding accomplishments, exceptional leadership, and innovative contributions in the area of welding inspection and welding inspection technology. Individuals receiving the award may be currently working as a CWI, or have worked as one in the past. The selection committee is seeking nomination packages for qualified individuals who have demonstrated specific accomplishments in one or more of the following areas:

- Advancements in the field of welding inspection.
- Mentorship of individuals entering the field of welding inspection.
- Effective application of existing and new inspection technology.

This could be evidenced by one or more of the following:

1. Development of novel concepts or tools related to welding inspection.
2. Participation in activities directly related to the recruitment, training, education and/or mentorship of individuals entering the field of welding inspection.
3. Leadership in AWS or private industry, particularly as it impacts advancement of the welding inspection profession.
4. Consultancy in technical matters or welding industry business matters, including expert witness activities related to welding inspection.
5. Publication of books, papers, articles or other significant works related to welding inspection.
6. Meaningful participation in AWS committees, Sections or other AWS voluntary contributions related to welding inspection.

For more specifics on the nomination requirements, please contact Chelsea Steel at nationalawards@aws.org, or at **aws.org/about/awards/aws-cwi-lifetime-achievement-award/**

Please remember, we all benefit in the honoring of those who have made major contributions to our chosen profession and livelihood. The deadline for submission is **July 1, 2025**. The CWI Lifetime Achievement Award Committee looks forward to receiving numerous nominations for 2026 consideration.

Sincerely,

Kerry Shatell
Chair, CWI Lifetime Achievement Award Committee

Nominate your colleague for the American Welding Society CWI Lifetime Achievement Award.
Submission Deadline **July 1, 2025**.

Stay Connected

aws.org

Focus on Cutting

Manual Plasma Cutting Systems Feature Double-Tap Triggers and Glove Friendly Knobs

The Cutmaster 50+ and 70+ manual plasma cutting systems feature a 4.3-in. TFT LCD paired with a glove-friendly knob for selecting and setting parameters. The systems have a built-in 14-pin CPC port for easy CNC mechanization. Through the TFT display, users can access, set, and see features such as normal and grate-cutting modes and 2T (standard) or 4T (trigger latch) modes. The 4T mode lets the operator press and release the trigger and cut without holding it, reducing hand fatigue on long cuts. The torch features a double-tap trigger; tapping the trigger twice shuts the gas solenoid valve, extending the cutting time when using small portable compressed air or nitrogen cylinders. Other features include automatic inlet/outlet air pressure detection, automatic postcut air purge to extend consumables life, and an automatic voltage detection function. The Cutmaster 50+ has a recommended pierce and cut capacity of ⅝ in. and severs metal up to 1¼ in. thick. It has a rated cutting output of 50 A at 60% duty cycle and weighs 35.3 lb. The Cutmaster 70+ has a recommended pierce and cut capacity of ¾ in. and severs metal up to 1½ in. It has a rated cutting output of 70 A at 60% duty cycle and weighs 35.3 lb. Both machines are available in 110–240 V single-power and 480 V triple-power versions and come with an SL60 1Torch™, long-life Black Series consumables, and a 15-ft cable.

ESAB
esab.com
(800) 373-2123

Slat Cleaner Eliminates Slag from Laser Cutting Machines

Featuring a 1700-W motor and customized gearbox with an integrated slipper clutch, the TSC 200 slat cleaner efficiently removes slag up to 25 mm thick from laser cutting machines. Its serrated cutting edges break up the slag while the continuous cutting edges scrape it off. This process runs continuously, allowing cleaning to proceed at a speed of 13–32 ft/min. The cleaner is available in two versions, one for slat thicknesses of 0.080–0.120 in. and another for 0.120–0.150-in.-thick slats. The front handle allows the machine to be easily placed on the pallet for cleaning. Position markings on the housing cover and handle help operators find the position of the slat to be cleaned. A polyoxymethylene roller transports the slat cleaner to the laser cutting system. The roller does not need to be removed before cleaning the slats. The cleaner's smart box is mounted on the handlebar and has an off switch and LED indicators for maintenance intervals; the operator receives notifications when service to the slat cleaner is required.

TRUMPF
trumpf.com
(860) 255-6000

AWS Announces B5.16:2025, *Specification for the Qualification of Welding Engineering Personnel*

AWS B5.16:2025, *Specification for the Qualification of Welding Engineering Personnel*, establishes the requirements for the qualification of welding engineering technologists and welding engineers employed in the welding industry. The minimum experience, examination, application, qualification, and requalification requirements

and methods are defined. This specification is a method for engineering personnel to establish a record of their qualifications and expertise in welding industry work, such as the development of procedures, processes controls, quality standards, problem solving, and more.

AWS
aws.org
(800) 443-9353

Carbide Burs Provide Greater User Control and Quicker Cutting Action

A new line of ten-carbide burs, each designed for different applications — including deburring, contouring, surface milling, and more — are available in single, double, and aluminum cuts. The single cut is designed for general material removal and workpiece finishes. For stainless steel and ferrous materials, the double cut makes smaller chips to achieve quicker cutting action while improving operator control. The aluminum cut is for nonferrous and other soft materials and is designed with a wide flute to guarantee quick, easy material removal with minimal loading. The burs are available in a variety of shapes, including cylinder, ball, oval/egg, rounded tree, pointed tree, flame, taper, and pointed cone. Each shape is available in different cut lengths, head diameters, and shank diameters dependent on the series and type of cut, with overall lengths ranging from 2–7 in.

Weldcote
weldcotemetals.com
(704) 739-4115

Cutting and Grinding Wheels Offer Accuracy and Long Product Life

The Tiger Ceramic 2.0 and INOX 2.0 cutting, grinding, and combination wheels address the challenges of metal fabrication industries such as shipbuilding, pressure vessel, and heavy equipment fabrication. The Tiger Ceramic 2.0 features a ceramic grain that cuts cool and easily removes material while providing control for an improved operator experience. Wheel life has been improved over previous models by increasing grain retention, ensuring precise product wear and longer life with no reduction in cut speed. The INOX 2.0 wheels are designed for high performance when cutting and grinding high-value stainless steel parts. Premium aluminum oxide grains provide a smooth cut rate and consistent performance. Both versions are contaminant-free and safe to use on high-value stainless steel parts. They feature a QR code for quick access to important safety information and a patent-pending Optimum Use Line to help get the most out of the product. An advanced bond formulation on the grinding wheels reduces uneven edge wear and chipping, improving operator experience and extending wheel life.

Weiler Abrasives
weilerabrasives.com
(800) 835-9999

CNC with 5-Axis Integrated Technology Enhances Operation

The Series 500*i*-A computer numerical control (CNC) advances machine performance with 5-axis integrated technology

and supports both machine tool builders' and users' evolving needs, including easier operation, greater security, and optimized efficiency. With its dual engine architecture, the new control has 270% higher CPU processing power than previous models and comes with updated modern hardware and graphically enhanced software. This higher performance, including improvements in block processing time and macro program processing, is designed to help machine shops reduce cycle times and improve productivity. It also provides machine tool builders with tools to optimize their equipment, including digital twin technology to assist in complex machine design. Enhanced graphics and a simplified one-task-to-one-screen display eliminate the need to switch to different screens. IoT security guards against cybersecurity issues with features such as FOCAS3, user authentication, and data access protection.

FANUC
fanucamerica.com
(888) 326-8287

U.S. Cutting Tool Shipments Up for First Nine Months of 2024

According to the *Cutting Tool Market Report*, cutting tools shipments totaled $209.3 million in August 2024. Orders increased 9.1% from July 2024 but dropped 4.5% from August 2023. Year-to-date shipments totaled $1.67 billion, up 1.5% from shipments made in the first eight months of 2023. The year-to-date growth rate has declined every month since April 2024. As stated by the U.S. Cutting Tool Institute, challenges continue with work stoppages in the aerospace sector. Instability in world events is also significantly impairing market confidence. Defense spending continues to be strong, while other markets stagnated. Early expectations for continued growth in 2025 originally showed promise, but a lackluster 2025 is more realistic with many factors in flux.

The Association for Manufacturing Technology
amtonline.org
(703) 893-2900

AWS Introduces D.1.7/D.7M: 2024, *Guide for Strengthening and Repairing Existing Structures*

AWS D1.7/D1.7M: 2024, *Guide for Strengthening and Repairing Existing Structures*, provides information on strengthening and repairing existing steel structures, including welded repairs, heat-assisted straightening, fatigue improvements, and nonwelded but related repairs, such as partial or complete member replacement. It offers direction and guidance for both engineers and contractors, specifically background information that will be useful to the engineer who is obligated under the "Strengthening and

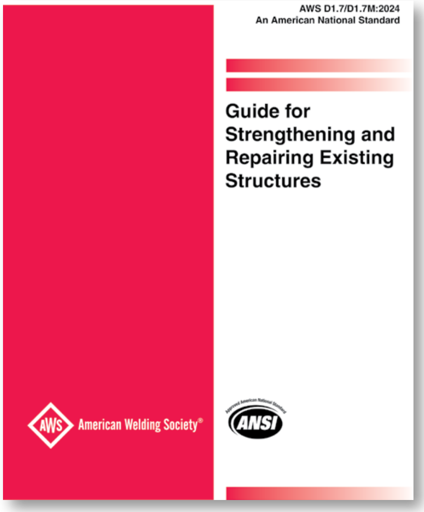

Repair of Existing Structures" clause of AWS D1.1/D1.1M, *Structural Welding Code — Steel*, or other contract provisions to provide a comprehensive plan for strengthening and repairing steel structures. This guide applies to existing structures made of carbon or low-alloy steel with a minimum specified yield strength of 100 ksi (690 MPa) or less, cast iron, and wrought iron.

AWS
aws.org
(800) 443-9353

Cutting Head Feature Expands Reach, Allows Nonstop Beveling without Torch Turning

The BevelArc 3D feature adds an additional axis to Tecoi's line of plasma, oxyfuel, and laser plate processing machinery, increasing the equipment's cutting reach capability. Cutting heads can be positioned from 0–90 deg from a vertical position, providing added efficiency. This expanded cutting head reach capability can be especially useful for cutting and fabricating pressure vessel tank heads as well as cutting difficult shapes and profiles from beams, plates, and tubes. Users can perform continuous beveling by tilting without torch turning. Since the torch does not have to move, making loops to recover the torch position is not necessary, except in rare cases where it's required by the finishing of corners. It cuts shapes that cannot be processed on typical thermal cutting machines. Additional features include easy operation and adjustment, automatic restart after collision, automatic proportional height control, and high-precision roller runners.

Tecoi
tecoi.com
(833) 878-3264

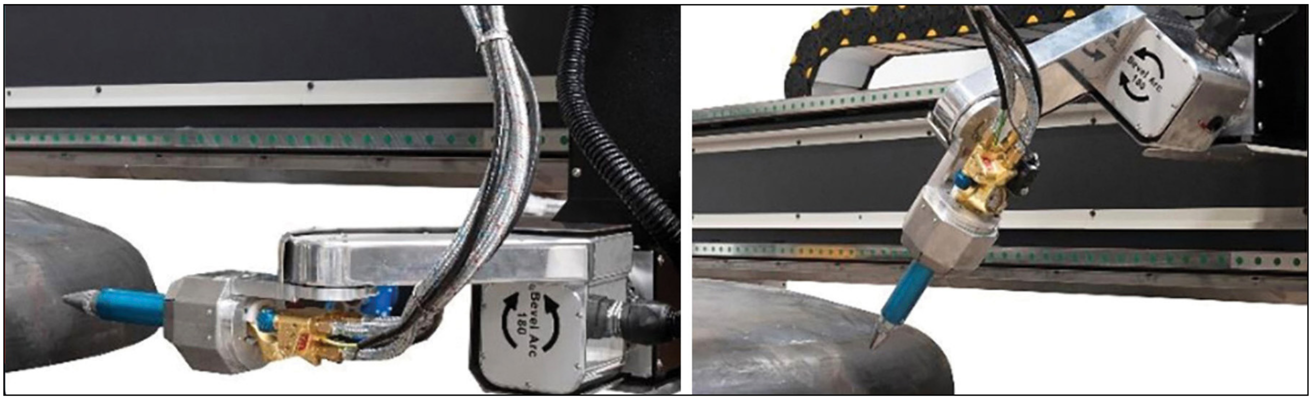

AWS COUNSELOR NOMINATION

Friends and Colleagues:

The American Welding Society established the honor of Counselor of the Society to recognize members for a career of distinguished leadership contributions in the advancement of welding science and technology. Election as a Counselor is based upon an individual's career of outstanding achievements and accomplishments. The selection committee is seeking qualified individuals who can demonstrate their leadership in the welding industry as evidenced by:

- Sustained service and performance in the advancement of welding science and technology
- Publication of papers, articles and books which enhance knowledge of welding
- Innovative development of welding technology
- Society, National and Section contributions
- Professional recognition
- Leadership in AWS or other corporate levels, particularly as it impacts the advancement of welding technology
- Facilitating others to participate as a volunteer in the advancement of welding technology

For specifics on the nomination requirements, please contact Chelsea Steel at nationalawards@aws.org at AWS headquarters in Miami, or simply follow the instructions within the Counselor nomination portal link located at **aws.org/about/awards/counselor-and-fellow/**.

Please remember, we all benefit in the honoring of those who have made major contributions to our chosen profession and livelihood. The deadline for submission is **June 1, 2025**. The Counselor Committee looks forward to receiving numerous Counselor nominations for 2026 consideration.

Sincerely,

David J. Nangle
Chair, Counselor Committee

Nominations for Counselor of the Society are open. Submission Deadline **June 1, 2025**.

Stay Connected

aws.org

POINT OF VIEW

BY KRISTIN CAMPBELL

The Motor City's Sheet Metal Conference Maintains Its Driving Force

This AWS Section-led event attracts participants and presenters with advanced welding research

Over the last decade, I've been fortunate to attend and report on the AWS Detroit Section's Sheet Metal Welding Conference (SMWC) many times. Every time the event is held — typically every other year — it continues to leave a lasting impression. SMWC XX: Advances in Automotive Welding & Joining Conference, held October 22–24, 2024, was no exception, highlighting recent developments in welding and joining solutions that enable new generations of vehicle design and construction. Conference committee members take pride in organizing this event, which has been held since the 1980s. Their responsibilities include early planning (sometimes in conjunction with another organization), choosing the theme, calling for abstracts, securing a venue, selecting the welding and joining research that will be presented, booking keynote speakers, seeking sponsorships for breakfasts and breaks, and providing on-site services when the event begins.

The Next Generation Steps Up. SMWC XX, led by the next generation of welding professionals, proved inspiring and encouraging, setting a high standard for AWS Section members to aspire to in the future.

Andrea Orr, a research engineer at Ford Motor Co. and a past AWS Future Leader, served as conference chair. The role required extensive behind-the-scenes coordination — answering queries, building the event's agenda, and thinking critically. After the event, she assembled several members of the 19-person committee to go over highlights and discuss ideas for the next conference.

Another example of positive involvement came from Robert Watson, a past AWS Future Leader and a welding engineer at General Motors (GM), who took on the role of site coordinator. He planned the meals and room setups at the event's venue, Laurel Manor. Kevin Teng, a weld development engineer at GM, served as the vendor chair. Other committee members helped with advising, technical chair, member, webmaster, and treasurer duties.

Keynote Speeches, Sessions, and More. The conference featured three keynote speeches. Hassan Ghassemi-Armaki with GM presented "Artificial Intelligence in Automotive Welding: From Body-in-White to Battery Cell Welding," and Marco Opitz with TRUMPF discussed "Advancements in Laser Technology: From Science Fiction to Modern Manufacturing." Read their feature articles in this *Welding Journal* to learn about those topics. The last keynote was by John Catterall from JCAT Engineering on "The Road to 100% Simulation."

The organized sessions showcased liquid metal embrittlement (LME), battery welding, aluminum spot welding, steel linear welding, resistance welding predictive tools, inspection and simulation for electrification, aluminum resistance spot welding (RSW), laser welding, advancement in RSW, aluminum fusion welding, inspection methods for RSW, mixed material joining, and characterization of electrode behavior. More than 40 presentations occurred and many stood out, including but not limited to determination of LME-free process windows for component-scale RSW of 3rd generation advanced high-strength steel, investigating performance and reliability of resistance spot welds on additively manufactured battery tabs, production comparison of an automotive door assembly using RSW and refill friction stir spot welding, the effect of multiphased current and external magnetic field on RSW of hot-stamped AA7075, and development of constant DC chopping spot welding technology for three sheets stacks with high sheet-thickness ratio.

SMWC presentations are significant within the welding industry, and some have been published in papers in the *Welding Journal*. Notable examples include "Improving Aluminum Resistance Spot Welding in Automotive Structures" in 2013 about GM's Multi-Ring Domed electrode, "Spot Welding Different Sheet Metal Grades and Gauge" in 2014, "Effects of Welding Wire Composition in Aluminum Laser Beam Welds" in 2017, and "Pulsed Arc Welding of Battery Tabs for Vehicle Electrification" in 2022.

Attendees Continue to Return. Attendees vary from students and professors from all over the country to professionals in the field employed by various automakers, resistance welding companies, major manufacturers, suppliers, and institutions (from near and far, including Honda in Japan, Technische Universität Dresden in Germany, and Tecna in Italy). Retired individuals and past chairs continue to participate, pitching in where needed and learning from the sessions. Attendees can meet well-known leaders in the field and recent graduates launching their careers, access conference proceedings, and earn professional development hours.

Over 145 people, 100 of whom were first-time visitors, attended the conference. Additionally, 65 individuals participated in the vendor display. I like seeing familiar faces and hearing about their successes. A great example of this was reuniting with Liya Amanuel. She presented at the last SMWC as a graduate fellow in the welding engineering program at OSU. Since then, she has graduated, moved to Detroit, become a welding engineer at Tenneco, and returned to this year's conference as the chair of the mixed material joining session.

Vendor Display Highlights. The SMWC vendor display is an enjoyable night to which the welding community is invited. Participating companies typically specialize in automated welding and assembly lines, machine vision technology, resistance and projection welding consumables, cutting tool innovations in tip dressing, and more. Knowledgeable representatives talk to guests at booths while showing their brochures and equipment. In addition to visiting vendors, participants can socialize and dine on hors d'oeuvres. This year, more than 30 companies participated, matching numbers in recent years.

Attend the Next Conference. Don't forget to check *sections.aws.org/detroit* for details about the next event, set to take place in 2026, where a new chair and committee will be in charge. WJ

KRISTIN CAMPBELL (*kcampbell@aws.org*) is managing editor of the *Welding Journal*. Pictures courtesy of SMWC XX Advisor Michael Palko.

At the registration area, Jerry Gould from EWI (center), who has attended and chaired sessions at many SMWC conferences, picks up his badge.

More than 40 presentations took place during the conference, spotlighting recent developments.

SMWC XX Keynote Speakers (from left) John Catterall, Hassan Ghassemi-Armaki, and Marco Opitz pose with Conference Chair Andrea Orr.

Michael Karagoulis, another long-time attendee, asks questions after a talk. He also served as chair of the characterization of electrode behavior session and a committee advisor to the event.

During the 2024 SMWC vendor display, Andrea Orr and Kevin Teng made rounds speaking to exhibitors, and attendees reunited with industry colleagues and made new connections.

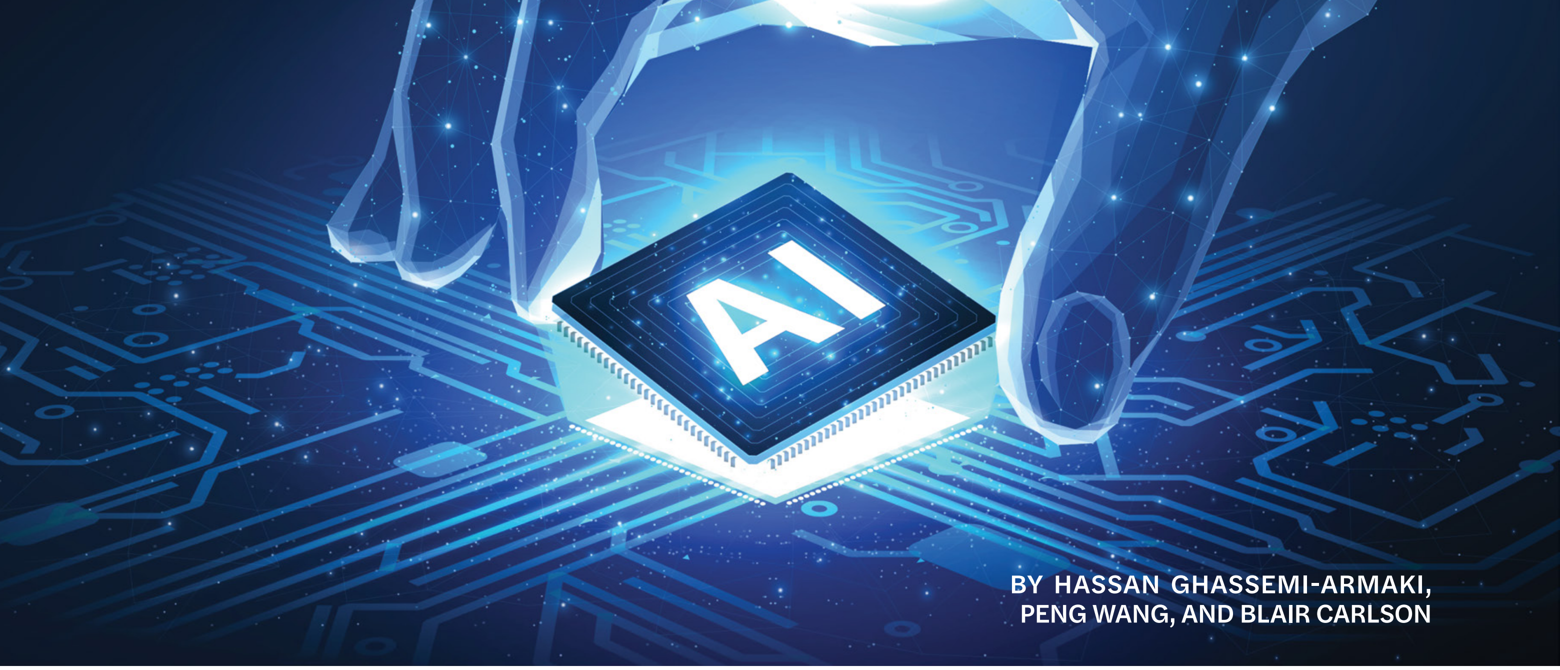

BY HASSAN GHASSEMI-ARMAKI,
PENG WANG, AND BLAIR CARLSON

AI IN AUTOMOTIVE WELDING

Learn about virtual sensing, four-phase resistance spot welding models, and machine learning methods

Welding processes in the automotive industry are dynamic and complex, making monitoring and quality assurance challenging. Traditionally, manual inspections have been the norm. To improve welding and automate quality control, two key elements are needed: advanced process sensing and data analytics. Advanced sensing enhances process characterization and anomaly detection. For example, in resistance spot welding (RSW), monitoring electrode force and displacement can identify faults during nugget formation. In laser welding, laser welding monitoring (LWM) captures thermal conditions and plasma emissions, allowing for comprehensive weld pool monitoring. Once data is collected, data analytics algorithms are essential for decision-making. The complex dynamics and nonlinear relationships between welding quality and sensing data require artificial intelligence and machine learning (ML) for effective modeling and analysis, enabling tasks like defect detection and predicting weld properties.

What's RIPTiDE?

To improve RSW sensing, a virtual sensing model, the resistance inferred process time-series by dense encoder (RIPTiDE), has been developed (Ref. 1). It addressing the limitations of traditional in-line quality monitoring in RSW, particularly the costly and labor-intensive process of directly measuring mechanical signals like electrode force and displacement. RIPTiDE leverages the time-series dense encoder (TiDE) architecture, modifying it to predict mechanical signals from the dynamic resistance (DR) signal that is commonly measured during RSW.

In early trials, RIPTiDE 1.0 showed that it could recreate trends in the mechanical signals but was plagued by noise and discrepancies in signal magnitude, especially in expulsed welding cases. Subsequent adjustments were made, including experimenting with different network configurations and activation functions, incorporating L1 loss alongside the mean squared loss to smoothen signal noise, and adding a new input called "large drops" to focus the model on significant DR signal drops caused by the welding expulsion defect. Experimental results demonstrated that RIPTiDE

2.0-generated mechanical signals closely matched the real electrode force and displacement data and achieved performance comparable to physical measurement in modeling toward weld quality prediction and defect detection. For instance, RIPTiDE achieved an R-squared value of 0.926 (± 0.019) for interdiffusion layer (IDL) thickness prediction, a notable improvement over the DR-only model, which attained an R-squared value of 0.849 (± 0.019). This virtual sensing approach offers an efficient, cost-effective pathway to enhanced in-line RSW monitoring, aligning well with Industry 4.0's goals of robust, sensor-driven manufacturing analytics.

Identifying a Four-Phase RSW Model

In the context of RSW modeling, traditional RSW models often overlook the role of IDL, limiting predictive accuracy in real production environments where coated materials are prevalent, particularly in the automotive industry. A four-phase RSW model has been proposed to incorporate IDL removal as a distinct phase (Ref. 2). The four identified phases are as follows:

- Material expansion
- IDL removal
- Premolten joining
- Nugget formation

This additional phase allows for a more granular understanding of the welding dynamics and a more effective prediction of defect occurrences, such as expulsions. To operationalize this model, a systematic phase-detection methodology combining data filtering, topographic prominence, and logical rules was developed to autonomously identify phase transitions within the RSW process.

Phase-specific features, such as maximum resistance, force stabilization, and maximum displacement, were then extracted and served as critical indicators for understanding IDL removal dynamics and their impact on weld quality and defect occurrences, as shown in Fig. 1A. These features were used in a multilayer perceptron model for predicting IDL thickness (Fig. 1C) and detecting expulsions (Fig. 1D). Experimental validation involving over 600 welds with varying process conditions demonstrated the robustness of this approach. For expulsion detection, the model incorporating predicted IDL thickness achieved a notable 84% accuracy, a significant improvement over the 70% accuracy of traditional methods that do not consider IDL thickness.

Laser Welding Monitoring Importance

Laser welding is the most critical process in electric vehicle (EV) battery manufacturing. Due to its high energy and speed, laser welding presents a challenge in ensuring quality through real-time monitoring. LWM, which measures plasma, thermal emissions, and laser reflections, has the potential for in-line defect detection. However, traditional data-driven models often suffer from poor explainability and limited generalizability across welding conditions.

Addressing these challenges, an ML framework that systematically extracts and selects meaningful features from LWM data has been developed to enhance model robustness and interpretability (Ref. 3), as shown in Fig. 2. Initially, a comprehensive feature set was created by analyzing the time, frequency, and time-frequency domains of LWM signals. After correlation analysis reduced the feature set from 69 to 32 features, principal component analysis further reduced feature redundancy, and SHapley Additive exPlanations quantified the contributions from individual input features to the model's outputs, a final subset of six critical features was produced. These six features could perform comparable to the original 69 features in detecting and classifying the welding defects, but they greatly improved the computational and decision-making efficiency.

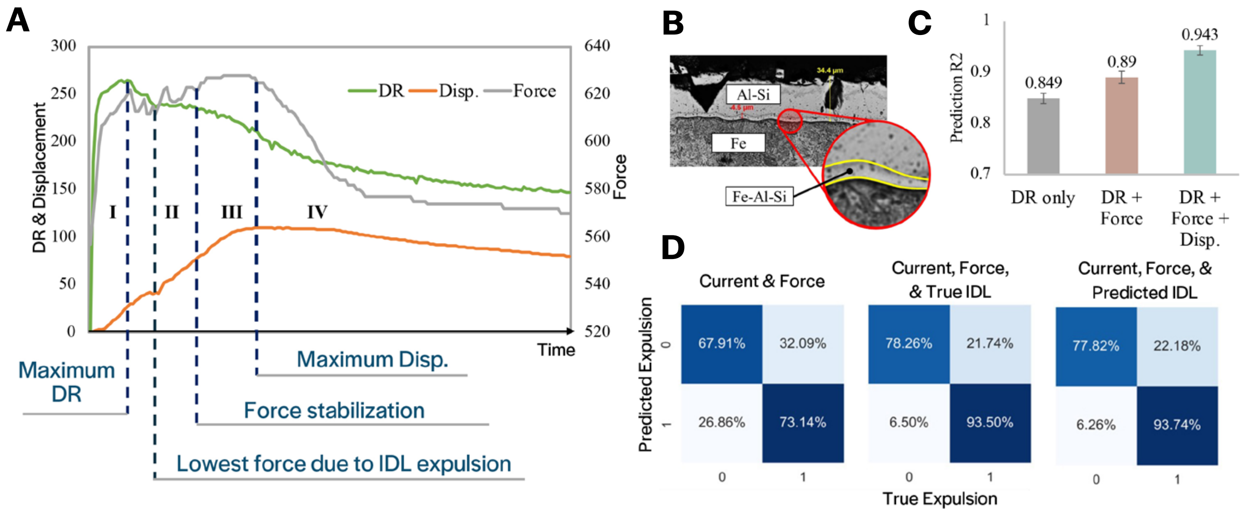

Fig. 1 — A — Illustration of the proposed four-phase detection for welding with IDL; B — IDL in between the base metal and coating; C — IDL prediction performance under different input conditions; D — predicted vs. true expulsion confusion matrices for all input combinations, where 0 represents normal welds and 1 represents expulsed welds. (Sourced from Ref. 2.)

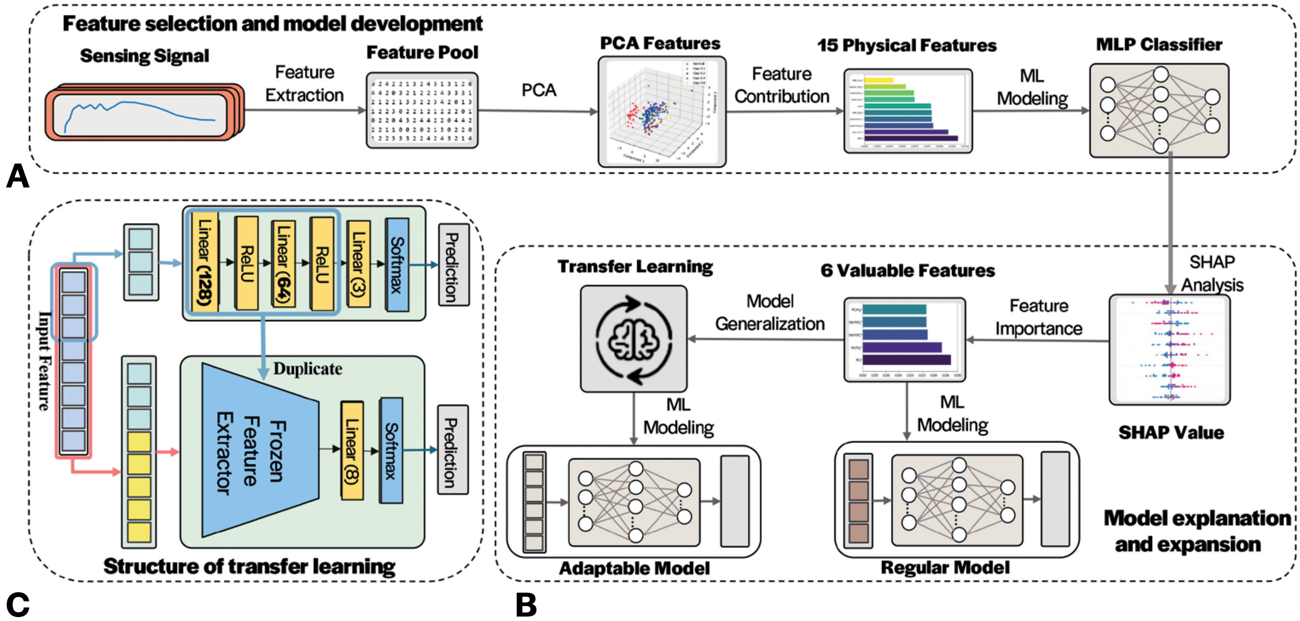

Fig. 2 — Overview of the ML framework for the welding system defect detection in laser welding. A — Feature extraction and classifier development; B — model explanation and generalization; C — transfer learning model employed in this study. (Sourced from Ref. 3.)

To improve welding and automate quality control, two key elements are needed: advanced process sensing and data analytics.

Ending Thoughts

To further improve ML model adaptability, the model previously described underwent transfer learning, fine tuning it to detect unseen defects with limited retraining on new data. The results showed that the model maintained high accuracy across various defect types, confirming both the utility of the selected features and the adaptability of the ML framework in dynamic welding environments. The framework demonstrated strong potential for real-time process monitoring and quality control in EV manufacturing, contributing to more reliable and adaptable laser welding processes aligned with Industry 4.0 standards. WJ

References

1. Kershaw, J., Wang, P., Ghassemi-Armaki, H., and Carlson, B. E. 2024. Virtual sensing by dense encoder for process signals in resistance spot welding. *International Symposium on Flexible Automation* Vol. 87882: V001T08A002. New York, N.Y.: American Society of Mechanical Engineers.
2. Kershaw, J., Ghassemi-Armaki, H., Carlson, B. E., and Wang, P. 2024. Advanced process characterization and machine learning-based correlations between interdiffusion layer and expulsion in spot welding. *Journal of Manufacturing Processes* 109: 222–234.
3. Zhao, X., Kershaw, J., Pour, M., Ma, J., Ghassemi-Armaki, H., Carlson, B., and Wang, P. 2024. Efficient and generalizable machine learning for inline defect detection in battery laser welding. *Proceedings of the 20th International Conference on Precision Engineering* (ICPE 2024). Japan: The Japan Society for Precision Engineering/School of Engineering, Tohoku University.

This article is based on a keynote speech presented at the AWS Detroit Section's Sheet Metal Welding Conference held October 22–24, 2024, in Livonia, Mich.

HASSAN GHASSEMI-ARMAKI (*hassan.ghassemi-armaki@gm.com*) and **BLAIR CARLSON** are with global research and development, General Motors, Warren, Mich. **PENG WANG** is with the Department of Mechanical and Aerospace Engineering, Case Western Reserve University, Cleveland, Ohio.

AWS FELLOW NOMINATION

Friends and Colleagues:

The American Welding Society, in 1990, established the honor of Fellow of the Society to recognize members for distinguished contributions to the field of welding science and technology, and for promoting and sustaining the professional stature of the field. Election as a Fellow of the Society is based on outstanding accomplishments and the technical impact of the individual. Such accomplishments will have advanced the science, technology and application of welding, brazing, or soldering, as evidenced by:

- Sustained service and performance in the advancement of welding and joining science and technology
- Publication of papers, articles and books which enhance knowledge of welding and allied processes
- Innovative development of welding and allied technologies
- Society and Section contributions
- Professional recognitions

I want to encourage you to submit nomination packages for those individuals whom you feel have a history of accomplishments and contributions to our profession consistent with the standards set by the existing AWS Fellows. In particular, I would make a special request that, in considering members for nomination, you look to the most senior members of your Section or District. In many cases, the colleagues and peers of these individuals who are the most familiar with their contributions, and who would normally nominate the candidate, are no longer with us. I want to be sure that we make the extra effort required to ensure that those truly worthy are not overlooked because no obvious individual was available to start the nominating process.

For specifics on nomination requirements, please contact Chelsea Steel at nationalawards@aws.org. Please remember, we all benefit in the honoring of those who have made major contributions to our chosen profession and livelihood. The deadline for submission is **August 1, 2025**.

The Fellows Committee looks forward to receiving numerous Fellow nominations for 2026 consideration.

Sincerely,

Todd Palmer
Chair, AWS Fellows Committee

Nominations for Fellow of the Society are open. Submission Deadline **August 1, 2025**.

Stay Connected

aws.org

BY MARCO OPITZ

The image illustrates gas-tight laser welding of cooling plates with a Multifocus approach. (Photo courtesy of TRUMPF.)

ADVANCEMENTS IN LASER TECHNOLOGY: From Science Fiction to Modern Manufacturing

This article explores the evolution of laser technology and the shift from CO_2 to solid-state lasers in welding

The evolution of laser technology has been nothing short of remarkable. From their theoretical origins in Einstein's theory of stimulated emission in 1917 to their widespread applications in modern manufacturing, lasers have transformed industries and enabled unprecedented levels of precision and efficiency. This article explores the fundamental principles of lasers, their various types, and the advanced techniques that have emerged to address the challenges accompanying the shift from CO_2 to solid-state lasers in welding applications.

Laser Basics and Types

At its core, a laser is an energy converter that amplifies light through stimulated emission. It consists of three key components: an active medium, an excitation mechanism, and a resonator. The active medium, which can be a solid, gas, or liquid, determines the wavelength of the emitted light. The excitation mechanism, such as a flash lamp or diode laser, provides the energy needed to excite the atoms in the active medium to a higher energy state. The resonator uses reflective elements to amplify and collimate the emitted light, producing a highly focused and intense beam. The unique properties of laser light, such as monochromaticity, collimation, and coherence, make it highly focusable and intense, enabling precise and efficient material processing.

Over the years, laser technology has progressed from early ruby lasers (1960) to CO_2 and modern solid-state lasers, each with its own distinct advantages and drawbacks. While CO_2 lasers were once the workhorses of industrial laser processing, solid-state lasers have largely displaced them in many applications, as they can be transported over simple fused silica fibers and have higher efficiency, compactness, and beam quality. However, the unique properties of CO_2 lasers, especially their ability to generate plasma, still make them interesting for certain applications.

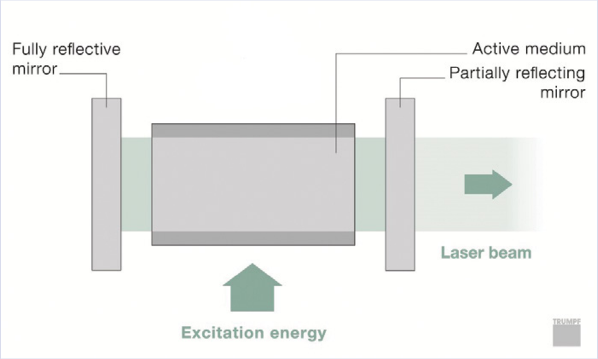

The diagram shows an optical resonator that demonstrates the laser principle. (Photo courtesy of TRUMPF.)

the keyhole backside. This results in a more stable weld pool and reduced spatter formation. The technology has found applications in diverse materials and fields, including automotive, e-motor manufacturing, and battery cell welding, where it has significantly increased productivity and yield rate.

■ Oscillating beam: This technique involves rapid beam oscillations, which can bridge larger gaps, increase weld width, and minimize defects like porosity and inclusions. The oscillating motion creates a wider weld pool, resulting in stronger and more aesthetically pleasing welds. It is particularly effective for welding dissimilar materials and achieving high-quality welds in challenging applications.

■ Multispot + BrightLine: Combining beam splitting with BrightLine Weld enhances process stability and enables gas-tight aluminum weld joints, which are crucial for applications like power electronics housings and battery pack cooling

CO_2 Lasers and the Plasma Effect

Due to their longer wavelength (10.6 µm), CO_2 lasers can ionize metal vapor and create plasma during the welding process. This plasma, reaching temperatures of around 15,000 K, acts as an additional energy source and significantly influences the weld quality.

The plasma creates a localized high-pressure zone, which helps suppress spatter formation, a common issue in laser welding. Additionally, the plasma has a shielding effect, preventing oxygen from reaching the molten material and thereby reducing oxidation. These combined effects result in cleaner, more aesthetically pleasing welds with minimal spatter and reduced postprocessing requirements.

In contrast, solid-state lasers, characterized by their shorter wavelengths (typically around 1 µm or shorter), generally do not generate plasma during the welding process. The absence of plasma leads to a higher degree of direct laser light absorption within the weld pool, which can be advantageous for certain applications. However, it also contributes to keyhole instabilities and highly dynamic weld pool behaviors. Consequently, solid-state lasers are more susceptible to spatter and other weld defects, mainly when operating at elevated power densities. To overcome these challenges, advanced techniques such as beam shaping (e.g., BrightLine Weld or beam splitting), oscillation, power modulation, and the use of frequency-doubled green lasers have been developed.

Advanced Laser Welding Techniques

Several advanced laser technology options address the challenges of laser welding with solid-state lasers. Here are some examples:

■ BrightLine Weld: This TRUMPF-patented dual-core technology utilizes a ring beam alongside the core beam to increase weld speed, reduce spatter, and improve weld quality. The ring beam creates a larger keyhole opening, facilitating the escape of metal vapor and minimizing fluctuations in

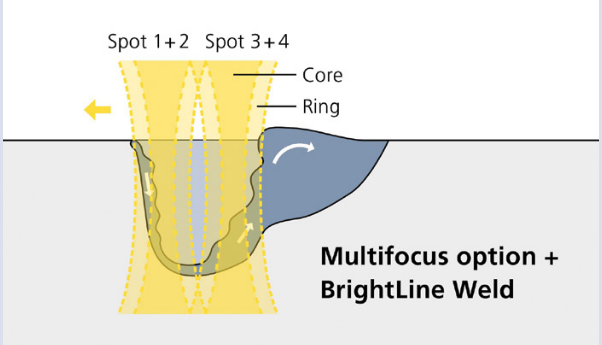

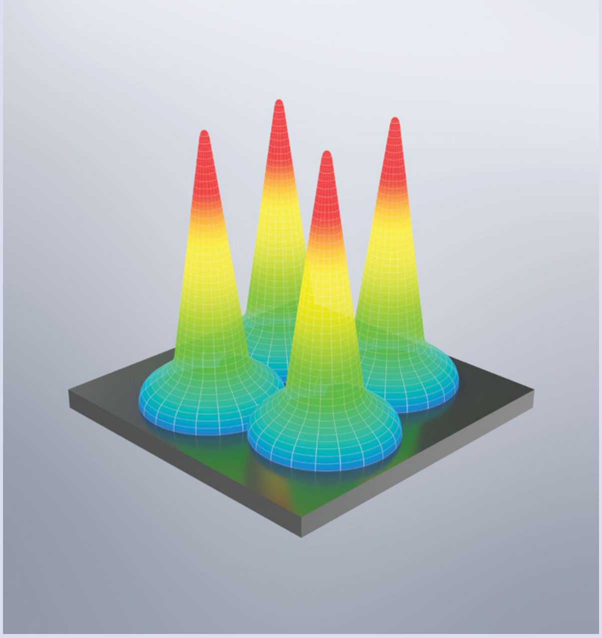

The diagram shows the effect on keyhole shape (top) and the beam profile of Multifocus optics (bottom). (The top photo courtesy of TRUMPF. The bottom photo copyright Electronic Publishing Stefan Berner GmbH / TRUMPF GMBH + Co. KG.)

plates. The multiple focus points enlarge and stabilize the keyhole opening, reducing the risk of porosity and improving the overall weld quality. This technique is ideal for applications requiring high levels of productivity and gas-tight joints.

■ Welding with modulated power: This approach involves varying the laser power in a controlled manner to intentionally disrupt the solidification mechanism that leads to hot cracking. By carefully adjusting the frequency and amplitude, it is possible to achieve crack-free results in challenging materials like high-strength steel.

■ Influence of wavelength: The absorption rate of materials is highly dependent on the laser's wavelength. Infrared lasers, for instance, are particularly sensitive to copper surface condition variations, especially at slower travel speeds and lower energy densities. This sensitivity can impact welding outcomes. In contrast, green lasers exhibit a higher absorption rate in copper, making them well-suited for welding copper up to 1.5 mm (0.06 in.) thick.

The Future of Laser Welding

As laser technology continues to advance, we expect to see further improvements in cost, efficiency, sensor integration, and miniaturization. These advancements will make laser welding more accessible and versatile, enabling new applications and driving innovation across various industries. As laser technology advances and the range of options expands, the power of choice can overwhelm customers. A customer-centric approach counters this complexity by focusing on specific application needs. This strategy encompasses comprehensive support, from initial feasibility assessments to selecting the ideal equipment, and extends to on-site assistance during production ramp-up. This commitment to exceptional service sets companies apart from competitors who merely promote lasers as commodities, highlighting the value of a true partner in navigating the complexities of laser technology. WJ

MARCO OPITZ (*marco.opitz@trumpf.com*) is technology specialist — laser welding, TRUMPF Inc., Plymouth, Mich. This article was presented as a keynote speech during the AWS Detroit Section's Sheet Metal Welding Conference in October 2024.

THE AWS FUTURE LEADERS PROGRAM IS SEEKING APPLICATIONS FOR 2025

If you are a current AWS member and aspire to become an industry leader, apply to become an AWS Future Leader.

Benefits include:

- A 1-3 year term as an AWS Future Leader, representing the welding industry's next generation
- Mentoring by AWS leadership
- Attendance at two (2) AWS Board of Directors (BOD) meetings annually, one in conjunction with FABTECH. AWS will pay for travel, lodging and per diem.
- Participation in AWS policy-setting committee meetings
- Networking with industry leaders and influencers

Eligibility requirements:

- Current AWS Member
- Must be between the ages of 18-35 on January 1 of the first year in office
- Currently working in the welding industry (welder, CWI, educator, engineer, sales, etc.)

Apply by April 15, 2025

Stay Connected

aws.org

2025 AWS PROFESSIONAL PROGRAM

September 8-11 | McCormick Place | Chicago, IL

Abstracts are now being accepted for presentations for the 2025 AWS Professional Program.

Abstract submissions on novel developments and research related to materials joining, including brazing/soldering, surfacing, and additive manufacturing, are welcome. Although full manuscripts are not required for abstract submission, authors are encouraged to submit suitable manuscripts to the *Welding Journal* at **editorialmanager.com/wj/default.aspx** for possible publication.

Topics of interest for abstracts include but are not limited to:

- **Additive Manufacturing**
- **AI/ML for Joining Applications**
- **Automation, Sensors and Controls**
- **Battery and Energy Systems Joining**
- **Brazing and Soldering**
- **Industrial Applications and Technologies**
- **Modeling and Numerical Analysis**
- **Performance of Welded Components, including Corrosion, Creep and Fatigue**
- **Surfacing, Overlay and Repair**
- **Weldability and Characterization of Welded Components**
- **Welding Processes/Methods, including:**
  - **Arc Welding Processes**
  - **High Energy Density (Laser & EB) and Laser Hybrid Welding**
  - **Solid State Welding**

FABTECH

Speakers with accepted abstracts will be required to give oral presentations at FABTECH 2025 within the AWS Professional Program. They will also receive complimentary registration for the 2025 Professional Program and free access to FABTECH 2025, North America's largest metal forming, fabrication, welding and finishing event.

Presenters are also welcome to attend the following events:

- **Opening Ceremony:** Join us as the AWS President, Richard Holdren and Officers are introduced, and the new AWS Fellows and Counselors are recognized.
- **The Comfort Adams Lecture:** Dr. Zhili Feng, *Oak Ridge National Laboratory*
- **Plenary Presentation:** Prof. Ninshu Ma, *Osaka University*
- **Plenary Presentation:** Prof. Antonio Ramirez, *The Ohio State University*
- **Plenary Presentation:** Prof. Joel Andersson, *University West Sweden*
- **Poster Competition:** Visit **weld.ng/postercompetition**

The deadline for abstract submission is **April 1, 2025**. For submission details and updates, visit **programmaster.org/2025AWSProfessional**

Not a member? Join AWS today for even more savings on AWS products, including conferences and events. Visit **aws.org/membership** for more information.

Stay Connected

aws.org

Lorem ipsur

BY PETER HUANG AND DENISE CHAMPAGNE

AUTO MANUFACTURING Benefits from Plasma and Abrasive Waterjet Cutting

Find out how these machines keep the production line moving

Depending upon the make, model, and manufacturer, an automobile has between 5000 and 7000 spot welds on the white structure body. Many of those welds are on components essential to vehicle integrity and safety. Subframes, bumper and door beams, front headers, and other structural components all contain multiple weld positions — in some cases, more than 50 in a single component. Quality welds are a vital aspect of vehicle performance and safety. In auto-body production, there is no room for error. Defective welds can have catastrophic consequences.

As a result, testing weld integrity is a crucial step in the manufacturing process. Every day, the first components off the line must be checked for any welding imperfections that might cause a failure: cracking, fissures, slag inclusions, incomplete fusion, or any other irregularity that causes the weld to be substandard. Subsequent spot checks are conducted throughout the day to ensure weld and component quality.

To check the weld, manufacturers must get inside it. The joint is cut, polished to a mirror finish, and then examined under a microscope for minuscule defects that could cause significant problems. Production, however, does not stop for testing. The production line is halted only if test data suggests a significant and ongoing issue that requires an adjustment to the welding parameters. Stopping the entire line for weld checks is too costly, given the amount of testing that must be accomplished.

For example, one operator on one line may cut between ten and 25 parts for testing in a single day. In some cases, sample cutting a component with complicated geometries and numerous welds can consume an hour of operator time. To complete the wide variety of test cuts, automotive manufacturers rely on handheld plasma cutting and abrasive waterjet machines.

Cut to the Chase

Plasma cutting provides manufacturers with the fastest, most efficient, and most agile cutting application available to avoid bottlenecks and keep pace with the continuous parade of components. Focusing on ionized gas superheated to some 40,000°F, plasma cutting machines are accessible, easily mastered cutting tools. More importantly, they are safer and cut three to four times faster than grinding wheels.

Versatility and Ease of Use

Cutting, gouging, and flush cutting conductive metals such as carbon, stainless steel, and aluminum are relatively straightforward with plasma cutting machines. However, using a plasma cutting machine with features and capabilities suited to the specific application is important. Some units combine the five elements of a traditional plasma cutting machine into a single-piece cartridge consumable. Operators can change out swirl rings, electrodes, nozzles, retaining caps, and shield caps quickly and all at the same time with a one-piece cartridge system, saving time and ensuring reliable performance — Fig. 1. Such cartridge systems also allow operators to quickly change cutting functions by simply changing a cartridge.

Fig. 1 — Plasma operators can opt for single-piece cartridge consumables to save time and ensure performance.

Advanced smart technology is also available that uses RFID chips to collect data on arc starts, use time, and machine performance, helping optimize cutting machine application and maintenance — Fig. 2. Additionally, some equipment manufacturers have designed systems that sync cartridges

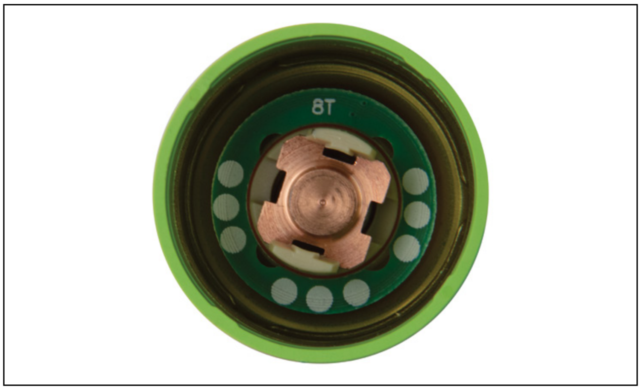

Fig. 2 — Smart technology for plasma applications includes RFID data collection to maximize output.

with machine functions, making them easy to set up and use for a variety of operations. In many cases, with the right system, workers do not necessarily need to be proficient drag cutting and plasma cutting operators. They only need to understand how to change a cartridge.

Get into a Tight Spot

While a robotic plasma cutting machine can perform a substantial amount of sample cutting, many components must be simplified and require a handheld cutting machine. Most weld sampling is performed on metal only 10 to 12 mm thick. The requirement for efficient, lightweight vehicles has eliminated the use of heavy-gauge metals. However, the complex contours of modern unibodies and subframe components prevent the complete use of robotic plasma cutting machines for weld testing. Highly portable handheld plasma cutting machines can weigh as little as 20 to 30 lb, making them easy to maneuver in various cutting scenarios.

Repair When Possible and Scrap When Not

Plasma-cutting units that use an integrated cartridge system transition between various functions quickly with a simple cartridge change. Where welds are found to be defective but deemed repairable, gouging is appropriate and can be quickly accomplished. The old weld is removed, and the material is ejected in preparation for a new weld. Where repair is neither possible nor appropriate, however, the component must be cut down to unserviceable condition to prevent it from inadvertently entering the market.

Cut Cool with Water

Modern auto manufacturing increasingly integrates a wide range of materials into vehicle design. Alloys, plastics, and composites are growing in popularity with the need to match lighter vehicles for efficient fuel mileage with structural strength. Like with weld sampling, engineers need to know whether the materials they select for a given function are performing as expected. With the sheer number of testing applications — from large components of high-strength steel to tiny microchips in electronic modules — material performance testing requires a tool that is as versatile as it is precise.

Abrasive waterjet machines provide all the capabilities of standard machining and manufacturing cutting operations with versatility that is unmatched by traditional technology. Waterjets can cut virtually any material — from steels, super alloys, and exotics to composites, plastics, stone, and more at a wide range of thicknesses. Equally important, they cut without creating a heat-affected zone (HAZ) caused by traditional machining methods that can alter the physical characteristics of a sample, making accurate testing difficult — Fig. 3.

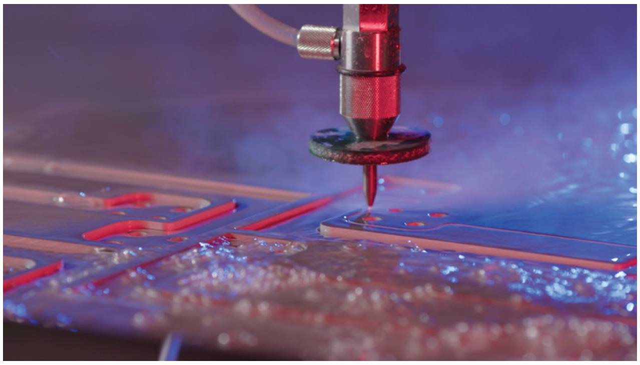

Fig. 3 — Shown cutting aluminum, waterjet cutting offers versatility to test welds on virtually any material without creating a HAZ.

Similarly, the impact of waterjet cutting on the residual stress of an object's surface is extremely minimal. Residual stresses within and on the surfaces of materials can affect the results of material performance tests. ASTM standards require that these residual stresses must be effectively relieved before testing is conducted. Because of their cutting characteristics, abrasive waterjet machines alter a material's inherent properties less than any existing technology does.

Waterjet cutting prevents HAZs, minimizes a material's residual stress, and provides the precise, smooth finish required for detailed inspection and testing. Waterjet machines are available in a variety of sizes, from small, fully enclosed integrated systems to much larger, fully integrated abrasive waterjet systems.

Keeping the Wheels Turning

The economies of automotive manufacturing demand that production lines keep moving with minimum downtime. If defects occur, they must be caught and corrected as quickly as possible. Plasma cutting machines and abrasive waterjets are ideally suited for sample cutting and testing, ensuring a safe, high-quality product while keeping the lines rolling. WJ

PETER HUANG (*peter.huang@hypertherm.com*) is senior marketing specialist and **DENISE CHAMPAGNE** (*denise.champagne@hypertherm.com*) is director, corporate communications, Hypertherm Associates, Hanover, N.H.

BY JOHN HENDERSON

When performing oxyfuel cutting, it is recommended to position your head so you can see the direction of the cut and look ahead of where you're cutting.

An Inside Look at the OXYFUEL PROCESS

Discover the benefits and expert tips for success

Many metalworkers use oxyfuel processes to fabricate, cut, dismantle, maintain, repair, preheat, temper, anneal, bend, and shape products that are part of our daily lives. Despite this, some school administrations are considering removing oxyfuel processes from their curricula because they believe it is an archaic process. However, instructors and industry professionals understand that oxyfuel processes have been essential to the domestic fabrication industry since 1907 when the Brooklyn Navy Yard used oxyacetylene torches to cut portholes in 3-in. armor plates (Ref. 1).

For those advocating for the removal of oxyfuel processes, it's important to note that many welding codes require minimum preheat and interpass temperatures as well as postweld heat treatment — all of which students practice with oxyfuel processes. Additionally, oxyfuel remains widely used because of its convenience, cost-effectiveness, portability, and versatility in performing a range of tasks, from cutting and heating to gouging, scarfing, washing, welding, and brazing.

From a financial perspective, equipping a school or training facility with a professional-grade oxyfuel outfit costs a few hundred dollars and can last for decades. Factoring in the educational discounts (often 30–40% below the manufacturer's suggested retail price), schools can acquire ten booths with cutting, heating, and welding/brazing outfits and required personal protective equipment (PPE) for $5000–$10,000, depending on the outfit.

Building Core Competencies

Teaching oxyfuel processes equips students with essential knowledge for a successful career in metalworking. Key topics include the following:

- Identifying hazards of metalworking (heat, sparks, molten metal, and UV light) and understanding the importance of PPE.
- Understanding the triangle of combustion or "fire triangle" (fuel, oxygen, and heat) and learning how to control each element.
- Practicing good housekeeping by maintaining a work area free of combustible materials that could fuel a fire.
- Properly identifying, handling, and securing cylinders in use and storage.
- Safely installing, operating, and shutting down gas flow and pressure regulation devices — Fig. 1.
- Inspecting and maintaining equipment for safety and performance.
- Recognizing oxyfuel-specific hazards like reverse flow, flashback, backfire, and sustained backfire.
- Understanding basic metallurgy and chemistry principles (rapid oxidation, tempering, quenching, work hardening, and microstructure).
- Using measuring and math skills to compensate for kerf, ensure proper fit-up, and apply good workholding techniques.
- Preparing materials for welding by following proper weld prep procedures.
- Reading the weld pool, developing a cadence for adding filler metal, and mastering weld pool manipulation.

Fig. 1 — Students learn the fundamentals of regulator operation and gas safety by using oxyfuel processes.

Practical Advice for Oxyfuel Processes

The remainder of this article presents fundamental advice and a few more advanced tips for oxyfuel processes. For clarity, they are divided into gas choices, lighting the torch, cutting advice, and shutdown.

Gas Choices

- Use acetylene for a more focused heat-affected zone — Fig. 2.
- Use alternate fuels (e.g., not acetylene) to heat larger areas because they release more heat in the secondary flame. For example, when heating a large area to cherry red with acetylene, the starting point cools before the torch reaches the end of the plate.
- Use acetylene for gas welding because it gives off CO_2 during combustion, shielding the weld pool from atmospheric contamination.
- Recognize that most people won't notice the cutting speed difference between acetylene and propane. The former burns about 10% hotter (5720° vs. 5112°F), but propane has a greater total heat of combustion, making it equally as fast at cutting. Also, remember that the cutting oxygen does the real work. Any speed difference is usually related to technique.
- Choose torches with a spiral mixer for fuel gas flexibility. These torches are calibrated to work with both high-pressure fuels, like acetylene, and low-pressure fuels, such as propane.
- Use regulators and cutting/heating tips only with their intended gases. These components are fuel gas specific because of the density and pressure differences between gases.

Lighting the Torch

- Open the oxygen valve on the handle when using a standard combination torch and adjust the flame from the oxygen valve on the cutting attachment. This ensures maximum oxygen flow to the cutting lever.
- Set a neutral flame by observing how the length of the secondary flame shortens as preheat oxygen is added. In a proper neutral flame, the inner and outer cones are nearly equal in length, indicating the correct oxygen-to-fuel ratio.
- Recognize a carburizing flame by its excess acetylene. As acetylene is added, the inner cone becomes much smaller than the outer cone, which appears rough and feathery.
- Identify an oxidizing flame by its excess oxygen. When too much oxygen is added, a loud hissing sound occurs, and the inner cone remains sharp.

- Use different lighting techniques for alternate fuels. If wind extinguishes the flame, place the tip at a 45-deg angle on the work surface to create back pressure on the flame and reduce its burn velocity. Light the torch, then, while keeping the torch in place, open the cutting oxygen valve until the flame audibly snaps into place.
- Check for a neutral flame with alternate fuels by placing the torch near the workpiece. The preheat flames create a star pattern with clearly defined legs about 2–3 in. long. An oxidizing flame will have shorter, sharper legs, while a carburizing flame will have longer, more feathery legs.

Tips for Cutting

- Support the torch with your off-hand, brace your elbows, and hold the torch tip about ¼ in. from the workpiece for a steady cut. Practice movements before lighting the torch, and learn to slide your elbows. Oxyfuel makes a precise cut, but any hand movement will be reflected in the cut.
- Preheat the starting point of the metal to a bright cherry red, indicating "kindling temperature," at which oxygen can react with the ferrite in the steel to start the cutting process. Only then should you depress the cutting oxygen lever.
- Follow through for a good drop cut by continuing to depress the cutting oxygen lever and moving the cutting oxygen stream past the edge of the metal.
- Don't focus on the leading edge of the cut. Instead, look where you want to go, and your hands will follow.
- Use your ears. A consistent sizzling sound is the best indicator of proper travel speed.

Shutdown

Regardless of fuel gas, always follow the same shut-off procedure: oxygen first, fuel gas last. Shutting off the oxygen first removes the most critical leg of the fire triangle and lets the operator check for a fuel gas valve leak after shutting off the fuel valve. If a small flame remains attached to the torch, it might be time to repair the fuel valve.

Closing Thoughts

While anyone can learn to use a torch safely, mastering fast and precise cuts takes practice and skill. The effort is well worth it, as these skills are essential for a successful career in metalworking.

In 2023, North America's acetylene market reached $3.2 billion, with approximately 40% of use coming from metal fabrication applications (Ref. 2). Natural gas, propane, and propylene are also used across the industry. Those gases do not burn themselves; welders are expected to be proficient with a torch and familiar with various gases. As a result, many welding trade and technical schools teach oxyfuel processes to meet the needs of the skilled trades. WJ

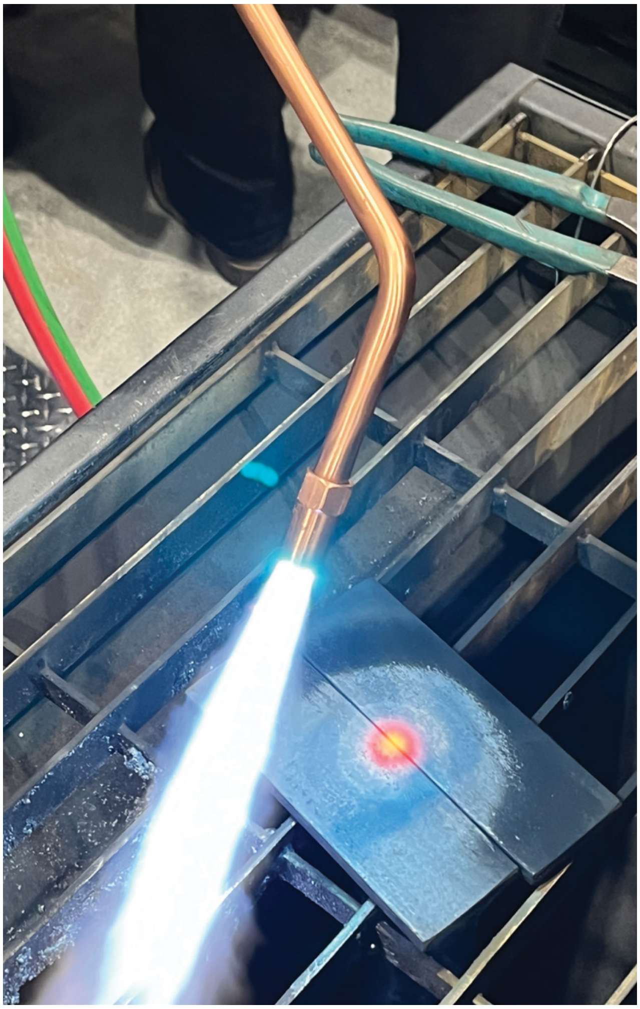

Fig. 2 — Choose acetylene to create a focused heat zone, as shown here. Propane will heat a larger area (e.g., big beams, larger-diameter pipe, buckets, etc.) and cost less.

References

1. Henderson, J., and Hussary, N. 2013. A history of the oxy-acetylene and plasma cutting processes. *Welding Journal* 92(10): 44–49.
2. Industry Arc. Acetylene Market Research Report- Market size, Industry Outlook, Market Forecast, Demand Analysis, Market Share, Market Report 2024-2030. Retrieved from *industryarc.com/Research/Acetylene-Market-Research-509334*.

JOHN HENDERSON (*john.henderson@esab.com*) is sales director, gas equipment, at ESAB, North Bethesda, Md. This article was presented at FABTECH 2024.

Certified Welding Inspector (CWI)

Seminar covers Parts A, B, and C of the CWI exam. Only Part B of the exam is taken following the conclusion of the seminar. Parts A and C are given at Prometric testing centers.

In-Person Location	Seminar Dates	Part B Exam Date
Waco, TX	Feb. 23–28	March 1
Cleveland, OH	Feb. 23–28	March 1
Anchorage, AK	Feb. 23–28	March 1
Kennesaw, GA	Feb. 23–28	March 1
The Woodlands, TX	March 2–7	March 8
Lehi, UT	March 2–7	March 8

Certified Welding Inspector (CWI) Two-Week

The two-week in-person CWI seminar is designed to give candidates sufficient time to prepare for all three parts of the exam in a focused classroom environment.

In-Person Location	Seminar Dates	Part B Exam Date
Richardson, TX	March 17–28	March 29
Tampa, FL	June 2–13	June 14

Please visit *aws.org/Certification-and-Education/Education/2-Week-Online-CWI-Seminar* to see online CWI two-week seminar dates.

Certified Welding Inspector (CWI) Part B

Course covers only Part B of the CWI exam. The Part B exam follows the conclusion of the three-day course.

In-Person Location	Seminar Dates	Part B Exam Date
San Diego, CA	Feb. 12–14	Feb. 15
Richardson, TX	March 26–28	March 29

Online Certified Welding Inspector (CWI) Eight-Week

The eight-week online CWI seminar is designed to prepare students for all three parts of the CWI exam from the comfort of their own homes. The seminar consists of two-hour online sessions hosted by an AWS instructor.

Please visit *aws.org/certification-and-education/education/8-week-online-cwi-seminar-and-exam.*

Nine-Year Recertification for Certified Welding Inspector (CWI)/Senior CWI (SCWI)

For current CWIs and SCWIs needing to meet education requirements without taking the exam.

In-Person Location	Seminar Dates
Pittsburgh, PA	Feb. 23–28
St. Louis, MO	March 2–7
Tukwila, WA	March 16–21
Dallas, TX	April 6–11
Denver, CO	April 27–May 2
Miami, FL	May 4–9
Boston, MA	May 4–9
Columbus, OH	June 1–6
Pittsburgh, PA	June 22–27
Charlotte, NC	July 13–18
The Woodlands, TX	Aug. 3–8

Certified Resistance Welding Technician (CRWT)

Showcases a technician's expertise in resistance welding principles, processes, and equipment achieved through relevant education, experience, and examination.

Please visit *bit.ly/CRWTOnline* to see online CRWT seminar dates and *aws.org/certification-and-education/education/crwt-in-person* for in-person CRWT seminar dates.

Welder Performance Qualifier Endorsement

In-Person Location	Seminar Dates
Birmingham, AL	March 4, 5

Welding Procedure Qualifier Endorsement

In-Person Location	Seminar Dates
Chattanooga, TN	April 22, 23

Certified Radiographic Interpreter (CRI)

In-Person Location	Seminar Dates
The Woodlands, TX	Feb. 24–28
Richardson, TX	April 21–25

Note: *The 2025 schedule for all certifications is posted online at* aws.org/education. ***IMPORTANT:*** *This schedule is subject to change without notice. Please verify your event dates with AWS Customer Service to confirm your course status before making travel plans. Applications are to be received at least six weeks prior to the seminar/exam or exam. Applications received after that time will be assessed a $395 Fast Track fee. Please verify application deadline dates by visiting our website at* aws.org/education. *For information on AWS seminars and certification programs, or to register online, visit* aws.org/education *or call (800) 443-9353.*

National and District Officers Elected for 2025

AWS has elected national and district officers to serve beginning January 1.

The National Nominating Committee was chaired by Past President W. Richard Polanin. Serving on the committee with Polanin were Thomas J. Lienert, John R. Bray, Sayee P. Raghunathan, Dale Flood, Ronald Stahura, Phillip Temple, Lynn Showalter, Thomas Holt, Daryl E. Peterson, Denis E. Clark, Jeff Davis, and Jeff Jones. Ashley Albertson served as secretary.

Richard L. Holdren, elected to serve as president, is senior welding engineer at ARC Specialties Technical Services, president/principal welding engineer at Welding Consultants LLC, and owner of Holdren Engineering LLC. He has served over 40 years as an AWS member and chair of numerous AWS certification, education, and technical committees. He also served as director-at-large. He is an AWS Counselor, Life Member, Senior CWI (SCWI), and Certified Welding Engineer (CWEng).

Dr. D. Joshua Burgess, elected to serve as vice president, is senior program manager of metallurgical and welding at the Tennessee Valley Authority. Throughout his 22-year membership with AWS, he has served the Society in many capacities at the board, Section, and committee levels. This includes serving as chair of the Northeast Tennessee Section in 2013 and Dist. 8 director from 2013 to 2019. He is also an AWS CWI and AWS Level III Expert Welder.

Kerry E. Shatell, elected to serve as vice president, is retired from Pacific Gas & Electric Co., where he worked as a senior advising welding engineer. A 27-year member of AWS, he has served the organization in multiple capacities, including director-at-large for three years; chair of the CWI Lifetime Achievement Award Committee; Dist. 22 director from 2013 to 2015 and 2016 to 2019; and chair, vice chair, treasurer, newsletter editor, and executive board member of the Sacramento Valley Section. He is also an AWS CWI and CWEng.

J Jones, elected to serve as vice president, is district sales manager at The Harris Products Group. Throughout his over 35-year membership with AWS, he has held leadership roles at the Section and national levels. This includes serving as executive committee director in 2019 and AWS Dist. 17 director for 15 years. He is also an AWS CWE.

Nicholas Peterson, elected to serve as director-at-large, is a curriculum developer/welding engineer for Miller Electric Mfg. An AWS member since 1990, he has been a member and leader in numerous AWS and national committees. He is vice chair of the AWS Skills Competition Committee, a member of the AWS Education Committee, and a member of the SkillsUSA National Tech Committee. He previously served as AWS director-at-large from 2022 to 2024.

SOCIETY NEWS

Karen Gilgenbach, elected to serve as director-at-large, is zone vice president for Matheson Gas. She has been a member of numerous AWS committees and serves as chair of the AWS D16 Committee on Robotic and Automatic Welding. She is also a former chair, treasurer, secretary, and membership chair of the AWS Milwaukee Section. She is an AWS CWI, Certified Welding Supervisor (CWS), and Certified Robotic Arc Welder-Technician (CRAW-T).

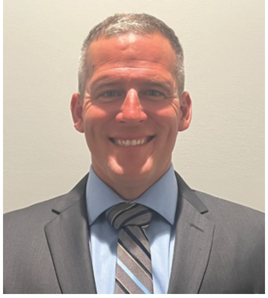

Bradley Brandmeir, elected to serve as Dist. 3 director, is a welding instructor at Lehigh Career & Technical Institute, Schnecksville, Pa. He has taught the school's welding program for the past ten years. He also works for a local steel fabrication shop specializing in structural buildings, fabrication and installation of hospital operating room light booms and fixtures, hospital support structures, stairs and handrails, and specialty custom designs for customers. He has served as chair of the Lehigh Valley Section and Dist. 3 deputy director. He is an AWS CWI and CWE.

Ronald H. Stahura, elected to serve as Dist. 6 director, is a strategic account manager at ESAB Welding & Cutting Products. An AWS Life Member, he has served in numerous leadership positions in the AWS Niagara Frontier Section, including chair from 1987 to 1988 and treasurer from 2015 to 2019. He previously served as Dist. 6 director from 2020 to 2023. He is also an AWS CWI and CWE.

Anthony D. Blakeney, elected to serve as Dist. 9 director, is an instructor of welding and inspection technology/industrial technology at Southeastern Louisiana University. He is the Dist. 9 deputy director and chair of the New Orleans Section. He also serves on the AWS Handbook Committee. He is an AWS CWI, CWE, Six Sigma Green Belt, and a Certified Senior Industrial Technologist. He is also an AWS Silver Member and 2019 AWS Counselor.

Benjamin Newcomb, elected to serve as Dist. 12 director, is a welding instructor at Madison College, Madison, Wis. He has held numerous positions in the Madison-Beloit Section since 2007, including chair, co-chair, and vice chair. He has been the Dist. 12 deputy director since 2013. He is also an AWS CWI and CWE.

Dale J. Szabla, elected to serve as Dist. 15 director, is a senior manufacturing engineering supervisor/weld engineer for nVent HOFFMAN Enclosures. He oversees the internal and external weld training programs, oversees the company's Anoka, Minn., campus CWI duties, supports all welding process-related concerns, and introduces new welding technologies to improve manufacturing process efficiencies. He has been an AWS member for more than 28 years and served on the executive committee of the Northwest Section in numerous roles. He is an AWS CWI, CWE, and ASNT ACCP Level II.

Caitlyn Brown, elected to serve as Dist. 18 director, is lead instructor and operations manager at her company, MadSkills Certified Welding Services. She joined the board of the AWS Houston Section in 2017 and has served as education chair, secretary, treasurer, vice chair, and 2023–2024 chair. She's a member of the Scholarship Committee. She is also involved with the Texas High School Welding Series and is the certification chair.

Nicholas Martinez, elected to serve as Dist. 21 director, has been with Salt River Project for more than a decade. He currently manages the power generation construction and maintenance team. His career has spanned 22 years in welding, inspection, certification, and manufacturing. He is the AWS Arizona Section chair. WJ

AWS Bylaws Article IX, Section 3

Section 3. Nominations.

Nominations, except for Executive Director and Secretary, shall proceed as follows:

(a) Nominations for District Directors shall be made by the District Nominating Committees [see Article III, Section 2(c)]. The National Nominating Committee shall select nominees for the other offices falling vacant. The names of the nominees for each office, with a brief biographical sketch of each, shall be published in the July issue of the *Welding Journal*. The names of the members of the National Nominating Committee shall also be published in this issue of the *Welding Journal*, along with a copy of this Article IX, Section 3.

(b) Any person with the required qualifications may be nominated for any national office by written petitions signed by not less than 200 members other than Student Members, with signatures of at least 20 members from each of five Districts, provided such petitions are delivered to the Executive Director and Secretary before August 26 for the elections to be held that year. A biographical sketch of the nominee (and acceptance letter) shall be provided with the petition. Any such nominee shall be included in the election for such office. A District Director may be nominated by written petitions signed by at least 10 members each from a majority of the Sections in the District, provided such petitions are delivered to the Executive Director and Secretary before August 26 for the elections to be held that year. A biographical sketch and acceptance letter of the nominee shall be provided with the petition. Any such nominee shall be included in the election.

In More AWS News . . .

MX3D Receives "Outstanding Development in Welded Fabrication" Award from AWS

The MX3D team celebrate their AWS "Outstanding Development in Welded Fabrication" award.

SOCIETY NEWS

AWS awarded Dutch scale-up MX3D with the "Outstanding Development in Welded Fabrication" for its groundbreaking MX3D Bridge, a 3D metal-printed structure located in Amsterdam.

The AWS Outstanding Achievement Awards recognize remarkable contributions in welding, achievements in historical structures, innovative fabrication techniques, safety practices, and technical advancements in multiple categories.

"Receiving the 'AWS Outstanding Development in Welded Fabrication Award' for the MX3D Bridge is a remarkable honor. This award highlights the innovation, collaboration, and perseverance that went into bringing the MX3D Bridge from concept to reality," said Gijs van der Velden, CEO of MX3D. "I am really proud of the close-knit team of partners that pushed the boundaries of what's possible with welded fabrication."

Measuring 12 meters (39.4 ft), the bridge is the first of its kind and was fabricated using MX3D's proprietary robotic wire arc additive manufacturing (WAAM) technology. This method combines 3D metal printing with welding robots, all controlled by the company's MetalXL workflow. The bridge was officially opened in 2021 by Queen Maxima of the Netherlands.

Designed by Joris Laarman Lab in close collaboration with lead engineer Arup, the bridge showcased the capabilities of WAAM technology to 3D-metal print a fully functional, intricate steel bridge using advanced welding processes. Since completing the bridge, MX3D has successfully introduced its technology into industries such as space, maritime, nuclear, and energy.

The bridge design was created using generative design and topology optimization techniques. This combination of digital design tools and advanced robotic 3D metal printing technology allowed for greater design flexibility and significant reduction in material waste. The environmental impact of metal parts manufacturing can thus be improved significantly using WAAM.

Building a complete digital twin of the bridge serves to allow inspection of the current state of the structure, log its use in real-time, and enable predictive maintenance.

As the bridge continues to serve as a platform for innovation, its new location will be announced shortly, further cementing its role as a symbol of cutting-edge engineering and collaboration.

Final touches are made before the opening of the MX3D Bridge.

Tech Topics

Opportunities to Contribute to AWS Committees

The following committees and their subcommittees welcome new members. Some committees are recruiting members with specific interests in regard to the committee's scope: Producers (P), General Interest (G), Educators (E), and Users (U).

For additional information, contact the staff member listed at *aws.org/standards/committeesandstandards program*. Also visit this website for the complete list of AWS subcommittees.

A — Fundamentals

- A1 Metric Practice (E)
- A2 Definitions and Symbols (E)
- A5 Filler Metals and Allied Materials (E)
- A9 Computerization of Welding Information

B — Inspection and Qualification

- B1 Methods of Inspection (E)
- B2 Procedure and Performance Qualification (E, G)
- B4 Mechanical Testing of Welds (E, G, P)

C — Processes

- C1 Resistance Welding (E, G, U)
- C2 Thermal Spraying (E, G, U)
- C3 Brazing and Soldering (E, G)
- C4 Oxyfuel Gas Welding and Cutting (E, G)
- C6 Friction Welding (E)
- C7 High Energy Beam Welding and Cutting (E, G)

D — Industrial Applications

- D1 Structural Welding (E, G, P, U)
- D3 Welding in Marine Construction (E, G, U)
- D8 Automotive Welding (E, G, U)
- D9 Sheet Metal Welding (G, P)
- D10 Piping and Tubing (E, U)
- D11 Welding Iron Castings (E, G, P, U)
- D14 Machinery and Equipment (E, G, U)
- D15 Railroad Welding (E, G, U)
- D16 Robotic and Automatic Welding (E)
- D17 Welding in the Aircraft and Aerospace Industry (E, G)
- D18 Welding in Sanitary Applications
- D20 Additive Manufacturing (E, G)

F — Safety and Health (SHC)

- SHC Safety and Health (E, G)

G — Materials

- G1 Joining of Plastics and Composites (E, G)
- G2 Joining Metals and Alloys (E, G, U)

J — Welding Equipment

- J1 Resistance Welding Equipment (E, G, U)

Technical Committee Meetings

All AWS technical committee meetings are open to the public. Contact the staff members listed or call (305) 443-9353 for information. Events can be found on the AWS calendar at *aws.org/Community-and-Events/calendar*.

Jan. 20. SH1 TAC Winter Meeting (remote). Contact: P. Portela, *pportela@aws.org*.

Standards for Public Review

AWS was approved as an accredited standards-preparing organization by the American National Standards Institute (ANSI) in 1979. AWS rules, as approved by ANSI, require that all standards be open to public review for comment during the approval process. Standards open for public review can be found at *aws.org/standards/page/standards-notices*. This column also advises of ANSI approval of documents. A draft copy may be obtained by contacting the secretary listed.

C2.20/C2.20M (R202X), *Specification for Thermal Spraying Zinc Anodes on Steel Reinforced Concrete*. Revised Standard. $40. Contact: J. Rosario, *jrosario@aws.org*.

D1.8/D1.8M, *Structural Welding Code-Seismic Supplement*. Revised Standard. $102. Contact: J. Molin, *jmolin@aws.org*.

New Standards Approved by ANSI

A5.1/A5.1M-2024, *Specification for Carbon Steel Electrodes for Shielded Metal Arc Welding*. Approval Date: 9/30/2024.

A5.02/A5.02M-2025, *Specification for Filler Metal Standard Sizes, Packaging, and Physical Attributes*. Approval Date: 10/1/2024.

AWS D1.5M/D1.5 Official Interpretation

Date: September 30, 2024
Subject: Undercut Allowance
Code Edition: D1.5M/D1.5:2015-AMD1
Code Provision: Subclause 6.26.1.5
AWS Log: D1.5-15-I10

Inquiry: AWS D1.5M/D1.5:2015-AMD1, subclause 6.26.1.5 addresses allowable undercut as being no more than 0.25 mm [0.01 in.] when the weld is transverse to the tensile stress under any design loading condition and no more than 1 mm [1/32 in.] for all other cases:

Does the attached sketch correctly represent the intent of AWS D1.5M/D1.5:2015-AMD1, subclause 6.26.1.5?

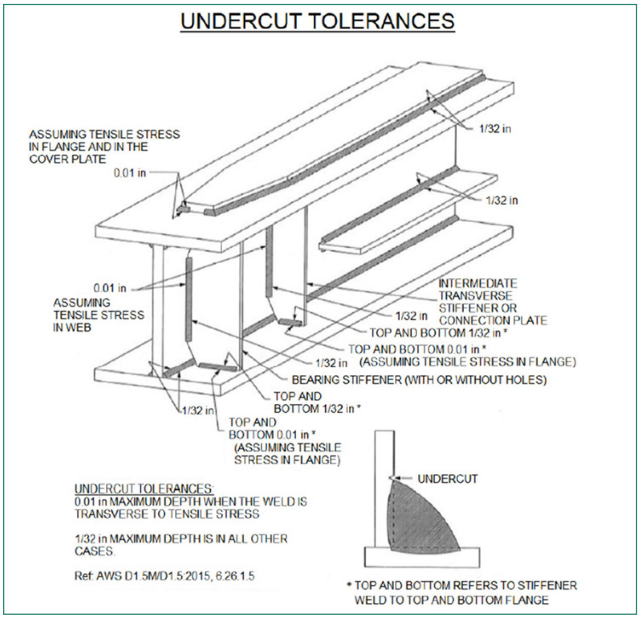

Response: The schematic illustrates the provisions of AWS D1.5M/D1.5:2015-AMD1, subclause 6.26.1.5, except the top toe of the fillet weld at the end of the cover plate is 1/32 in., and both toes of the fillet weld on the tapered part of the cover plate are 1/32 in.

AWS standards are prepared by AWS technical committees. Because many AWS standards are written in the form of codes or specification, they cannot present background material or discuss the committee's intent.

The nature of inquiries directed to the American Welding Society and their technical committees have indicated that there are some requirements in AWS standards that are either difficult to understand or not sufficiently specific.

It should be recognized that the fundamental premise of AWS standards is to provide general stipulations applicable to any situation and to leave sufficient latitude for the exercise of engineering judgment. Another point to be recognized is that AWS standards represent the collective experience of AWS technical committees, and, while some provisions may seem overly conservative, they have been based on sound engineering practice.

Membership Activities

AWS Member Counts

November 1, 2024

Sustaining	560
Supporting	303
Educational	1090
Affiliate	560
Welding Distributor	45
Total Corporate	**2558**
Individual	50,051
Student + Transitional	15,511
Early Career	455
Total Members	**66,017**

New AWS Supporters

Sustaining Corporate Members

Tate Fabricating Co. Inc.
419 Industrial Dr.
White House, TN 37188

United Steel Inc.
164 School St.
East Hartford, CT 06108

WELD X INC
326 Little Iris Ct.
Ocoee, FL 34761

Welding Distributor Member

EDGE Welding Supply
706 Performance Rd.
Unit C
Mooresville, NC 28115

Supporting Company Members

3GSD LLC
85 Newark Pompton Tpke.
Riverdale, NJ 07457

Brycoat Inc.
207 Vollmer Ave.
Oldsmar, FL 34677

Mandina's Inspection Services Inc.
209 Pi St.
Belle Chasse, LA 70037

Titan Specialty Doors
10 Millpond Dr.
Units 4 & 5
Lafayette Township, NJ 07848

Weldcoa
335 E. Sullivan Rd.
Aurora, IL 60505-9762

Educational Institution Members

Central Texas College
6200 W. Central Expy.
Killeen, TX 76549

Chabot Community College Welding Department
25555 Hesperian Blvd.
Hayward, CA 94545

Columbiana County Career and Technical Center
9364 State Rte. 45
Lisbon, OH 44432

Design and Technology Institute
P.O. Box KN 85 Kaneshie
Accra, 233
Ghana

Foundation Builders International Inc.
8033 Iona Wy.
Milford, DE 19963

Fusion Welding Institute
2930 NE 24 St.
Ocala, FL 34470

Innovative Laser Safety
8211 Blaikie Ct.
Sarasota, FL 34240

Killeen Independent School District Career and Technical Education
1320 Stagecoach Rd.
Killeen, TX 76542

LEOTEK Inspections and Training Services
Deira
534–536 Business Village
Dubai, DU 187007
United Arab Emirates

M.C. Dean
1765 Greensboro Station Pl.
Tysons, VA 22102

Muskegon Correctional Facility
2400 S. Sheridan Dr.
Muskegon, MI 49442

Namibian Institute of Welding
P.O. Box 1757
Swakopmund, 9000
Namibia

Newberry Correctional Facility
13747 E. County Rd. 428
Newberry, MI 49868

Passaic County Community College
1 College Blvd.
Paterson, NJ 07505

Richard A. Handlon Correction Facility
1728 W. Bluewater Hwy.
Ionia, MI 48846

Rochester Arc & Flame Center
125 Fedex Wy.
Rochester, NY 14624

School District of Ashland
2000 Beaser Ave.
Ashland, WI 54806

STEM U Foundation — NDE Institute
1971 Lincoln Rd.
York, SC 29745

Tennessee College of Applied Technology Hartsville
716 McMurry Blvd. E.
Hartsville, TN 37074

Utah State University Blanding
576 W. 200 S.
Blanding, UT 84511

West Ashley Center for Advanced Studies
4066 W. Wildcat Blvd.
Charleston, SC 29414

West Virginia University Parkersburg
300 Campus Dr.
Parkersburg, WV 26104

Wrangell High School
312 Reid St.
Wrangell, AK 99929

Affiliate Corporate Members

Ametco Manufacturing Corp.
4326 Hamann Pkwy.
Willoughby, OH 44094

BuhlerPrince Inc.
670 Windcrest Dr.
Holland, MI 49423

DeGeest Corp.
115 N. Sundowner Ave.
Tea, SD 57064

DEM Elevating Equipment
27685 Rockawalkin Ridge Rd.
Salisbury, MD 21801

Energy Fusion LLC
128 Read Ave.
Rupert, ID 83350

Honduran Structural Steel Construction and Commerce S. de R.L. de C.V.
Colonia El Prado Calle Golan,
Calzada Diaz Zelaya
Casa # 2326
Tegucigalpa, Honduras

HRV Conformance Verification Associates Inc.
420 Rouser Rd.
Ste. 400
Moon Township, PA 15108

IQT Chile Spa
Av. Los Aromos #4205, Cs 16,
Alto Hospicio, Tarapacá, Chile

Monterrey Precision Metals
Calle Triángulos
Zona Industrial Arco Vial, 66023
Mexico

Prime Point Solutions LLC
9322 Guess St.
Rosemead, CA 91770

AWS Corporate Milestones

AWS Corporate Members are vital to the strength and advancement of the Society's global mission and to the welding industry in general. In appreciation of the ongoing membership and support of our Corporate Members, AWS launched the Corporate Member Milestone Appreciation Program recognizing companies that have achieved significant membership milestones. AWS is pleased to recognize Corporate Members that achieved Gold, Silver, and Sapphire Member status in November 2024.

Gold — 50 Years

Name	Location	Member Category
Strate Welding Supply Co.	Buffalo, NY	Welding Distributor

Silver — 25 Years

Name	Location	Member Category
Alpena High School	Alpena, MI	Educational Institution
AZCO Inc.	Appleton, WI	Sustaining Corporate
Blue Hills Regional Technical	Canton, MA	Educational Institution
Container Technologies Industries LLC	Helenwood, TN	Supporting Corporate
Komatsu America Mining Systems Inc.	Peoria, IL	Sustaining Corporate

Sapphire — 10 Years

Name	Location	Member Category
Applied Technical Services Inc.	Marietta, GA	Sustaining Corporate
Arc Enterprises Inc.	Kingfield, ME	Welding Distributor
Jenmar Specialty Products	Pounding Mill, VA	Affiliate Corporate
Lawrence Fabrication Inc.	Simpsonville, SC	Affiliate Corporate
ML Ruberton Construction Co. Inc.	Hammonton, NJ	Supporting Corporate
Rich Mountain Community College	Mena, AR	Educational Institution
Southwest Texas Junior College	Uvalde, TX	Educational Institution

AWS Individual Milestones

AWS Individual Members are vital to the strength and advancement of the Society's global mission and to the welding industry in general. In appreciation of ongoing membership and support of our Individual Members, AWS launched the Individual Member Milestone Appreciation Program recognizing those who have achieved significant membership milestones. AWS is pleased to recognize Individual Members who achieved Gold, Life, and Silver status in January 2025.

Gold — 50+ Years

Name	Section	Milestone Year
Carmen V. Cavacini	Tri-River	75
Ronald A. Dennis	New Mexico	70
Raymond Hemzacek	Chicago	70
Rayburn Johnson	Greater Huntsville	70

Gold — 50+ Years (continued)

Name	Section	Milestone Year
Robert Alexander	Cleveland	65
J. W. Arthurs	Detroit	65
Mike W. Bulaw	Milwaukee	65
Gerald R. Crawmer	Northern New York	65
Thomas E. Drawbaugh	Tri-River	65
David G. Dykstra	Greater Oregon	65
D. H. Nordstrom	North Texas	65
Fritz Saenger	South Carolina	65
John W. Staudt	Los Angeles/Inland Empire	65
C. E. Strickland	Syracuse	65
Erroll C. Sult	Charlotte	65
David C. Crawford	Houston	60
L. D. Crawford	Kansas City	60
Pete W. Marshall	Santa Clara Valley	60
E. G. Morgan	North Florida	60
G. M. Rough	Maine	60
Urban A. Schneider	Birmingham	60
Roger C. Yackey	Chicago	60
L. C. Yeardley	Tri-State	60
Brian T. Connolly	Central Texas	55
John F. Daamen	International	55
Kenneth W. Maidment	Charlotte	55
Gary I. Senff	Nebraska	55

Gold — 50 Years

Name	Section
Lonnie W. Benn	Spokane
Frank Cox	Indian
Kenneth H. Holko	San Diego
Khalid H. Khan	Greater Oregon
Robert Odell	Philadelphia

Life — 35 Years

Name	Section
Brad A. Bosworth	Central Valley
Michael D. Cameron	North Texas
Anver E. Classens	Charlotte
Norwood L. Clemens	Florida West Coast
Charles E. Crumpton Jr.	Florida West Coast
Carl F. Ducote	New Orleans
Keith A. Hahn	Corpus Christi
Jerry Krzeminski	Philadelphia

Life — 35 Years (continued)

Name	Section
James P. Morford	Pittsburgh
Barry P. Norton	Boston
Dennis R. Richardson	Cincinnati
Marc E. Shattuck	Green — White Mountains
Jack W. Sparks	Mobile
Troy A. Torres	Southern Colorado
James G. Veillon	Lake Charles
James E. Wynegar	York-Lancaster
Derreld Yost	Utah
John D. Kinsman	J.A.K.
Jeffery W. Newberry	Charlotte

Silver — 25 Years

Name	Section
Carlos Alfaro	San Diego
Michael E. Bryant	Southwest Virginia
Bruce H. Burdick	Western Carolina
Brian R. Diorio	Central Massachusetts/Rhode Island
Charles V. Droddy	Houston
Stewart A. Harris	Triangle
Steve Hidden	Fox Valley
Scott B. Holcomb	Sierra Nevada
Larry L. Kilgore	Oklahoma City
Stuart A. Kleven	J.A.K.
Edward P. Leach	San Francisco
Richard F. Lovelace	Sierra Nevada
Erick E. Martin	Chicago
Eric W. Schetting	New Jersey
Isaac C. Spilde	Greater Oregon
Douglas R. Stauffer	North Central Florida
Michael T. Tupa	North Texas
Charles W. Weimer	Houston
Kyle R. West	Oklahoma City

Access the Online WJ Research Papers Archive

Did you know that the *Welding Journal* grants access to hundreds of its Research Supplement papers online for free? By visiting ***wjresearch.org***, you can read research papers from 1970 to the present day.

Written by some of the world's foremost scientists, engineers, teachers, and industry professionals, the *Welding Journal* Research Supplement papers cover a range of topics, including welding procedures, metallurgy, equipment, processes, testing, quality control, and more.

AWS Member Profile

Exploring the Path of a Future Welding Professional

Hallee Tretow

Welding is a craft that requires both skill and passion. For some, the journey to a career in welding begins at an early age, driven by a curiosity for hands-on work. One such individual is Hallee Tretow, a welding student, AWS student member, and budding professional in the welding industry who is carving out her future in this field.

From Fredonia to the Welding World

Born and raised in Fredonia, Wis., Tretow's story began in the small town where her interest in hands-on work was fostered early on. Growing up in a close-knit community, she developed a love for practical, skill-based work.

After graduating from Ozaukee High School in Fredonia, she already had a head start in welding.

"My senior year of high school, I was taking all welding courses at Milwaukee Area Technical College [in Wisconsin]. So when I graduated high school, I also got my technical diploma in welding," she said. Now, she is continuing her education and working toward an associate's degree in welding technology at the same college.

The Spark for Welding

The journey into welding wasn't an accident; it was a natural evolution of her interests in hands-on work.

"From an early age, I have taken interest in hands-on jobs," she said. This curiosity led her to explore shop classes in high school, from woodshop to metalshop, where she first encountered welding. "I believe I was a sophomore in high school when I first welded, and I really enjoyed the craft behind it," she said, highlighting how that first experience ignited her passion for welding.

Mentorship: Learning from the Best

Having mentors has been an integral part of Tretow's journey in the welding world. She credits several key figures with shaping her growth.

"I like to say that I have a lot of mentors because I have learned so much from a lot of people in this field," she said.

Her instructors at Milwaukee Area Technical College — Bill Peterson, Darrel Iwanski, and Lee Cerveny — have been particularly influential in her education.

"They have all helped me so much to continue my education and have all talked with me one-on-one about what I can do to advance my career," she said. "Hearing about how long they have been in this field and how far it has taken them in life really is special to me as someone who is just starting out."

Additionally, her current job at Wisconsin Stamping and Manufacturing, Germantown, Wis., offers Tretow many opportunities to learn and grow and encourages her professional development.

"I have a wonderful job at Wisconsin Stamping and Manufacturing, and they are supportive of the fact that I want to try new things and learn as much as I can," she said.

Family Support: A Strong Foundation

For many students, family support plays a crucial role in their success, and Tretow is no different. She was raised in a single-parent household, and her mother has been a constant source of encouragement.

"My mom has always been very supportive of my studies of welding. She always pushes me to take all of the opportunities I am given and to always try my best," Tretow shared with gratitude, acknowledging how her mother's belief in her has helped fuel her determination.

Thriving in the Welding Industry

Welding, like many trades, remains a male-dominated field, but this rising star navigates this challenge with confidence.

"My whole working career, I have always worked in male-dominated fields. So I guess I just got used to it," she said.

Being one of the few women in her welding classes hasn't discouraged her; in fact, it has been a learning opportunity. "When I would be in school with a majority of men, I could start to see that we all are learning at the same pace," Tretow said.

She admits that certain physical demands in the job — such as tasks requiring heavy muscular strength — can present a challenge, but she remains undeterred.

"The only thing for me that I struggle with sometimes is that I have to work harder when it comes to jobs that need a lot of muscular strength," she said. Nevertheless, her resilience and commitment to the craft continue to drive her forward.

The Value of Being an AWS Student Member

Becoming an AWS member has proven to be a pivotal decision in her career. Membership has opened doors to a wide range of opportunities, including scholarships that have helped fund her education.

One of the highlights of her AWS membership was attending FABTECH, a major welding industry conference. "I was able to go to FABTECH last year because my local AWS group shuttled people to it," she explained.

FABTECH allowed her to meet industry professionals, connect with like-minded individuals, and explore different career paths within welding.

"I have even met a lot of people who had different experiences in this field, which helped me learn more about this industry and all of the different jobs I can get into," Tretow added.

Tretow learns how to use a laser welding machine at Wisconsin Stamping and Manufacturing (upper left). Tretow works on a robotic welding program at Milwaukee Area Technical College (above).

Looking to the Future

While her career path is still unfolding, her passion, drive, and willingness to explore various facets of welding promise a bright future. With a supportive family, mentors who have guided her journey, and an eagerness to embrace new challenges, she is well on her way to becoming a respected professional in the welding industry.

While many professionals in the welding field have specific career goals, Tretow is still exploring the various avenues that this industry offers. "Right now, I do not have any specific career goals. I am mainly focusing on finishing my degree," she said. "I'm just focusing on learning as much as I can right now and taking advantage of every opportunity that comes my way."

Her diverse interests within the field, from robotic welding to gas tungsten arc welding and even becoming a weld inspector, make it clear that she's open to many possibilities.

American Welding Society®

8669 NW 36 St., #130
Miami, FL 33166-6672
(800/305) 443-9353

AWS PRESIDENT

Richard L. Holdren / *president@aws.org*
Welding Consultants LLC/ARC Specialties

SENIOR LEADERSHIP TEAM

Interim Executive Director & CEO
Robert "Bob" W. Roth / *rroth@aws.org*
(786) 937-9510

Chief Financial Officer/
Chief Administrative Officer
Gesana Villegas / *gvillegas@aws.org*
(786) 937-9552

Vice President Marketing, Strategy, and Communications
Cassie Burrell / *cburrell@aws.org*
(786) 937-9553
Marketing Communications

Vice President
Richard L. Arn / *rarn@aws.org*
(786) 937-9572
Welding & Technology

Executive Director, AWS Foundation
Monica Pfarr / *mpfarr@aws.org*
(786) 937-9641
Foundation

Chief People Officer
Tatiana Milan / *tmilan@aws.org*
(786) 937-9509
Human Resources

Vice President Operations and Membership
John Perry / *jperry@aws.org*
(786) 937-9547
IS, PMO, Membership & Operational Services

Managing Director
Annette Alonso / *aalonso@aws.org*
(786) 937-9599
Standards & Publications

Managing Director
Alicia Garcia / *agarcia@aws.org*
(786) 937-9529
Education & Training

Managing Director
Matthew Rubin / *mrubin@aws.org*
(786) 937-9539
Exposition & Sales

EXECUTIVE OFFICE

Executive Assistant
Malisa Mercado / *mmercado@aws.org*
(786) 937-9593

GOVERNMENT LIAISON SERVICES

Hugh Webster / *hwebster@wc-b.com*
Webster, Chamberlain & Bean, Washington, D.C.
(202) 785-9500; Fax: (202) 835-0243
Monitors federal issues of importance to the industry.

CERTIFICATION SERVICES

Managing Director
Denny Smith / *dsmith@aws.org*
(786) 937-9581

Director, Accreditation
Cassy Scheffer / *cscheffer@aws.org*
(786) 937-9564

CONFERENCES & EVENTS

Director, Conferences
Margaret Jamborsky / *mjamborsky@aws.org*
(786) 937-9513

CUSTOMER SERVICE & SUPPORT

Dept. information / *customerservice@aws.org*

EXPOSITIONS & SALES

Senior Sales Executive, Expositions
Sarah Dickson / *sdickson@aws.org*
(786) 937-9597

Senior Sales Executive, Education
Efram Abrams / *eabrams@aws.org*
(786) 937-9633

Manager, Advertising Sales Operations
Lea Owen / *lea@aws.org*
(786) 937-9520

Senior Sales Executive, Advertising Sales
Scott Beller / *sbeller@aws.org*
(786) 937-9619

RWMA, WEMCO, and ITSA

Program Manager
Adrian Bustillo / *abustillo@aws.org*
(786) 937-9595

MEMBER SERVICES

Director, Membership
Darrill Gaschler / *dgaschler@aws.org*
(786) 937-9560
Serves as a liaison between members and AWS headquarters.

PUBLISHING & EDITORIAL

Welding Journal

Managing Editor
Kristin Campbell / *kcampbell@aws.org*
(786) 937-9557

Section News Editor
Cindy Weihl / *cweihl@aws.org*
(786) 937-9556

Society News Editor
Roline Pascal / *rpascal@aws.org*
(786) 937-9603

News of the Industry Editor
Alexandra Quiñones / *aquinones@aws.org*
(786) 937-9623

Digital Editor
Ryan Litton / *rlitton@aws.org*
(786) 937-9637

Inspection Trends

Editor
Carlos Guzman / *cguzman@aws.org*
(786) 937-9503

STANDARDS DEVELOPMENT

Director, Standards Committee Operations
Jennifer Molin / *jmolin@aws.org*
(786) 937-9604
Structural Subcommittees on Seismic Applications and Titanium, Safety and Health

Director, Standards Product Development
Peter Portela / *pportela@aws.org*
(786) 937-9611
Technical Activities Committee

Program Managers
Stephen Borrero / *sborrero@aws.org*
(786) 937-9634
Definitions and Symbols, Structural Subcommittees on Bridge Welding, Reinforcing Steel and Stainless Steel, Joining of Metals and Alloys, Piping and Tubing

Kevin Bulger / *kbulger@aws.org*
(786) 937-9607
Filler Metals and Allied Materials, International Filler Metals, UNS Numbers Assignment, Brazing and Soldering, Welding of Machinery and Equipment, Welding in Marine Construction

Ady Celaya / *acelaya@aws.org*
(786) 937-9605
Automotive, Resistance Welding, Resistance Welding Equipment, Thermal Spraying, Robotic and Automatic Welding

Exsenet Esler / *eesler@aws.org*
(786) 937-9569
Welding and Brazing in Aerospace, Additive Manufacturing, Sheet Metal Welding, and High Energy Beam Welding & Cutting

Marandi Gills / *mgills@aws.org*
(786) 937-9505
Computational Weld Mechanics, Methods of Weld Inspection, Oxyfuel Gas Welding and Cutting, Friction Welding, Sanitary Welding

Jennifer Padron / *jpadron@aws.org*
(786) 937-9606
Structural Subcommittees on Aluminum and Strengthening and Repair, Procedure and Performance Qualification, Joining of Plastics & Alloys, and Mechanical Testing of Welds

Jennifer Rosario / *jrosario@aws.org*
(786) 937-9608
Railroad Welding, Welding of Iron Castings, Structural Welding, Mechanical Testing of Welds

***Welding Handbook* Editor**
Stephen Borrero / *sborrero@aws.org*
(786) 937-9634

TECHNICAL SERVICES

Regional Director, Welding Technology Services – Americas and Europe
Nathan Carter / *ncarter@aws.org*
(786) 937-9602

Regional Director, Welding Technology (Asia, Africa, & Oceania)
Steve Snyder / *ssnyder@aws.org*
(786) 937-9600

Director, International Activities
Andrew Davis / *adavis@aws.org*
(786) 937-9624
International Standards Activities, American Council of the International Institute of Welding

AWS FOUNDATION INC.

aws.org/foundation

Chair, Board of Trustees
William A. Rice / *war8257@gmail.com*

Associate Director, Foundation
John Douglass / *jdouglass@aws.org*
(786) 937-9512

The AWS Foundation is a not-for-profit 501(c)(3) charitable organization established to provide support for the educational and scientific endeavors of the American Welding Society. You can support the AWS Foundation by visiting *aws.org/donate.*

District Directory

District 1

Timothy Kinnaman, director
(401) 323-0535
tckinnaman@gmail.com

District 2

Justin Mixon, director
(410) 422-0994
jmixon3382@gmail.com

District 3

Bradley Brandmeir, director
(610) 799-1328
brandmeirb@lcti.org

District 4

Anver Classens, director
(704) 443-1223
anver.classens@gmail.com

District 5

Daryl Peterson, director
(813) 523-5436
daryl.peterson@outlook.com

District 6

Ronald Stahura, director
(716) 207-7869
rstahura@esab.com

District 7

Roger E. Hilty, director
(740) 317-9073
rhilty@comcast.net

District 8

James Thompson, director
(256) 347-6481
jthompsonwelds@gmail.com

District 9

Anthony Blakeney, director
(985) 549-2071
anthony.blakeney@selu.edu

District 10

Tom Kostreba, director
(814) 881-0632
kostreba@hotmail.com

District 11

Wesley Doneth, director
(810) 844-2759
doneth.wesley@fronius.com

District 12

Ben Newcomb, director
(608) 279-8108
bpnewcomb1@madisoncol-lege.edu

District 13

Ronald Ashelford, director
(815) 218-8766
ron_ash@hotmail.com

District 14

Travis Jumper, director
(618) 468-4931
tjumper@lc.edu

To find an AWS Section near you, visit:
aws.org/membership/sectionsmap

District 15

Dale Szabla, director
(612) 419-3869
djszabla@hotmail.com

District 16

Jeffrey Jones, director
(918) 638-2787
jwjones@herzog.com

District 17

Viji Kuruvilla, director
(501) 517-1594
vijik@lexicon-inc.com

District 18

Caity Brown, director
(812) 821-4884
caity@madskillsllc.com

District 19

Boyce Towell, director
(609) 284-7449
boyce.towell@gmail.com

District 20

Denis Clark, director
(208) 357-6626
denis.clark.51@gmail.com

District 21

Nicolas Martinez, director
(480) 822-8019
nicholas.martinez@srpnet.com

District 22

Randy Emery, director
(559) 285-1803
randye@cos.edu

District Activities

District 1 — Boston

Oct. 23

LOCATION: Theo Laser, Westborough, Mass.

SUMMARY: Section members had the opportunity to tour the northeast headquarters and laser lab of Theo Laser. Participants were also able to try their hand at handheld laser welding with the Theo MA1 system.

BOSTON — Seen during the facility tour are (from left) District Director Tim Kinnaman, Section Chair Tom Ferri, Theo Laser Director of Sales Jonathan Proctor, Theo Laser Welding Technician Harrison Shoupe, and Boston Section members John Siegiewz Jr. and Andres Moreno.

District 1 — Green and White Mountains

Sept. 12

LOCATION: Tunbridge World's Fair, Tunbridge, Vt.

SUMMARY: The Section hosted its annual Tunbridge World's Fair interactive AWS information/welding booth, featuring live hands-on welding and cutting demonstrations, a virtual welding station, scholarship and membership information, welding career/industry information, a welding equipment raffle, and a welding contest. The contest was open to anyone wanting to test their skills, at no charge, for the chance to win a new Jackson welding helmet. Winners were awarded helmets each day, with a total of eight helmets won during the four-day event. More than 200 people visited the AWS booth over the course of the event. The Northland Job Corps welding program in Vergennes, Vt., sent a bus full of welding students for a visit on day two. District 1 and Green and White members and volunteers managed the event. The event was also co-sponsored by several businesses that donated equipment, time, and products. The AWS booth won a third-place fair ribbon for content, interest, and layout.

GREEN AND WHITE MOUNTAINS (top left) — The Section's booth at the Tunbridge World's Fair.
(top right) The virtual welding station with Section booth organizer Aaron Emmons and an aspiring welder.
(below left) Pictured are members, volunteers, and business supporters.
(below right) Northland Job Corps welding program students visited the fair and the AWS booth.

SECTION NEWS

District 3 — Lehigh Valley

Oct. 22

LOCATION: Philadelphia Shipyard, Philadelphia, Pa.

SUMMARY: Project MFG's annual welding competition at the Philadelphia Shipyard drew Section and District participation. In conjunction with the welding competition, a job fair was held for students and adults looking to connect with shipyard employers or those who supply the shipyard with raw goods.

LEHIGH VALLEY (left) — Instructor Brad Brandmeir (center) with his two students, Logan R., who took second place, and Shawn B., who took fourth place. (inset) Logan R. from Lehigh Career & Technical Institute is seen welding/fabricating this year's submarine project.

District 3 — York-Lancaster

Sept. 26

LOCATION: Drunken Smithy, Lebanon Valley Mall, Lebanon, Pa.

SUMMARY: Members participated in a tour of a forging workshop and saw demonstrations related to making various hand-forged items such as axes, swords, knives, and hammers.

YORK-LANCASTER — Meeting attendees included (from left) Evan Martz, Ralph Davis, Blacksmith Eitry Jones, Mark Malone, Erin Jones, Justin Stahl, Section Chair Ed Calaman, Dean Whitmer, and Rich Schulde.

District 4 — Northeastern Carolina

Nov. 6

LOCATION: Beaufort Community College, Washington, N.C.

SUMMARY: Area high school students and Beaufort students learned why AWS membership is important and the benefits that come along with it. The Section's Mark Sapp gave a presentation about AWS to the students while they enjoyed Subway sandwiches for dinner. Following Sapp's presentation, local vendors from Arc3 Gases, Airgas, and Dillon Supply gave presentations about their products and what the companies do for the community. After the vendor presentation, there was a raffle for AWS hats. Then Instructors Ted Clayton and Eric Braddy gave a tour of their shop and showed off a sculpture that Braddy and some of his students made.

NORTHEASTERN CAROLINA — Attendees posed for a group photo.

District 4 — Tidewater

Nov. 14

LOCATION: Virginia Peninsula Community College, Hampton, Va.

SUMMARY: Members enjoyed a presentation by retired welding engineer Paul Hebert titled "History of Welding — The Enabling Technologies." Hebert recently retired from Newport News Shipbuilding, where he spent 38 years as a welding engineer and managed the weld engineering department for the last 20 years.

TIDEWATER (top left) — Section Chair Kristie Miller (left) is seen with special guest speaker Paul Hebert.
(above) Section Vice Chair Pierrette Swan and her students from New Horizons are seen at the meeting.
(left) Attendees are seen during the meeting.

SECTION NEWS

District 5 — Atlanta

Oct. 15

LOCATION: Sunbelt Ag Show, Moultrie, Ga.

SUMMARY: Southern Regional Technical College Welding Instructor Brad Simmons and his students volunteered at the AWS Careers in Welding trailer during its visit to the Sunbelt Ag Show. Trailer visitors competed for the highest virtual welding score inside the trailer. Dayton Wilkes and Connor Mullin each won a $1000 AWS scholarship for their high scores.

ATLANTA — Dayton Wilkes (left) won a $1000 AWS scholarship.

District 5 — Atlanta

Nov. 14

LOCATION: Gerdau Steel Mill, Cartersville, Ga.

SUMMARY: Gerdau Steel Mill welcomed members to its plant. Employees Taylor Thorton and Henrique Lize discussed the process of making steel billets and cutting them into flat bars. During the plant tour, members also visited the testing lab.

ATLANTA (left) — Jonny Thorton and Robert Trudelle presented Taylor Giddens and Henrique Lize of Gerdau Steel with a plaque for hosting the meeting.
(right) Tour attendees gathered for a group photo.

District 5 — North Central Florida

Oct. 29

LOCATION: College of Central Florida, Jack Wilkinson Levy Campus, Chiefland, Fla.

SUMMARY: The Section hosted its North Central Florida, Section 188 Annual Welding Competition at the College of Central Florida. Participating schools included Bradford High School, Dixie County High School, Columbia High School, College of Central Florida, Santa Fe College, Marion Technical College, Marion Technical Institute, North Florida Technical College, and Big Bend Technical College. The winners were as follows: first place — Brett Jones, Big Bend Technical College; second place — Richard Tyre, Big Bend Technical College; and third place — Connor Valentine, Dixie County High School. The event had an amazing turnout with many sponsors like Alien Engineered Products, Airgas, Lincoln Electric, Crom, Weldtest Services, Red-D-Arc Welderentals, E-One, Edge Welding Supply, Full Penetration Welding and Fabrication, Tunnel Master, and Citrus Mobile Welding and Fabrication LLC donating welding helmets, grinding tools, hats, shirts, and more.

District 5 — North Central Florida (continued)

Oct. 29

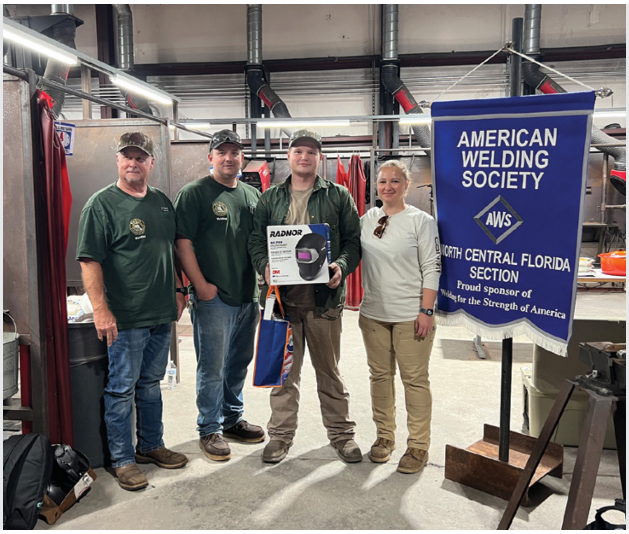

NORTH CENTRAL FLORIDA — The Section's Annual Welding Competition attracted many schools and sponsors.

District 6 — Northern New York

Sept. 19

LOCATION: Russell Sage Dining Hall, Troy, N.Y.

SUMMARY: Section members attended technical presentations from Rensselaer Polytechnic Institute on current research involving sensing for the wire-arc additive manufacturing (WAAM) process and from Servo-Robot on laser vision systems for bringing intelligence to industrial robots for arc and laser welding, joint finding, joint tracking, weld inspection, and automated teaching. A live demonstration followed, during which a fan blade was printed in the WAAM cell with live data from the Servo-Robot sensor.

NORTHERN NEW YORK (above) — Attendees view a demonstration of automated weld inspection technology.
(above right) Meeting attendees gathered for a group photo.
(right) Participants saw the Rensselaer sensor-enabled WAAM system.

District 9 — Auburn-Opelika

Sept. 14

LOCATION: National Center for Asphalt Technology, Montgomery, Ala.

SUMMARY: Travis Walbeck conducted a presentation and tour of the National Center for Asphalt Technology (NCAT) for Section members. The center was established in 1986 as a partnership between Auburn University and the National Asphalt Pavement Association Research and Education Foundation to provide practical research and development to maintain America's highway infrastructure.

AUBURN-OPELIKA — Members posed with guest speaker Travis Walbeck.

District 9 — New Orleans

Oct. 15

LOCATION: Plumbers and Steamfitters UA Local 60 Assembly Hall, Metairie, La.

SUMMARY: The Section's October general meeting was sponsored by Boh Bros Construction. Speakers included Vincent Rabalais, William (Trey) St. John, and Tyler Unsworth with Boh Bros., who delivered a very informative presentation on work ethics. This presentation focused on what it takes to succeed in a career in welding as well as the opportunities and benefits available to those just getting started.

NEW ORLEANS — Pictured at the October meeting are (from left) Section Vice Chair Aldo Duron, William (Trey) St. John, Tyler Unsworth, Vincent Rabalais, and Section Chair Jacob Newton.

District 9 — New Orleans

Nov. 9

LOCATION: New Orleans Pipe Trades, Metairie, La.

SUMMARY: The Section held its 18th Annual Student Welder Competition. Student members from surrounding high schools, career centers, technical and community colleges, universities, trades schools, and apprenticeship programs competed in two levels of competition, with first, second, and third place awards. The turnout was great, with strong support from sponsors, Section officers, judges, instructors, parents, and family members participating in the event. Rougarou BBQ did an awesome job of serving up great food for everyone. Lincoln Electric, Milwaukee Tools, and other supporting sponsors donated door prizes, awards, and consumables. The Section would like to thank New Orleans Pipe Trades for hosting the event and Plumbing and Steamfitters UA Local 60 for providing the use of their assembly hall for the awards ceremony. Prize monies for awards were provided by the proceeds of the AWS New Orleans Section Annual Fishing Rodeo (Tournament), held every spring. This was the largest event to date with nearly 100 industry participants.

District 9 — New Orleans (continued)

Nov. 9

NEW ORLEANS — Competition winners included Luis Reyes (Delgado Community College), Orrin Cobb (Southeastern Louisiana University), first-place winner Jason Almendares (New Orleans Pipe Trades), first-place winner Catherine Helgason (Delgado Community College), Rodrigo Ortiz (NOPT HS Program), and Kevin Barahona (NOPT HS Program).

District 9 — Mobile

Sept. 26

LOCATION: The Original Oyster House, Spanish Fort, Ala.

SUMMARY: Section members gathered for Welding Trivia and Scholarship Night. The meeting was sponsored by Miller Electric and WESCO Gas & Welding Supply Inc. There were 52 people in attendance despite rescheduling due to inclement weather. Scholarship recipients in attendance at the meeting were recognized; a split-the-pot drawing was held; door prizes were awarded; and students, along with others, participated in some welding trivia. The Section is appreciative to all who helped make it a fun and successful meeting.

MOBILE — Scholarship recipients in attendance were recognized, including (from left) Section Chair Derrick Lett; scholarship recipients Jessie Levron, Will Stanhope, and Lauren (Mo) Kelly; and Section Scholarship Chair Jody Heusman.

District 9 — Mobile

Sept. 28

LOCATION: Camp Maubila, Grove Hill, Ala.

SUMMARY: The Section was honored to assist in the South Region Scouts of America Five Rivers Fall Camporee 2024. The camporee included welding. Tim DeVargas, a welding instructor at Faulkner Career Technical Center in Mobile, Ala., attended on behalf of the Mobile Section and assisted with the welding portion of the event. This year's theme was "Galactic Heist" and special permission was given by Disney to use Star Wars. Approximately 350 people attended the event, but welding was limited to those randomly selected. Scouts were divided up into various groups and participated in firefighting, a drone obstacle course, water safety, soldering, welding, and more. Within the groups, five Scouts from each group were chosen into three smaller groups to weld with assistance from DeVargas, Scout Master Will Gates of Troop 292, and Scout Master Jason Wolfenden of Troop 90. Scouts donned their personal protective equipment (PPE), and after a quick welding lesson, they created TIE fighters, the symbol of the Imperial fleet in *Star Wars*. At the end of the day, all the completed TIE fighters were welded together to create a monument. Local companies, schools, and individuals loaned the Scouts the use of welding equipment and donated electrodes, steel, PPE, and other materials for the project. The Section purchased and donated welding gloves, jackets, safety glasses, and a couple of welding helmets. There was a lot of planning that went into this event to make it happen, and the Section was honored to help and hopes to participate in similar events in the future.

MOBILE (far left) — Scouts took a break from their busy day of welding to enjoy lunch. (left) A Scout received welding instruction. (bottom left) Welding Instructor Tim DeVargas (seated) with two Scouts showing off the TIE fighters they welded. (below) The Scouts' finished welding project.

District 10 — Drakewell/Oil Region Student Chapter

Oct. 16

LOCATION: Venango Technology Center, Oil City, Pa.

SUMMARY: Travis Crate spoke with the morning and afternoon Oil Region Student Chapter members and guests. Topics discussed included "Robert's Rule of Order," AWS involvement, networking, and the election of Student Chapter officers. The newly elected morning class officers are Kyle Phips, chair; Ethan Conway, vice chair; Sam DeNinno, treasurer; and Abby Walentoski, secretary. The newly elected afternoon class officers are Korryn Schmader, chair; Zach Carroll, vice chair; Trevor Hardin, treasurer; and Archer Zuck, secretary.

DRAKE WELL/OIL REGION STUDENT CHAPTER — Pictured are the new National Technical Honor Society members. In the first row (from left) are Parker Findlay and Hayden Bellis. In the second row (from left) are Samuel Shaffer and Cole Edwards. In the third row (from left) are Karter Hoffman and Sam DeNinno. Not pictured are Jacob Dengel and Trevor Hardin.

District 11 — Ferris State University Student Chapter

Oct. 18

LOCATION: Hemlock Park, Big Rapids, Mich.

SUMMARY: The Section hosted its 2nd Annual Pumpkin Carving Contest for members and their friends. There was a great turnout, and members had lots of fun with their peers.

FERRIS STATE UNIVERSITY STUDENT CHAPTER — Contest participants showed off their pumpkin creations.

District 11 — Ferris State University Student Chapter

Oct. 19

LOCATION: Big Rapids, Mich.

SUMMARY: Section members participated in the annual fall highway cleanup to help keep their community clean.

FERRIS STATE UNIVERSITY STUDENT CHAPTER — Section members posed for a group photo after spending the day doing a highway cleanup.

District 14 — St. Louis

Sept. 26

LOCATION: Hillsdale Fabricators, St. Louis, Mo.

SUMMARY: Hillsdale Fabricators Plant Manager Thomas Milleville led members on a facility tour. The company has been fabricating and erecting steel as a division of Alberici Corp., one of the largest general contractors in North America. The company performs most of its steel fabrication in a 250,000-sq-ft fabrication shop on its 60-acre property in St. Louis, Mo. The shop is equipped with computer numerical control equipment, and it has a professional team of fitters, operators, and welders as well as a production management team.

ST. LOUIS — Hillsdale Fabricators tour participants gathered for a group photo.

District 17 — Central Texas

Aug. 6

LOCATION: Dynamic Systems, Buda, Tex.

PRESENTER: Michael Hinterlach, AWS Certified Welding Inspector, Dynamic Systems Inc.

SUMMARY: Hinterlach led Section members on a tour of the Dynamic Systems plant. The company fabricates and installs turnkey mechanical and process equipment throughout North America. The Buda plant specifically fabricates HVAC pipe spools and assemblies; HVAC rectangular and spiral sheet metal duct; and mechanical, electric, and plumbing skids and modules.

CENTRAL TEXAS — Pictured are August tour attendees.

District 17 — Central Texas (continued)

Aug. 6

CENTRAL TEXAS — (left) Duct work fabrication at Dynamic Systems.
(above) Meeting attendees are seen touring Dynamic Systems' fabrication shop.

District 17 — Central Texas

Oct. 17

LOCATION: Patriot Erectors Inc., Dripping Springs, Tex.

SUMMARY: Section volunteers manned a booth at the Patriot Erectors AISC Steel Day Celebration. Patriot Erectors provided welding contests, vendor booths, presentations, a fundraiser, tour, and lunch. Almost 200 high school students were in attendance. Section volunteers Kristin Burke and Daniela Lowry judged the welding competition.

CENTRAL TEXAS (above) — Central Texas Section volunteers pose for a photo.

(left) AWS Certified Welding Inspectors Kristin Burke and Daniela Lowry judged the welding competition.

District 17 — East Texas

Oct. 24

LOCATION: Priefert, Mount Pleasant, Tex.

PRESENTER: Craig Easley, plant manager, Priefert

SUMMARY: Members, along with students from Tyler Junior College and LeTourneau University, had the opportunity to tour Priefert's plant, where the company fabricates livestock panels and related equipment. Tour attendees witnessed how the company utilizes robotic welding, watched the tubing mill produce steel tubing, and walked through Priefert's powder coating shop. It was a great experience for members and students to see different aspects of the welding industry in one facility.

EAST TEXAS (top) — Priefert Plant Manager Craig Easley spoke to attendees about the different products the company produces.

(far left) Students and Section members toured the cattle panel welding area of the plant.

(left) Tour participants posed for a group photo.

District 17 — Oklahoma City

Sept. 19

LOCATION: Metro Tech South Bryant Campus, Oklahoma City, Okla.

PRESENTER: JD Douglas, Hypertherm

SUMMARY: Douglas gave Section members an informative presentation and product demonstration of Hypertherm's plasma cutting technology.

OKLAHOMA CITY (right) — JD Douglas spoke to students about the capabilities of plasma cutting.
(below) Cary Reaves (left) presented guest speaker JD Douglas with a gift from the Section.
(below right) September meeting attendees gathered for a group photo.

District 18 — Houston

Sept. 25

LOCATION: Cadillac Bar, Houston, Tex.

SUMMARY: The Section's September meeting welcomed special guest speaker Michael Krupnicki, AWS 2024 president. Krupnicki engaged members and students with his presentation, and $500 was raised for the Ron Theiss Scholarship. The Section will match the donation for a total of $1000.

HOUSTON — (above) District 18 Director Caity Brown spoke to attendees.
(below) Section Chair Ed Peterson presenting during the September meeting.

HOUSTON — Attendees of the September meeting.

District 18 — Houston

Oct. 23

LOCATION: Cadillac Bar, Houston, Tex.

SUMMARY: Special guest speaker and past AWS District 18 Director Thomas Holt mentored Section members and students during the October meeting.

HOUSTON (below) — Thomas Holt spoke to and mentored Section members during his October visit.

(below) The top five prize winners of the Section's crossword puzzle game.

(bottom left) Students from Arc Labs at the October meeting.
(below) Lead Instructor Mike Frazier with Welding Instructor Ryan Rodgers and students from Elite Welding Academy.

District 19 — Inland Empire

Oct. 17

INLAND EMPIRE — Meeting attendees are seen touring OXARC.

LOCATION: OXARC LLC, Pasco, Wash.

PRESENTER: Sonny Knotts, director of operations, OXARC

SUMMARY: Over the course of 32 and a half years, OXARC employee Sonny Knotts has learned the ins and outs of welding gases and ensuring they meet today's industry standards. Knotts was able to show Section members the rigorous steps in receiving, testing, and filling of everyday welding gases. During the presentation and tour, students and professionals learned how OXARC upholds the highest quality levels of testing and handling its products to ensure they meet today's standards.

District 20 — Colorado

May 10

LOCATION: Pickens Technical College, Aurora, Colo.

SUMMARY: Past AWS President Bob Teuscher, Pickens Technical College welding student Trenton Carlson, and Pickens Technical College Welding Instructor Jeff Oliver celebrated Carlson's Top Gun win in the AWS Colorado High School Welding Skills 2024 contest that was held at Buckeye Welding Supply in Henderson, Colo., and co-sponsored by Industrial Constructors Managers (ICM) in Commerce City, Colo. Bill Brack, owner at Buckeye Welding Supply; Myron Delgado of Buckeye Welding Supply; and Vince Staff of ICM were instrumental in setting up and running the first-ever event. The Top Gun and the Test Pilot winners, along with other Section members and welding industry supporters, celebrated the event's winners at the Buckeye Welding Supply Annual BBQ and Nut Fry. Carlson has completed his first year of welding courses. He received a $1500 Section scholarship for his win.

COLORADO — (from left) Past AWS President Bob Teuscher, Pickens Technical College welding student Trenton Carlson, and Pickens Technical College Welding Instructor Jeff Oliver celebrated Carlson's Top Gun win in the AWS Colorado High School Welding Skills 2024 contest.

District 20 — New Mexico

Oct. 17

LOCATION: Albuquerque Job Corps, Albuquerque, N.Mex.

PRESENTERS: Derek Chino, Jacob Gonzales, and Victor Garcia, welding instructors

SUMMARY: Section members received a tour of the Albuquerque Job Corps center. With over 120 campuses across the United States, Job Corps provides career training and education for low-income 16- through 24-year-olds. The students get the experience they need to begin a career or apprenticeship, go on to college, or join the military. In addition to career training, Job Corps can help students earn a high school diploma or equivalent and a driver's license.

NEW MEXICO (top) — Meeting attendees gathered with Job Corps staff, including (second row, from left) Victor Garcia, Rebecca Chavez (training manager), Derek Chino, and Jacob Gonzales. (right) Meeting attendees during the tour.

Visit ***aws.org/Community-and-Events*** for more information.
Note: These events/opportunities are subject to change.

AWS-Sponsored Events

Emmet A. Craig Resistance Welding School

Jan. 22, 23

This intensive two-day course at Amada Weld Tech, High Point, N.C., provides operators, production supervisors, engineers, and other professionals with a comprehensive understanding of the theory, applications, and equipment used in resistance welding. Through demonstrations and hands-on participation with classroom welding machines and auxiliary equipment, attendees will gain practical knowledge and skills immediately applicable in their work. This school will also be held in Spanish on May 7 and 8 at Cintermex, Monterrey, Mexico.

Failure Analysis of Welded Components: Cracking & Corrosion

Feb. 4

At the Marriott St. Louis Grand, St. Louis, Mo., start your Inspection Expo & Conference (IEC) experience early with an in-depth exploration of welding failure analysis. Designed for engineers, inspectors, and industry professionals, this focused session will cover the root causes of cracking and corrosion in welded components, featuring real-world case studies and advanced techniques. Register separately or bundle with your IEC registration.

Inspection Expo & Conference (IEC)

Feb. 5–7

Professionals from AWS, the American Institute of Steel Construction, the Association for Materials Protection and Performance, and the Nondestructive Testing Management Association will meet at the Marriott St. Louis Grand, St. Louis, Mo., to explore topics concerning nondestructive examination, steel construction, and welding inspection. The conference offers the opportunity to engage with industry experts and gain valuable insights, participate in expert panel presentations and breakout sessions, and forge meaningful connections. Attendees can earn 20 professional development hours.

WEMCO Annual Meeting

Feb. 5–7

At Luminary Hotel & Co., Fort Myers, Fla., attendees will hear from an engaging lineup of guest speakers, see an expert panel discussion, and have numerous opportunities to connect with welding equipment manufacturing industry leaders and peers.

ASME Section IX Decoded: A Workshop

Feb. 25–27

This comprehensive three-day workshop at AWS Headquarters, Miami, Fla., will train participants to comply with the requirements of ASME *Section IX — Welding, Brazing, and Fusing Qualifications*. Attendees will receive a hard copy of the current edition of ASME's *Section IX* and earn 20 professional development hours. This workshop will also be held May 6–8 at T.I.C. Kiewit in The Woodlands, Tex.; Aug. 19–21 at PIT Instruction & Training in Mooresville, N.C.; and Dec. 2–4 at T.I.C. Kiewit in Aurora, Colo.

FABTECH Mexico

May 6–8

Meet with world-class suppliers, see the latest industry products and developments, and find tools to improve productivity and increase profits at this event, held at Cintermex in Monterrey, Mexico. Visit *mexico.fabtechexpo.com*.

Welding Summit

Aug. 6–8

Experts from different backgrounds and segments of the industry will gather at The Woodlands Resort in The Woodlands, Tex., to share their ideas, expertise, and perspectives on a wide variety of topics, including the latest trends in welding. Attendees will witness presentations and demonstrations; visit the exhibits of industry experts; network; and learn about the key advancements, latest technical approaches, and innovations required to support the industry. Attendees can also earn up to 21 professional development hours.

U.S., Canada, Mexico Events

AMPP Annual Conference + Expo

April 6–10

Join over 6000 materials protection experts, industry leaders, and tech visionaries at Music City Center, Nashville, Tenn. The program will feature more than 600 hours of content, the opportunity to participate in technical sessions led by industry pioneers, and peer-reviewed research. Visit *ace.ampp.org*.

Automate 2025

May 12–15

Presented by the A3 Association for Advancing Automation, Automate 2025 will attract over 850 automation manufacturers and providers worldwide. Exhibitors and visitors will gather at Huntington Place in Detroit, Mich., to showcase their innovations. The event also serves as the North American edition of the International Symposium on Robotics, sponsored by the International Federation of Robotics. Visit *automateshow.com*.

National Association of Manufacturers and Its Divisions Announce Personnel Changes

T. O'Neal

The Manufacturing Leadership Council (MLC), the digital transformation division of the National Association of Manufacturers (NAM), elected Tim O'Neal and Bryan Van Itallie to its board of governors. O'Neal is Dow Global's operations director for operational excellence and leveraged services. Van Itallie is president of Michigan-based PIC Trailers, where he oversees all aspects of PIC's semi-truck trailer business and has led the development of a new metrics-driven vision, mission, core values, and strategic plan for the company. In addition, NAM added Kelly Schindler to its board of directors. Schindler, national managing principal of manufacturing at the licensed certified public accounting firm Grant Thornton Advisors LLC and audit partner at Grant Thornton LLP, joins the board to bolster NAM's leadership in policy advocacy, legal action, workforce solutions, and operational excellence. Lastly, the Manufacturing Institute, NAM's workforce development and education affiliate, selected Susan Elkington as chair of the Women MAKE Awards initiative. Elkington is senior vice president of electric vehicle supply for Toyota Motor North America. She will guide the Women MAKE Awards program in its mission to celebrate and elevate women shaping the future of manufacturing. She is a previous Women MAKE Awards Honoree.

B. Van Itallie

K. Schindler

S. Elkington

TRUMPF Appoints Vice President of Technical Services

TRUMPF Inc., a provider of manufacturing solutions in machine tools and laser technology, has named Heidi-Melanie Maier as vice president of technical services. She will be responsible for governing the technical service, spare parts, and training groups for North American customers. Maier has worked at the company for over 24 years and has been national service director since 2021. She also held the positions of director of sales and marketing for TruServices and Smart Services at TRUMPF's North American headquarters, Farmington, Conn. Previously, she served in various leadership roles in communications at TRUMPF Group headquarters in Germany.

H. M. Maier

Oak Ridge National Laboratory Researchers Receive Elmer L. Hann Award

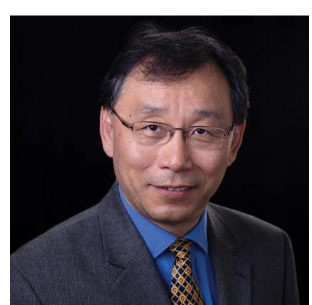

Z. Feng

J. Chen

Zhili Feng, a distinguished R&D staff member, and Jian Chen, a senior R&D staff member, of the Materials Science and Technology Division at the Department of Energy's Oak Ridge National Laboratory received the Elmer L. Hann Award at the Society of Naval Architects and Marine Engineers (SNAME) Convention, Oct. 15, in Norfolk, Va. The award is presented to authors of the best paper on ship production delivered at a SNAME event. Feng and Chen presented "Develop a Fast Analysis Solver for Welding Sequence Optimization" at the SNAME Maritime Convention in San Diego, Calif., in September 2023. The paper by Feng, Chen, and researchers from Ingalls Shipbuilding describes the scientists' creation of a user-friendly software tool that can quickly analyze and determine the best order for performing welds on ship structures. The tool is designed to reduce distortion caused by welding, improve the accuracy of ship parts, and decrease the need for corrective work after welding.

Roth Retires from the U.S. Navy

W. Roth

Captain William Roth retired from the U.S. Navy after over 30 years, including six on active duty and more than 24 in the U.S. Navy Reserve. Roth served as a nuclear propulsion officer on aircraft carriers while on active duty. As an engineering duty officer in the reserves, he supported maintenance and new construction for Naval Sea Systems Command at all four Navy shipyards and several Supervisor of Shipbuilding commands. He was awarded the Legion of Merit following his retirement ceremony. He was Proctor & Gamble's corporate welding and materials engineer for over 20 years and formed Welding Engineering Consultants, West Chester, Ohio, in 2018; he is president of the company. Roth is an AWS Life Member, a Certified Welding Inspector (CWI), an instructor for AWS CWI classes, a contributor to the *Welding Journal*, a member and past chair of the AWS D18 Committee on Welding in Sanitary Applications, a past member of the AWS Technical Activities Committee, a past chapter and volume chair of the *Welding Handbook*, and a member of the D10C Subcommittee on Welding Practices and Procedures for Austenitic Steels.

Bridge Fabrication Expert Picked for 2025 T. R. Higgins Lectureship Award

R. Medlock

The American Institute of Steel Construction honored Ronnie Medlock of High Steel Structures LLC, Lancaster, Pa., with the 2025 T. R. Higgins Lectureship Award for his contributions to the Federal Highway Administration's Bridge Welding Reference Manual. The award recognizes an outstanding lecturer and author whose technical paper or papers published during the eligibility period are an outstanding contribution to the engineering literature on fabricated structural steel. Medlock is vice president of technical services at High Steel Structures, where he is responsible for quality control and fabrication and inspection technology advancements. He played a crucial role in developing the Texas Steel Quality Council (an interdisciplinary group that became the model collaborative innovation) and what is now the AASHTO/NSBA Steel Bridge Collaboration.

Inductotherm Group Names Coleaders

M. Nallen

S. Prabhu

Inductotherm Group, Rancocas, N.J., a global provider of thermal processing technologies, announced Mick Nallen and Satyen Prabhu as the company's new coleaders. Nallen, a veteran of the industry with 32 years at the company, has a track record of driving operational excellence and strategic growth in North America and the Asia Pacific region. Prabhu, an industry veteran with 37 years at the company, brings vast experience in fostering the exchange of best practices and induction technologies across Inductotherm Group's companies.

Solar Atmospheres Chooses Quality Manager of New Facility

C. Caldwell

Solar Atmospheres of Michigan, a provider of vacuum treating and brazing services, named Charles "Charlie" Caldwell quality manager of its new facility in Chesterfield, Mich. Caldwell has over ten years of experience in the commercial heat treating industry, including in quality control, regulatory compliance, and operations. He has managed all aspects of pyrometry processes and has been instrumental in developing procedures to ensure compliance with industry-critical standards.

ANCA Honors Female Machinist of the Year

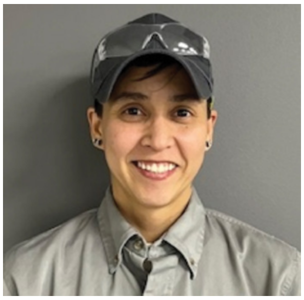

S. Chrystal

ANCA, a global manufacturer of grinding machines, awarded the 2024 Female Machinist of the Year to Stephanie Chrystal. A grinding specialist at Sandvik Coromant's solid round tools production unit, Westminster, S.C., Chrystal was recognized for her problem-solving skills, leadership in expanding and training her team, and ability to deliver results under pressure. She has played a pivotal role in introducing solid round tools at Sandvik Coromant and has been instrumental in building and training a skilled workforce.

Pemamek Installs Sales Director for the Czech Republic and Slovakia

M. Trávníček

Pemamek Ltd., a provider of welding and production automation solutions headquartered in Finland, appointed Miroslav Trávníček as sales director for the Czech Republic and Slovakia. The appointment comes in response to the growing demand for advanced automation solutions in the region. Trávníček has over 16 years of experience in technical sales in welding automation. In his new role, he will be responsible for sales operations, key partnerships, and addressing evolving customer needs in both countries. WJ

GRADUATE RESEARCH FELLOWSHIPS

To: Professors Engaged in Joining Research
Subject: Request for Proposals for 2025-26 AWS Fellowships

The American Welding Society (AWS) Foundation seeks to foster university research in joining and to recognize outstanding faculty and student talent. We are again requesting your proposals for consideration by the AWS Foundation.

The Research Fellowships are $35,000 per year. $17,500 installments are paid following the submission of progress statements on November 1 and March 1. Proposals may be funded for a period of up to three years, however, renewal applications must be submitted for the second and third years. Renewal by AWS will be contingent on demonstration of reasonable progress in the research or in graduate studies.

Proposals must be received by **April 15, 2025**. New Fellowships will be announced in May 2025. The AWS Foundation reserves the right not to make awards if the Committee does not find any satisfactory candidates.

The AWS Fellowship is awarded to the student for graduate research toward a Masters or Ph.D. Degree under a sponsoring professor at a North American University. The qualifications of the Graduate Student are key elements to be considered in the award. The academic credentials, plans, and research history (if any) of the student should be provided in the application package. **The student must prepare the proposal for the AWS Fellowship**. However, the proposal must be developed under the guidance of a professor and accompanied by letters of recommendation from the sponsoring professor and others acquainted with the student's technical capabilities. Should the student selected by AWS be unable to accept the Fellowship or continue with the research at any time during the period of the award, the award will be forfeited, and no further funding will be provided by the AWS Foundation. The bulk of funding should be for student support.

RESEARCH TOPICS
Topics for the AWS Fellowship may span the full range of the joining industry. Proposals for both applied and fundamental research topics are welcome.

DETAILS

The technical portion of the proposal package should include:

1. Executive Summary
2. Annualized Breakdown of Funding Required and Purpose of Funds (Student Salary, Tuition, etc.)
3. Matching Funding or Other Support for Intended Research
4. Duration of Project
5. Statement of Problem and Objectives
6. Current Status of Relevant Research
7. Technical Plan of Action
8. Qualifications of the Student Researcher and Professor
9. Pertinent Literature References and Related Publications
10. Special Equipment Required and Availability
11. Statement of Critical Issues Which Will Influence Success or Failure of Research

The technical portion of the proposal should not exceed 15 typewritten pages. The title page, which may include the executive summary, is not included in the page count limit. The maximum file size for the technical portion is 2 megabytes. Proposals that exceed either the page limit or file size limit will be considered non-conforming and will not be evaluated.

In addition, the proposal must include:

1. Student's Academic History, Resume and Transcript (Both undergraduate and graduate)
2. Recommendation(s) Indicating Qualifications for Research must include one or more letters of recommendation from the sponsoring professor or others acquainted with the student's technical capabilities. A maximum of three support letters may be submitted.
3. Brief Section or Commentary on Importance of Research to the Welding Community and to AWS, Including Technical Merit, National Need, Long Term Benefits, etc.
4. Statement Regarding Probability of Success

Proposal should be typed in a minimum of 12-point font in Times, Times New Roman, or equivalent. Proposals received after the deadline will not be evaluated. Proposals should be sent electronically by **April 15, 2025** to John Douglass, Associate Director, AWS Foundation at jdouglass@aws.org.

AWARD REQUIREMENTS
Recipients will be expected to submit at least one manuscript for publication in the *Welding Journal* Research Supplement and to present in the Professional Program at a future FABTECH Conference event during the time you are funded under this fellowship (up to three years). The manuscript will be reviewed just like all other submissions, and no special treatment will be given during review resulting from the AWS Graduate Fellowship status.

ACCEPTING PROPOSALS NOW! Submission Deadline **April 15, 2025**.

Stay Connected

aws.org


MPD
MARKING PEN DEPOT
The World's Biggest Selection of Markers
The world's largest selection of Markal markers & more for the welding industry
FREE SHIPPING OVER $50
FREE samples available!
PAINT-RITER
PAINT-RITER+ CERTIFIED
PAINTSTIK
Millions of Markers!
ORDER NOW: 888.906.9370
WWW.MARKINGPENDEPOT.COM


ORDER ONLINE
SUPER MET-AL
Draw Fine Lines On Any Fabrication
MARK ON ALL SURFACES
METAL
STONE
GLASS
WOOD
& MORE!
Use For Every Kind Of Fabrication
METAL TIP
SCAN ME!
TO CLAIM YOUR FREE SAMPLE
SKM
www.skmproducts.com
OR CALL 1-800-851-8464

Sponsored by the
American Welding Society

WELDING JOURNAL RESEARCH SUPPLEMENT

VISIT *WJRESEARCH.ORG*

TO VIEW AND DOWNLOAD MORE THAN 2200 WELDING RESEARCH PAPERS FROM 1970 UNTIL TODAY

- Read current peer-reviewed reports of research on welding procedures, metallurgy, equipment, processes, testing, and quality control by the world's foremost scientists, engineers, scholars, and industry professionals.
- Published online continuously at ***wjresearch.org***.

SUBMIT RESEARCH PAPERS

Please submit research papers through **Editorial Manager** (*www.editorialmanager.com/wj*), where you will find more information on submission guidelines and author responsibilities. The *Welding Journal* Impact Factor (JIF) for 2023 is 2.2. Email *wjrs@aws.org* if you have any questions.

Strain-Based Heating of Polymers under Ultrasonic Excitation

An investigation of the physical properties that affect viscoelastic heating of polymers under ultrasonic vibration

BY M. MARCUS AND E. SANCAKTAR

Abstract

Ultrasonic welding is the most common type of polymer joining used in industry today. It is critical that the energy transfer and heating mechanisms be well understood to enable the use of this process for more challenging applications. This work seeks to provide new tools to predict the heating rate in a molded polymer part excited by ultrasonic energy. Current assumptions for the mechanics of energy transfer are explored, and new equations for attenuation and strain-based heating are proposed.

Keywords

- Ultrasonic Plastic Welding
- Ultrasonic Attenuation
- Ultrasonic Heat Generation

Introduction

Ultrasonic heating of a polymer relates to the out-of-phase relationship of the stress and strain waves in the material, an effect of viscoelasticity. The losses generated by this out-of-phase behavior cause heating, and the loss magnitude depends on the material's ultrasonic frequency, amplitude, and loss modulus. These losses also lead to attenuation, a reduction in amplitude, so that the amplitude of vibration at the joint is less than that at the surface where the ultrasonic wave is initially applied to the part (Ref. 1).

The main components of an ultrasonic welding system are shown in Fig. 1. The ultrasonic vibrations that initiate heating are applied via an ultrasonic stack. This stack consists of three components: a transducer (a converter), a booster, and a horn (a sonotrode). The transducer converts a high-frequency electrical signal from a generator into mechanical motion via piezo-electric ceramics that expand and contract in response to electrical impulses. The booster is used to either increase or decrease the amplitude of the vibrations depending on its mass ratio. The horn is configured to apply vibrations to the top surface of the plastic part over the joint (Ref. 2).

The ultrasonic stack is used to compress two polymer components placed in physical contact such that the ultrasonic vibrations are traveling perpendicular to the faying surface. The generated polymer melt is pushed away from the joint as force is applied. This step exposes a new solid-to-solid contact surface to generate more heating from vibrations. This cyclical process continues until the weld feature completely melts (Ref. 2).

The amplitude at the sonotrode face can be calculated based on the amplitude of the transducer, a value typically provided by the equipment supplier, and the expected gain of the booster and sonotrode based on their geometry. Gain is simply the ratio of the mass of the ultrasonic tool, such as the booster or sonotrode, before the nodal point versus after. As the wave passes through the component, the magnitude of the lengthwise deformation can be increased by reducing the mass present on the part's second quarter wavelength.

Because the ultrasonic sonotrode has the same density throughout, the gain can be calculated as the ratio of the cross-sectional area where the ultrasonic wave enters the sonotrode to the cross-sectional area where the ultrasonic wave exits the sonotrode. Figure 2 shows how this can be calculated using the example of an ultrasonic sonotrode with a rectangular front and a cylindrical back. The 0.8 factor is an estimated adjustment to account for the transition radius between the front and back of the sonotrode.

Experimentally, this calculated amplitude can be confirmed via optical or mechanical measurements. A mechanical approach is shown in Fig. 3. A standard displacement gauge can be placed in contact with the bottom surface of the sonotrode and zeroed. At this point, the ultrasonics can be activated using the "test" function of the ultrasonic generator. The response rate of the gauge is not fast enough to follow the motion of the ultrasonic sonotrode face, so a maximum value is displayed at

https://doi.org/10.29391/2025.104.001

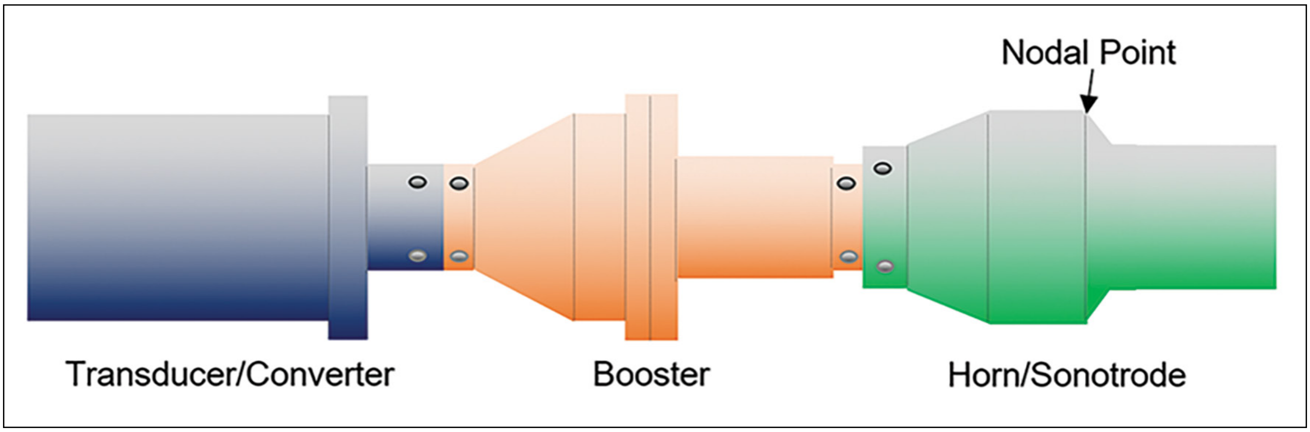

Fig. 1 — Ultrasonic stack diagram.

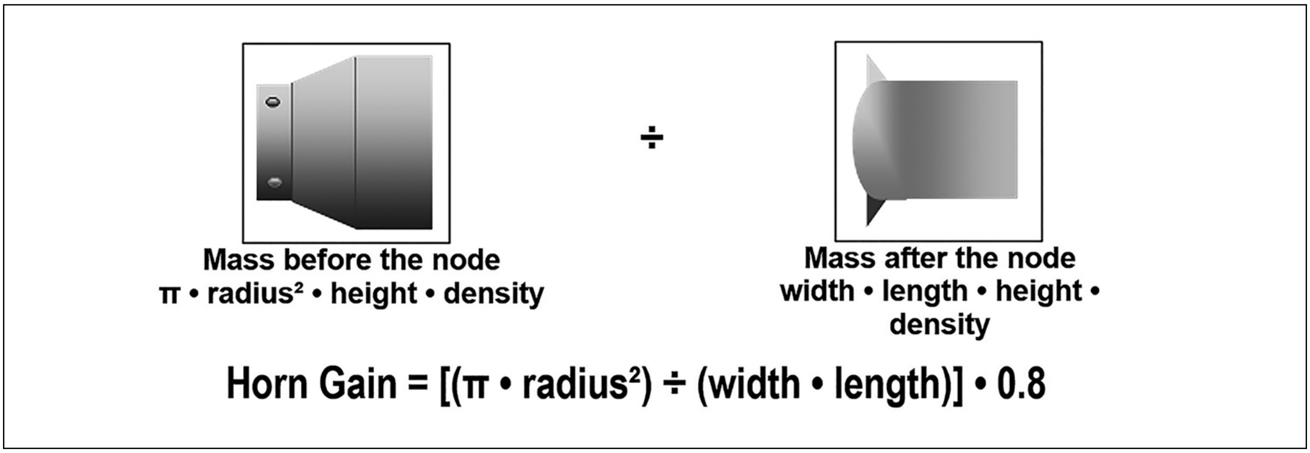

Fig. 2 — Method to calculate the gain of an ultrasonic component.

the maximum expansion of the sonotrode, which is equivalent to the 0-peak amplitude at the sonotrode face.

While the amplitude of vibration at the face of the ultrasonic sonotrode can be easily calculated and measured as described, it is more challenging to find the amplitude of the ultrasonic vibration at the weld joint interface.

If one assumes a simple bar or rod model, the ultrasonic wave transfers linearly through the polymer. The amplitude at the joint will then be affected by two phenomena: the wave's phase at the joint location and attenuation.

The wave phase at the joint location will depend on the velocity of the ultrasonic wave in the polymer and the distance from the sonotrode contact surface to the joint. The vibration wave will have a maximum amplitude at the sonotrode contact surface.

The amplitude of vibration at the weld joint has typically been used as the instantaneous deformation in the polymer to calculate heat generation. However, this approach neglects the effects of the part geometry and the force applied to the heating rate. In this work, the key components of ultrasonic heating are vibration amplitude, the mechanism of ultrasonic heating, and how strain is determined. Each of these is independently discussed, including the derivation of a simplified equation to predict the amplitude at the weld joint accounting for attenuation and phase shift. The strain heating mechanism for plastic welding is also evaluated and a new approach for estimating strain is proposed.

Background and Theory

Vibration Amplitude within Polymer

Attenuation is the loss of amplitude of the ultrasonic wave as it travels through a polymer due to the imperfect transfer of the vibrations through a viscoelastic material. While elastic materials (i.e., metals) are generally assumed to provide near perfect transfer of vibrations, the viscous portion of plastics does not transfer vibrations. The viscous portion of the polymer absorbs kinetic energy (resulting in heating), while the elastic portion transfers it, leading to an overall loss of peak amplitude (Ref. 3).

This viscoelastic response of polymers to mechanical deformation can be visualized as a spring and dashpot system. The most common models of this type are the Maxwell and Kelvin-Voight models. The idea is that polymers have both an elastic response, represented by a spring, and a viscous response, represented by a dashpot. Imagine pulling on the

Fig. 3 — Method for measuring amplitude at the ultrasonic sonotrode face using a displacement gauge.

end of the system depicted in Fig. 4; at high rates, the spring will present less resistance to movement than the dashpot. Similarly, some mechanical energy is transferred quickly and efficiently in plastics, but some is not (Refs. 4, 5). It is this resistance to transfer that causes a loss in ultrasonic amplitude at the weld joint due to attenuation — and it is also this loss that causes vibrations in polymers to generate heating.

Several methods of estimating the loss in amplitude as the wave travels through a polymer have been proposed. Sancaktar describes a method to determine the nodal point in the polymer or the points at which there is zero or maximum vibration (Ref. 6). This method is based on the description of ultrasonic waves as plane waves from the basic theory of elasticity. If a part has a simple geometry, the node points of the wave in the polymer can be predicted with the following equation:

$$L = \frac{V_L}{f} = \frac{1}{f}\left[\frac{E}{\rho}\frac{(1-v)}{(1+v)(1-2v)}\right]^{1/2} \quad (1)$$

where L is wavelength, V_L is the velocity of the wave propagation, f is frequency, E is Young's modulus, ρ is density, and v is Poisson's ratio.

If the distance from the sonotrode contact surface to the joint is L/2 (half wavelength), then very little or no amplitude will be available, resulting in a weak or no weld. If the part has a complex geometry, computer modeling is more efficient in determining the location of nodal points.

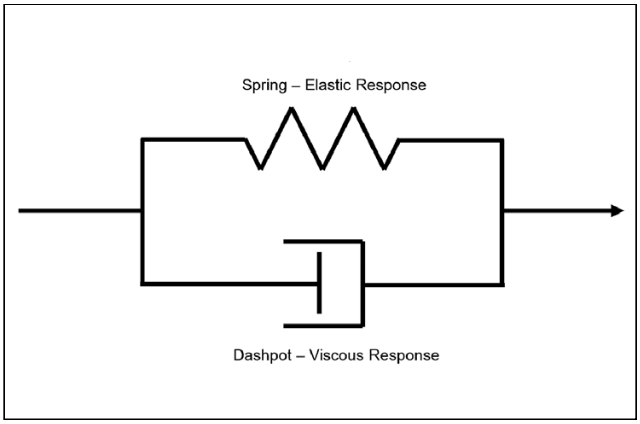

Fig. 4 — Kelvin-Voight model of viscoelastic response.

While this approach is very helpful to find the wavelength of the ultrasonic vibrations in a polymer, it cannot be used to find amplitude at a specific distance. Additionally, it only accounts for the phase of the wave and does not account for attenuation. However, it is useful during designing to determine optimum distances from the sonotrode contact surface to the weld joint or distances to be avoided.

Suresh et al. proposed that the attenuation of the ultrasonic wave in polymers, represented as a logarithmic decrease, can be applied to ultrasonic welding (Ref. 7). This model was originally proposed for use in ultrasonic nondestructive testing of plastics to model the response rate for low-power vibrations (Ref. 8). Following this method, the attenuation of the plastic material can be approximated by the equation:

$$2\alpha z = 20\log\frac{I_0}{I} \quad (2)$$

where α is the attenuation coefficient, z is the distance traveled by the wave, I_0 is the initial amplitude, and I is the final amplitude (Ref. 7).

For most weldable thermoplastics at 20 kHz and room temperature, the attenuation coefficient is generally in the range of ten to 100 (Ref. 8). The drawback to this method of modeling attenuation is that a specific coefficient must be measured for each material of interest.

An alternative method of calculating the attenuation of ultrasonic energy as the wave travels through a plastic part is proposed by Sancaktar, based closely on the Kelvin-Voight model of viscoelastic response (Ref. 6).

From this model, the following equation of transmissibility of the vibrations can be developed:

$$T_r = \frac{F_t}{F_0} = \frac{[E^2 + (\eta\omega_f)^2]^{1/2}}{[(E - m\omega_f^2)^2 + (\eta\omega_f)^2]^{1/2}} \quad (3)$$

where T_r is transmissibility, F_t is transmitted force, F_0 is exciting force, E is the elastic modulus, η is viscosity, ω_f is the forcing frequency, and m is the mass of the system (Ref. 6).

For a constant cross section, T_r is also equal to the ratio of the transmitted stress to the exciting stress. And, because Stress (σ) = Modulus (E) * Strain (ε), T_r is also equal to the ratio of transmitted strain (amplitude at the joint) to exciting strain (amplitude delivered by the ultrasonic sonotrode) within the same material.

This second method relieves the need to define an attenuation coefficient experimentally and relates to properties that can be easily measured.

Alternatively, Benatar and Cheng proposed and validated an approach to account for both phase shift and attenuation effects in a single equation based on the 1D-bar wave equation (Refs. 9, 10):

$$u(x,t) = u_0 e^{-\alpha x} e^{-i\omega\left(\frac{x}{v}-t\right)} \tag{4}$$

where u(x,t) is the amplitude of the wave as a function of time (s), t, and distance (mm), x, from the sonotrode contact surface; u_0 is the amplitude (mm) at x = 0 (at the sonotrode contact surface); ω is the frequency (cycles/s), and α is the unitless attenuation factor:

$$\alpha = \frac{\omega\sqrt{\rho}E^{IV}}{|E^*|} \tag{5}$$

and v is the phase velocity (1/s):

$$v = \frac{|E^*|}{\sqrt{\rho}E^{III}} \tag{6}$$

where ρ is the density, E* is the complex modulus, and E^{III} and E^{IV} are related to loss and storage modulus:

$$E^{III} - iE^{IV} = \sqrt{E' - iE''} \tag{7}$$

However, rearranging the presentation can simplify the equation as described below. The first step is to eliminate the imaginary component and to present a single equation in terms of commonly measured material properties. Note that the relationship of E^{III} and E^{IV} to the loss and storage moduli can also be expressed by the following two equations:

$$E^{III} = \sqrt{|E^*|}\cos\left(\frac{\delta}{2}\right) \tag{8}$$

$$E^{IV} = \sqrt{|E^*|}\sin\left(\frac{\delta}{2}\right) \tag{9}$$

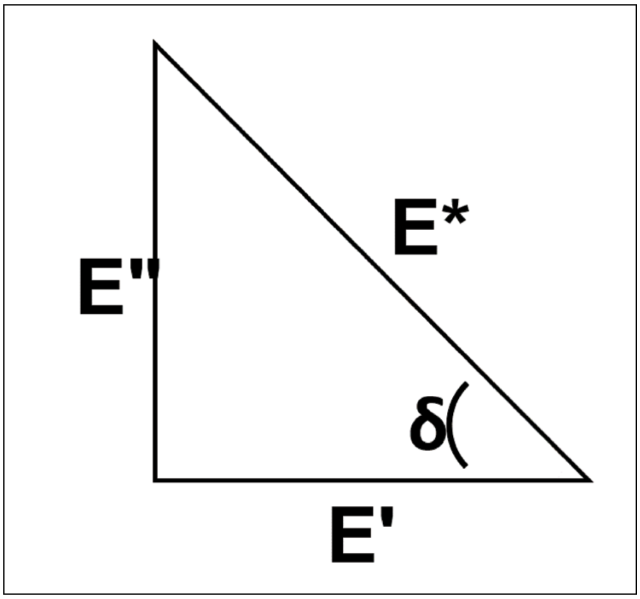

Fig. 5 — Geometric relationship between loss and storage: E" — the loss modulus; E' — the storage modulus; E — the complex modulus; δ — the loss factor.*

where δ is the damping factor (tanδ = E"/E'), and E* is the complex modulus:

$$|E^*| = \sqrt{E'^2 + E''^2} \tag{10}$$

A simplification of Equation 4 is proposed via the following process. To predict heat generation, only the maximum peak-to-peak amplitude is needed, so the equation can be isolated at a single point in time, when the ultrasonic wave is at the maximum amplitude, at t = 0. Therefore, Equation 4 can be simplified to the following:

$$u(x) = u_0 e^{-\alpha x} e^{-i\omega\left(\frac{x}{v}\right)} \tag{11}$$

By applying Euler's relation (Equation 12) to the phase shift portion of Equation 11, it can be further simplified as shown in Equations 13–14:

$$e^{ix} = cosx + isinx \tag{12}$$

$$e^{-i\omega\left(\frac{x}{v}\right)} = cos\left(\frac{-\omega}{v}x\right) + isin\left(\frac{-\omega}{v}x\right) \tag{13}$$

$$Real\left[cos\left(\frac{-\omega}{v}x\right) + isin\left(\frac{-\omega}{v}x\right)\right] = \cos\left(\frac{-\omega}{v}x\right) \tag{14}$$

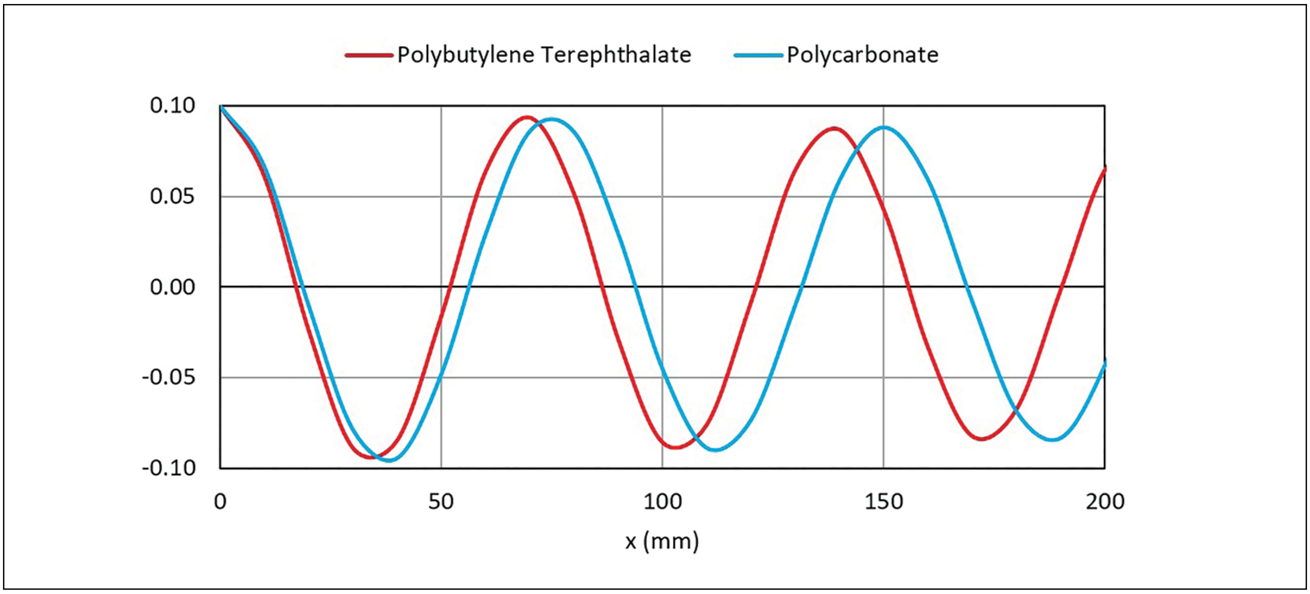

Fig. 6 — Peak-to-peak amplitude (mm) vs. distance from sonotrode contact surface, x (mm), for two polymers.

Thus, Equation 11 can be written as:

$$u(x) = u_0 e^{-\alpha x} \cos\left(\frac{-\omega}{\mathrm{v}} \mathrm{x}\right) \tag{15}$$

While this equation eliminates the imaginary component and allows for calculation of maximum amplitude vs. distances, instead of amplitude vs. time at each distance, it is also desired to eliminate the unwieldy E^{III} and E^{IV} material properties from the equation. These material properties are not well known or commonly used.

To begin the elimination process, the long form of the attenuation coefficient and the phase shift factor are applied to Equation 15:

$$u(x) = u_0 e^{-\frac{\omega\sqrt{\rho E^{IV}}}{|E^*|}x} \cos\left(\frac{-\omega}{\frac{|E^*|}{\sqrt{\rho E^{III}}}} \mathrm{x}\right) \tag{16}$$

Next, the long forms of the E^{III} and E^{IV} material properties are inserted into the equation:

$$u(x) = u_0 e^{-\frac{\omega\sqrt{\rho}\sqrt{|E^*|}\sin\left(\frac{\delta}{2}\right)}{|E^*|}x} \cos\left(\frac{-\omega}{\frac{|E^*|}{\sqrt{\rho}\sqrt{|E^*|}\cos\left(\frac{\delta}{2}\right)}} \mathrm{x}\right) \tag{17}$$

The complex modulus in the fractions can be simplified by manipulating the exponent by:

$$\frac{|E^*|}{\sqrt{|E^*|}} = \frac{|E^*|}{|E^*|^{0.5}} = |E^*|^{1-0.5} = |E^*|^{0.5} = \sqrt{|E^*|} \tag{18}$$

And the fraction in the cosine can be simplified so that Equation 17 becomes:

$$u(x) = u_0 e^{-\frac{\omega\sqrt{\rho}\sin\left(\frac{\delta}{2}\right)}{\sqrt{|E^*|}}x} \cos\left(\frac{-\omega\sqrt{\rho}\cos\left(\frac{\delta}{2}\right)}{\sqrt{|E^*|}} \mathrm{x}\right) \tag{19}$$

By changing the variable "u" to "A" to align with the variable definitions in this work and by assigning two new variables to the equation components to simplify writing it, Equation 19 can now be written as:

$$\mathrm{A(x)} = \mathrm{A_0} \cos(\mathrm{Dx} \cos\phi)\, e^{(\mathrm{Dx}\sin\phi)} \tag{20}$$

where A(x) is the function of maximum peak-to-peak amplitude as a function of distance into the material, A_0 is the peak-to-peak amplitude at the sonotrode contact surface, and ϕ is the unitless phase shift factor:

$$\phi = \frac{\delta}{2} = \frac{1}{2}\tan^{-1}\frac{E''}{E'} \tag{21}$$

and D is the damping coefficient:

$$D = \frac{-\omega\sqrt{\rho}}{\sqrt{|E^*|}} \tag{22}$$

A dimensional analysis of the damping coefficient, D, shows that this factor is also unitless:

$$D = \frac{\frac{1}{s} * \sqrt{\frac{g}{cm^3}}}{\sqrt{\frac{g}{s^2 * cm^3}}} \tag{23}$$

Thus, we have an equation for amplitude in terms of initial amplitude (amplitude at the sonotrode contact surface) multiplied by a ratio that varies with distance per the phase of the wave as well as per the loss in vibration energy due to viscous damping.

However, while Equation 20 eliminates the unwieldy E^{III} and E^{IV}, it is unclear how the damping and phase shift relate to the relevant material properties. Thus, further modification of the equation was pursued. First, consider the standard equation for wavelength:

$$\lambda = \frac{c}{f} \tag{24}$$

where c is the speed of sound in the medium and f is the frequency of the wave.

The speed of sound is given by the equation:

$$c = \sqrt{\frac{K}{\rho}} \tag{25}$$

where K is the material property relating to the sound propagation in the medium and ρ is the density.

In the case of ultrasonic wave propagation through a polymer, the relevant material property is the complex modulus. Referring to Equation 23, the damping coefficient, D, is a function of the wavelength and can be rewritten as:

$$D = \frac{-\omega\sqrt{\rho}}{\sqrt{|E^*|}} = \frac{-\omega}{c} = \frac{-1}{2\pi\lambda} \tag{26}$$

Next, consider cosΦ and sinΦ from Equation 20 and the definition of Φ from Equation 21. Figure 5 shows the geometry described by these geometric equations.

This illustrates the fundamental relationship described in Equations 27 and 28 below:

$$\tan\delta = \frac{E''}{E'} \tag{27}$$

$$|E^*| = \sqrt{E'^2 + E''^2} \tag{28}$$

Thus, sinΦ can be rewritten as:

$$\sin\phi = \sin\frac{\delta}{2} = \frac{1}{2}\frac{E''}{E^*} \tag{29}$$

And cosΦ is:

$$\cos\phi = \cos\frac{\delta}{2} = \frac{E'}{E^*} \tag{30}$$

Thus, the equation for amplitude as a function of distance becomes Equation 31:

$$A(x) = A_0 \cos\left(\frac{-2\pi x E'}{\lambda E^*}\right) e^{\frac{-\pi x E''}{\lambda E^*}} \tag{31}$$

This arrangement is preferred as each component is a commonly used and established parameter that does not require the definition of additional variables.

Further, when written in this format, the relationship between each component of the equation and its operator becomes clearer. The exponential decay of the ultrasonic wave amplitude is guided by the loss modulus of the material and the wavelength, which is appropriate and reasonable. The cosine component establishes the phase of the wave as it passes through the material, and this phase shifts in relation to the storage modulus and wavelength.

Ideally, the loss modulus (E') and storage modulus (E") of the material would be measured at, or extrapolated for, the frequency of vibration being used in the ultrasonic welding process. When using values that have been established previously for two polymers (Ref. 11), the graph shown in Fig. 6 can be produced.

Equation 31 can be simplified even further as the factor of E'/E* in the cosine function is nearly one for most polymer welding applications. Therefore, it can be eliminated, resulting in Equation 32:

$$A(x) = A_0 \cos\left(\frac{-2\pi x}{\lambda}\right) e^{\frac{-\pi x E''}{\lambda E^*}} \tag{32}$$

where A(x) is the function of maximum peak-to-peak amplitude as a function of distance into the material, A_0 is the peak-to-peak amplitude at the sonotrode contact surface, λ is the wavelength in the polymer, E" is the loss modulus, and E* is the complex modulus.

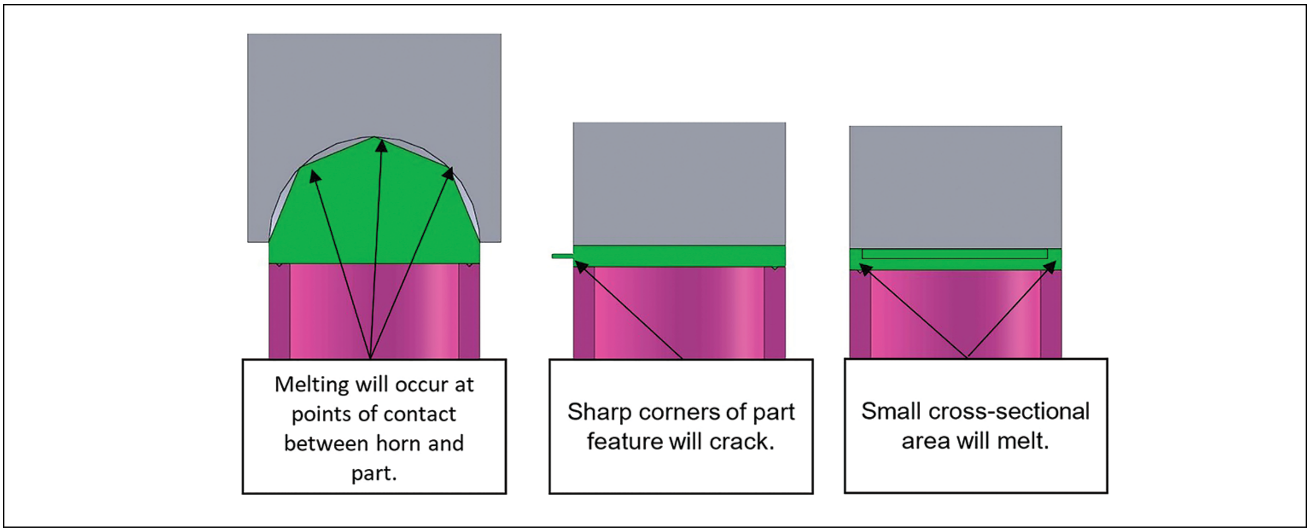

Fig. 7 — Diagram showing how the ultrasonic vibration affects areas outside the joint.

Heating Due to Ultrasonic Energy within Polymer

This amplitude calculation can be incorporated into the heat generation equation for ultrasonic welding. A derivation of this heating equation is described below for two reasons. First, to provide the first principles context for this paper, and second, to verify the units of the equation. With regard to the unit verification, this equation is often reported without the note that Q is the energy generated per volume, which is clarified here.

During the ultrasonic vibration of a polymer, the energy input into the joint of the plastic part is due to the mechanical deformations caused by the ultrasonic vibrations. To define this heating, we can start with the fundamental definition of work, W:

$$W = Fd \tag{33}$$

where F is the force applied, and d is the displacement over which the force is applied.

In ultrasonic welding, the force being applied is cyclical and is applied over very small deformations. Since the deformations are so small, we can assume linear viscoelastic properties govern the interaction. For the case of linear viscoelasticity, there is a direct relationship between stress and strain in the material when expressed in the Laplace Transform domain, i.e.,

$$\sigma(s) = E^*(s)\varepsilon(s) \tag{34}$$

where σ(s) is the stress, E*(s) is the modulus, and ε(s) is the strain expressed in Laplace Transform Domain.

The modulus, E*(s) of Equation 34, which describes how much of the vibrations are transferred, is called the complex modulus and is made up of a storage and a loss modulus. The storage modulus describes how much of the vibrational energy is transferred, and the loss modulus describes how much energy is dissipated as heat.

These moduli are typically measured using dynamic mechanical analysis. It is important to note that the storage and loss moduli are functions of both temperature and frequency of vibration. A constant modulus analytical approach simplifies modeling the heating behavior of polymers under ultrasonic vibration. The constant storage and loss moduli approach uses the moduli at room temperature and the driving frequency of the system. Previous research has shown this to be a valid approach (Refs. 11, 12).

It is, however, important to note that this approximation is being made, typically using material properties measured at lower frequencies via dynamic mechanical analysis (DMA) and extrapolated to higher frequencies through time temperature superposition (TTS). This approximation is known to be imperfect, but it has been the only available approach historically. However, recent research has suggested a much more accurate approach using custom high-frequency activation accompanied by simulation to extract the material properties based on observed effects (Ref. 13).

Now, from the definition of stress, we know that:

$$\sigma = F/a \tag{35}$$

where σ is the stress, F is the force being applied, and a is the area over which it acts.

From the definition of strain, it is known that:

$$\varepsilon = \frac{\delta x}{dx} \tag{36}$$

where ε is the strain, δx is the displacement, and dx is the reference length of the object being acted on. In our case,

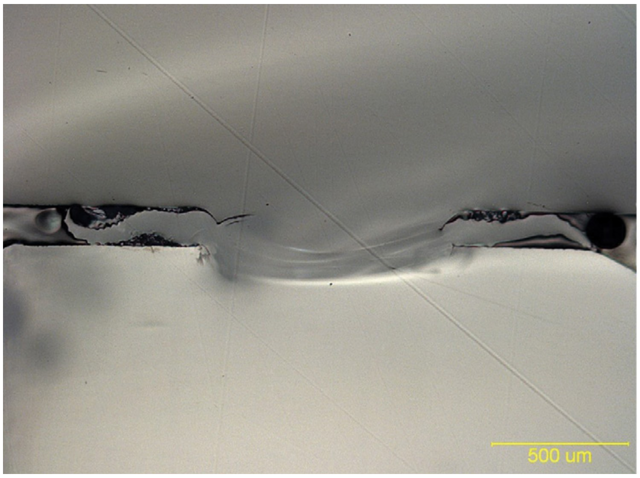

Fig. 8 — Cross section of weld joint with partially melted energy director.

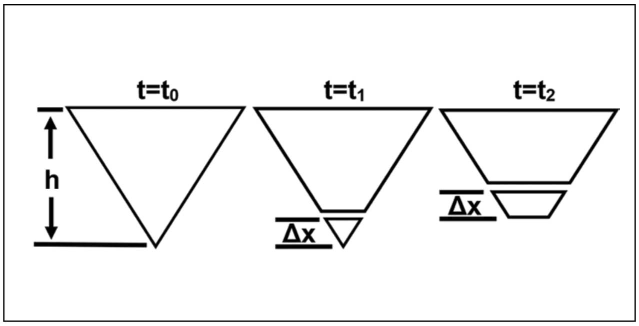

Fig. 9 — Diagram of how melt progresses over time in the energy director.

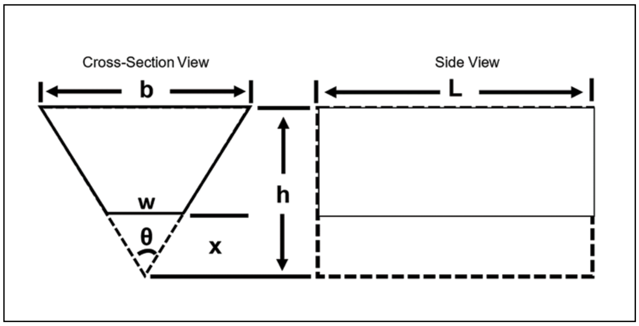

Fig. 10 — Diagram of energy director geometry after some melting has occurred.

we take the reference length as the energy director height on the plastic part.

Equations 34–36 can be combined:

$$W = \sigma a * \varepsilon dx \tag{37}$$

$$\frac{W}{adx} = \sigma * \varepsilon \tag{38}$$

where W is work, a is the area, dx is the instantaneous reference length, σ is the stress, and ε is the strain.

To find the work per volume per vibration cycle, the stress and strain are integrated over a single cycle, 0 to 2π/ω:

$$\frac{W}{V} = \int_0^{\frac{2\pi}{\omega}} \sigma \, d\varepsilon \, dt \tag{39}$$

During ultrasonic vibration, deformation is applied cyclically, which can be modeled as following a cosine wave:

$$\varepsilon(t) = \varepsilon_0 cos\omega t \tag{40}$$

where ε_0 is the 0-peak maximum amplitude at the beginning of the cycle.

Thus, the storage modulus, or transferred portion of the ultrasonic vibrations, can be assumed to follow this cosine. Conversely, the loss modulus, or out-of-phase portion of the ultrasonic vibrations, can be assumed to follow the sine:

$$E^* = E' cos\omega t - E'' sin\omega t \tag{41}$$

Physically, this means that at t = 0, the strain is equivalent to the maximum deformation induced by the ultrasonic vibration, ε_0. After this, the strain diminishes and grows with the vibration cycle.

Subsequently, the stress is given by:

$$\sigma = E^*\varepsilon = (E' cos\omega t - E'' sin\omega t)\varepsilon_0 \tag{42}$$

Physically, this means that at t = 0, the stress is equal to the storage modulus times the initial (maximum) strain, and thereafter, it varies according to the complex modulus.

Combining Equations 39 and 42, the equation becomes:

$$\frac{W}{V} = \int_0^{\frac{2\pi}{\omega}} [E' cos\omega t - E'' sin\omega t)\varepsilon_0][-\varepsilon_0 \omega sin\omega t] \, dt \tag{43}$$

Following the steps of integration, this equation simplifies to:

$$\frac{W}{V} = \pi E'' \varepsilon^2 \tag{44}$$

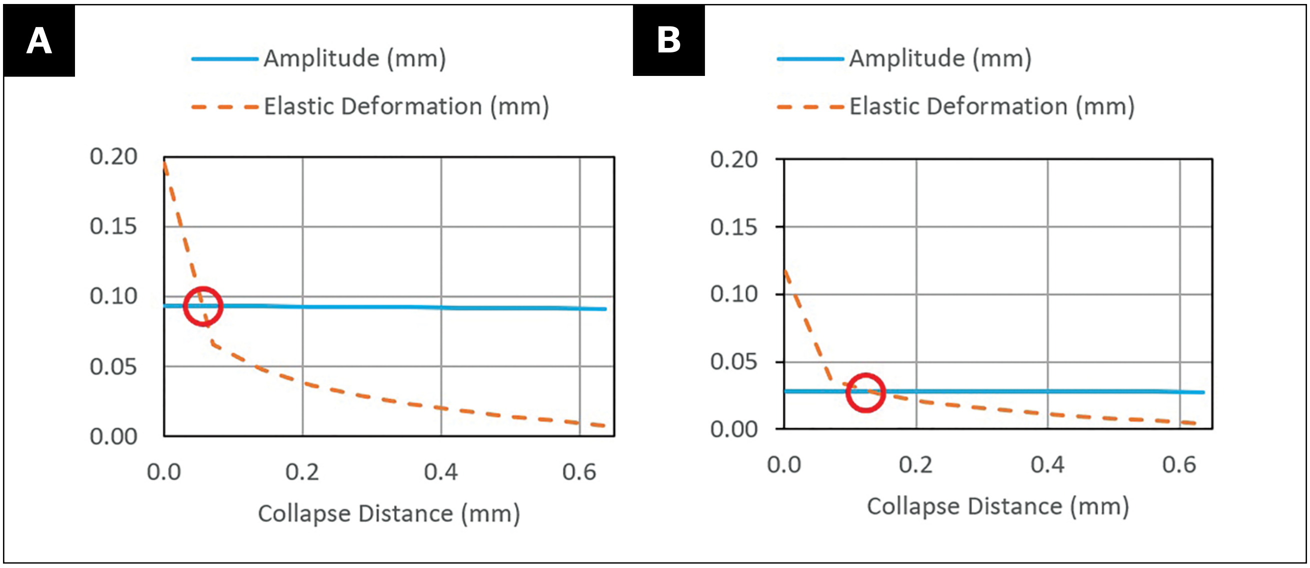

Fig. 11 — Amplitude and elastic deformation (mm) vs. collapse distance (mm) for a part with a 60-deg energy director: A — Polybutylene terephthalate (PBT), 0.1-mm amplitude input; B — polycarbonate (PC), 0.03-mm amplitude input.

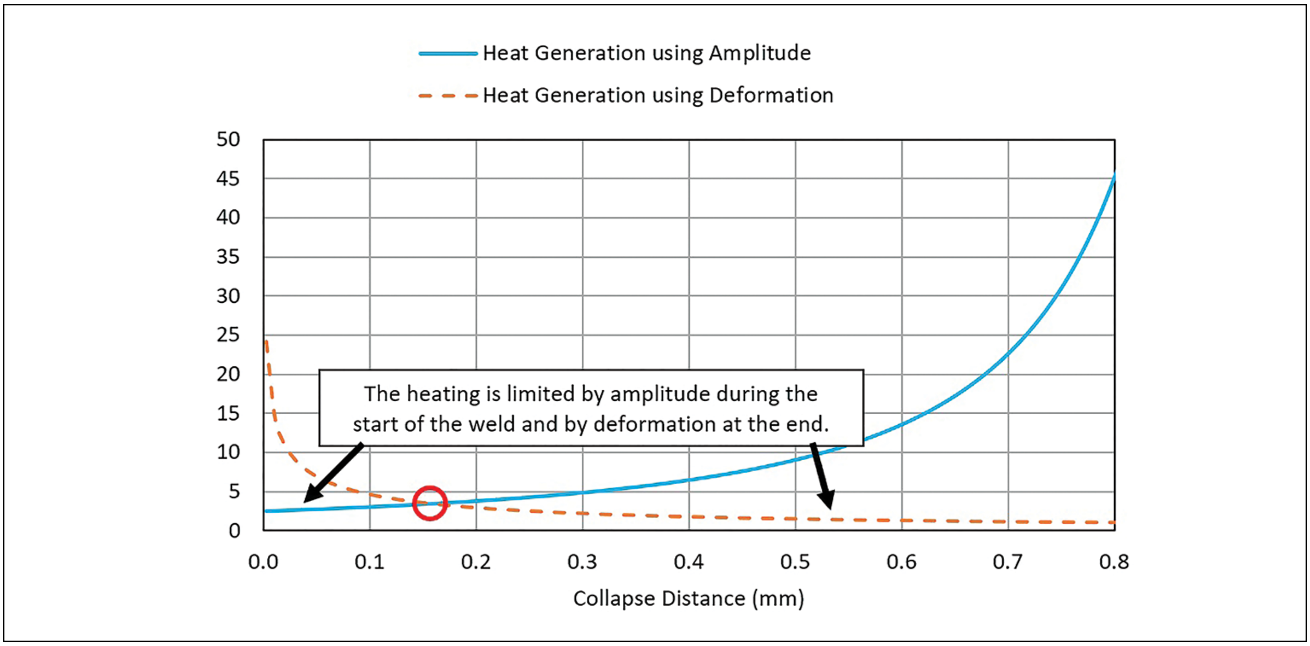

Fig. 12 — Internal heat generation rate (J/cm³/s) calculated using the amplitude at the joint vs. calculated using pressure-induced deformation as a function of collapse distance for a 1-mm-wide polycarbonate (PC) energy director.

This gives the work per volume per cycle. To find the average work, or average energy dissipation (Q) per volume into the plastic, the equation is multiplied by the period (ω/2π):

$$\frac{Q}{V} = \frac{1}{2}\omega E"\varepsilon^2 \tag{45}$$

where Q is the heat generation rate, V is the volume, ω is the frequency in radians, E" is the loss modulus, and ε is the strain.

A dimensional analysis of Equation 45 is given below, for reference:

$$\frac{Joules/sec}{cm^3} = \frac{1}{2}\left(\frac{1}{sec}\right)\left(\frac{Joules}{cm^3}\right)\left(\frac{cm}{cm}\right) \tag{45A}$$

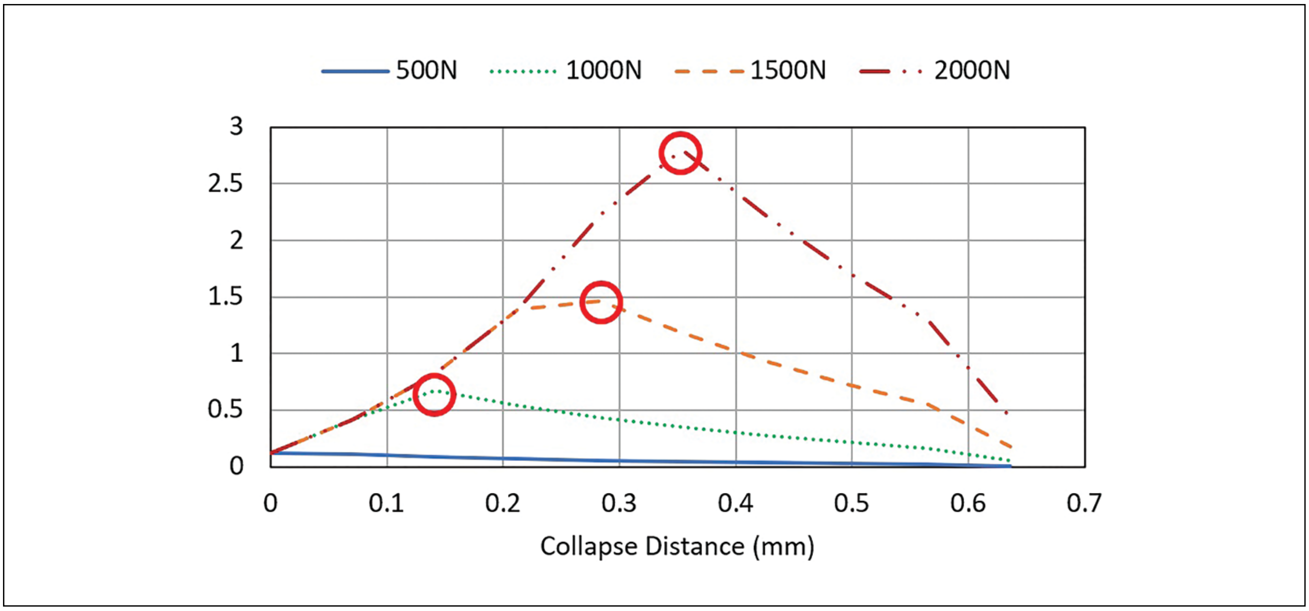

Fig. 13 — Heat generation rate (J/s) vs. collapse distance (mm) when elastic deformation limit is included for polycarbonate (PC) at various loads.

It is convenient to employ units of cm in this equation due to the small size of the volume being heated. Additionally, the loss modulus is typically found in terms of MPa, which is equivalent to J/cm^3.

Strain for the Heat Generation Equation

An engineering strain is typically used in the heat generation equation (Equation 45). This engineering strain is approximated as the amplitude produced at the joint divided by the energy director height. However, this approximation does not account for the effect of force and geometry on heat generation.

Experimentally, it has been shown that the energy director tip heats faster than nearby geometry. This is to be expected as the apex of the triangular energy director is subject to high-stress concentration when contacting the joint surface under force. Chuah et al. applied thermocouples to various points in a part and showed that the heating in the assembly is significantly concentrated at the energy director (Ref. 14).

However, using the energy director height as the reference length for the strain does not explain the heat generation when using no energy director. It is known that heating occurs throughout the part in contact with the ultrasonic sonotrode because heating of the entire part under ultrasonic activation is seen. For example, areas of a small cross section outside the joint can fracture, the sonotrode contact surface may melt, and sharp corners crack. In several cases of ultrasonic welding applications, it has been noted that if the sonotrode contact surface has a sufficiently small cross-sectional area, it will heat even before the energy director heats. Figure 7 shows examples of where undesired heating can occur during ultrasonic welding.

These observations suggest that the portion of the system that undergoes the most elastic deformation is the area of

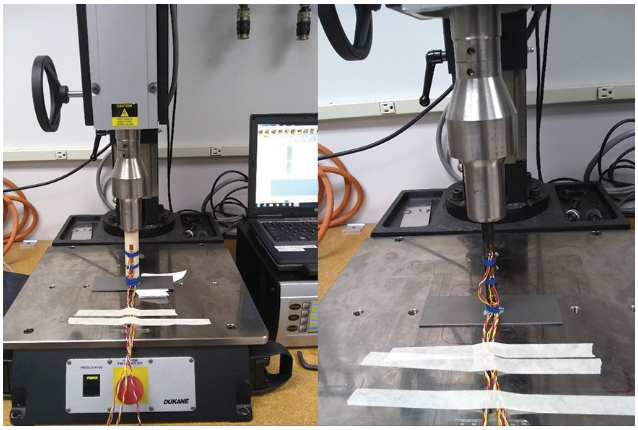

Fig. 14 — Experimental setup for strain measurement on acrylonitrile butadiene styrene (ABS) rods with a 2.54 cm diameter (left) and a 1.27 cm diameter (right).

greatest heat generation. Therefore, a new method of considering heat generation in the ultrasonic part is proposed. It uses the portion of the ultrasonically activated plastic part that undergoes large elastic deformation under the applied force.

Generally, it is assumed that the entire energy director heats simultaneously and melts uniformly. This approximation is useful to help predict weld time, where the heat generation rate can be considered an average if the full energy director is welded. The approximation, however, is not representative of reality. With any incomplete weld cross section, unmelted geometry is visible at the base of the energy director. This is a clear indication that melt starts at the triangular tip of the energy director and only moves into the base of the energy director as the melt is pushed out into the joint. Figure 8

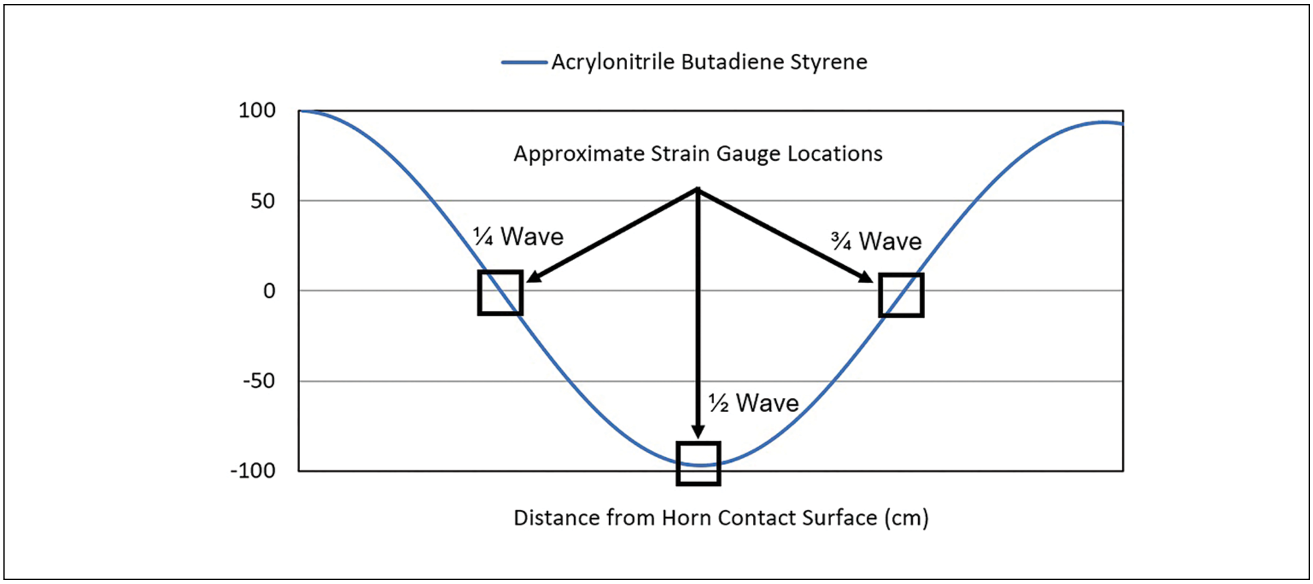

Fig. 15 — Placement of the strain gauges in relation to the expected percent of total amplitude of the ultrasonic wave at each location.

shows an example. Figure 9 shows how the energy director is expected to melt over time in discrete segments.

We note that the strain used in Equation 45 is not solely the amplitude over a function of energy director height. The maximum deformation can be approximated as the elastic deformation of the energy director, considering that any plastic deformation under the applied load will occur before ultrasonic energy is applied to the part.

This proposed approach to finding the deformation of the energy director under a static load begins with the stress-strain relationship:

$$\sigma = E\varepsilon \tag{46}$$

where σ is the stress, E is the modulus of elasticity, and ε is the strain:

$$\varepsilon = \frac{\delta x}{dx} \tag{47}$$

The stress is equal to the applied load (F) divided by the area (a), given by:

$$a = \frac{b}{h} xL \tag{48}$$

where b is the width of the energy director base, h is the height of the energy director, and L is the overall length of the energy director, as shown in Fig. 10.

Rearranging and integrating over the cross section:

$$\delta x = \frac{F}{E}\int_0^{x/h} \frac{1}{\frac{b}{h}xL} \tag{49}$$

which resolves to Equation 50:

$$\delta x = \frac{F}{E}\frac{h}{bL}\ln\left(\frac{x}{h}\right) \tag{50}$$

where F is the force applied, h is the energy director height, E is the elastic modulus, b is the energy director width, and L is the energy director length.

If we assume that insufficient force is applied to cause plastic deformation without ultrasonic vibration, then it makes sense that the actual effective amplitude is simply the elastic deformation of the energy director. However, the initial deformation of the energy director is limited by the amplitude of the ultrasonic wave at the joint.

Once the load is applied, the part has already experienced the deformation caused by the static load alone. Any further deformation is caused by the ultrasonic wave passing through the part. Therefore, while the sharp energy director geometry may allow significant elastic deformation, it cannot deform any more than the wave's amplitude at that location. This is especially important at the start of welding when the contact cross-sectional area of the energy director is still very small because the potential elastic deformation may be greater than the amplitude at that point.

Figure 11 compares the amplitude calculated using Equation 32 to find the amplitude at the weld joint vs. elastic deformation calculated per Equation 50 for two hypothetical scenarios. These are a 60-deg energy director on a (a) polybutylene terephthalate (PBT) part and (b) polycarbonate (PC) part. For this geometry and material, with an applied

Table 1 — Strain Gauge Specifications

Thermal Output Coefficients for 2024-T4 Aluminum at Gauge Factor of 2.00		Other
Order	Celsius	
0	−2.83E+1	Grid Resistance in Ohms: 120.0 +/− 0.3%
1	+2.56E+0	Gauge Factor at 24°C: 2.115 +/− 0.5%
2	−6.54E−2	Transverse Sensitivity: (+0.8 +/− 0.2)%
3	+3.56E−4	Temperature Compensation of Gauge Factor (%/100°C): (+1.3 +/− 0.2)
4	−3.85E−7	

Table 2 — Test Conditions

Rod Diameter (cm)	Force (N)	Ultrasonic Amplitude (microns)	Strain Gauge Locations Where Data Was Recorded
2.54	2224	0	¼, ½, ¾
		16	
		39	
	890	0	¼, ½
		16	
1.27	2224	0	¼, ½, ¾
		16	
		39	

load of 250 N assumed, the elastic deformation starts limiting the effective amplitude after about 10%-20% of the energy director is melted. This is at the crossover point where the amplitude at the joint and the deformation are equivalent, which is circled in Fig. 11.

When the deformation is used in the heat generation equation, the expected relationship of decreasing heat generation as the energy director collapses is predicted due to the increasing cross section of the energy director and reduction in the stress concentration on it. Conversely, when the traditional amplitude is used to calculate the strain in the heat generation equation, the predicted heating increases as the energy director collapses.

Figure 12 compares the two heat generation approaches (Equations 32 and 50 input into Equation 45) for PC. In this case, a 60-deg energy director on a PC part with an applied amplitude at the sonotrode face of 0.03 mm and a constant load of 250 N are assumed.

The smaller potential strain at each point in the weld process limits heat generation in the part. At the beginning of the weld, the amplitude is much less than the potential pressure-induced deformation. Thus, the heating is limited by the amplitude of the ultrasonic wave early in the weld cycle. As the energy director collapses, the joint's surface area increases, reducing the pressure-induced deformation to less than the amplitude of the ultrasonic wave. Thus, the heating is limited by the pressure-induced strain later in the weld cycle. The shift occurs at the cross-over point, as circled on Figs. 11 and 12.

When the strain is based on the applied weld pressure and joint geometry rather than amplitude, the rate of internal heat generation tapers down to zero as the energy director collapses fully. This is expected if the joint outside the energy director is large enough to have minimal elastic deformation under the applied load. However, it has been demonstrated experimentally that increasing amplitude does increase heating. This suggests that it may be appropriate to consider initial

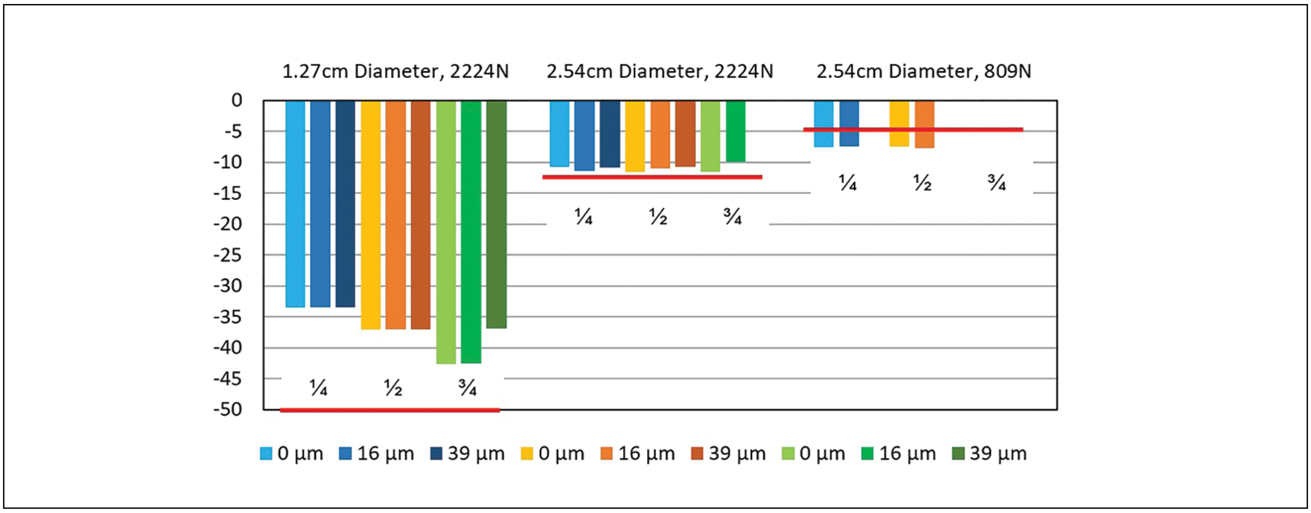

Fig. 16 — Measured displacement at three locations (¼, ½, ¾ wavelengths) using three amplitudes (0, 16, 39 µm) compared to the calculated elastic deformation (red lines).

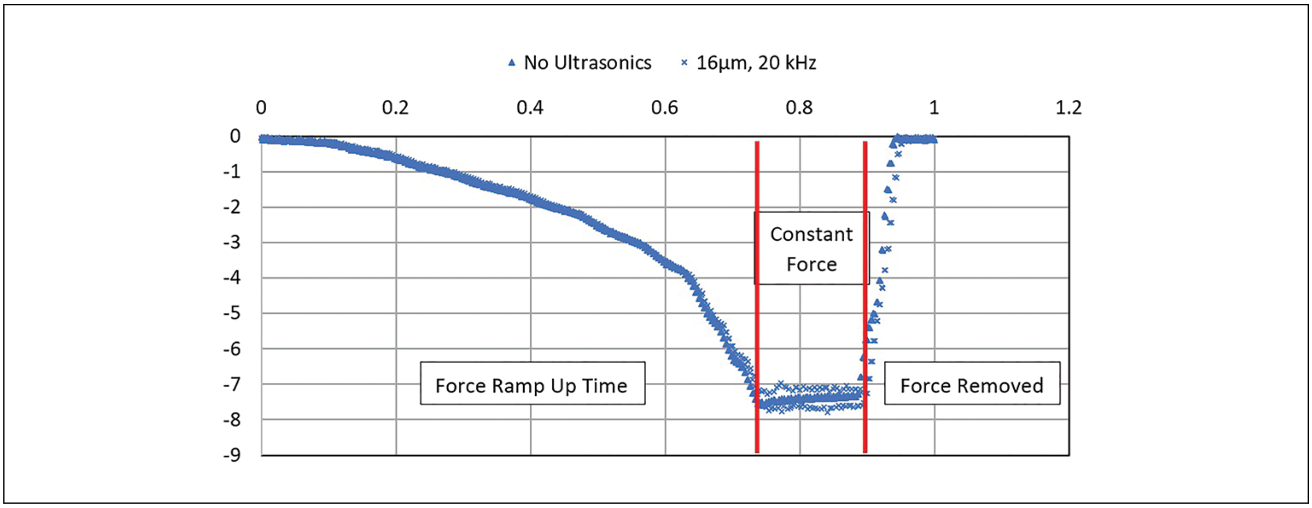

Fig. 17 — Displacement (µm) vs. time (s) for 2.54-cm-diameter rod at 890 N in the ¼ wave location.

heating to be controlled by the amplitude and later heating to be controlled by pressure-induced deformation. Due to the necessity of heating material from room temperature, initiating melt requires much greater energy input than maintaining melting since nearby material is already heated due to thermal conduction. This would explain the significant difference in weld time when amplitude is adjusted.

By accounting for the reduction in heating that occurs when elastic deformation is reduced, the noted effects of increased pressure and reduced contact area (by using an energy director at the joint instead of a flat contact surface) can be incorporated into the model. Figure 13 shows how pressure affects heating when accounting for elastic deformation. In this figure, the heating is calculated by limiting the achievable deformation at the joint to what is mechanically possible once this deformation is smaller than the amplitude of the ultrasonic wave at the joint. This crossover point is circled on Fig. 13 for each load.

The graph in Fig. 13 clearly shows that the initial heat generation increases monotonically at every force level but then drops off as the pressure-induced deformation starts limiting the effective strain at the energy director. The induced deformation is greater than the amplitude at higher pressure, even as the contact area widens as the energy director collapses. For this reason, the amplitude is less than the potential deformation for a longer period, and thus, the amplitude at the joint limits the effective strain at the energy director for more of the collapse distance. Because the pressure-induced deformation is greater at higher applied loads, the total energy input is greater when pressure is increased.

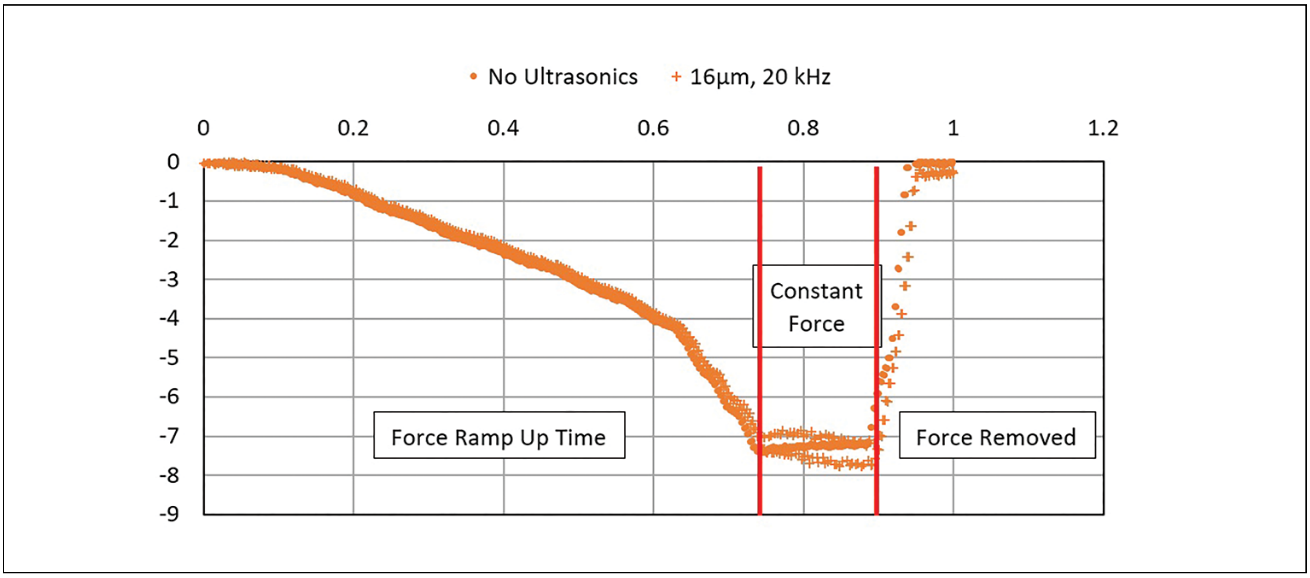

Fig. 18 — Displacement (µm) vs. time (s) for 2.54-cm-diameter rod at 890 N in the ½ wave location.

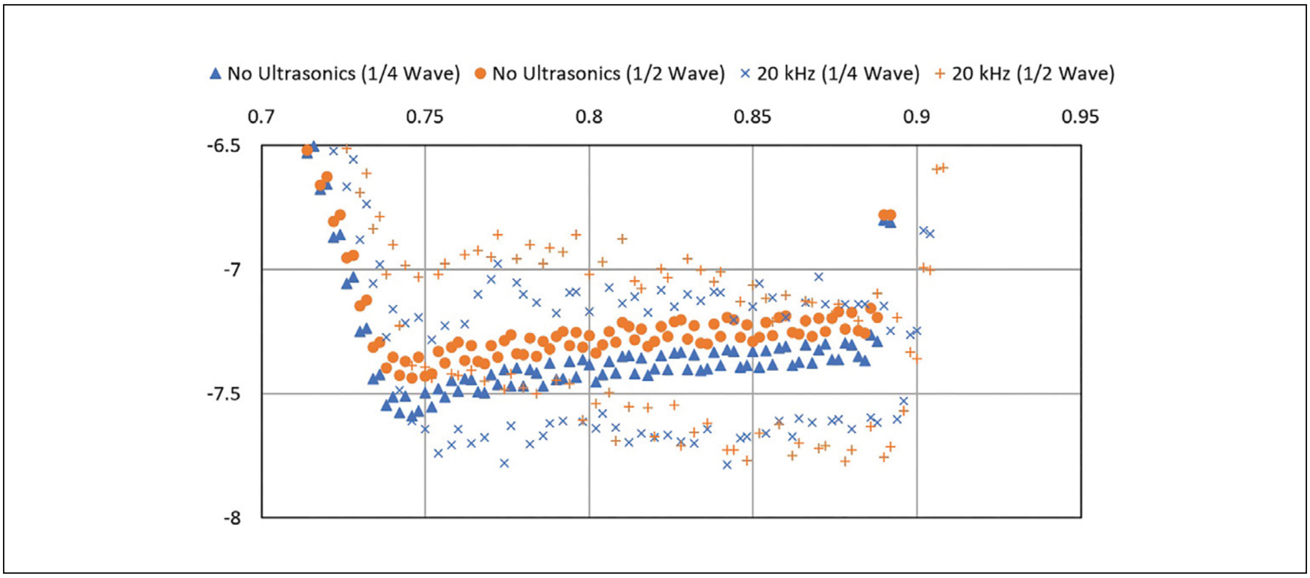

Fig. 19 — Displacement (µm) vs. time (s) for 2.54-cm-diameter rod at 890 N in the ¼ and ½ wave locations.

Experimentation

Methodology

It has been proposed that the actual change in length experienced by the plastic part is not limited by the amplitude but by the elastic strain that the part can experience under the applied load. To test this, strain gauges were used to measure the displacement in a polymer rod when compressed with and without ultrasonics. If the ultrasonic amplitude is transmitted through the rod independently of the applied load and geometry, then the measured displacement would correlate to the applied amplitude.

Two diameters of acrylonitrile butadiene styrene (ABS) rods were used: 1.27 cm and 2.54 cm. The rods were cut to about one full wavelength as calculated using Equation 51:

$$\lambda = \frac{c}{f} \tag{51}$$

where c is the speed of sound in the medium and f is the frequency of the wave.

The speed of sound for an ultrasonic wave passing through a polymer is given by the equation:

$$c = \sqrt{\frac{|E^*|}{\rho}} \tag{52}$$

For ABS, the modulus is 2.27 GPa (22,700,000,000 dyne/cc) and its density is 1.03 g/cc. Therefore, at 20 kHz, the wavelength in ABS is:

$$\lambda = \frac{\sqrt{\frac{|E^*|}{\rho}}}{f} \tag{53}$$
$$= \frac{\sqrt{\frac{22700000000}{1.03}}}{20000} = 7.4\text{cm}$$

High-accuracy CEA-13-250UW-120 strain gauges from micro measurements with the specifications listed in Table 1 were used for testing. These strain gauges have a length of 0.635 cm and are accurate to about 5% for frequencies up to 40 kHz (Ref. 15).

As the wave travels through the polymer rod, some energy losses are expected to reduce amplitude. This attenuation is described by Equation 32.

Figure 15 shows the expected amplitude, as a percent of the total, in the rod of a fully transferred resonant wave at the relevant strain gauge locations. If fully coupled to the horn and not restrained, then it is expected that no displacement would be measured at the ¼ and ¾ locations and that the displacement at the ½ wavelength location would be nearly the same as the input amplitude.

For this experiment, data was gathered at the test conditions listed in Table 2. Multiple rod geometries, loads, and amplitudes were selected so that the effect of each variable on the measured displacement in the rod could be analyzed. The chosen loads were selected because they are similar to those used in typical ultrasonic welding applications. The amplitudes selected were small enough to prevent melting so that the tests could be duplicated.

The expected displacement in each strain gauge, ΔL, based solely on the static load applied, can be calculated per Equation 54:

$$\Delta L = \frac{FL}{EA} \tag{54}$$

where F is the applied load, L is the total length of the gauge, E is the elastic modulus, and A is the cross-sectional area of the rod.

For an applied force of 2224 N, a strain gauge length of 0.635 cm, a radius of 1.27 cm (area of 5.07 sq.cm), and an elastic modulus of 2275 MPa, the displacement in the strain gauge is expected to be:

$$\Delta L = \frac{2224 * 0.635}{227500 * 5.07} \tag{55}$$
$$= .0012\text{ cm} = 12\ \mu\text{m}$$

For a force of 890 N, a strain gauge length of 0.635 cm, a radius of 1.27 cm (area of 5.07 sq.cm), and an elastic modulus of 2275 MPa, the displacement in the strain gauge is expected to be:

$$\Delta L = \frac{890 * 0.635}{227500 * 5.07} \tag{56}$$
$$= .00049\text{ cm} = 4.9\ \mu\text{m}$$

For a force of 2224 N, a strain gauge length of 0.635 cm, a radius of 0.635 cm (area of 1.27 cm^2), and an elastic modulus of 2275 MPa, the displacement in the strain gauge is expected to be:

$$\Delta L = \frac{2224 * 0.635}{227500 * 1.27} \tag{57}$$
$$= .0049\text{ cm} = 49\ \mu\text{m}$$

Results

The average displacement measured for each of the experimental conditions and the calculated elastic displacement, shown by the red line, are shown in Fig. 16. Each measurement was taken three times, with the exception of the 39 micron amplitude test on the 0.635-in.-radius rod at 2224 N, which was only tested once.

The calculated elastic displacement for the 2.54-cm-diameter rod under high load matched the measured displacement well. The measurements are a bit further off for the other conditions. This discrepancy is likely due to an estimated elastic modulus used from literature rather than a measurement of the value for these specific rods. However, for all welding trials, the modulus of the material used was tested directly.

For all the strain test conditions, the measured displacements with and without ultrasonic vibration are very close. The displacement measured by the strain gauge is not significantly affected by the addition of ultrasonic vibration. However, changes in the material geometry and the applied load strongly affect it.

These results may suggest that the strain gauges could not measure the oscillations due to the applied ultrasonic vibration. However, the oscillation due to vibration is apparent when the displacement is graphed vs. time for a cycle with and without ultrasonics. This can be seen in the displacement vs. time graphs at the lower force of 890 N — Figs. 17 and 18.

The displacement response is nearly the same with and without the addition of ultrasonic vibration. The biggest difference is that, with ultrasonics, once the maximum load has been reached, the displacement oscillates around the constant displacement measured when there are no ultrasonic vibrations. This is true for both the ¼ wave and ½ wave locations. While there should be no displacement at the node, in the ¼ wave location, the strain gauge covers a much larger area of the rod than a single node.

This data supports the hypothesis that the displacement in the polymer is limited by the geometry and force, even when more ultrasonic amplitude is applied than the calculated elastic displacement, as was the case for the trial performed on the 2.54-cm-diameter rod at 200 lb, which is seen in Fig. 19. We note that these strain gauges have been placed in the main body of specimens and not at an energy director where large stress concentration exists. The strain gauge results only prove our hypothesis that energy losses at the main body of the specimens to be welded are minimal and that mostly elastic deformations of these areas can be assumed.

The small cross-sectional area of the designed joint, such as an energy director, where a large stress concentration exists, increases the deformation and results in faster heating of such a small volume of material. At the beginning of the weld, the small point of the energy director means that the displacement is larger than the amplitude at the joint, helping melt initiation, which requires the most energy.

Summary

Ultrasonic welding is the most-used polymer welding process. It is widely applicable in the medical, electronics, consumer, and automotive industries. It is important to understand the heating mechanisms at work in this process to design parts for welding properly and to select proper welding parameters.

It was hypothesized that the traditional approach to estimating strain at the weld, based purely on the amplitude of the ultrasonic vibration at the joint, was imperfect. It was proposed that the elastic deformation defined by the part's geometry and the load applied would limit the actual strain produced in the system. This was validated through the experimental trials described, which showed that the strain in the parts during ultrasonic vibration oscillated around the strain that was recorded when no vibration was applied.

In this paper, the physical and material property contributions to polymer heating during ultrasonic excitation have been thoroughly discussed and equations to account for all factors proposed. The updated approach to estimating strain allows for the part geometry and the force being applied during welding to be taken into account in addition to the amplitude of the ultrasonic wave applied. This approach accounts for observable phenomena that previous approaches did not.

The following formulae have been proposed:

Amplitude at distance (x) from the horn contact surface:

$$A(x) = A_0 \cos\left(\frac{-2\pi x}{\lambda}\right) e^{\frac{-\pi x E''}{\lambda E^*}} \tag{58}$$

where A(x) is the function of maximum peak-to-peak amplitude as a function of distance into the material, A_0 is the peak-to-peak amplitude at the sonotrode contact surface, λ is the wavelength in the polymer, E" is the loss modulus, and E* is the complex modulus.

Deformation of the energy director:

$$\delta x = \frac{F}{E}\frac{h}{bL} \ln\left(\frac{x}{h}\right) \tag{59}$$

where F is the force applied, h is the energy director height, E is the elastic modulus, b is the energy director width, and L is the energy director length.

Acknowledgments

The researchers would like to thank Matt Nitsch for his excellent technician support.

References

1. Levy, A., Le Corre, S., and Villegas, F. 2014. Modeling of the heating phenomena in ultrasonic welding of thermoplastic composites with flat energy directors. *Materials Processing Technology* 214: 1361–1371.

2. Grewell, D., Benatar, A., and Park, J. 2003. *Plastics and Composites Welding Handbook*.

3. Potente, H., Fiegler, G., Haterkamp, H., Fargas, M., von Busse, A., and Bunte, J. 2006. An approach to model the melt displacement and temperature profiles during the laser through-transmission welding of thermoplastics. *Polymer Engineering and Science* 46: 1565–1575.

4. Himenz, P., and Lodge, T. 2007. Crystalline polymers. *Polymer Chemistry*.

5. Tadmor, Gogos. 2006. *Principles of Polymer Processing*.

6. Sancaktar, E. 1999. Polymer adhesion by ultrasonic welding. *Journal of Adhesion Science and Technology* 13(2): 179–201.

7. Suresh, K., Roopa Rani, M., Prakasan, K., and Rudramoorthy, R. 2007. Modeling of temperature distribution in ultrasonic welding of thermoplastics for various joint designs. *Journal of Materials Processing Technology* 186: 138–146.

8. Krautkrammer, J., and Krautkrammer, H. 1993. Chapter 6: Attenuation of ultrasonic waves in solids. *Ultrasonic Testing of Materials*: 108–116.

9. Benatar, A., and Cheng, Z. 1989. Ultrasonic welding of thermoplastics in the far-field. *Journal Polymer Engineering Science* 29(23): 1699–1704.

10. Gallego-Juarez, J., and Graff, K. 2015. *Power Ultrasonics: Applications of High Intensity Ultrasound*.

11. Marcus, M., Anantharaman, S., and Aldaz, B. 2013. Advantages of a servo-driven ultrasonic welder. *ANTEC*.

12. Grewell, D., and Benatar, A. 2008. Semi-empirical, squeeze flow, and intermolecular diffusion model. II. Model verification using laser microwelding. *Polymer Engineering and Science* 48(5): 543–1549.

13. Hopmann, C., Dahlmann, R., Weihermuller, M., Wipperfurth, J., and Sommer, J. 2022. Determination of the frequency and temperature dependent stiffness and damping properties of thermoplastics for the prediction of the vibration and heating behaviour during ultrasonic welding. *Welding in the World* 67(1).

14. Chuah, C., and Chang, L. 2000. Effects of the shape of the energy director on far-field ultrasonic welding of thermoplastics. *Polymer Engineering and Science* 40(7): 157–167.

15. Ueda, K., and Umeda, A. 1998. Dynamic response of strain gauges up to 300 kHz. *Experimental Mechanics* 38(2): 93–98.

MIRANDA MARCUS (*mmarcus@ewi.org*) is with the Edison Welding Institute, Columbus, Ohio, and **EROL SANCAKTAR** is with the University of Akron, Akron, Ohio.

Study of GTA-Welded Joints of ZW61 Magnesium Alloy — Effect of Welding Current on the Microstructure and Mechanical Properties

The welded joints' microstructure evolution and softening mechanism as well as the effect of limiting heat input were concretely analyzed

BY W. ZHOU, Q. LE, Q. LIAO, Y. SHI, T. WANG, AND W. HU

Abstract

An attempt has been made to weld ZW61 magnesium alloy extruded plates by gas tungsten arc welding (GTAW). In this paper, the zone with the largest average grain size in the welded joint was the fusion zone (FZ) rather than the heat-affected zone (HAZ). The grains of the FZ were nearly equiaxed, and their average size increased gradually with the increase of welding current. Simultaneously, the mechanical properties of the joints decreased with the increase of welding current under the set conditions of this experiment. The optimum mechanical properties of the joints were obtained at a welding current of 100 A. Their ultimate tensile strength (UTS), yield strength (YS), and elongation (EL) were 230 MPa, 103 MPa, and 19.2%, respectively, while the joint efficiency (σ_b / σ_b^{BM}) was only 77.7%. The fracture locations of all the joints were found in the FZ. Excessive grain size was one of the significant factors contributing to the weakness of this zone. In addition, the semicontinuous second phase on the grain boundary induced high-stress concentrations, contributing to the fracture of the welded joint. The tensile properties of the joints can be improved by limiting heat input.

Keywords

- Welding Current
- Welded Joints
- Fusion Zone
- Microstructure
- Mechanical Properties

https://doi.org/10.29391/2025.104.002

Introduction

In the global efforts to achieve carbon neutrality, the development of magnesium alloy as the lightest structural metal has attracted more and more attention (Ref. 1). Magnesium alloys have a strong potential for development with high specific strength, excellent vibration-damping properties, and recyclability (Ref. 2). These advantages facilitate their application in automotive, aerospace, and electrocommunication (Ref. 1). Consequently, sophisticated magnesium alloy structural parts are bound to encounter challenges with joining technology. However, due to the poor weldability of magnesium alloy (Ref. 3), welding has become one of the bottleneck technical problems affecting the broader application of magnesium alloy.

Recently, many scholars have employed various welding techniques to study magnesium alloy joining. Some of these magnesium alloy welding techniques are also becoming more mature and typically include gas tungsten arc welding (GTAW), resistance spot welding (RSW), friction stir welding (FSW), laser beam welding, and electron beam welding (Ref. 3). GTAW is widely utilized in magnesium alloy joining because of its high flexibility and low cost (Ref. 4). Many efforts have been made to investigate the GTAW of magnesium alloys. Liu and Dong (Ref. 5) observed the microstructure and fracture of AZ31 magnesium alloy GTA-welded joints. It was shown that the grain size in the heat-affected zone (HAZ) of the welded joints filled with wire varied considerably compared to that of the welded joints not filled with wire. Moreover, the change in the HAZ's microstructure altered the fracture location and strength of the joints. The effect of heat input on the microhardness distribution of AZ61 magnesium alloy GTA-welded joints was studied by Xu et al. (Ref. 6). The welding heat input induced different microhardness distributions at the top and bottom of the welded joints. A combination of grain size and dispersion strengthening determined this. The microstructure of the GTA-welded joints for AZ91 mag-

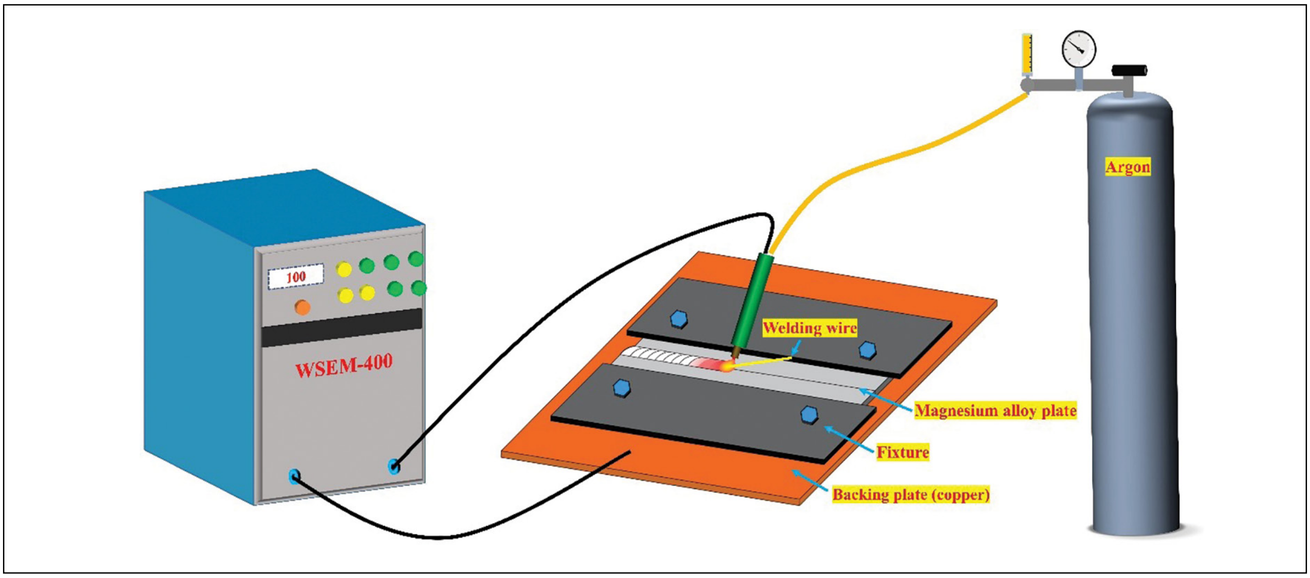

Fig. 1 — Schematic diagram of the welding platform.

nesium alloy was investigated by Braszczyńska-Malik et al. (Ref. 7). The width, depth, and dendrite arm size of the fusion zone (FZ) decreased with the increase in welding speed. In addition, Min and Shen et al. (Refs. 8, 9) explored the effects of heat input and preheat treatments on the microstructure and mechanical properties of tungsten inert gas arc-welded AZ61 magnesium alloy plates. Chen and Zhou et al. (Refs. 10, 11) also investigated the GTAW of AZ91D magnesium alloy. However, the existing GTAW investigations of magnesium alloys focus on AZ-series alloys, while few relevant works are on Mg-Zn series magnesium alloys.

As one of the two main alloying elements of magnesium alloy, the strengthening effect of Zn is quite conspicuous (Ref. 12). The Mg-Zn series magnesium alloys are an interesting path for developing high-strength and tough magnesium alloys. Specifically, the Mg-Zn-Y alloys have gathered a lot of attention. Y is one of the elements with a relatively large degree of solid solution in magnesium alloy (Ref. 13). The high solid solubility of Y makes the alloy form a supersaturated solid solution, acting as a strong solid solution and age-strengthening. The alloy is currently used in mechanical structural components and biomedical devices (Ref. 14). Previous studies have revealed that the phase constitution in Mg-Zn-Y alloys highly depends on the Zn/Y ratio (Ref. 15). Three ternary equilibrium phases exist in Mg-Zn-Y alloys, namely Mg_3Zn_6Y (I-phase icosahedral quasi-crystal structure and quasi-periodic order), $Mg_3Zn_3Y_2$ (W-phase face-centered cubic structure) and $Mg_{12}ZnY$ (X-phase long period stacked ordered structure) (Ref. 16). The I-phase is characterized by high strength, high hardness, low coefficient of friction, and low interfacial energy (Ref. 16). The W-phase is usually distributed at the grain boundaries of magnesium alloys, and its addition in appropriate amounts can enhance the mechanical properties of the alloy (Ref. 17). The X-phase, with its unique crystalline structure, coherent interfaces with the Mg matrix, and the formation of kink bands, also significantly enhances the strength of the alloys (Ref. 16). The low Y content of Mg-Zn-Y alloys could reduce the cost of expensive rare earth elements. Therefore, Mg-Zn-Y alloys containing I-phase or W-phase have turned out to be a hot topic of discussion. Xu et al. (Ref. 17) investigated the microstructure and mechanical properties of the cast Mg-Zn-Y-Zr magnesium alloy with a Zn/Y ratio of about 0.97. The studies showed that the coarsened W-phase at the grain boundaries deteriorates the mechanical properties of the alloy. The effects of yttrium addition on the microstructure and mechanical properties of extruded Mg-Zn-Y-Zr magnesium alloys were investigated by Chen et al. (Ref. 18). The addition of Y led to the formation of W-phases distributed at grain boundaries and inside grains. Moreover, the addition of Y improved the yield strength (YS) of Mg-Zn-Y-Zr alloys, but the improvement of ultimate test strength (UTS) was not significant. Chen et al. (Ref. 19) employed a dual-frequency ultrasonic field to refine quasi-crystal-reinforced Mg-Zn-Y alloy. The results revealed that the dual-frequency ultrasonic field treatment could remarkably refine the Mg grains and I-phase. Thus, the corrosion resistance and mechanical properties of the material were improved. The microstructure and mechanical properties of as-cast Mg-6Zn-1.2Y alloy at room and elevated temperatures were studied by Jung et al. (Ref. 20). The coherent interface of the I-phase and α-Mg phase allowed the alloy to have superior tensile and creep properties.

Table 1 — Chemical Compositions of the ZW61 Alloy (wt-%)

Material	Elements			
	Zn	Y	Zr	Mg
ZW61	5.93	0.90	0.49	Bal.

With the development of Mg-Zn-Y alloy applications, welding this series of alloys will undoubtedly be a pressing

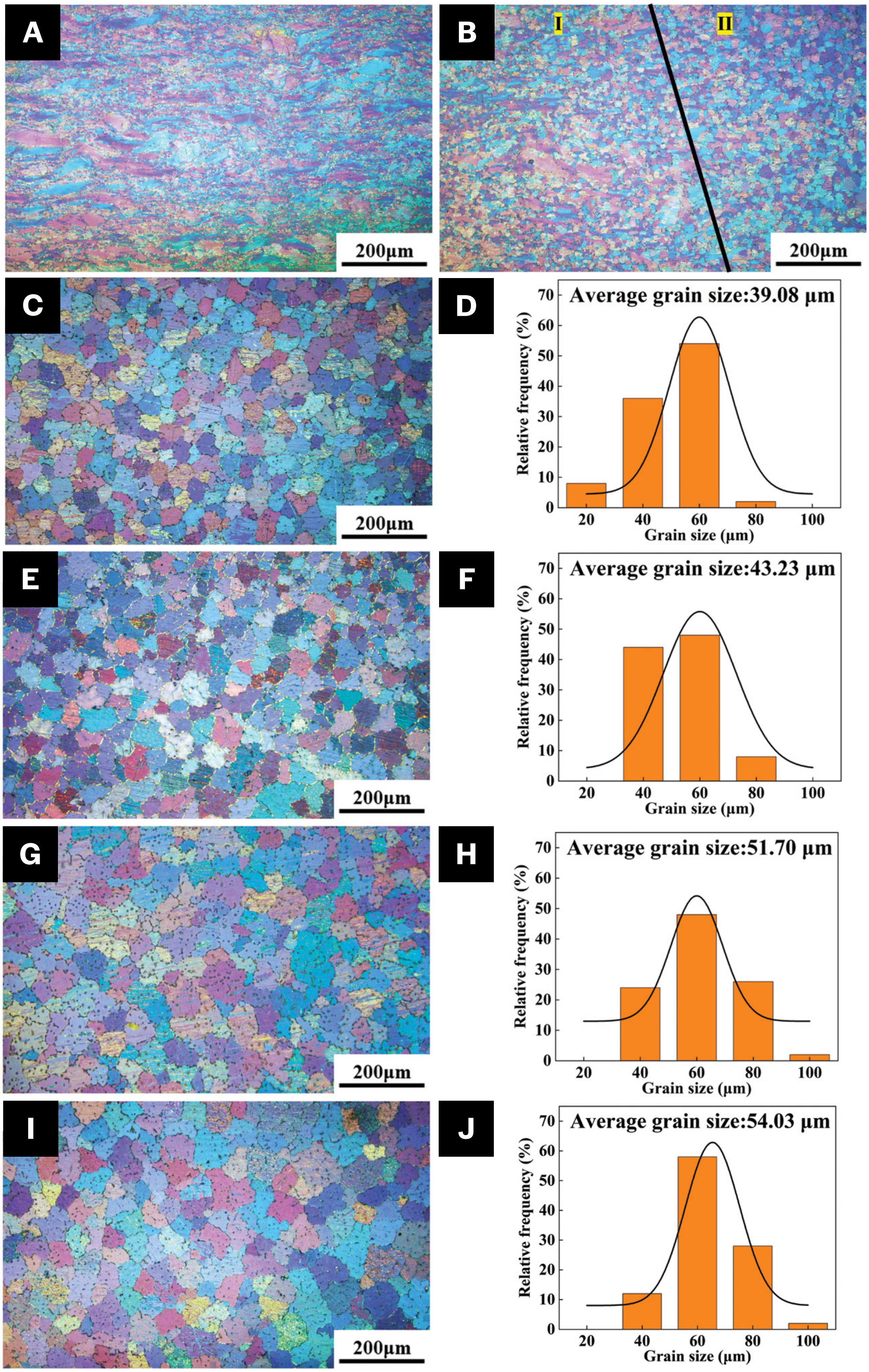

Fig. 2 — Microstructure of the welded joints: A — BM, 100 A; B — HAZ, 100 A; C and D — FZ, 100 A; E and F — FZ, 110 A; G and H — FZ, 120 A; I and J — FZ, 130 A.

Table 2 — The Main Welding Parameters Used in the Test

Current (A)	Voltage (V)	Speed (mm/min)	Gas Flow (L/min)	Heat Input (J/mm)
100	10	110	12	355
110	10	110	12	390
120	10	110	12	425
130	10	110	12	461

challenge. Currently, the welding of Mg-Zn-Y alloys is dominated by FSW (Ref. 21) with little research on arc welding. Consequently, GTAW was carried out for the ZW61 magnesium alloy in this paper. Welding current is one of the critical factors affecting the microstructure and properties of GTA-welded joints for magnesium alloys. Accordingly, the effect of welding current on the microstructure and mechanical properties of ZW61 magnesium alloy GTA-welded joints was discussed in detail. Meanwhile, the welded joints' microstructure evolution and softening mechanism were concretely analyzed.

Experimental Method

Welding Materials

The test base material (BM) was the as-extruded ZW61 magnesium alloy plate of 2 mm thickness. Welded specimens were prepared by a wire-cutting process of 200 mm × 40 mm × 2 mm. The composition of the welding wire was the same as that of the BM. The chemical composition of ZW61 magnesium alloy is shown in Table 1. Before the welding experiment, the surface of the magnesium alloy plate was sandpapered to remove the oxide film on the surface. Then, it was cleaned with acetone to remove the residual metal powder and oil on the surface.

Welding Process

A WSME-400 pulsed AC/DC argon arc welder was used to conduct the welding. The current type and polarity were sinusoidal AC. The tungsten electrode and nozzle diameters were 2.3 and 8 mm, respectively. The joint type was the butt joint, and the joint was not beveled. The schematic diagram of the welding platform is shown in Fig. 1. A copper plate was placed on the back side of the magnesium alloy plate to expedite heat dissipation. Furthermore, the inert gas (argon) was supplied during welding to shield the weld area. The main welding parameters, such as welding current, welding speed, welding voltage, gas flow, and welding heat input (calculated from Equation 1 [Refs. 22–23]), are shown in Table 2.

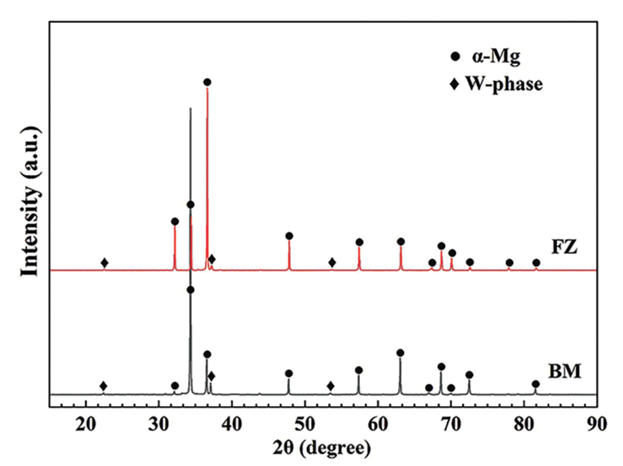

Fig. 3 — XRD patterns of the BM and FZ.

$$E=\eta UI/V \tag{1}$$

where $\eta = 0.65$ is the thermal efficiency coefficient (Refs. 22–23), I is the welding current, U is the welding voltage, and V is the welding speed.

Characterization

A specimen block of 20 mm × 5 mm was intercepted at the joint in the direction perpendicular to the weld as a metallographic specimen. After grinding and polishing, the metallographic specimen was etched with an etching solution (2 g picric acid + 10 ml glacial acetic acid + 10 ml distilled water + 75 ml ethyl alcohol). The optical microstructure of the welded joints was observed with an Olympus BX53-P polarizing microscope. The phase composition was identified by x-ray diffraction (XRD) with scanning angles of 15~90 deg and a scanning speed of 5 deg/min. Morphology and distribution of the phases and fracture morphology were performed by a field emission scanning electron microscope (SEM, Thermo Scientific Apreo 2) equipped with an ener-

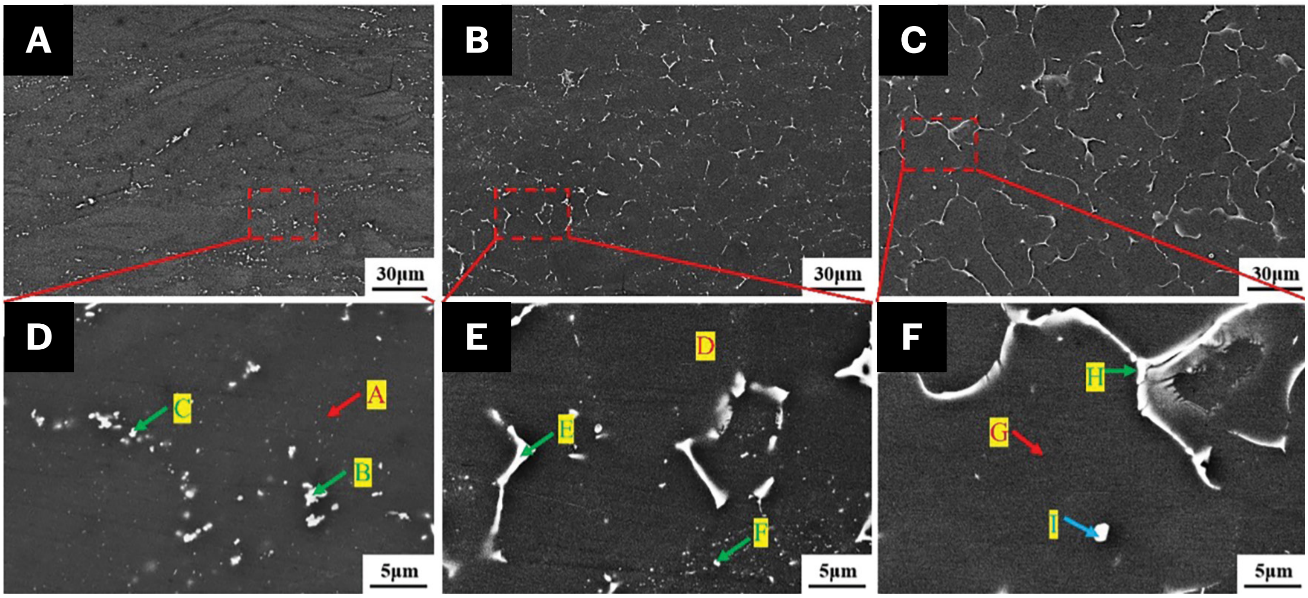

Fig. 4 — SEM images of various zones of the welded joints with a welding current of 100 A: A and D — BM; B and E — HAZ; C and F — FZ.

Table 3 — Results of the EDS Analysis in Fig. 4. (at.-%)

Position	Mg	Zn	Y	Zr
A	98.20	1.75	0.00	0.05
B	61.63	25.94	12.16	0.27
C	81.74	12.18	6.08	0.00
D	98.32	1.42	0.13	0.13
E	58.15	27.79	13.38	0.68
F	89.97	6.86	2.98	0.19
G	99.21	0.67	0.02	0.10
H	65.32	23.61	10.81	0.26
I	85.71	11.52	2.76	0.01

gy-dispersive spectroscope (EDS). The microhardness of each area of the welded joint was measured by a Vickers hardness tester (MH-5L) with a 200 gf load for 10 s. The tensile test was performed on an electronic universal material testing machine (AG-X100KN) with a 0.5 mm/min speed. To ensure the stability of the experimental results, the same mechanical experimental test was repeated three times.

Results

Microstructures

The microstructures of the GTA-welded joints for ZW61 alloys are shown in Fig. 2. The welded joints mainly included in the BM, HAZ, and FZ. As can be seen from Fig. 2A, most of the grains in the BM were elongated by extrusion. A few fine equiaxed grains were also involved. The opposite was confirmed in the HAZ, where the microstructure was almost entirely uniform and contained fine equiaxed grains, as

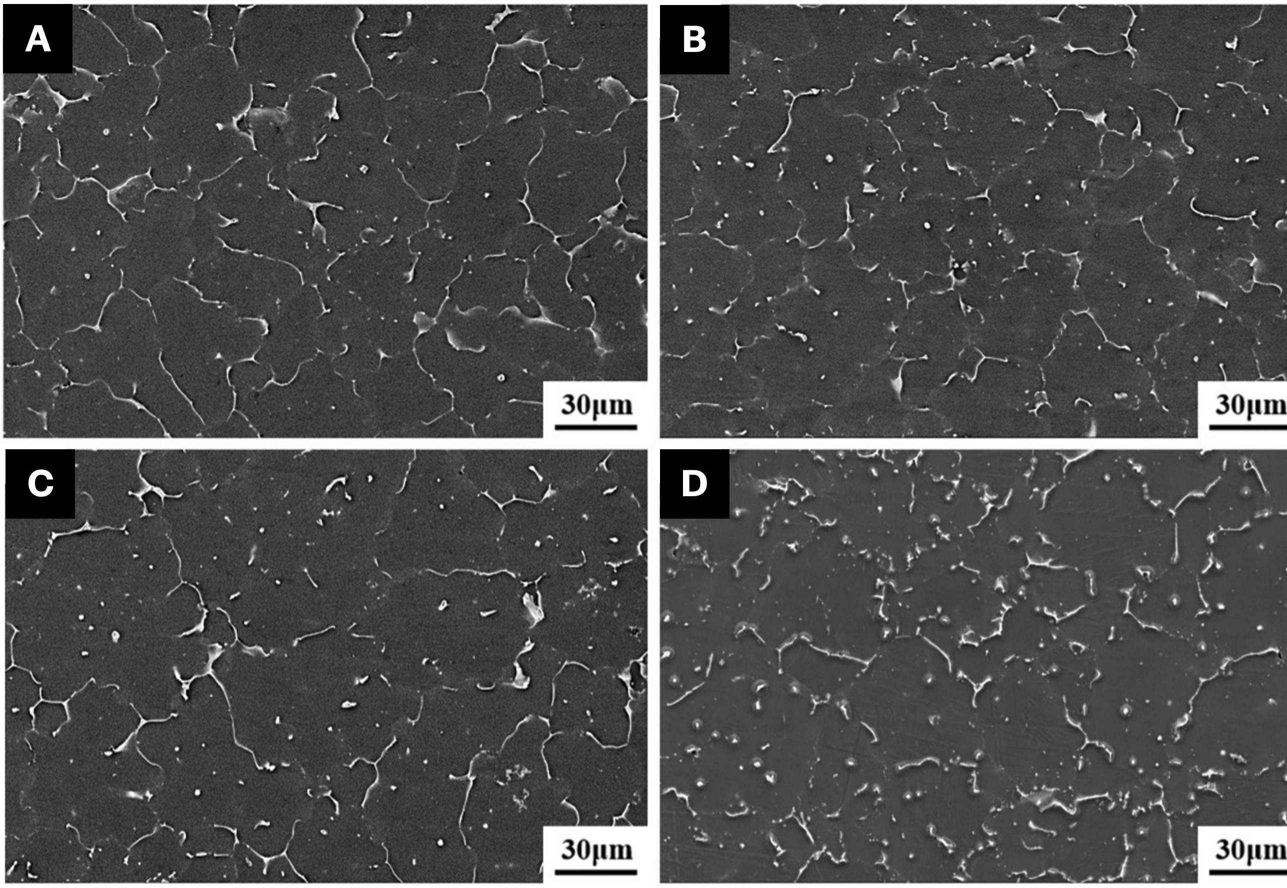

Fig. 5 — SEM images of the FZ with different welding currents: A — 100 A; B — 110 A; C — 120 A; D — 130 A.

presented in Fig. 2B. Only a few deformed grains could be observed. Figures. 2C–J demonstrate the microstructure of the FZ with different welding currents. All grains in the FZ were coarser and equiaxed, and the grain size increased with increasing current. The average grain size of the FZ was smallest at 39.08 μm when the welding current was 100 A. The average grain size of the FZ increased by 38% as the welding current increased to 130 A. As indicated by Equation 1, the increase in welding current inevitably caused a rise in welding heat input. At such a high heat input, the grain of the FZ was larger.

Figure 3 exhibits the XRD patterns of the FZ and BM. From the XRD patterns, no change in the type of the second phase of the FZ following welding was observed compared to that of the BM. The microstructure of the FZ was composed of α-Mg and W-phase ($Mg_3Zn_3Y_2$). The diffraction peak at 34.4 deg of the XRD pattern of the BM was significantly higher than other diffraction peaks. This was due to the forming of a stronger fiber texture in the ZW61 alloy during extrusion deformation.

The SEM images of various zones of the welded joints with a welding current of 100 A are presented in Fig. 4. Table 3 demonstrates the results of the corresponding EDS analysis. As shown in Fig. 4A, the second phase of the BM was distributed along the boundaries of the deformed grains in a granular shape. The EDS analysis results indicated that this second phase was a Mg-Zn-Y phase and the Zn/Y was about 1.5. Combined with the XRD results, this second phase was a W-phase. The shape and distribution of the second phase in the HAZ were entirely different from that of the second phase in the BM, as depicted in Fig. 4B. During the welding process, the temperature of the HAZ was much higher than the solid solution temperature of the W-phase under the action of the residual heat of welding. The W-phase was dissolved and reprecipitated during the welding process. The W-phase in the HAZ was mainly distributed in a semicontinuous network at the grain boundaries, as shown in Fig. 4E. Also, a portion of the second phase was distributed in the grain in the form of dots. Figures 4C and F display the shape and distribution of the second phase in the FZ. Like the HAZ, most of the second phases in this zone were distributed at the grain boundaries. However, this type of second phase was much more abundant and considerably coarser. Meanwhile, the EDS results showed that this phase was a W-phase, consistent with the XRD results. Moreover, a granular second phase existed within the grains. The EDS results indicated that this phase had a Zn/Y of about 4, from which it was inferred that this phase was an I-phase. As given in Fig. 4C, the I-phase was present in low amounts in the FZ, leading to no diffraction peaks of this phase being found in the XRD pattern.

Figure 5 displays the SEM images of the FZ with different welding currents. The change in welding current did not induce the shape and distribution of the second phase

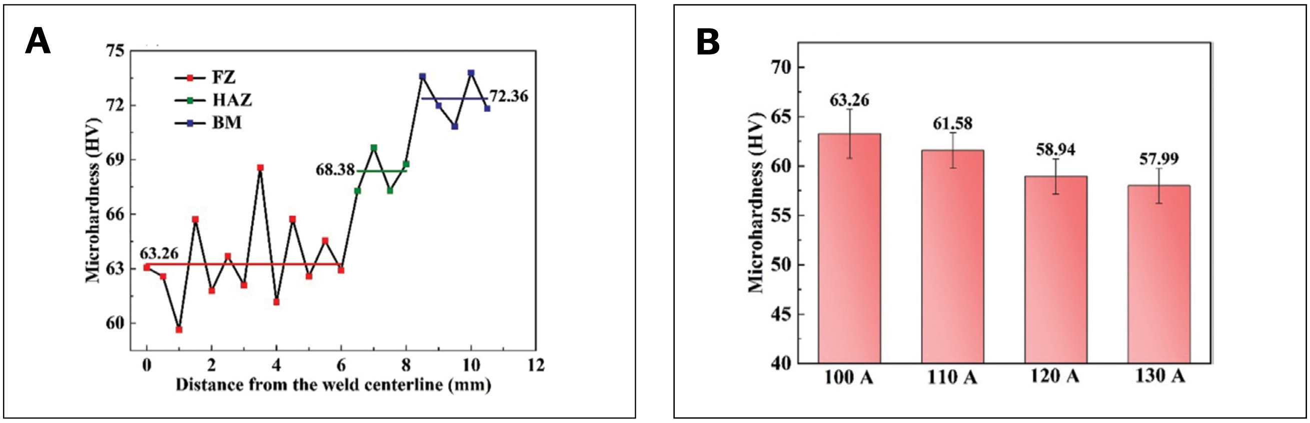

Fig. 6 — A — Microhardness distribution of the welded joints from FZ to BM with welding current of 100A; B — statistical charts of microhardness in the FZ with different welding currents.

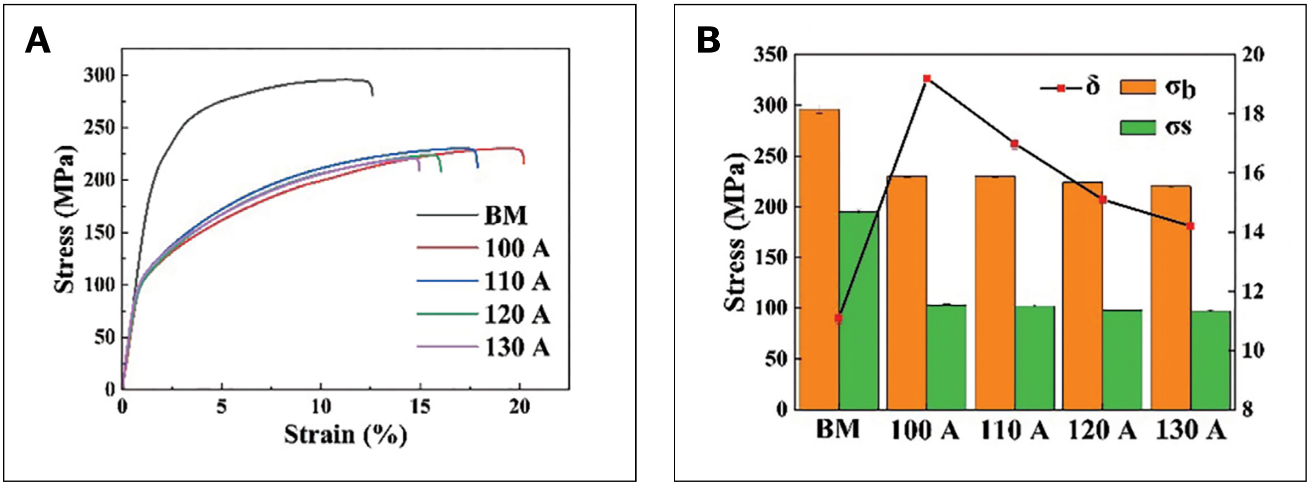

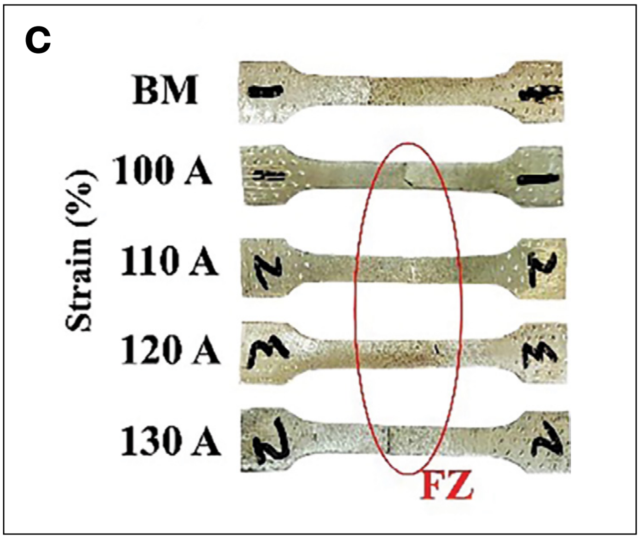

Fig. 7 — A — Engineering stress-strain curves; B — the effect of welding current on tensile properties of the welded joints; C — fracture locations of the BM and welded joints.

in the FZ. However, the increase in welding current elicited a less-pronounced increase in the second phase size. The amount of the second phase in the FZ increased gradually with the welding current, which was 2.52, 2.74, 3.20, and 3.93%, respectively. From the previous section, an increase in welding current increased welding heat input, further decelerating the cooling rate. At lower cooling rates, solute atoms had ample time to diffuse, ultimately leading to an increase in the volume fraction of the second phase at grain boundaries.

Mechanical Properties

As displayed in Fig. 6A, the microhardness within each zone of the welded joint floated around a particular value without substantial change at a welding current of 100 A. However, the microhardness of different zones varied significantly; the microhardness of the BM had a maximum value of 72.36 HV, while the microhardness of the FZ had a minimum value of 62.36 HV. Larger grain size and lower dislocation density induced a marked decrease in the microhardness of the FZ. Fig. 6B presents the statistical charts of microhardness in the FZ with different welding currents. The FZ's microhardness decreased with an increase in welding currents, but the decrease was slight. The microhardness

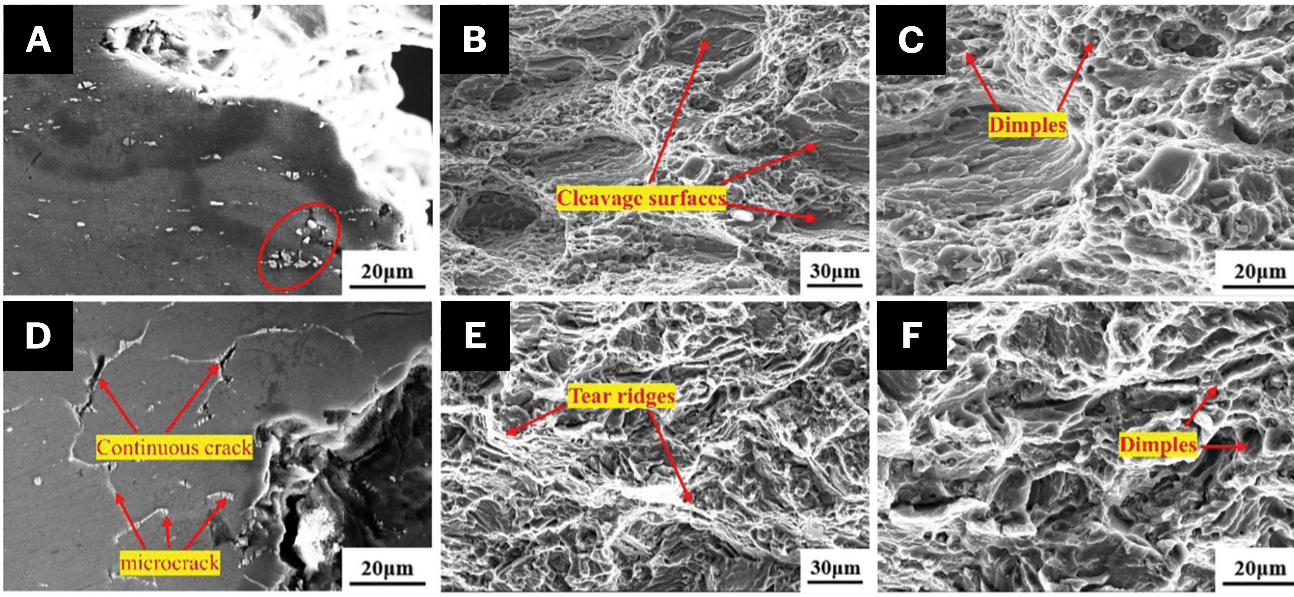

Fig. 8 — Morphologies and longitudinal section of the fracture: A–C — BM; D–F — FZ.

Table 4 — Mechanical Properties of the BM and Welded Joints

	σ_b (MPa)	σ_s (MPa)	δ (%)	Joint Efficiency (σ_b/σ_b^{BM}) (%)
BM	296 ± 4	195 ± 2	11.1 ± 0.2	/
100 A	230 ± 1	103 ± 1	19.2 ± 0.2	77.7
110 A	230 ± 1	102 ± 1	17.0 ± 0.2	77.7
120 A	224 ± 2	98 ± 2	15.1 ± 0.1	75.7
130 A	220 ± 1	97 ± 1	14.2 ± 0.1	74.3

of the FZ was minimized when the welding current was 130 A. The microhardness of the FZ was only degraded by 8% compared to that of the FZ with a welding current of 100 A.

Figures 7A and B demonstrate the tensile properties of the BM and welded joints. The corresponding data are shown in Table 4. The UTS, YS, and EL of ZW61 extruded magnesium alloy were 296 MPa,195 MPa, and 11.1%, respectively. In comparison, the UTS and YS of all welded joints were much weaker, but the EL improved considerably. As indicated in Fig. 7A, the UTS and YS of the welded joints did not fluctuate much with the increase in welding current. As displayed in Fig. 7B, the EL decreased gradually with the increase in the welding current. From Table 4, it can be summarized that the mechanical properties of the welded joints were optimal under the use conditions in this study (where the welding current was 100 A). The EL was significantly improved to 19.2% compared to the BM. However, the UTS and YS decreased by 22.3 and 47.2%, respectively. The joint efficiency was only 77.7%, which did not meet the service standard (90%) of welded joints. In addition, it can be seen from Table 4 that the poorest welded joint properties occurred at a welding current of 130 A. In this case, the UTS and YS of the welded joints decreased slightly compared to those of the optimized welded joints, but the EL decreased tremendously (26%). Figure 7C exhibits the fractured locations of the BM and welded joints. The weak location of all welded joints occurred in the FZ. Previous studies showed a weakness in a different location from the magnesium alloy GTA-welded joints (Refs. 24, 25) for reasons that will be detailed below.

Figure 8 shows the morphologies and longitudinal section of the fracture of the BM and welded joint. As indicated in Fig. 8A, cracks and micropores were formed at the second phase aggregation near the fracture. It was inferred that stress concentration was generated here during the tensile process. The presence of cleavage surfaces and dimples can be observed in Figs. 8B and C. The fracture of the BM exhibited a combination of brittleness and ductility, as evidenced by these features. However, the small amount and tiny size of the dimples on the fracture surface indicated that

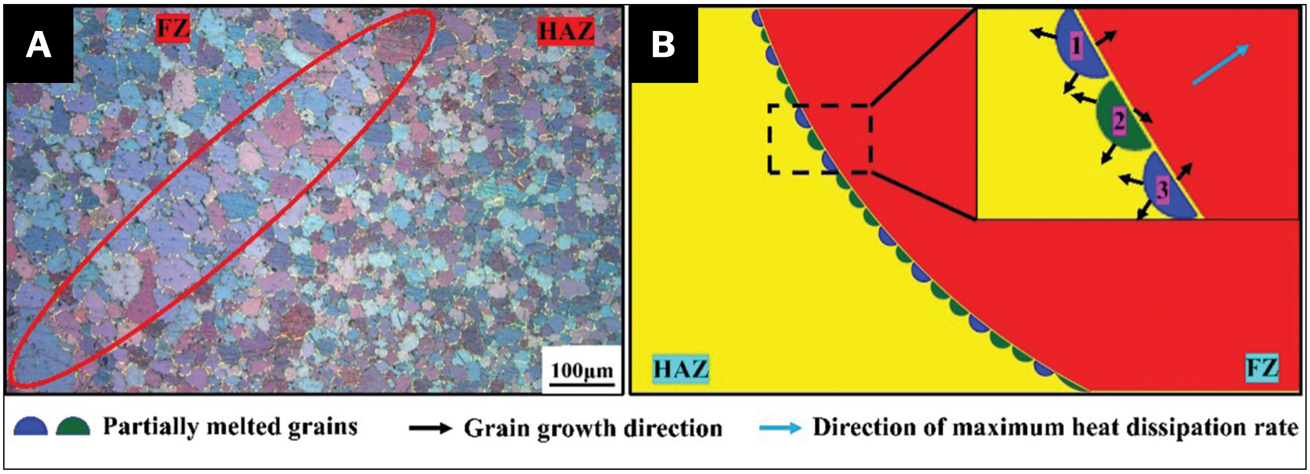

Fig. 9 — A — Microstructure at the junction of the FZ and HAZ; B — schematic of grain growth at the junction of the FZ and HAZ.

the fracture mode was dominated by brittle fracture and supplemented by ductile fracture. As illustrated in Fig. 8D, microcracks and continuous cracks nearly perpendicular to the tensile direction were generated at the location of the second phase at the grain boundary. The second phase was still preferred for stress concentration, which was consistent with the analysis of the BM. Meanwhile, the grains near the fracture were coarse equiaxed grains. This microstructure appeared only in the FZ of the welded joint, further proving the analysis in Fig. 7C. As shown in Figs. 7E and F, the fracture surfaces of the welded joints were characterized by cleavage surfaces, tear ridges, and dimples. However, the size of the cleavage surface was smaller, and the dimple's size was larger than that of the BM. These features supported the fact that the welded joints had superior plasticity to the BM, as shown in Fig. 7.

Discussion

Microstructure Evolution of the Welded Joint

As depicted in Fig. 2A, the microstructure of the BM mainly consisted of deformed grains, while there were few recrystallized grains. During the welding process, static recrystallization and potential grain growth of the deformed grains in the HAZ occurred under the effect of welding heat. The energy provided by welding heat only supported recrystallization nucleation and initial growth. Therefore, the HAZ did not exhibit excessive grain size, as shown in Fig. 2B. Furthermore, as the distance from the center of the weld increased, the heat received at each location of the HAZ was different, which resulted in a variable degree of recrystallization at each location. Some zones were wholly recrystallized (Fig. 2B–II), while some zones still had the presence of deformed grains (Fig. 2B–I). Also, the size of the recrystallized grains in all regions of the HAZ was much less than the size of the grains in the FZ.

Most heat absorbed by the welded joint was supplied to the FZ, where solidification, epitaxial regrowth, and competitive growth occurred. The grain size of the FZ was mainly controlled by the temperature gradient (G) and solidification growth rate (R) at the solid/liquid interface front during solidification in the molten pool. G·R characterizes the cooling rate of the solidification process and affects the microstructure scale. Under the condition of constant welding speed, the G·R value tended to decrease with the increase of welding heat input, thus leading to an increase in the grain size of the FZ. From Figs. 2C–J, most of the grain size in the FZ exceeded 40 μm. This was an essential factor contributing to the FZ being the weakest position of the welded joint. In addition, as shown in Fig. 9A, there was a region with the largest grain size at the junction of the HAZ and FZ. This phenomenon has also appeared in previous studies (Ref. 26) and presupposes that the welding wire is made of the same material as the BM. As displayed in Fig. 9B, some grains were only partially melted in this region. Some partially melted grains grew in the direction of maximum heat dissipation rate, such as grains 1 and 3, and these grains grew preferentially. Some grains grew in other directions, such as grain 2, which were restricted or engulfed. Meanwhile, the temperature in this region exceeded the liquation temperature of the second phase. Without the limitation of the second phase, the grains also grew further in other directions. However, the growth rate along these directions was slighter than that along the direction with the maximum heat dissipation rate.

Compared with AZ series magnesium alloys, ZK series magnesium alloys have a wider crystallization temperature interval, which makes it easy to form thermal cracks during welding (Ref. 27). After adding the Y element to the ZK alloy, the Y element can change the dissolution degree of Zn, thus improving the weldability of the alloy (Ref. 17). Simultaneously, the Y element affects grain refinement in the ZK alloy (Ref. 28). However, in this experiment, due to the high content of alloying elements, the W-phase mainly existed in the form of a network, significantly weakening this effect. Moreover, under the conditions of different welding currents set in this experiment, the change of W-phase content was inconspicuous, as shown in Fig. 5. Therefore, the effect of W-phase on the microstructure of the welded joint was minimal. Welding heat input was the main factor causing changes in the grain size of the FZ.

Weakening Mechanism of the Welded Joint

Fine-grain strengthening is one of the most essential strengthening mechanisms for magnesium alloys. Grain coarsening significantly deteriorates the strength of magnesium alloys. In this experiment, the size of the grains in the HAZ was much less than that in the FZ. Therefore, unlike most of the previous studies (Refs. 24, 25), the weak location of the welded joints in this experiment was the FZ. As shown in Figs. 2C–F, the average grain size of the FZ rose with the increase of welding current. However, the strength of the welded joint did not decrease significantly, which is well explained by the Hall-Petch formula (Ref. 29). Calculated from Equation 2, the differences in strength with increasing welding current are 2.2, 5.8, and 6.7 MPa, consistent with the experimental results. Additionally, the size of the grains significantly contributes to the plasticity of the welded joint. Finer grains result in more grains taking on plastic deformation in a given volume. Uniform deformation yields low-stress concentrations. Also, fine grains have zigzag grain boundaries that are not conducive to crack propagation. Therefore, as the welding current increases, the EL of the welded joints decreases.

$$\sigma_y = \sigma_0 + k d^x \tag{2}$$

where σ_y is the yield stress, σ_0 is the stress for dislocation motion in grain interior, and k is the Hall-Petch slope (0.28 $MPa \cdot m^{1/2}$) (Ref. 30), d is the grain diameter, and x is the exponent, which is close to $-1/2$ for random crystallographic textures and close to -1 for many solidification structures due to texturing.

As depicted in Fig. 5, the second phase with a semicontinuous network was distributed at the grain boundaries in the FZ. The location of the second phase on the grain boundaries is often a point of stress concentration (Refs. 30, 31). Under high tensile stresses, microcracks can develop at such positions. Microcracks link up to form continuous cracks, inducing fracture in welded joints, as indicated in Fig. 8D. Therefore, the second phase at the grain boundary is another vital factor in the deterioration of the mechanical properties of the welded joints.

Conclusions

In this paper, the ZW61 magnesium alloy extruded plate was successfully welded using GTAW. The influence rule of the welding current on the microstructure and mechanical properties of the welded joints was analyzed. The specific conclusions were as follows:

1. The grains were uniform and fine in the HAZ of the welded joints. On the other hand, most of the grains in the FZ exceeded 40 μm in size. In addition, the welding heat input increased with the increase in welding current, which led to an increase in grain size.
2. In the FZ of the welded joints, the microstructure consisted of α-Mg, I-Mg_3Zn_6Y and W-$Mg_3Zn_3Y_2$ phases. The I-phase was distributed inside the grains in a granular form, and the W-phase was distributed at the grain boundaries in a semicontinuous network.
3. As the welding current increased, the strength of the welded joints changed insignificantly, but the EL decreased gradually. Under the set conditions of this experiment, the welded joint with optimum mechanical properties was formed at a welding current of 100 A, and its UTS, YS, and EL were 230 MPa, 103 MPa, and 19.2%, respectively. In contrast, the joint efficiency was only 77.7%.
4. The FZ was the weakest position of a welded joint. Excessive grain size was one of the significant factors contributing to the weakness of this zone. Furthermore, the semicontinuous second phase at the grain boundary induced high-stress concentrations, leading to the fracture of the welded joint. The tensile properties of the joints can be improved by limiting heat input.

Acknowledgments

This research was financially supported by the National Natural Science Foundation of China (Grant No. 51974082, 52274377, 52304391) and the Natural Science Foundation of Liaoning Province, China (Grant No. 2023-MSBA-133).

References

1. Zeng, Z., Stanford, N., and Davies, C. H. J., et al. 2019. Magnesium extrusion alloys: a review of developments and prospects. *International Materials Reviews* 64: 27-s to 62-s. DOI: 10.1080/09506608.2017.1421439

2. Huang, Z., Qi, C., and Zou, J., et al. 2023. Edge crack damage analysis of AZ31 magnesium alloy hot-rolled plate improved by vertical roll pre-rolling. *Journal of Magnesium and Alloys* 11: 2151-s to 2164-s. DOI: 10.1016/j.jma.2021.08.038

3. Czerwinski, F. 2011. Welding and joining of magnesium alloys. *Magnesium Alloys – Design, Processing and Properties*. DOI: 10.5772/13947

4. Liu, L. M. 2010. Welding and joining of magnesium alloys. *Woodhead Publishing Series in Welding and Other Joining Technologies*. DOI: 10.1533/9780857090423.1.38

5. Liu, L. M., and Dong, C. F. 2006. Gas tungsten-arc filler welding of AZ31 magnesium alloy. *Materials Letters* 60: 2194-s to 2197-s. DOI: 10.1016/j.matlet.2005.12.120

6. Xu, N., Shen, J., and Xie, W. D., et al. 2010. Abnormal distribution of microhardness in tungsten inert gas arc butt-welded AZ61 magnesium alloy plates. *Materials Characterization* 61: 713-s to 719-s. DOI: 10.1016/j.matchar.2010.04.003

7. Braszczyńska-Malik, K.N., and Mróz, M. 2011. Gas-tungsten arc welding of AZ91 magnesium alloy. *Journal of Alloys and Compounds* 509: 9951-s to 9958-s. DOI: 10.1016/j.jallcom.2011.07.105

8. Min, D., Shen, J., Lai, S., and Chen, J. 2009. Effect of heat input on the microstructure and mechanical properties of tungsten inert gas

arc butt-welded AZ61 magnesium alloy plates. *Materials Characterization* 60: 1583-s to 1590-s. DOI: 10.1016/j.matchar.2009.09.010

9. Shen, J., and Xu, N. 2012. Effect of preheat on TIG welding of AZ61 magnesium alloy. *International Journal of Minerals, Metallurgy, and Materials* 19: 360-s to 363-s. DOI: 10.1007/s12613-012-0564-8

10. Zhou, W., Long, T. Z., and Mark, C. K. 2007. Hot cracking in tungsten inert gas welding of magnesium alloy AZ91D. *Materials Science and Technology* 23: 1294-s to 1299-s. DOI: 10.1179/174328407X213026

11. Chen, Y., Fan, C., Lin, S., and Yang, C. 2023. Effect of tungsten inert gas welding parameters on hot crack sensitivity of cast magnesium alloy. *Journal of Materials Engineering and Performance* 32: 1382-s to 1389-s. DOI: 10.1007/s11665-022-07192-7

12. Zhang, E., Yin, D., and Xu, L., et al. 2009. Microstructure, mechanical and corrosion properties and biocompatibility of Mg–Zn–Mn alloys for biomedical application. *Materials Science and Engineering*: C 29: 987-s to 993-s. DOI: 10.1016/j.msec.2008.08.024

13. Yin, S., Zhang, Z., and Liu, X., et al. 2019. Effects of Y content on the microstructures and mechanical properties of Mg-5Zn-xY-0.6Zr Alloys. *Journal of Wuhan University Technology-Materials Science* 34: 138-s to 144-s. DOI: 10.1007/s11595-019-2027-9

14. Sun, M., Cheng, G., and Li, X., et al. 2024. Research status and prospect of Mg-Zn-Y magnesium alloys. *Nonferrous Metal Materials and Engineering* 45: 66-s to 77-s.

15. Liu B., Yang J., Wang Z., and Fang D. 2020. Effect of Y/Zn ratio on microstructure and properties of as-extruded Mg-Y-Zn alloys. *Materials Research Express* 7: 036530. DOI: 10.1088/2053-1591/ab8094

16. Tahreen, N., Zhang, D. F., and Pan, F. S., et al. 2018. Strengthening mechanisms in magnesium alloys containing ternary I, W and LPSO phases. *Journal of Materials Science & Technology* 34: 1110-s to 1118-s. DOI: 10.1016/j.jmst.2017.12.005

17. Xu D. K., Tang, W. N., and Liu, L., et al. 2008. Effect of W-phase on the mechanical properties of as-cast Mg–Zn–Y–Zr alloys. *Journal of Alloys and Compounds* 461: 248-s to 252-s. DOI: 10.1016/j.jallcom.2007.07.096

18. Chen, M. B., Pan, F. S., and Wang, J. F., et al. 2010. Effects of yttrium addition on microstructure and mechanical properties of extruded Mg-Zn-Y-Zr magnesium alloys. *Materials Science Forum* 650: 279-s to 284-s. DOI: 10.4028/www.scientific.net/MSF.650.279

19. Chen, X., Ning, S., and Wang, A., et al. 2020. Microstructure, mechanical properties and corrosion behavior of quasicrystal-reinforced Mg-Zn-Y alloy subjected to dual-frequency ultrasonic field. *Corrosion Science* 163: 108289. DOI: 10.1016/j.corsci.2019.108289

20. Jung, Y. G., Yang, W., and Hyun, J. I., et al. 2021. Effects of I- and W-Phases under identical conditions on microstructure and mechanical properties of as-cast Mg–Zn–Y alloys at room and elevated temperatures. *Metals and Materials International* 27: 5154-s to 5164-s. DOI: 10.1007/s12540-020-00848-w

21. Wang, Y., Huang, Y., and Meng, X., et al. 2017. Microstructural evolution and mechanical properties of Mg-Zn-Y-Zr alloy during friction stir processing. *Journal of Alloys and Compounds* 696: 875-s to 883-s. DOI: 10.1016/j.jallcom.2016.12.068

22. Xu, N., Shen, J., and Xie, W. D., et al. 2010. Abnormal distribution of microhardness in tungsten inert gas arc butt-welded AZ61 magnesium alloy plates. *Materials Characterization* 61: 713-s to 719-s. DOI: 10.1016/j.jmatchar.2010.04.003

23. Li, Y. J. 2005. *Performance and quality control of the welding*. Beijing: Chemical Industry Press.

24. Xu, N., Bao, Y. 2016. Enhanced mechanical properties of tungsten inert gas welded AZ31 magnesium alloy joint using two-pass friction stir processing with rapid cooling. *Materials Science and Engineering*: A 655 :292-s to 299-s. DOI: 10.1016/j.msea.2016.01.009

25. Liu, X., Gu, S., and Wu, R., et al. 2011. Microstructure and mechanical properties of Mg-Li alloy after TIG welding. *Transactions of Nonferrous Metals Society of China* 21: 477-s to 481-s. DOI: 10.1016/S1003-6326(11)60739-5

26. Zhou, W., Le, Q., and Ren, L., et al. 2023. Effect of welding current and Laves phase on the microstructures and mechanical properties of GTAW joints for ZC63 magnesium alloy. *Materials Science and Engineering*: A 872: 144954. DOI: 10.1016/j.msea.2023.144954

27. Chen, Z. H. 2005. *Wrought magnesium alloys*. Beijing: Chemical Industry Press.

28. Ma, C., Liu, M., and Wu, G., et al. 2003. Tensile properties of extruded ZK60-RE alloys. *Materials Science and Engineering*: A 349: 207-s to 212-s. DOI: 10.1016/S0921-5093(02)00740-2

29. Xu, J., Guan, B., Xin, Y., et al. 2022. A weak texture dependence of Hall–Petch relation in a rare-earth containing magnesium alloy. *Journal of Materials Science & Technology* 99: 251-s to 259-s. DOI: 10.1016/j.jmst.2021.04.076

30. Lotfpour, M., Emamy, M., Dehghanian, C., and Tavighi, K. 2017. Influence of Cu addition on the structure, mechanical and corrosion properties of cast Mg-2%Zn alloy. *Journal of Material Engineering and Performance* 26: 2136-s to 2150-s. DOI: 10.1007/s11665-017-2672-0

31. Liu, Y., Deng, C., Gong, B., and Bai, Y. 2019. Effects of heterogeneity and coarse secondary phases on mechanical properties of 7050-T7451 aluminum alloy friction stir welding joint. *Materials Science and Engineering: A* 764: 138223. DOI: 10.1016/j.msea.2019.138223

WEIYANG ZHOU, QICHI LE (qichil@mail.neu.edu.cn), **YE SHI**, and **TONG WANG** are with Key Lab of Electromagnetic Processing of Materials, Ministry of Education, Northeastern University, Shenyang, China. **QIYU LIAO** is with School of Materials Science and Engineering, Northeastern University, Shenyang, China, as well as with Key Laboratory of Lightweight Structural Materials, Liaoning Province, Northeastern University, Shenyang, China. **WENXIN HU** is with Baotou Research Institute of Rare Earths, Baotou, China.

Research on the Strengthening Mechanism of MWCNTs-Cu_f Composite Interlayer for Si_3N_4/TC4 Brazed Joints

An innovative approach using MWCNTs-Cu_f composite interlayer to reduce residual stress and enhance Si_3N_4/TC4 joint strength

BY B. LI, L. CAO, Q. LIU, J. GAO, AND R. LI

Abstract

With the rapid development of aerospace technology, the high-quality brazing connection between Si_3N_4 ceramic and TC4 titanium alloy has become a key factor in advancing the development of aircraft antenna covers. To improve the mechanical strength of the joints, this study used the electrophoretic deposition method to prepare a multi-walled carbon nanotubes-foam copper (MWCNTs-Cu_f) composite interlayer and selected the optimal deposition parameters. The most suitable brazing parameters under this interlayer were also determined. The joints' formation mechanism and fracture mode were revealed to elucidate the synergistic strengthening mechanism of the composite interlayer. The results showed that MWCNTs, based on their phase characteristics, produced high-density dislocations and fine crystal strengthening effects during the brazing cooling process. This effectively resisted the corrosion of the brazing material on the foam copper (Cu_f), protected the integrity of the foam copper framework, and exerted the excellent plastic deformation ability of foam copper (Cu_f). It reduced the residual stress in the joints, resulting in the highest shear strength of the MWCNTs-Cu_f composite interlayer, reaching 96.23 MPa. Compared with only adding Ag-Cu-Ti active brazing filler metal and adding ordinary foam copper interlayer, the shear strength increased by 78.2% and 44.7%, respectively.

https://doi.org/10.29391/2025.104.003

Keywords

- Si_3N_4/TC4
- MWCNTs-Cu_f Composite Interlayer
- Shear Strength
- Fracture Mode
- Strengthening Mechanism

Introduction

Si_3N_4 ceramics have emerged as a cutting-edge material for missile radomes because of their superior wave transmission capabilities and mechanical strength (Refs. 1–3). However, the inherent processing challenges of Si_3N_4 necessitate using a metal connecting ring to join the radome with the missile structure. TC4 titanium alloy, notable for its high specific strength, corrosion resistance, and exceptional overall properties, is poised to be the preferred choice over Invar alloy for this purpose (Ref. 4) Consequently, a high-quality bond between Si_3N_4 ceramics and TC4 titanium alloy is pivotal for advancing the development of aircraft radomes. Compared with the problems of high cost and stress concentration caused by cementation (Ref. 5) and mechanical connection (Refs. 6–8), brazing has gradually become the most widely used connection mode in ceramic-metal connections (Ref. 9) because of its advantages of less damage to the base metal, high precision, and low production cost. However, due to the significant differences in chemical bond types, thermal expansion coefficients, and elastic modulus between ceramics and metals, there are two difficulties in realizing high-quality brazing between them: the wettability of brazing filler metals to ceramics is poor, and it is difficult for brazing filler metals to spread on ceramic substrates after being heated and melted; The residual stress produced by a brazed joint greatly affects joint strength (Refs. 10–12). One strategy to mitigate the

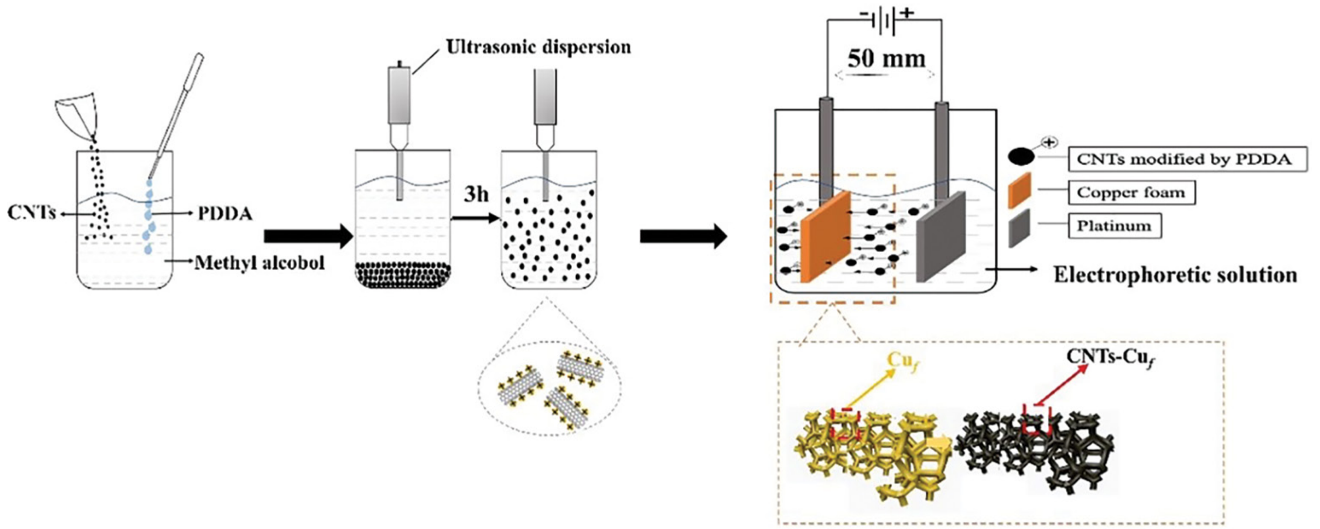

Fig. 1 — Schematic diagram of the electrophoretic deposition process.

residual stress in brazing involves incorporating reinforcement phases through direct mechanical ball milling or the in-situ reaction within traditional brazing filler metal to fine tune the thermal expansion compatibility with the base metal (Refs. 13–15). Song et al. (Ref. 16) integrated Si_3N_4 particles into the Ag-Cu-Ti brazing filler metal. This lessened the thermal expansion and modulus disparities between Si_3N_4 and the TiAl matrix, improving joint strength. Bridges et al. (Ref. 17) investigated the wetting and diffusion behavior of different shapes of silver nanomaterials (silver nanoparticles and silver nanowires) as filler materials during the laser brazing process of Inconel 718 and their influence on the strength of brazed joints. In addition, they achieved high joint strength of up to 243 MPa by synthesizing different nickel nanoparticles for Inconel 718 brazing joints. Based on this, they also elucidated the quantitative and qualitative influences of heating rate on microstructure and mechanical properties (Ref. 18). Alternatively, introducing an intermediate layer to create a composite brazing filler metal structure during brazing demonstrates great potential in improving bond performance (Refs. 19–21). Sun et al. (Ref. 22) utilized a W foil interlayer with Ag-Cu-Ti brazing filler metal to address the thermal expansion mismatch between Invar alloy and SiO_2 ceramics, preventing the formation of brittle Fe_2Ti and Ni_3Ti compounds, resulting in a 1.75-fold increase in shear strength. Brochu et al. (Ref. 23) selectively employed a Cu interlayer when brazing Si_3N_4 ceramics to FA-129 using 75Cu25Ti brazing filler metal, leveraging Cu's ductility to absorb residual stresses. Shirzadi et al. (Ref. 24) brazed Al_2O_3 ceramics to 316L stainless steel using a foam stainless steel interlayer and Ag-Cu-Ti brazing filler metal, exploring how the thickness of the foam interlayer impacts the joint's mechanical properties. Despite these advancements in strength optimization, relying solely on reinforcement methods such as adding nanoparticles or constructing a single intermediate layer does not yield the desired outcome in heterogeneous material bonding. In the composite brazing method, it is challenging to determine the optimal amount of reinforcement phase addition for improving the joint structure and performance. An insufficient reinforcement phase may not effectively reduce the thermal expansion coefficient of the brazing material. At the same time, excessive amounts can lead to phenomena such as accumulation in the brazing layer, resulting in decreased joint performance. In the intermediate layer method, new interfaces are formed at the joint, which is prone to cracks and voids due to differential properties with the brazing material and base metal. More importantly, they have not systematically elucidated dissimilar materials' reinforcement mechanisms and fracture modes.

To enhance the bonding quality between Si_3N_4 ceramics and TC4 titanium alloy, this study fully utilized the characteristics of multi-walled carbon nanotubes (MWCNTs), such as high strength and modulus and directed high thermal conductivity (Refs. 25–27), combined with foam copper, which possesses good ductility (Ref. 28). The electrophoretic deposition technique synthesized a multi-walled carbon nanotubes-foam copper (MWCNTs-Cu_f) composite interlayer. Comparative experiments led to the determination of optimal deposition parameters to achieve a uniform interlayer. The joint with the utmost strength was achieved by modifying the brazing temperature and dwell time. Additionally, analyses of the microstructure, elemental distribution, and fracture morphologies revealed three distinct fracture modes of the joint. The study sheds light on the collaborative reinforcement mechanism by which the MWCNTs-Cu_f composite interlayer fortifies the brazed joints, affirming the composite's reinforcing impact.

Experimental Procedures

The experimental base materials comprised MWCNTs sourced from Pioneer Nanomaterials Technology Co., Ltd., featuring diameters between 5–15 nm, lengths spanning 10–30 µm, and a purity exceeding 95%. The Ti-6Al-4V alloy, commonly recognized as TC4 titanium alloy, consisting pri-

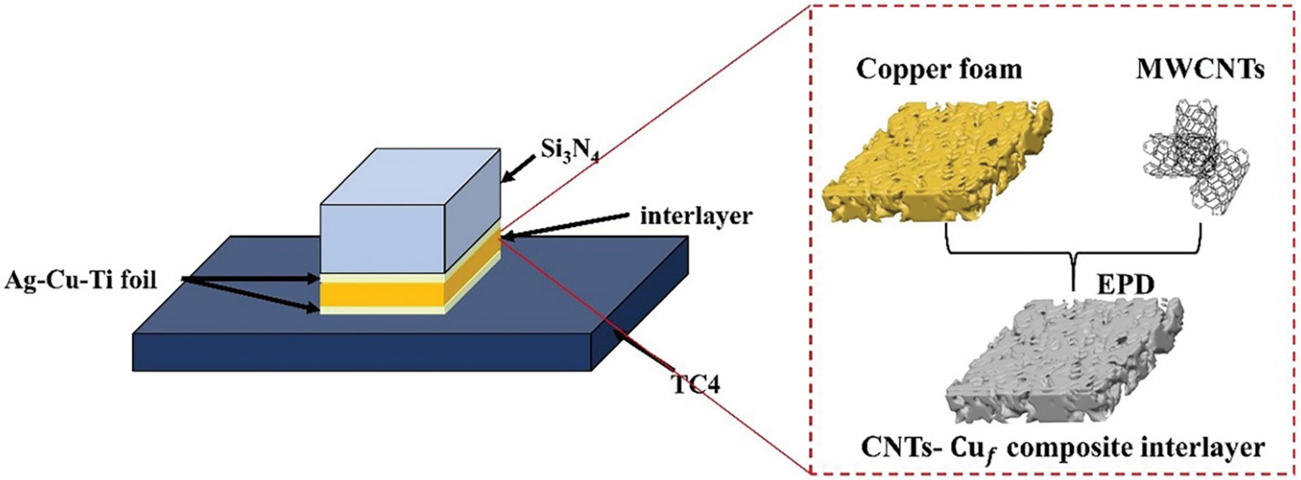

Fig. 2 — Schematic diagram of assembly form of sample to be brazed.

marily of α and β phases, was procured commercially. Si_3N_4 ceramics were obtained from Hyde Precision Ceramics, measuring 5 × 5 × 5 mm^3, with a 3.2 g/cm^3 density and a coefficient of thermal expansion (CTE) of 3.2×10^{-6}/K.

The foam copper was sectioned into 5 × 5 × 1 mm^3 pieces, followed by degreasing in a 1:1 volumetric mixture of acetone and absolute ethanol for 30 min to eliminate any oil residues. Subsequently, the foam underwent a 30-min immersion in a 6 mol/L hydrochloric acid (HCl) solution to remove surface oxides. The preparation of the electrolyte involved weighing 30 mg of acid-cleaned MWCNTs and 60 mg of dimethyl diallyl ammonium chloride (PDDA), which were then introduced into 100 ml of methanol, stirred thoroughly, and dispersed via ultrasonic agitation for three hours.

The MWCNTs-Cu_f composite interlayer fabrication employed the electrophoretic deposition technique to embed MWCNTs within the copper foam, as depicted in Fig. 1. The copper foam served as the cathode for the electrophoretic deposition process, with platinum acting as the anode. The plates were positioned with a fixed separation of 50 mm.

The TC4 titanium alloy was sectioned into specimens of dimensions 20 × 10 × 3 mm^3 and 10 × 10 × 3 mm^3 using a wire-cutting machine followed by sanding to achieve a smooth surface. Similarly, Si_3N_4 ceramic samples were sliced to 5 × 5 × 5 mm^3 using a diamond wire saw and subsequently polished to remove any surface imperfections. The Ag-Cu-Ti brazing foil and the MWCNTs-Cu_f composite interlayer were trimmed to 5 × 5 mm square pieces. Before brazing, the base metals, brazing foil, and interlayer were cleansed in an acetone solution for 15 min. This process was repeated three times to ensure the removal of any surface contaminants.

The prepared MWCNTs- Cu_f composite interlayers were an intermediary in brazing Si_3N_4 ceramics to TC4 titanium alloy. The base metal, brazing filler metal, and interlayer were stacked in a sandwich configuration and secured using an adhesive, as depicted in Fig. 2. To ensure optimal contact and adherence during the brazing process, the assembled stack was placed into a custom-designed metal fixture, where pressure was applied to maintain tight interfacing between the brazing filler metal and the base metals.

The TL1200 vacuum tube furnace was utilized for the brazing process, with a maximum operational temperature cap of 1200°C. Vacuum levels within the tube during the heating cycle were maintained between 1×10^{-3} and 5×10^{-3} Pa, achieved by sequential usage of a mechanical pump followed by a molecular pump. Initially, the tube furnace was ramped up to 300°C at a rate of 10°C/min and held at this temperature for 30 min to ensure complete volatilization of the binder used in sample assembly. The temperature was then increased to the target value at a rate of 6°C/min and maintained for a designated duration. This study explored how variations in brazing temperature and hold time influenced the strength of the joint. During the cooling phase, the furnace's decrement rate was regulated at 5°C/min down to a temperature of 400°C. This controlled rate of cooling was intended to avert potential thermal deformation and the generation of residual stress that could arise from rapid temperature change. After reaching 400°C, the assembly was allowed to cool to ambient temperature within the furnace's environment.

Results and Discussion

Morphology and Characterization of Intermediate Layer

Given the nanoscale dimensions and significant aspect ratio of MWCNTs, they tend to tangle owing to van der Waals forces within a solution, making their even distribution in an electrolyte a challenge. To address this, an acid washing process was applied to not only cleanse the surface of oily contaminants but also to introduce hydroxyl functional groups. When ionized in the solution, these functional groups endow MWCNTs with a negative charge, enhancing the electrostatic repulsion between the individual MWCNTs (Ref. 29). Nonetheless, acid washing alone does not suffice to induce a directional movement of MWCNTs under an electric field; the addition of electrolyte ions is necessary. To this end, dimethyl diallyl ammonium chloride (PDDA) was incorporated at a mass ratio of 2:1 concerning MWCNTs to facilitate surface modification through ion introduction. The process harnesses π-π bonding (Ref. 30) through conjugation, enabling PDDA to attach to the MWCNTs' exterior, consequently imparting a positive charge to them. Post ultrasonic agitation, this treatment yielded a stable dispersion of MWCNTs within methanol. This stable dispersion was subsequently deposited onto the foam copper to fabricate the composite interlayer.

To achieve an optimally uniform deposition morphology, various experimental parameters were systematically varied, as illustrated in Fig. 3. At excessively low deposition voltages, abbreviated deposition durations, and minimal MWCNT concentrations, the surface of the foam copper was coated with a mere single layer of MWCNTs. This suboptimal coverage failed to harness the potential reinforcement properties of MWCNTs for subsequent brazing tests. Conversely, when deposition times are unduly prolonged and MWCNT concentrations are heightened, the predicament of MWCNT agglomeration arises, which may culminate in localized stress concentrations, undermining the strength of the resultant brazed joints. Through comparative assessment of disparate deposition voltages (80 V, 100 V, 120 V), varying deposition times (10 min, 20 min, 30 min), and distinct MWCNTs concentrations (0.2 mg/mL, 0.3 mg/mL, 0.4 mg/mL), the ideal set of parameters was pinpointed to attain a uniform interlayer morphology, specifically a voltage setting of 120 V, a deposition time of 20 min, and a MWCNTs concentration of 0.3 mg/mL. In addition, during the acid treatment process, acidic solutions can chemically corrode the surface of MWCNTs, leading to the formation of surface irregularities or corrosion pits. Subsequently, when using PDDA to modify the surface of carbon nanotubes to form functionalized carbon nanotubes, the surface is decorated by PDDA, and the uneven modification behavior inevitably results in surface roughening of the MWCNTs. This phenomenon can be observed in Fig. 3.

Effect of Composite Interlayer on Joint Strength under Different Brazing Temperatures and Holding Time

Brazing temperature and holding time also have a great influence on joint morphology, thus affecting joint strength. Fig. 4 shows the interface morphology of brazed Si_3N_4 ceramics and TC4 titanium alloy with a MWCNTs-Cu_f composite interlayer at different temperatures. Fig. 5 shows the interface morphology of brazed Si_3N_4 ceramics and TC4 titanium alloy with a MWCNTs-Cu_f composite interlayer under different holding times. When the brazing temperature was too low,

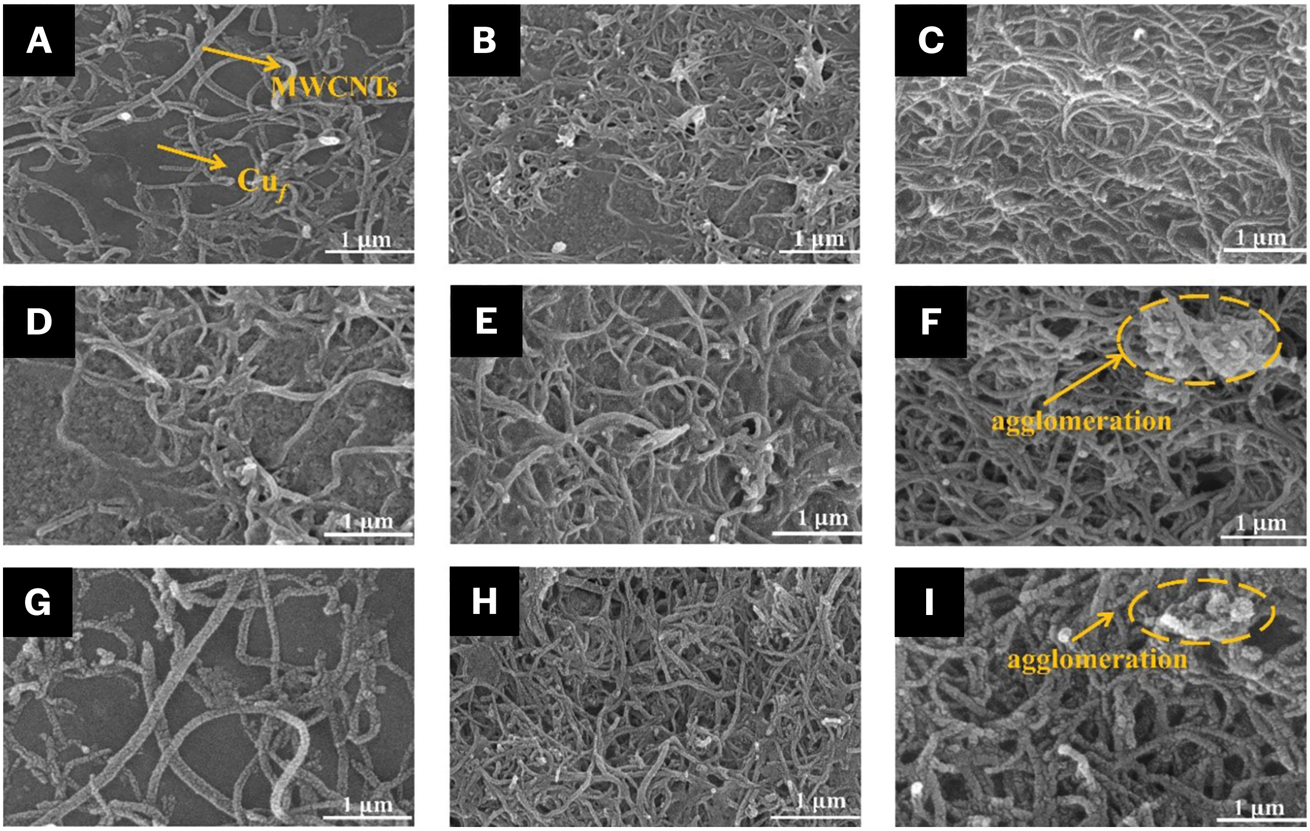

Fig. 3 — SEM of different processes: (A–C) SEM of interlayer under different deposition voltages: A — 80 V; B — 100 V; C — 120 V; (D–F) SEM at different deposition times: D — 10 min; E — 20 min; F — 30 min; (G–I) SEM of interlayer under different MWCNTs: G — 0.2 mg/mL; H — 0.3 mg/mL; I — 0.4 mg/ml.

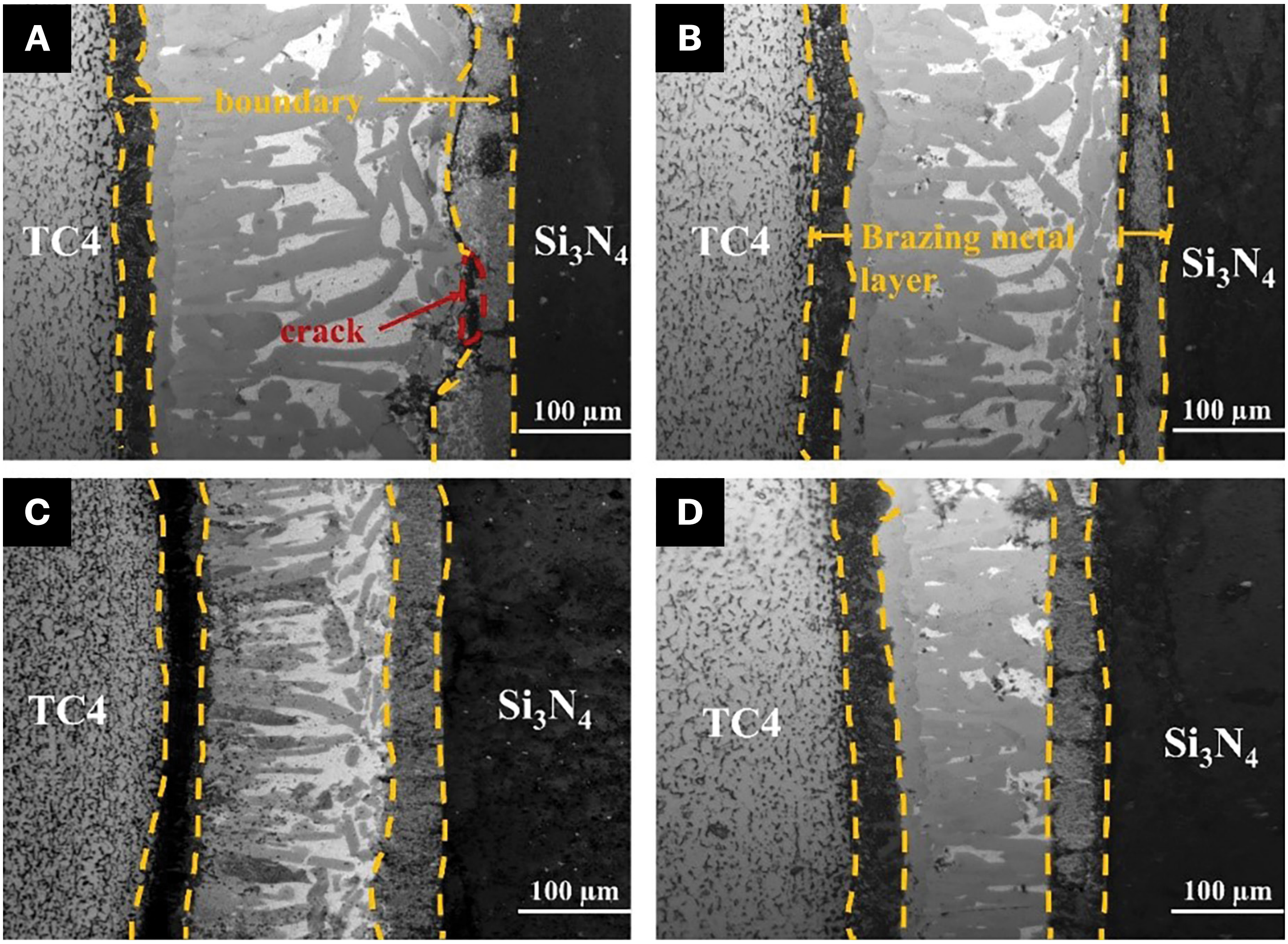

Fig. 4 — Effect of different brazing temperatures on microstructure and morphology of joint interface (holding time 10 min): A — 820°C; B — 850°C; C — 880°C; D — 910°C.

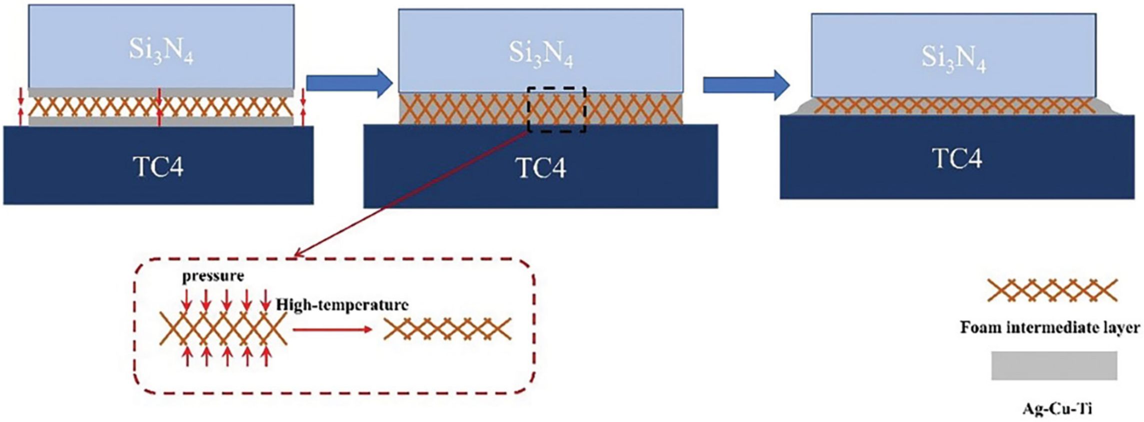

Fig. 5 — The mechanism of softening and collapse of foam copper.

the fluidity of brazing filler metal was poor and could not completely flow into and fill the foam copper with porous structure, resulting in pores, which reduced the actual contact area and produced local stress concentration. Cracks initiated and developed here, which affected the joint strength. The shear strength of the joint was 75.64 Mpa. When the brazing temperature was slightly higher than the melting point of Ag-Cu-Ti, the pores of MWCNTs-Cu_f were filled by brazing filler metal, the whole brazing layer remained compact and continuous, and the foam copper skeleton further

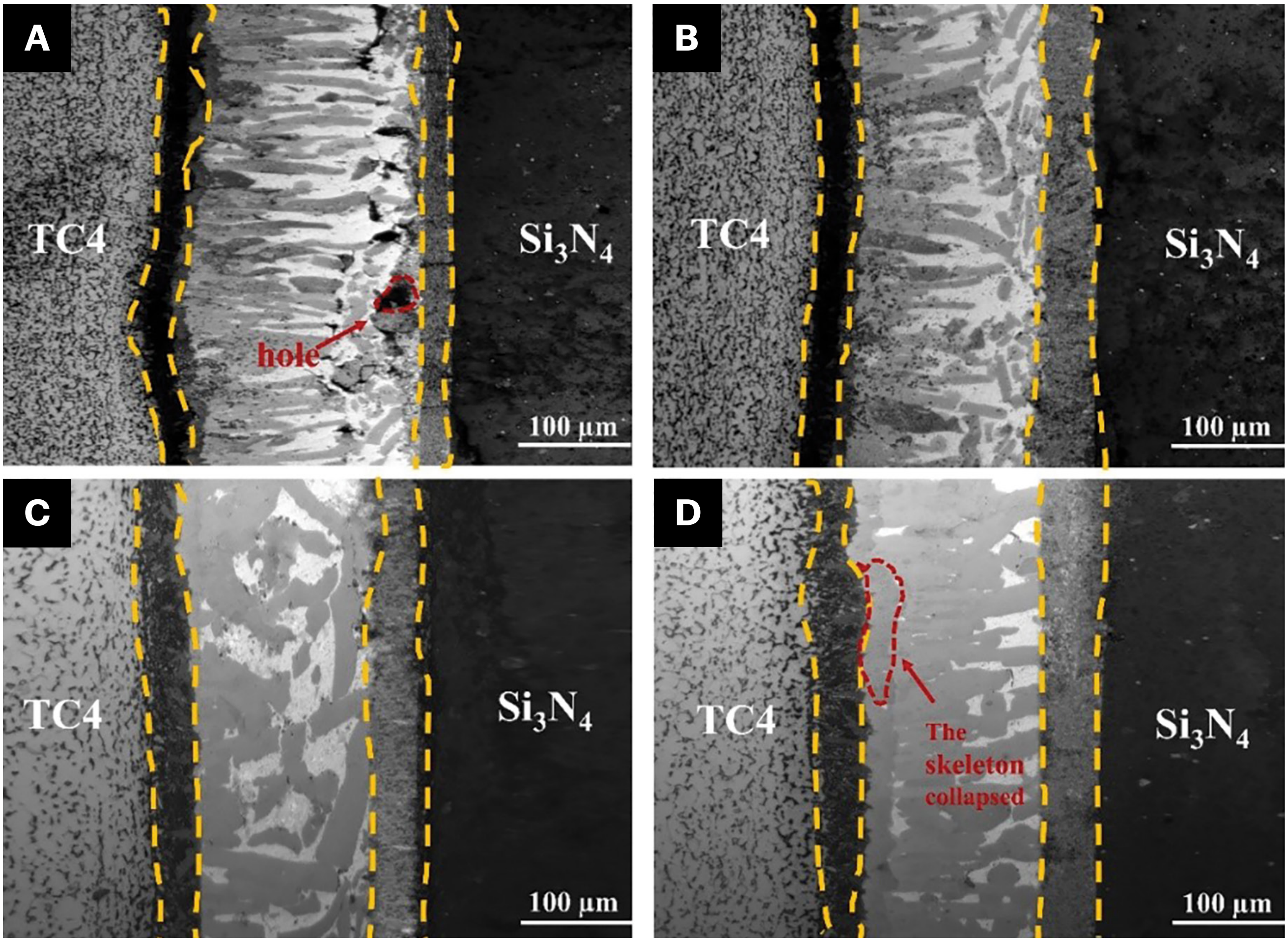

Fig. 6 — Effect of different holding times on microstructure and morphology of joint interface (brazing temperature 880°C): A — 5 min; B — 10 min; C — 15 min; D — 20 min.

softened. However, due to the existence of MWCNTs, the collapse of copper foam was hindered to a certain extent, so q was uniformly distributed in the brazing layer. At this time, the shear strength of the joint reached the maximum value of 96.23 MPa. Under the same process parameters, the shear strength of the joint without interlayer was only 54.24 MPa, and that of the joint with only common foam copper was 66.72 MPa. (Compared with the above two joints, the shear strength of the joint with MWCNTs-Cu_f composite interlayer was increased by 77% and 44%, respectively). When the brazing temperature was too high, the copper-based solid solution (Cu (s, s)) was distributed in the brazing seam in the form of blocks, which made the protection of MWCNTs to copper foam beyond the bearable range. At high temperatures, copper foam completely contacts with molten brazing filler metal, which leads to excessive softening and collapse and finally leads to the residual stress in the joint not being alleviated, resulting in a significant decrease in shear strength of the joint to 63.17 MPa. The reason for the collapse is that copper is a soft metal with good ductility and plastic deformation ability. Pure copper undergoes compressive deformation at high temperatures, and its peak stress decreases with increasing temperature. This indicates that as the brazing temperature increases, copper is more prone to plastic deformation. Foam copper, as a porous scaffold structure, has greater deformation capability compared to bulk copper, and its high-temperature softening phenomenon is more pronounced. Therefore, with the increase of brazing temperature or prolongation of insulation time, the degree of plastic deformation of the MWCNTs-Cu_f composite intermediate layer increases continuously while reacting with the brazing filler metal, and in actual brazing processes, to ensure tight contact between the brazing filler metal and the substrate without movement, pressure is usually applied to the top of the brazed sample. Considering the above reasons, the deformation softening of foam copper gradually intensifies, and collapse may even occur under excessively high brazing temperatures or prolonged insulation times, as shown in Fig. 5. The holding time also affects the flow of brazing filler metal. When the holding time was 5 min, a small number of holes appeared in the brazing seam. Because the holding time was too short, the brazing filler metal in the molten state began to cool down and solidify before filling the pores of the MWCNTs-Cu_f composite interlayer, the interfacial reaction layer was very thin, the load could not be effectively transmitted, and the shear strength of the joint was low, only 83.48 MPa. With the prolongation of holding time, Ag-Cu-Ti active brazing filler metal had enough time to flow into the MWCNTs-Cu_f skeleton and fill its pores, and the pores disappeared. Therefore, when the holding time was 10 min and 15 min, the whole brazed layer was continuous and intact, and the shear strength of the brazed joint was 96.23 MPa and 91.63 MPa, respectively. Under the above two conditions, MWCNTs always play an important role in preventing copper foam from being eroded by Ti in brazing filler metal. It can be observed from Figs. 6B and 6C that Cu (s, s) kept a uniform distribution, while when the holding time was extended to 20 min, some structures of MWCNTs collapsed at high temperatures for a long time, which seriously affected their properties, as shown in Fig. 6D. At the same time, the copper foam completely exposed to brazing filler metal softened seriously at continuous high temperature, and Cu (s, s) agglomerated and existed on the TC4 side in block form. The residual stress caused by the difference in thermal expansion coefficient of the joint could not be alleviated, and the shear strength of the joint was 86.47 MPa. On the whole, the change of holding time had little effect on the shear strength of brazed joints, as shown in Fig. 7B.

Subsequent analysis of joint element distribution with the improved parameters demonstrated that the brazing filler metal exhibited robust continuity and lacked apparent cracks, as evidenced by Fig. 8. The joint can be segregated into three distinct zones: Zone I is the could reaction layer adjacent to the TC4 titanium alloy; Zone II represents the brazing seam's core layer, while Zone III primarily comprises the Si_3N_4 ceramic interface reaction layer. These three zones were magnified, and EDS energy spectrum analysis was performed on different phases, with the outcomes presented in Table 1. Fig. 9 illustrates the microstructure of the three zones in greater detail. Per the EDS findings, Point A predominantly consists of Ti, Al, and V, with Ti present in the highest concentration, derived principally through the dissolution and diffusion of TC4. As for Points B through E, their composition is chiefly of Ti and Cu, albeit in varying ratios, suggesting the formation of a Ti-Cu intermetallic compound. Detailed element composition analysis of each point in Table 1 allows for delineating the reaction layer in Zone I as TC4/diffusion layer/Ti_2Cu/TiCu/Ti_3Cu_4/$TiCu_4$. Zone II is identified as the brazing layer, where a substantially dispersed, gray phase F predominantly consists of copper, signifying a copper-based solid solution (Cu (s, s)) resulting from the high-temperature softening and cooling solidification of foam copper. The lustrous white phase G is constituted of a silver-based solid solution (Ag (s, s)) and a minute quantity of the black J phase, consisting of Ti and C with an approximate 1:1 composition ratio, indicating the formation of TiC through the reaction between the brazing filler metal and TC4 substrate's Ti, as well as MWCNTs within the MWCNTs-Cu_f composite interlayer. Moreover, the brazing layer contains a eutectic structure, H. EDS data reveals an Ag-to-Cu ratio closely approximating 3:2, deduced as an Ag-Cu eutectic structure based on its morphological features. Zone III is the Si_3N_4 ceramic interface reaction layer, characterized by a predominance of Ti, N, and Si elements. It is inferred that Ti from the brazing filler metal reacts with the Si_3N_4 ceramic substrate upon diffusion, eventually forming a TiN + Ti_5Si_3 interface reaction layer, in concurrence with results obtained from Si_3N_4 ceramic brazing experiments using Ti-based brazing filler metal (Refs. 31, 32). Consequently, the reaction layer in Zone III is Ti_5Si_3/TiN/Si_3N_4. The copper diffusion and the erosive action of Ti flux on the copper foam are hypothesized to disrupt the foam's integrity, and the brittle phase precipitated by diffusion, such as TiC, may induce joint cracks and diminish structural fidelity. Concurrently, the reaction layer's thickness directly influences the brazing filler metal bead's breadth and engenders disparate residual stresses. Subsequently, we shall elucidate the specific mechanism by which MWCNTs impede elemental diffusion and employ finite element simulation to appraise the impact of brazing filler metal thickness on residual stress.

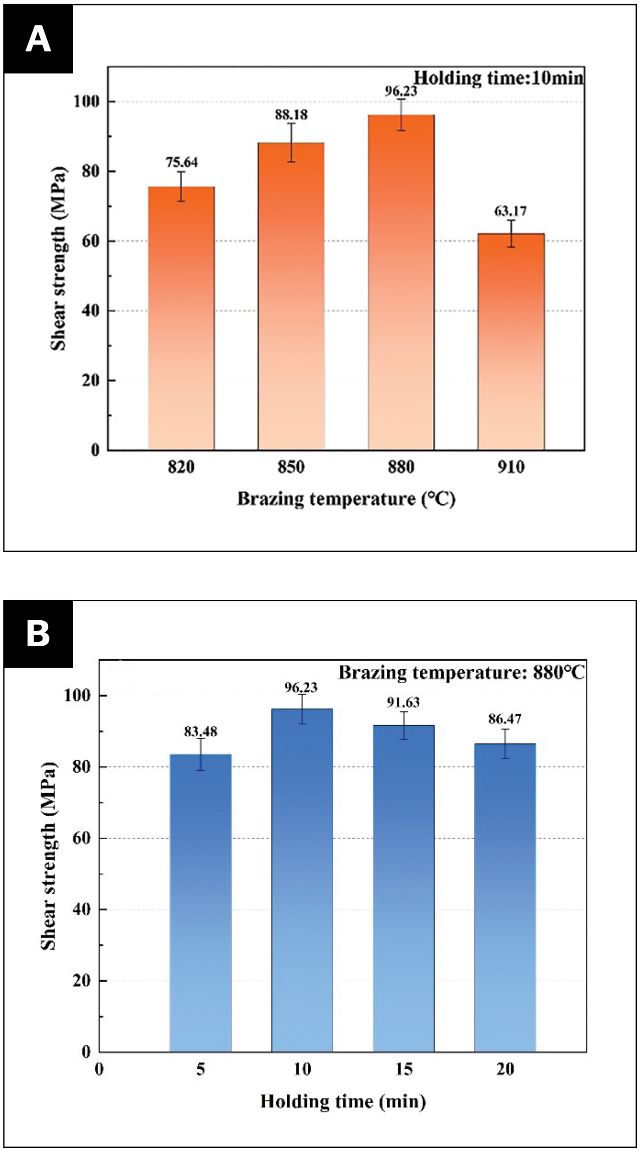

Fig. 7 — Shear strength of joint under different brazing parameters: A — Holding time 10 min and different brazing temperatures; B — brazing temperature 880°C and different holding times.

Formation Mechanism of Joint Morphology and Fracture Mode of Joint

Through the analysis of Table 1 and the EDS results, the formation mechanism of the overall morphology of the joint can be summarized as shown in Fig. 10. Fig. 10A shows the joint state at 25°C ≤ T ≤ 780°C (780°C is the melting point of Ag-Cu-Ti brazing filler metal). With the increase in temperature, the brazing filler metal kept close contact with the composite interlayer and brazing base metal under the pressure of Si_3N_4 ceramics. Atoms began to move violently, but they did not interact with the base metal, and the brazing filler metal remained solid because it had not reached its melting point. Fig. 10B shows that when the temperature reached the melting point of the brazing filler metal, the molten brazing filler metal began to spread between the base metals and immerse into the MWCNTs-Cu_f composite interlayer. Under the action of high-temperature liquid brazing filler metal, some of the base metals on both sides began to dissolve. Ti diffused in the direction of Si_3N_4 ceramics, while Cu diffused in the direction of the TC4 base metal. At the same time, many Ti elements and some Al elements in TC4 dissolved and diffused in the direction of the brazing filler metal, and the MWCNTs-Cu_f composite interlayer softened due to high temperature. Fig. 10C shows the holding stage, in which a large number of dissolved Ti elements and a small amount of Al elements attached to the TC4 side to form a diffusion layer, and Ti elements with the largest proportion reacted with Cu elements in the brazing filler metal to form TiCu compounds. Ti reacted with Si_3N_4 particles on the ceramic side to form TiN and Si, while the newly formed Si reacted with Ti to form Ti_5Si_3, forming a TiN + Ti_5Si_3 reactive layer on the ceramic side. Due to the protection of MWCNTs deposited on the surface, the diffusion of copper in copper foam was hindered, and the integrity of the foam copper structure was ensured. However, MWCNTs will adsorb a small amount of diffused Ti to the surface and react with it to form TiC. Fig. 10D shows the cooling stage. With the decrease in temperature and the consumption of Ti elements, Ti_3Cu_4/$TiCu_4$ reaction layers began to be formed in turn on the TC4 side. At the same time, Ti elements dissolved and diffused in TC4 have difficulty reaching equilibrium with the formed TiCu phase, and the solid solubility will decrease with the decrease of temperature, providing more nucleation driving force and forming Ti_2Cu compounds. Therefore, the final reaction layer on the TC4 side was composed of TC4/Ti_2Cu/TiCu/Ti_3Cu_4/$TiCu_4$. Ti and Si_3N_4 on the ceramic side were cooled and solidified by mutual reaction, and finally, Si_3N_4/TiN/Ti_5Si_3 was formed. The Cu foam maintained its skeleton structure after softening under the action of MWCNTs and dispersed in the brazing layer as a copper-based solid solution after

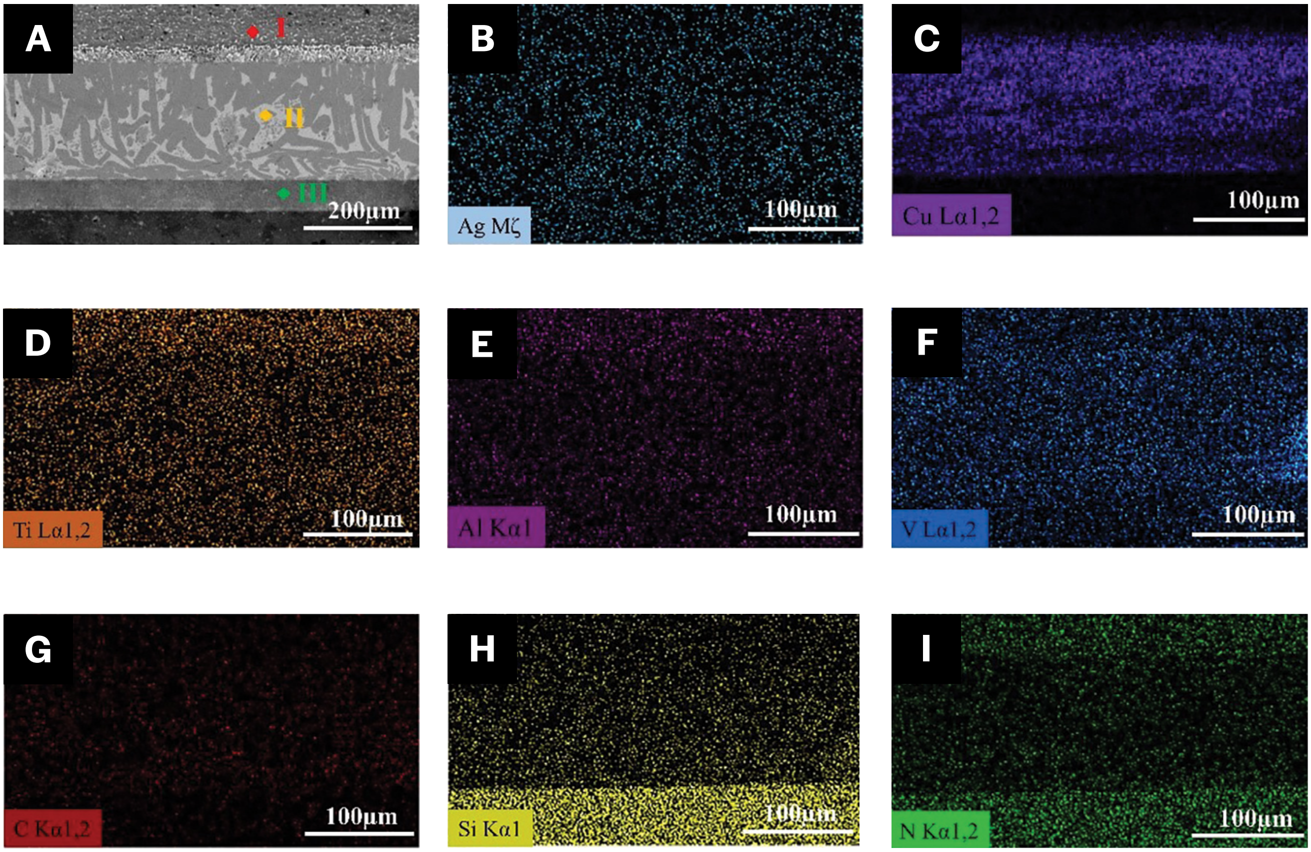

Fig. 8 — Microstructure and element distribution of Si_3N_4/Ag-Cu-Ti/MWCNTs-Cu_f/Ag-Cu-Ti/TC4 brazing joint (brazing temperature 880°C, holding time 10 min): A — The overall morphology of the joint; B — Ag; C — Cu; D — Ti; E — Al; F — V; G — C; H — Si; I — N.

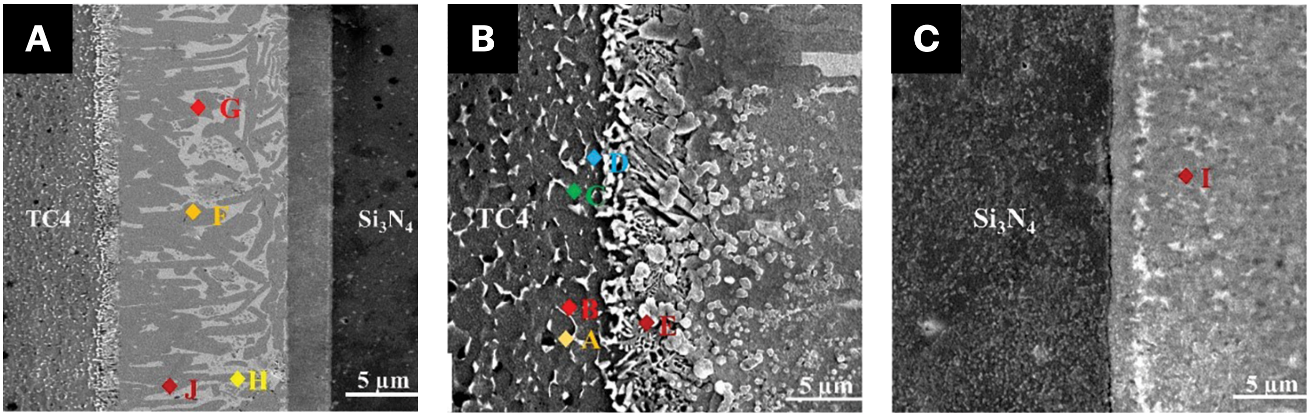

Fig. 9 — Interface microstructure of Si_3N_4/Ag-Cu-Ti/MWCNTs-Cu_f/Ag-Cu-Ti/TC4 joint in each region: A — Overall morphology; B — amplified portion of area (I); C — amplified part of area (III).

Table 1 — EDS Energy Spectrum Analysis Results of Elements at Each Point in Fig. 9 (at.-%)

Point	Ag	Cu	Ti	Al	V	Si	N	C	Phase
A	—	9.68	77.75	6.74	5.83	—	—	—	Diffusion layer
B	2.45	29.42	63.39	2.78	1.96	—	—	—	Ti_2Cu
C	0.58	47.42	49.17	1.68	1.15	—	—	—	TiCu
D	1.84	53.74	42.16	1.24	1.02	—	—	—	Ti_3Cu_4
E	2.87	74.87	18.62	1.35	0.67	—	—	1.62	TiCu4
F	2.56	94.64	2.58	—	—	—	—	—	Cu(s,s)
G	90.11	6.44	0.66	—	—	—	—	2.78	Ag(s,s)
H	63.46	34.79	1.75	—	—	—	—	—	Ag-Cu
I	1.02	9.11	44.04	0.62	0.38	17.93	26.91	—	TiN, Ti_5Si_3
J	3.65	4.42	46.57	—	—	—	—	45.36	TiC

cooling. At the same time, the molten brazing filler metal also cooled and solidified to form an Ag-Cu eutectic structure, with only a small amount of TiC compounds in the brazing layer, which improved the overall joint strength.

Finite Element Calculation Method

Based on the relationship between the thickness of the reaction layer and the width of the brazed joint, COMSOL Multiphysics finite element simulation software was used in this study to calculate the residual stress under different brazed joint widths and to investigate the effect of the reaction layer thickness on joint strength (Ref. 33). In this study, a geometric model of the assembly of Si_3N_4 ceramic and TC4 titanium alloy brazing samples was first established in a 1:1 ratio, and the constructed Si_3N_4/TC4 brazing geometric model meshed, as shown in Fig. 11. In analyzing residual stress distribution in Si_3N_4/TC4 brazed joints, the core research area was the composite brazed seam and its interface with the base material. Therefore, an ultra-fine mesh division method was applied to this area. The mesh of the composite brazed seam and its interface with the base material was set to be a free tetrahedral mesh, with a maximum element size of 0.7 mm, a minimum element size of 0.03 mm, a maximum element growth rate of 1.35, and a curvature factor of 0.3. To ensure both accurate calculation results and computational efficiency, relatively sparse mesh division methods were applied to other areas of the TC4 titanium alloy and Si_3N_4 ceramic base materials. Similarly, the mesh of this area was also set to be a free tetrahedral mesh, with a maximum element size of 1.6 mm, a minimum element size of 0.2 mm, a maximum element growth rate of 1.45, and a curvature factor of 0.5. as shown in Figs. 11C and D. In this finite element analysis of residual stress distribution, the Si_3N_4/TC4 brazing geometric model had 12,309 mesh elements, with a minimum element quality of 0.2204 and an average element quality of 0.6427.

After solving with COMSOL software, the final result was obtained. Fig. 12 shows the calculated equivalent stress ofSi_3N_4/TC4 joints with MWCNTs-Cu_f composite intermediate layers brazed using different brazed joint widths. The MWCNTs-Cu_f composite intermediate layer with brazed joint widths of 0.1 mm,0.2 mm, 0.3 mm, and 0.4 mm were used. The von Mises stress on the TC4 side of the joint was very small, and it gradually increased as it approached the brazed layer, with a jump-like increase at the interface between TC4 and the brazed layer. The residual stress of the joint gradually decreased after reaching the maximum value at the interface between the brazed layer and the Si_3N_4 ceramic. The maximum residual stresses were 179 MPa,167 MPa, 134 MPa, and 146 MPa, respectively, and the residual stress reached its minimum value when the brazed joint width was 0.3 mm, which resulted in the highest joint strength. Compared to joints brazed directly with brazing materials, the peak residual stress of the brazed joints with an added composite intermediate layer was reduced by 38.2%. (The material properties and simulation boundary conditions are in the Appendix.)

Based on a 10-min insulation period, fracture morphology images (Fig. 13) and fracture surface EDS microstructures (Figs. 14A–C were obtained at different brazing temperatures, identifying three distinct fracture modes (Figs. 14D–F). When

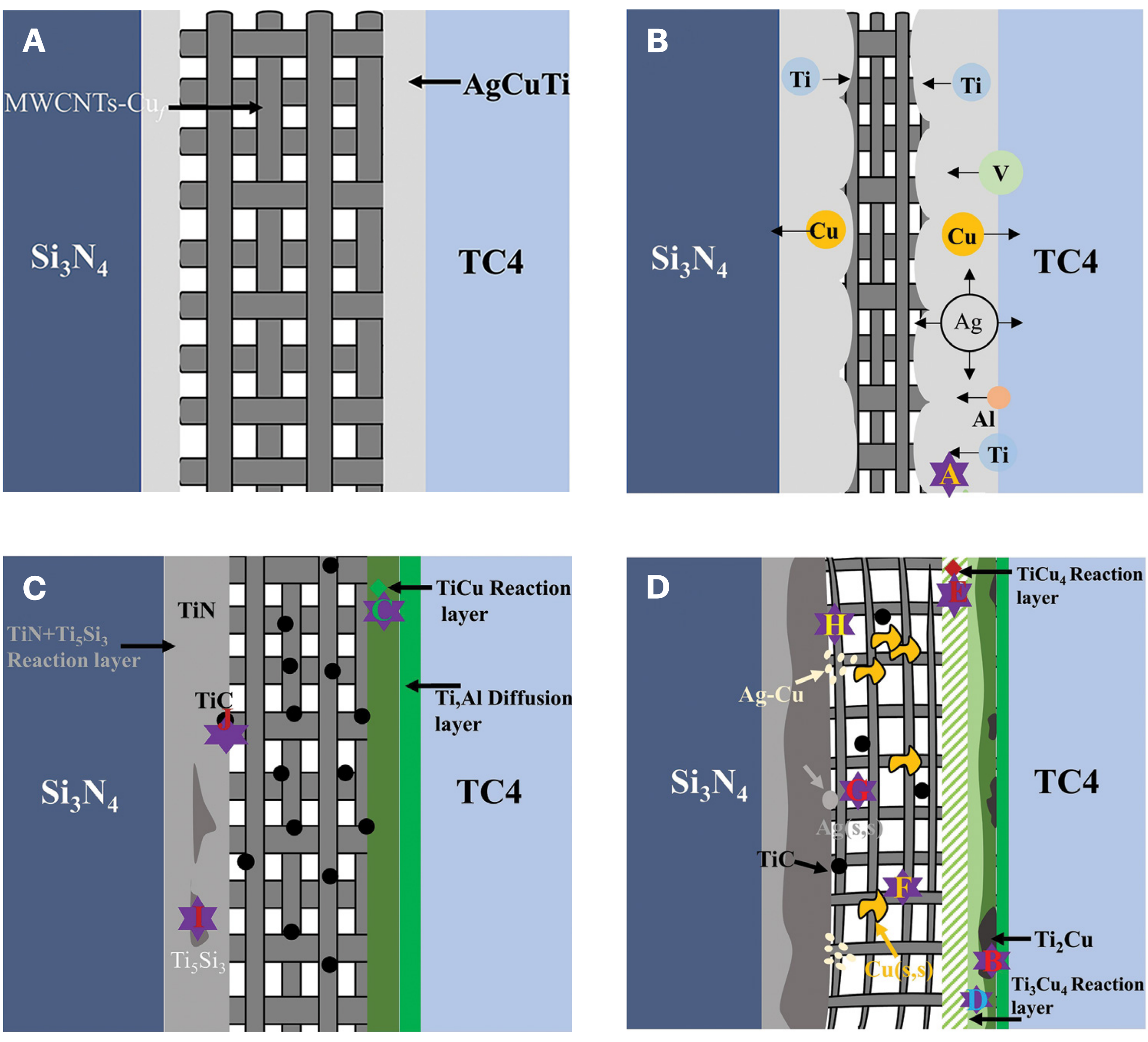

Fig. 10 — Schematic diagram of joint formation mechanism: A — Heating stage; B — the brazing filler metal melting stage; C — insulation stage; D — condensation stage (A-I is derived from the data in Table 1).

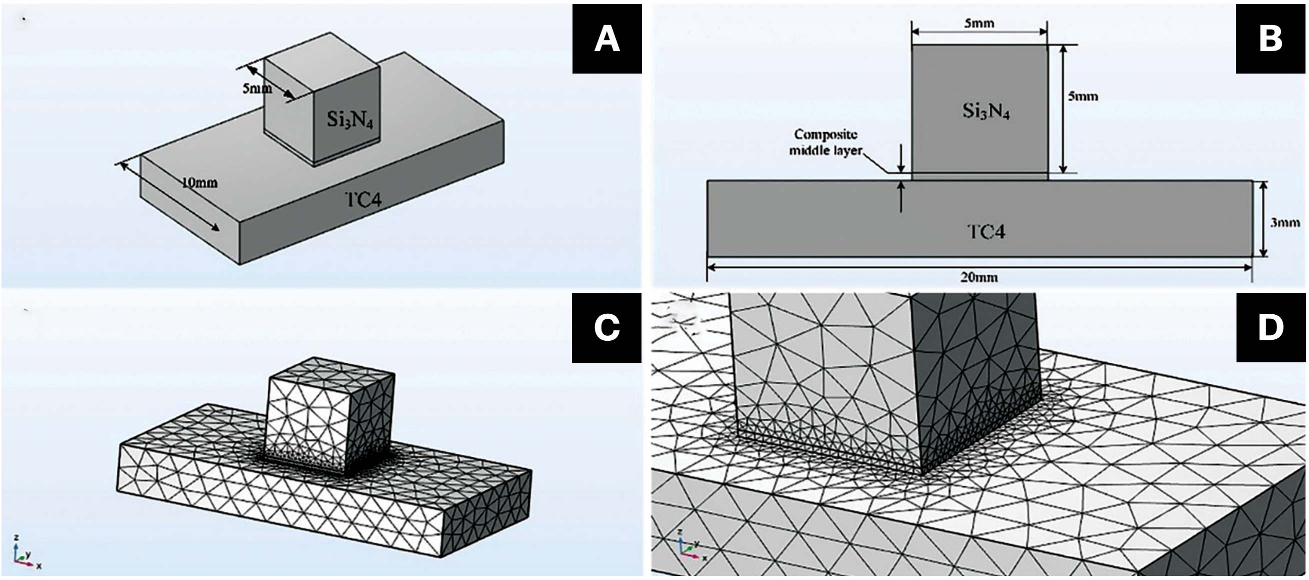

Fig. 11 — Geometric model and mesh partition diagram: A — Side view of the model; B — front view of the model; C — model meshing; D — partial enlarged view of model meshing.

the brazing temperature was 820°C, it was the first type of fracture mode, and cracks occurred from the interface and expanded along the interface. This was because the interface reaction layer was too thin, and the wettability of brazing filler metal to ceramic base metal was too poor. It lead to interface bonding failure and the lowest strength. When the brazing temperature was 850°C and 880°C, it was the second kind of fracture mode. Although this kind of fracture also occurred in the near-seam zone of ceramics, the crack did not only propagate in the near-seam zone of ceramics but passed through the brazing layer, and the fracture morphology had a small amount of brazing layer besides the ceramic base metal. The residual stress of the joint with this fracture mode is small. Therefore, under the action of external load, cracks occurred at the maximum stress of the joint and propagated along the brazing seam and finally broke. The joint strength of this fracture mode was higher. When the brazing temperature was further increased to 910°C, the third type of fracture mode occurred near the seam zone of ceramics, and the fracture path was arched. The interface adhesion between the ceramic and brazing filler metal layer was strong. Still, the difference in thermal expansion coefficients between the ceramic and metal brazing filler layer lead to axial tensile stress on ceramic base metal near the brazing filler metal layer during cooling. The maximum value occurred at the edges and corners of contact between the ceramic and brazing filler metal layer, so residual stress was difficult to release. Therefore, under the action of external load, cracks occurred and propagated at the edges and corners of the contact between ceramics and the brazing filler metal and finally showed an arched fracture path, resulting in low joint strength.

Through the above analysis, this paper summarizes the strengthening mechanism of composite interlayer: Firstly, the excellent plastic deformation ability and porous structure of foam copper as an intermediate layer in assisting brazing result in lower strain energy at the joints (Ref. 34) reduces residual stresses generated at the joint interface. Additionally, the carbon nanotubes deposited on its surface act as a barrier, preventing direct contact between Cu elements and the brazing filler metal at high temperatures, thus inhibiting their dissolution and diffusion. Therefore, throughout the brazing process, foam copper can maintain its porous scaffold structure, effectively mitigating the occurrence of collapse phenomena. This ensures the foam copper can uniformly disperse Cu (s,s) within the joint after cooling and solidification. Furthermore, the porous nature of foam copper allows the filling metal to occupy its voids, increasing the contact area between the filling metal and the intermediate layer. After cooling, Cu (s,s) distributes more evenly in the joint, resulting in refined microstructures. Secondly, the main issue with brazing filler metal to ceramic is the significant difference in the coefficient of thermal expansion between the base materials, leading to residual stresses during the cooling process. According to empirical formulas based on the mixture law, the coefficient of thermal expansion for Ag-Cu-Ti active filler metal is calculated to be 18.07×0^{-6}/K, which differs greatly from that of Si_3N_4 ceramic (3.2×10^{-6}/K). Adding carbon nanotubes can leverage their low coefficient of thermal expansion, reducing the joint's overall coefficient of thermal expansion. This effectively mitigates the difference in thermal expansion coefficients between Si_3N_4 ceramic and the joint, reducing residual stresses at the joint interface. Additionally, carbon nanotubes' extremely low coefficient of thermal expansion can generate high-density dislocations during brazing cooling, thereby inducing dislocation strengthening through slip bands (Ref. 35). According to the Orowan strengthening mechanism (Refs. 36, 37), MWCNTs act as second-phase particles belonging to non-deformable particles. When dislocation lines encounter them, they are bent around the NWCNTs due to obstruction. With increasing external stress, the bending intensifies until dislocations around the carbon nanotube particles meet and cancel out at the meeting point, leaving a dislocation loop around the MWCNTs. The entire process requires additional work, and

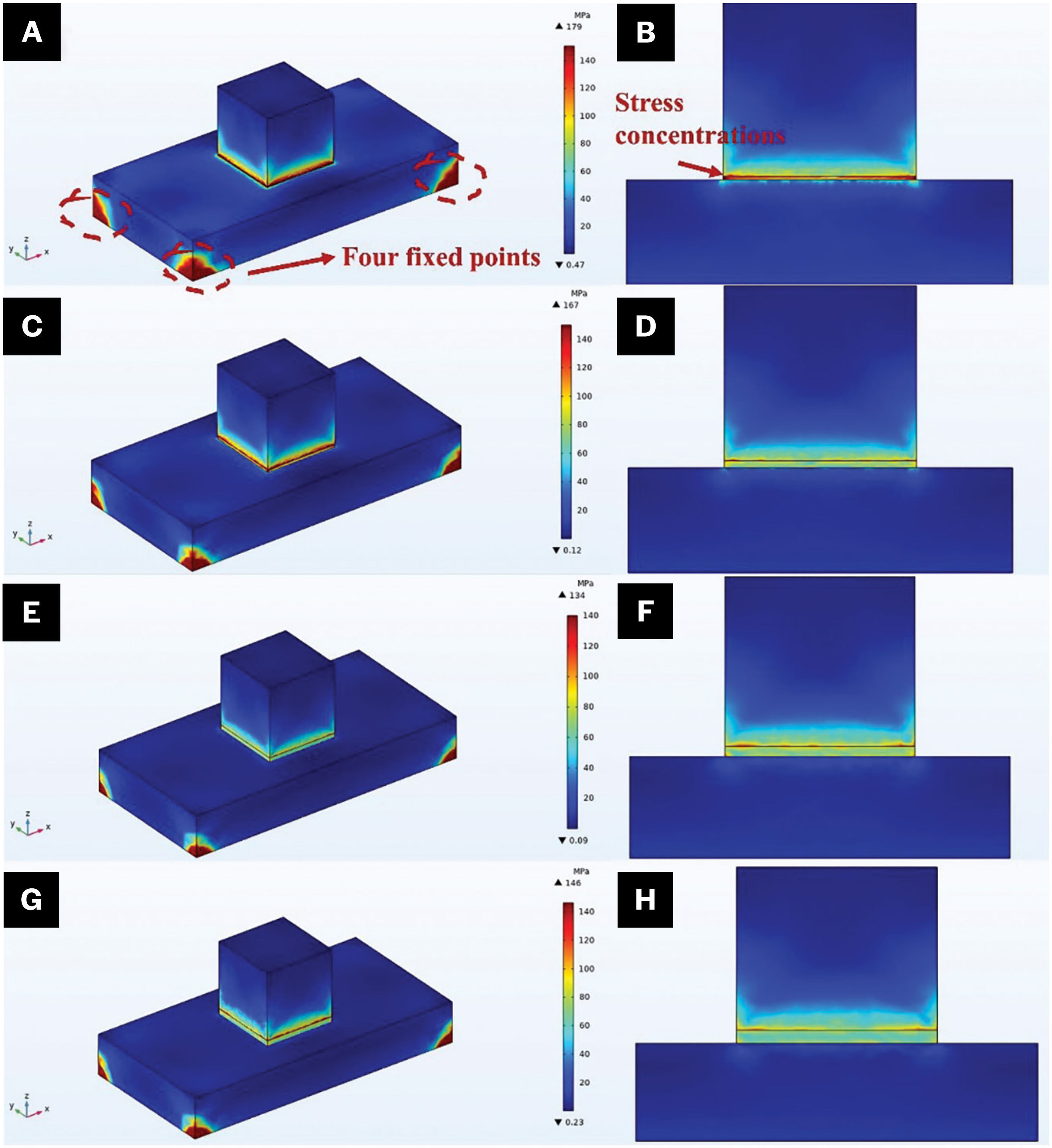

Fig. 12 — Equivalent stress distribution of Si_3N_4/TC4 joints brazed based on MWCNTs-Cu_f composite interlayer with different brazing widths: A–B — 0.1 mm; C–D — 0.2 mm; E–F — 0.3 mm; G–H — 0.4 mm.

the dislocation loop also hinders the movement of subsequent dislocations, leading to an increase in joint strength. Furthermore, the Orowan strengthening effect of carbon nanotubes is related to their diameter and spacing; the larger the diameter and the smaller the spacing, the more pronounced the Orowan strengthening effect. Moreover, according to the Hall-Petch theory (Ref. 38), when the material-to-surface area ratio is larger, the surface activity is greater, and the adsorption capacity is better. The good adsorption capacity of carbon nanotubes can adsorb Ti elements during the brazing reaction, thereby partially inhibiting the formation of Ti-Cu brittle compounds. The growth of the Ag-Cu eutectic structure requires overcoming interfacial free energy. At the same time, MWCNTs have a higher interfacial free energy, which can effectively inhibit the

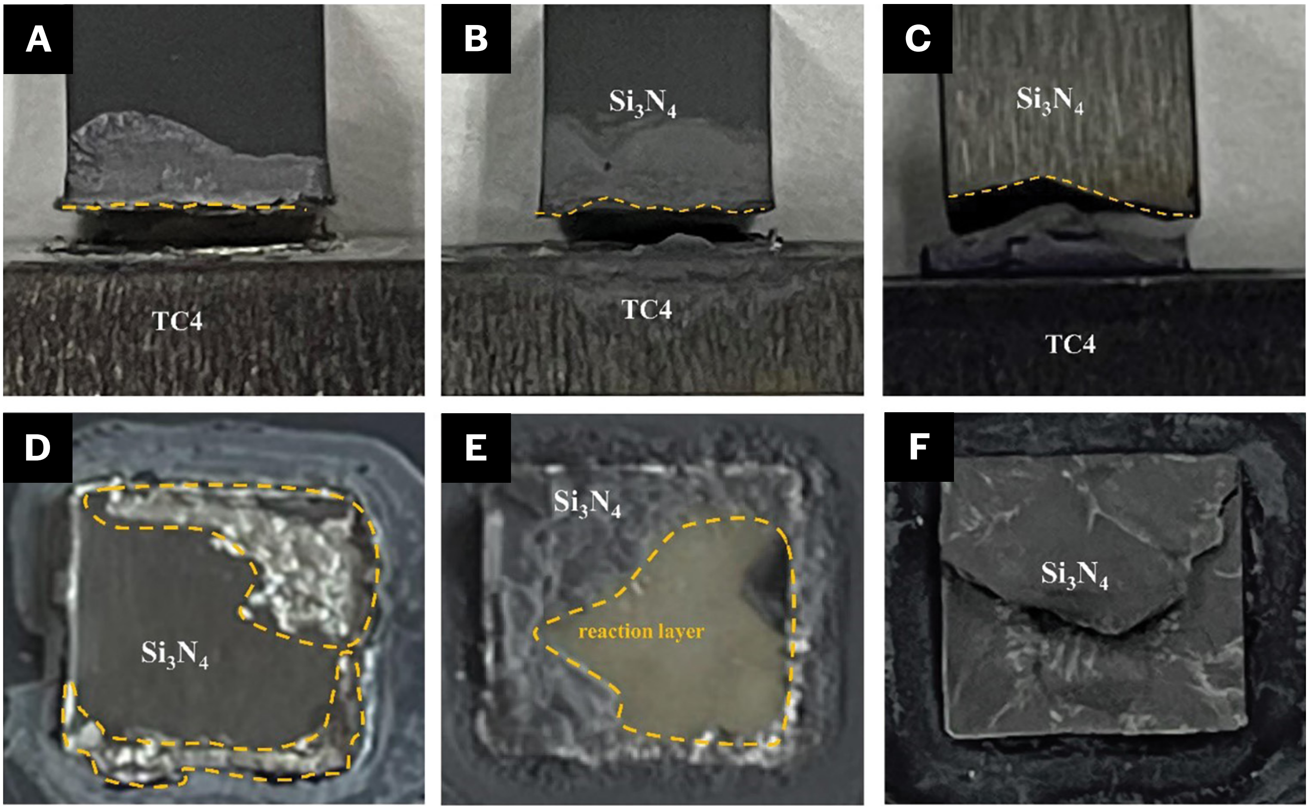

Fig. 13 — Sketch diagram of fracture morphology, fracture path of a joint under different brazing temperatures at 10 min holding time: A, D — 820°C; B, E — 880°C; C, F — 910°C.

Table 2 — EDS Energy Spectrum Analysis Results of Elements at Each Point in Fig. 14 (at.-%)

Point	Si	N	Ti	Cu	Ag	Al	C	O	Phase
A	37.45	49.65	—	—	—	—	7.27	5.63	Ceramic matrix
B	36.46	49.39	—	—	—	2.54	6.58	5.03	Ceramic matrix
C	18.57	11.54	41.77	7.69	0.88	7.94	5.23	6.38	Ceramic reaction layer
D	—	—	56.61	10.21	4.97	1.89	26.32	—	Brazed layer
E	15.31	12.58	45.66	8.32	2.38	3.69	2.38	9.68	Ceramic reaction layer

growth of the eutectic structure and refine the microstructure. According to the Hall-Petch formula: $\Delta\sigma_{\text{Hall-petch}} = Kd^{-1/2}$ (where K is a constant; d is the grain size in micrometers), the finer the grains, the higher the strength. A refined microstructure implies the presence of more grain boundaries, which can effectively prevent the generation of dislocations during brazing, thereby significantly enhancing the strength of the joint.

Conclusion

In this paper, the MWCNTs-Cu_f composite interlayer was prepared by electrophoretic deposition, and the best process of electrophoretic deposition was screened out. The effects of brazing temperature and holding time on the microstructure and shear strength of the joint were discussed in depth. The joint formation mechanism and fracture mode were analyzed, and the strengthening mechanism of

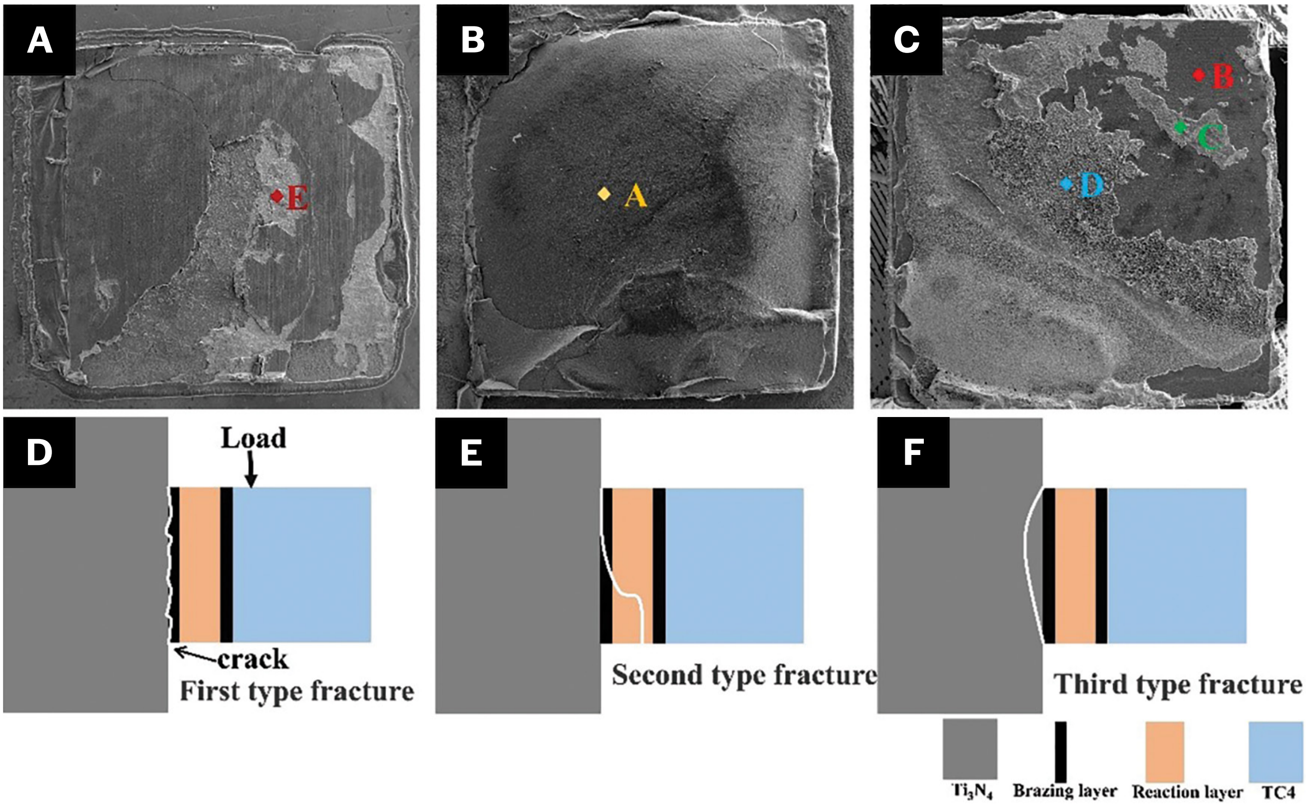

Fig. 14 — Fracture surface morphology diagrams and three types of fracture modes: A, D — 820°C; B, E — 880°C; C, F — 910°C (A-E is derived from the EDS data in Table 2).

MWCNTs and copper foam on brazed joints was clarified. The main conclusions are as follows:

1. When the concentration of MWCNTs was 0.3 mg/mL, the concentration of dimethyl diallyl ammonium chloride was 0.6 mg/mL, the deposition voltage was 120 V, and the deposition time was 20 min, the MWCNTs were deposited on the copper foam uniformly and densely. The optimum brazing parameters are a brazing temperature of 880°C and holding time of 10 min. The shear strength of the joint can reach 96.23 MPa, which is 78.2% and 44.7% higher than that of the joint with only Ag-Cu-Ti active filler metal and foam copper interlayer, respectively.

2. The porous structure and excellent plasticity of copper foam can enhance the contact area between copper foam and brazing filler metal, and the small strain energy can reduce the residual stress. The deposition of MWCNTs generated by electrophoresis on the surface of copper foam blocks the dissolution of Cu in copper foam to maintain the three-dimensional skeleton structure after brazing, giving full play to the porous structure and excellent plastic deformation characteristics of copper foam. The ratio of elements in brazing filler metal can remain unchanged so that the residual stress of the joint can be effectively relieved, and the shear strength can be improved.

3. When the width of the composite brazing seam is 0.3 mm, the residual stress reaches the minimum value of 134 MPa. Compared with the direct brazing of Si_3N_4/TC4 joint with Ag-Cu-Ti active brazing filler metal, the residual stress of the joint is reduced by 38.2% by adding a MWCNTs-Cu_f composite interlayer, which effectively relieves the residual stress of the brazing seam.

Authors' Contributions

Binbin Li conducted the experiment and numerical modeling. Binbin Li led data processing and manuscript preparation with contributions from all authors.

References

1. Guo, C., Fang, Y., and Laifei, C. 2021. In situ growth of single crystal Si_3N_4 nanowire foam with good wave-transparency and heat insulation performance. *Composites Part B: Engineering* 224(11): 109129. DOI: 10.1016/j.compositesb.2021.109129

2. Nag, A., Ramachandra Rao, R., and Panda, P. K. 2021. High temperature ceramic radomes (HTCR) - A Review. *Ceramics International* 47(15): 20793–20806. DOI: 10.1016/j.ceramint.2021.04.203

3. Wang, K., Liu, R., and Xu, H. 2022. High-strength and wave-transmitting Si_3N_4-Si_2N_2O-BN composites prepared using selective laser sintering. *Ceramics International* 48(14): 20126–20133. DOI: 10.1016/j.ceramint.2022.03.291

4. Clemens, H., and Mayer, S. 2013. Design, processing, microstructure, properties, and applications of advanced intermetallic TiAl alloys. *Advanced Engineering Materials* 15(4): 191–215. DOI: 10.1002/adem.201200231

5. Qin, W., Lin, N., Jin, F., and Huang, D. 2024. Effects of cementing matrix characteristics and particle size on the adhesion rule and mechanical properties of cemented granular materials. *Construction*

and Building Materials 411(1): 134630. DOI: 10.1016/j.conbuildmat.2023.134630

6. De Santis, Y., Aloisio, A., Pasquale Pasca, D., Gavrić, I., and Fragiacomo, M. 2024. Mechanical characterization of soundproofed inclined screws connections. *Construction and Building Materials* 412(1): 134641. DOI: 10.1016/j.conbuildmat.2023.134641

7. Ouyang, Y., and Chen, C. 2022. Research advances in the mechanical joining process for fiber reinforced plastic composites. *Composite Structures* 296(9): 115906. DOI: 10.1016/j.compstruct.2022.115906

8. Wei, K., Chen, Y., Li, M., and Yang, X. 2018. Strength and failure mechanism of composite-steel adhesive bond single lap joints. *Advances in Materials Science and Engineering* 2018: 1–10. DOI: 10.1155/2018/5810180

9. Liu, Y., Zhuang, W., and Wu, S. 2020. Damage to carbon fibre reinforced polymers (CFRP) in hole-clinched joints with aluminium alloy and CFRP. *Composite Structures* 234(2): 111710. DOI: 10.1016/j.compstruct.2019.111710

10. Liu, J., Zhang, J., Zhang, M., Wang, K., Zhang, A., Xiao, A., and Mao, C. 2023. Finite element analysis and experimental verification of residual stress in brazed diamond with Ni-Cr filler alloy. *Diamond and Related Materials* 139(11): 110350. DOI: 10.1016/j.diamond.2023.110350

11. Shu, X., Li, K., Li, Y., Xiong, Z., Huang, Y., and Li, S. 2022. Experimental investigation on brazing residual stress distribution in 304 L stainless steel core plate. *Journal of Constructional Steel Research* 193(6): 107257. DOI: 10.1016/j.jcsr.2022.107257

12. Yi, R., Chen, C., Shi, C., Li, Y., Li, H., and Ma, Y. 2021. Research advances in residual thermal stress of ceramic/metal brazes. *Ceramics International* 47(15): 20807–20820. DOI: 10.1016/j.ceramint.2021.04.220

13. Han, G. H., Bian, H., Zhao, H. Y., Song, X. G., Li, Y., Liu, D., Cao, J., and Feng, J. C. 2018. Interfacial microstructure and mechanical properties of TZM alloy and ZrC particle reinforced tungsten composite joint brazed using Ti-61Ni filler. *Journal of Alloys and Compounds* 747(5): 266–275. DOI: 10.1016/j.jallcom.2018.02.258

14. Han, G. H., Wang, Y. F., Zhao, H. Y., Song, X. G., Cao, J., and Feng, J. C. 2017. Vacuum brazing of TZM alloy to ZrC particle reinforced W composite using Ti-28Ni eutectic brazing alloy. *International Journal of Refractory Metals and Hard Materials* 69(12): 240–246. DOI: 10.1016/j.ijrmhm.2017.08.019

15. Sun, Z., Chen, X., Zhang, B., Bai, Y, J., and Zhang, L. X. 2022. Study on 3-dimensional graphene sponge reinforced C/C composites-TiAl alloy brazed joints. *Materials Science and Engineering: A* 839(4): 142832. DOI: 10.1016/j.msea.2022.142832

16. Song, X. G., Cao, J., Wang, Y. F., and Feng, J. C. 2011. Effect of Si_3N_4-particles addition in Ag-Cu-Ti filler alloy on Si_3N_4/TiAl brazed joint. *Materials Science and Engineering: A* 528(15): 5135–5140. DOI: 10.1016/j.msea.2011.03.032

17. Bridges, D., Ma, C., Zhang, S., Xue, S., Feng, Z., and Hu, A. 2018. Diffusion and wetting behaviors of Ag nanoparticle and Ag nanowire pastes for laser brazing of Inconel 718. *Welding in the World* 62(1): 169–176. DOI: 10.1007/s40194-017-0526-x

18. Bridges, D., Xu, R., and Hu, A. 2019. Microstructure and mechanical properties of Ni nanoparticle-bonded Inconel 718. *Materials & Design* 174(7): 107784. DOI: 10.1016/j.matdes.2019.107784

19. Ba, J., Lin, J., Wang, H., Qi, B., Zhong, Z., Wang, Z., Ma, Q., Qi, J., Cao, J., and Feng, J. 2018. Carbon nanotubes-reinforced Ni foam interlayer for brazing SiO_2-BN with Ti6Al4V alloy Using TiZrNiCu brazing alloy. *Ceramics International* 44(4): 3684–3691. DOI: 10.1016/j.ceramint.2017.11.136

20. Li, S., Du, D., Jiu, Y., Qin, J., Liu, Q., and Long, W. 2022. Brazing of C/C composite and TiAl alloy using TiNiSi filler metal added Cu interlayer. *Journal of Materials Engineering and Performance* 31(2): 1277–1284. DOI: 10.1007/s11665-021-06251-9

21. Yang, J. H., Zhang, L. X., Sun, Z., and Feng, J. C. 2019. A novel composite interlayer assembled for C/SiC-GH99 brazed joints. *Journal of Manufacturing Processes* 38(2): 543–548. DOI: 10.1016/j.jmapro.2019.01.030

22. Sun, Z., Zhang, L. X., Chang, Q., Zhang, Z. H., Hao, T. D., and Feng, J. C. 2018. Active brazed Invar-SiO_{2f}/SiO_2 joint using a low-expansion composite interlayer. *Journal of Materials Processing Technology* 255(5): 8–16. DOI: 10.1016/j.jmatprotec.2017.11.058

23. Brochu, M., Pugh, M. D., and Drew, R. A. L. 2004. Brazing silicon nitride to an iron-based intermetallic using a copper interlayer. *Ceramics International* 30(6): 901–910. DOI: 10.1016/j.ceramint.2003.10.011

24. Shirzadi, A. A., Zhu, Y., and Bhadeshia, H. K. D. H. 2008. Joining ceramics to metals using metallic foam. *Materials Science and Engineering: A* 496(1–2): 501–506. DOI: 10.1016/j.msea.2008.06.007

25. Gupta, N., Gupta, S. M., and Sharma, S. K. 2019. Carbon nanotubes: synthesis, properties and engineering applications. *Carbon Letters* 29(5): 419–447. DOI: 10.1007/s42823-019-00068-2

26. Moghaddari, M., Yousefi, F., Aparicio, S., and Hosseini, S. M. 2020. Thermal conductivity and structuring of multiwalled carbon nanotubes based nanofluids. *Journal of Molecular Liquids* 307(6): 112977. DOI: 10.1016/j.molliq.2020.112977

27. Takakura, A., Beppu, K., Nishihara, T., Fukui, A., Kozeki, T., Namazu, T., Miyauchi, Y., and Itami, K. 2019. Strength of carbon nanotubes depends on their chemical structures. *Nature Communications* 10(1): 3040. DOI: 10.1038/s41467-019-10959-7

28. Wang, Z., Wang, G., Li, M., Lin, J., Ma, Q., Zhang, A., Zhong, Z., Qi, J., and Feng, J. 2017. Three-dimensional graphene-reinforced Cu foam interlayer for brazing C/C composites and Nb. *Carbon* 118(7): 723–730. DOI: 10.1016/j.carbon.2017.03.099

29. Hou, P. X, Liu, C., and Cheng, H. M. 2008. Purification of carbon nanotubes. *Carbon* 46(15): 2003–2025. DOI: 10.1016/j.carbon.2008.09.009

30. Chen, X. H., Cheng, F. Q., Li, S. L., Zhou, L. P., and Li, D. Y. 2002. Electrodeposited nickel composites containing carbon nanotubes. *Surface and Coatings Technology* 155(2–3): 274–278. DOI: 10.1016/S0257-8972(02)00118-4

31. Lemusruiz, J., Leonpatino, C., and Aguilarreyes, E. 2006. Interface behaviour during the self-joining of Si_3N_4 using a Nb-foil interlayer. *Scripta Materialia* 54(7): 1339–1343. DOI: 10.1016/j.scriptamat.2005.12.014

32. Zhang, J., Guo, Y. L., Naka, M., and Zhou, Y. 2008. Microstructure and reaction phases in Si_3N_4/Si_3N_4 joint brazed with Cu-Pd-Ti filler alloy. *Ceramics International* 34(5): 1159–1164. DOI: 10.1016/j.ceramint.2007.02.006

33. Zhang, J., He, Y. M., Sun, Y., and Liu, C. F. 2010. Microstructure evolution of Si_3N_4/Si_3N_4 joint brazed with Ag-Cu-Ti+SiCp composite filler. *Ceramics International* 36(4): 1397–1404. DOI: 10.1016/j.ceramint.2010.02.010

34. Hasanzadeh, R., and Moradian, M. 2022. Recent developments in research on porous metals and foamed metals. *Metals* 12(9): 1486. DOI: 10.3390/met12091486

35. He, Y., Xu, H., Liu, Y., Chen, Y., and Ji, Z. 2022. Strengthening mechanism of B_4C@APC/Al matrix composites reinforced with bimodal-sized particles prepared by hydrothermal carbonized deposition on chips. *Journal of Materials Science & Technology* 123(10): 60–69. DOI: 10.1016/j.jmst.2022.01.012

36. Hadadzadeh, A., Baxter, C., Amirkhiz, B. S. and Mohammadi, M. 2018. Strengthening mechanisms in direct metal laser sintered $AlSi_{10}Mg$: Comparison between virgin and recycled powders. *Additive Manufacturing* 23(10): 108–120. DOI: 10.1016/j.addma.2018.07.014

37. Lee, T. J., and Kim, W. J. 2020. Microstructure and tensile properties of magnesium nanocomposites fabricated using mag-

nesium chips and carbon black. *Journal of Magnesium and Alloys* 8(3): 860–872. DOI: 10.1016/j.jma.2020.05.007

38. Tsao, L. C., Huang, C. H., Chung, C. H., and Chen, R. S. 2012. Influence of TiO_2 nanoparticles addition on the microstructural and mechanical properties of Sn0.7Cu nano-composite solder. *Materials Science and Engineering: A* 545(5): 194–200. DOI: 10.1016/j.msea.2012.03.025

Appendix: Material Properties and Boundary Conditions for the Simulation Section

Material Parameter Settings

For the determination of thermophysical parameters of composite braze joints, according to the homogenization theory of composite materials, the empirical formula of

Table 3 — Thermophysical Parameters of Ag-Cu-Ti Brazing Material and Cu (Ref.4)

Material	T (°C)	K (GPa)	G (GPa)	α ($10^{-6}K^{-1}$)	σ_s (MPa)
Ag-Cu-Ti	20	121.7	36.7	19.0	230
	200	109.5	33.0	19.7	170
	400	97.3	29.4	20.2	98
	600	81.5	24.6	20.5	25
	800	70.6	21.3	21.0	20
Cu	20	137.8	45.9	16.5	65
	200	122.2	40.7	17.2	60
	400	111.1	37.0	17.8	45
	600	66.7	22.2	19.4	30
	800	44.4	14.8	20.5	20

Table 4 — Thermophysical Parameters of Composite Braze Joint

	20°C	200°C	400°C	600°C	800°C
K_e/GPa	121.93	109.71	97.56	86.62	75.34
G_e/GPa	36.84	33.16	29.48	26.18	22.83
$\alpha_e/10^{-6}K^{-1}$	18.95	19.65	20.15	20.37	20.74
E_e/GPa	100.41	90.39	80.36	71.37	62.23
$\rho_e/g \cdot cm^{-3}$			9.49		
$\lambda/W \cdot (m \cdot K)^{-1}$			400		
$c/J \cdot (kg \cdot K)^{-1}$			24.98		

Table 5 — Thermophysical Parameters of Si_3N_4 Ceramics and TC4 (Refs. 5 and 6)

Materials	Temperature (°C)	Elastic Modulus (GPa)	Poisson's Ratio	Coefficient of Linear Expansion (10^{-6}/K)	Density (g/cm^3)	Specific Heat Capacity (J·kg·K)	Thermal Conductivity (W·m^{-1}·K^{-1})
Si_3N_4	—	320	0.25	3.28	3.19	711.8	12.6
TC4	200	109.8	—	9.9	—	1003	126
	400	99.9	0.34	10.8	4.51	1080	138
	600	89.9	—	11.3	—	1162	140
	800	79.9	—	11.5	—	1240	143

mixing law is adopted for the thermophysical parameters of some composite materials in most studies:

$$P = P_m(1 - V_{re}) + P_r V_{re} \quad (1)$$

where P is the properties of composites, P_m is the properties of the matrix material, V_{re} is the volume fraction of the reinforced phase in the composite material, and P_{re} is the Enhanced phase performance.

In practice, the empirical formula of mixing law cannot reflect the change of stress and strain of the reinforcing phase in matrix material, so it is not suitable for calculating the mechanical properties of complex composite braze joints, and it is easy to produce large errors to affect the calculation results. Therefore, based on the Mori-Tanaka model (Refs. 1, 2), a method for estimating the macroscopic equivalent properties of two microstructure composites is proposed, and the volume confinement modulus and shear confinement modulus are introduced:

$$\frac{1}{K_e + K^*} = \frac{\varphi_{cl}}{K_{cl} + K^*} + \frac{\varphi_s}{K_s + K^*} \quad (2)$$

$$\frac{1}{G_e + G^*} = \frac{\varphi_{cl}}{G_{cl} + G^*} + \frac{\varphi_s}{G_s + G^*} \quad (3)$$

where K_e is the bulk modulus (GPa) of the composite braze joint, K_{cl} is the bulk modulus (GPa) of the MWCNTs-Cu_f composite interlayer, K_s is the bulk modulus (GP) of the Ag-Cu-Ti brazing filler material, φ_{cl} is the volume fraction of the MWCNTs-Cu_f composite intermediate layer in the composite braze joint, φ_s is the porosity of copper foam, G_e is the shear modulus (GPa) of the composite braze joint, G_{cl} is the shear modulus (GPa) of MWCNTs-Cu_f composite interlayer, and G_s is the shear modulus (GPa) of the Ag-Cu-Ti brazing filler material. K^* and G^* can be represented as:

$$K^* = \frac{4(K_s G_{cl} - K_{cl} G_s)}{3(K_s - K_{cl}) + 4(G_s - G_{cl})} \quad (4)$$

$$G^* = \frac{6G_s(K_s + 2G_s)}{9K_s + 8G_s} \quad (5)$$

According to the relationship between elastic modulus, Poisson's ratio, bulk modulus, and shear modulus, it can be obtained:

$$E_e = \frac{9K_e G_e}{3K_e + G_e} \quad (6)$$

$$\gamma_e = \frac{3K_e - 2G_e}{6K_e + 2G_e} \quad (7)$$

where E_e is the modulus of elasticity (GPa) of the composite braze joint, and γ_e is the Poisson's ratio of composite braze seams.

Because Ag-Cu-Ti filler metal and MWCNTs-Cu_f composite interlayer are isotropic, and the interface bonding between the two phases is good at high temperatures, it conforms to the Kerner model (Ref. 3). Therefore, the expansion coefficient of the composite drill stitch is expressed as:

$$\alpha_e = \varphi_{cl}\alpha_{cl} + \varphi_s\alpha_s + \left[\frac{4G_s}{K_c}\right] \left[\frac{\varphi_{cl}(K_c - K_{cl})(K_c - K_{cl})}{4G_s + 3K_{cl}}\right] \quad (8)$$

where E_e is the linear expansion coefficient of the MWCNTs-Cu_f composite intermediate layer, α_s is the linear expansion coefficient (K^{-1}) of the Ag-Cu-Ti brazing filler material, and

K_c is the Hashin bulk modulus coefficient (Ref. 2) of the composite braze joint, the expression of which is:

$$K_c = \frac{\dfrac{\varphi_{cl}K_{cl}}{3K_{cl}+4G_s}+\dfrac{\varphi_s K_s}{3K_s+4G_s}}{\dfrac{\varphi_{cl}}{3K_{cl}+4G_s}+\dfrac{\varphi_s}{3K_s+4G_s}} \quad (9)$$

Therefore, the mechanical properties of the MWCNTs-Cu_f composite interlayer and Ag-Cu-Ti filler metal can be calculated based on the above-mentioned model. The mechanical properties of the composite brazing joint can be calculated. The equivalent elastic modulus, linear expansion coefficient, and Poisson's ratio of the composite brazing joint can be obtained based on the calculated mechanical properties of the MWCNTs-Cu_f composite interlayer and Ag-Cu-Ti filler metal.

The thermal physical parameters of the Ag-Cu-Ti brazing material and Cu are shown in Table 3. Additionally, the equivalent density (ρ), equivalent thermal conductivity (λ), and equivalent specific heat capacity (c) of the composite brazed joint are not affected by temperature. Due to the similar properties of foam copper and Ag-Cu-Ti brazing material and the high thermal conductivity of MWCNTs, calculations for the thermal physical parameters of the composite brazed joint can be directly performed using Equation 3, yielding results as shown in Table 4. The material supplier provides the thermal physical parameters of Si_3N_4 ceramics and TC4 titanium alloy, as indicated in Table 5.

Setting of Joint Boundary Conditions and Initial Conditions

Initial Conditions

During the heating and holding phases of the brazing process between Si_3N_4 ceramics and TC4, all three substrates remain in a free state, and stress only develops during the cooling stage when the brazing material solidifies. Therefore, only the cooling process is considered when calculating the residual stress distribution. The reference temperature for volume is set at 880°C. Under the brazing conditions of 880°C and 10 min holding time, Si_3N_4 ceramics do not undergo plastic deformation. Hence, only elastic deformation of the ceramics is considered in this calculation. Additionally, due to the high brazing temperature, the mechanical and physical properties of TC4 will undergo corresponding changes with increasing temperature. It is assumed that the physical and mechanical properties of Si_3N_4, the composite brazed joint, and TC4 are all isotropic.

Thermal Boundary Conditions

During the brazing process between Si_3N_4 ceramics and TC4, the overall sample size is relatively small and the cooling rate is slow. For ease of calculation, it can be assumed that the temperature within and outside the brazing sample is uniform and there is no temperature gradient. Therefore, based on actual experimental conditions, an initial temperature of 880°C was set for the overall sample, and a temperature curve was established, cooling at a rate of 5°C/min until reaching room temperature.

Mechanical Boundary Condition

In the actual brazing process, a certain pressure will be applied at the top to ensure the stability of the sample and tight contact between interfaces. In contrast, the bottom of the sample directly contacts the tubular furnace. Therefore, in setting the mechanical boundaries, fixed constraints were applied to the four points at the bottom of the sample to prevent any movement or rotation of the sample model during the cooling process.

During the brazing process of Si_3N_4/TC4 using an MWCNTs-Cu_f composite interlayer, the residual stresses in the joint are primarily influenced by the brazing temperature and cooling rate. Generally, rapid cooling rates result in higher residual stresses in the joint, adversely affecting brazing shear strength enhancement. Therefore, the process parameters adopted for this finite element analysis were as follows: an initial temperature of 880°C and a cooling rate of 5°C/min until reaching room temperature.

References

1. Gong, S., Li, Z., and Zhao, Y. Y. 2011. An extended Mori–Tanaka model for the elastic moduli of porous materials of finite size. *Acta Materialia* 59(17): 6820–6830. DOI: 10.1016/j.actamat.2011.07.041

2. Tsukamoto, H. 2010. A mean-field micromechanical model of thermal-ratcheting behavior in short fiber-reinforced metal matrix composites. *Acta Materialia* 58(10): 3709–3717. DOI: 10.1016/j.actamat.2010.03.008

3. Balch, D. K., Mortensen, A., Suresh, S., Shen, Y. L., Fitzgerald, T. J., and Michaud, V. J. 1996. Thermal expansion of metals reinforced with ceramic particles and microcellular foams. *Metallurgical and Materials Transactions A* 27(11): 3700–3717. DOI: 10.1007/BF02595462

4. Li, J. L., Xiong, J. T., and. Zhang, F. S. 2008. Transient liquid-phase diffusion bonding of two-dimensional carbon-carbon composites to niobium alloy. *Materials Science and Engineering: A* 483–484(6): 698–700. DOI: 10.1016/j.msea.2006.11.170

5. Chen, C., Liang, X., Luo, M., Zhou, S., Ji, J., Huang, Z., and Xu, M. 2019. Preparation and characterization of porous Si_3N_4-Bonded SiC ceramics and morphology change mechanism of Si_3N_4 whiskers. *Ceramics International* 45(5): 5922–5926. DOI: 10.1016/j.ceramint.2018.12.060

6. Zou, Z., Zeng, F., Wu, H., Liu, J., Li, Y., Gu, Y., Yuan, T., and Zhang, F. 2017. The joint strength and fracture mechanisms of TC4/TC4 and TA0/TA0 brazed with Ti-25Cu-15Ni braze alloy. *Journal of Materials Engineering and Performance* 26(5): 2079–2085. DOI:10.1007/s11665-017-2554-5

BINBIN LI (*bbli@nuaa.edu.cn*), **LIANGLIANG CAO**, **QIANLI LIU**, **JINGMIN GAO**, and **RUIBIN LI** are with the College of Materials Science and Technology, Nanjing University of Aeronautics and Astronautics, Nanjing, People's Republic of China.

PEER REVIEW PANEL

All papers published in the *Welding Journal's Welding Research Supplement* undergo peer review before publication for: 1) originality of the contribution; 2) technical value to the welding community; 3) prior publication of the material being reviewed; 4) proper credit to others working in the same area; and 5) justification of the conclusions, based on the work performed.

The following individuals serve on the AWS Peer Review Panel and are experts in specific technical areas. All are volunteers in the program.

Principal Reviewers

B. Alexandrov
M. Balmforth
E. Barrick
R. E. Baumer
H. R. Castner
J. Chen
J. Z. Chen
C. B. Dallam
A. Debiccari
T. DebRoy
X. Deng
M. Eff
J. D. Farren
P. Gadhe
A. Gerlich
J. E. Gould
M. Harris
D. Hartman
A. Hintze Cesaro
P. Hochanadel
R. Kant
J. Klemm-Toole
K. Li
L. Li
T. W. Liao
T. J. Lienert
D. Lin
W. Lin
Y. Liu
P. F. Mendez
W. C. Mohr
T. Mukherjee
T. W. Nelson
A. J. Orr
T. A. Palmer
A. J. Ramirez
J. Ramirez
G. W. Ritter
D. Susan
W. Tan
M. Tumuluru
G. Wang
P. C. Wang
Y. Wang
P. S. Wei
G. Wood
Y.-P. Yang
G. Young
X. Yu
Z. Yu
H. Zhang
Wei Zhang
WeJie Zhang
Y. M. Zhang
Y. N. Zhou

Individual Reviewers

D. K. Aidun
N. Barnes
D. Bechetti
A. M. Beese
J. L. Caron
K. J. Chan
Z. Chen
J. Craig
T. Dai
A. De
Z. Feng
C. Fink
S. R. Fiore
D. Grewell
T. Hong
A. Hu
D. S. Kim
A. Kumar
N. Ma
M. Marcus
S. Massey
M. P. Miles
J. Morgan
S.-J. Na
P. B. Nagy
A. M. Nasiri
W. F. Newell Jr.
T. C. Nguyen
N. E. Nissley
J. T. Norris
T. Oyama
G. Palardy
P. Pant
W. A. Peterson
T. Pickle
N. Porter
M. Posada
P. Prangnell
M. Prime
A. Rabinkin
S. Rose
G. G. Roy
D. J. Rybicki
E. F. Rybicki
A. Savitski
V. Sengupta
D. Shaffer
A. Shapiro
W. Sperko
R. T. Stone
S. Tate
H.-P. Wang
W. Wang
Z. Wang
C. Williams
C. S. Wu
J. Xie
F. Q. Yang
Z. Yang
X. Yue
C. Zhang
K. Zhang
R. Zhang

Arcos Delivers Solutions to Stainless Steel Alloy Welding Challenges.

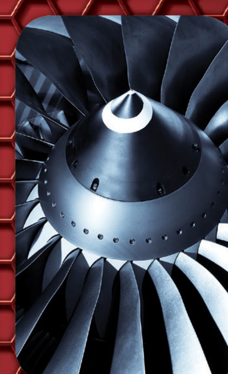

Arcos Industries, LLC offers over 100 stainless steel electrode products to handle the countless array of demanding welding applications that challenge you daily. Our reputation for exceptional quality and outstanding service ensures that you can depend on Arcos to provide you with the finest in bare wire, covered and tubular stainless steel alloy welding electrodes.

Discover for yourself how Arcos **stainless steel alloy electrodes** can help you solve your critical welding problems. Call us today at **800-233-8460** or visit our website at **www.arcos.us**.

Arcos

COOPER™ WELDING COBOTS

from The Welding Experts® at Lincoln Electric Automation

Cooper™ welding cobots safely deliver automation when and where you need it. Capitalizing on over 125 years of welding expertise, the Cooper Welding Cobot and easy-to-use Cooper App make collaborative welding as simple as Click Click Weld® - allowing operators to maximize quality, repeatability, and productivity quickly without being an expert.

Learn more about our game-changing, affordable cobot solutions at: lincolnelectric.com/cobots

AR24-02 | ©2024 Lincoln Global, Inc. All Rights Reserved.

LINCOLN® ELECTRIC